



# Heavy Higgs Boson Search in the Four Lepton Decay Channel with the ATLAS Detector

Denys Denysiuk

## ► To cite this version:

Denys Denysiuk. Heavy Higgs Boson Search in the Four Lepton Decay Channel with the ATLAS Detector. High Energy Physics - Experiment [hep-ex]. Université Paris-Saclay, 2017. English. NNT : 2017SACLS106 . tel-01681802v1

**HAL Id: tel-01681802**

**<https://theses.hal.science/tel-01681802v1>**

Submitted on 11 Jan 2018 (v1), last revised 17 Jan 2018 (v2)

**HAL** is a multi-disciplinary open access archive for the deposit and dissemination of scientific research documents, whether they are published or not. The documents may come from teaching and research institutions in France or abroad, or from public or private research centers.

L'archive ouverte pluridisciplinaire **HAL**, est destinée au dépôt et à la diffusion de documents scientifiques de niveau recherche, publiés ou non, émanant des établissements d'enseignement et de recherche français ou étrangers, des laboratoires publics ou privés.

NNT: 2017SACLS106

THESE DE DOCTORAT  
DE  
L'UNIVERSITE PARIS-SACLAY  
PREPARE A  
L'UNIVERSITE PARIS-SUD

LABORATOIRE : CEA SACLAY, IRFU/SPP

ECOLE DOCTORALE N°576

PARTICULES, HADRONS ÉNERGIE ET NOYAU: INSTRUMENTATION,  
IMAGE, COSMOS ET SIMULATION

SPÉCIALITÉ DE DOCTORAT : PHYSIQUE DES PARTICULES

PAR

**Denys Denysiuk**

**Heavy Higgs Boson Search in the Four Lepton  
Decay Channel with the ATLAS Detector**

Thèse présentée et soutenue à Gif-sur-Yvette, le 30 Juin 2017:

Composition du jury :

M. Stocchi, Achille	Professeur à l'Université Paris-Sud	President
M. Unal, Guillaume	Chercheur au CERN	Rapporteur
M. Bloch, Philippe	Chercheur au CERN	Rapporteur
M. Duehrssen, Michael	Chercheur au CERN	Examineur
M. Djouadi, Abdelhak	Chercheur à l'Université Paris-Sud	Examineur
M. Chauveau, Jacques	Professeur à l'Université Pierre et Marie Curie	Examineur
Mme. Hassani, Samira	Chercheur au CEA Saclay	Directrice de these
M. Schune, Philippe	Chercheur au CEA Saclay	Co-directeur de these





# Abstract

The thesis is focused on the heavy Higgs boson search in four lepton decay channel with Run-2 data from the ATLAS detector at the Large Hadron Collider. The analysis published at ICHEP 2016 conference that is based on  $14.8 \text{ fb}^{-1}$  of  $\sqrt{s} = 13 \text{ TeV}$  data is described in details, while the updated results that include  $36.1 \text{ fb}^{-1}$  of  $\sqrt{s} = 13 \text{ TeV}$  data are shown as well. The heavy Higgs search is carried out in a model independent way and it is covering different signal width hypotheses: narrow width approximation that assumes the signal natural width to be negligible comparing to the detector resolution, and the large width assumption including an effect of the interference with the Standard Model backgrounds. The search that benefits from additional kinematic discriminant under the scalar signal assumption is presented as well. This modification allows to increase the analysis sensitivity up to 25%.

The thesis also discusses an upgrade of the ATLAS Muons Spectrometer, namely the New Small Wheel project. In particular, simulation of the cavern background that will affect the upgraded detector and commissioning of the Micromegas modules produced at CEA-Saclay for the New Small Wheel are described.



# Contents

<b>1</b>	<b>Introduction</b>	<b>1</b>
<b>2</b>	<b>Theory overview</b>	<b>3</b>
2.1	The Standard Model . . . . .	3
2.1.1	General concept . . . . .	3
2.1.2	Particle dynamics . . . . .	4
2.1.3	Higgs boson as a consequence of spontaneous symmetry breaking . . . . .	6
2.2	The Standard model Higgs boson at LHC . . . . .	9
2.2.1	Mass constraints . . . . .	9
2.2.2	The SM Higgs production and decay modes at the LHC . . . . .	12
2.2.3	Discovery of the SM Higgs boson . . . . .	16
2.2.4	Properties of the new particle . . . . .	16
2.2.5	Summary . . . . .	20
2.3	Higgs sector beyond the Standard Model . . . . .	20
2.3.1	Real Electroweak singlet model (EWS) . . . . .	21
2.3.2	Two-Higgs-doublet model (2HDM) . . . . .	22
2.3.3	Considerations of the heavy Higgs search . . . . .	24
2.4	Heavy Higgs search with Run-1 data from ATLAS detector . . . . .	24
2.5	Signal line shape in LWA . . . . .	27
2.6	Interference . . . . .	29
2.6.1	Interference of the heavy Higgs with the SM Higgs . . . . .	30
2.6.2	Interference of the heavy Higgs with the SM $gg \rightarrow ZZ$ . . . . .	30
<b>3</b>	<b>The Large Hadron Collider and the ATLAS detector</b>	<b>33</b>
3.1	The Large Hadron Collider . . . . .	33
3.1.1	The accelerator complex . . . . .	33
3.1.2	The LCH experiments . . . . .	34
3.1.3	Luminosity and operation . . . . .	34
3.2	The ATLAS detector . . . . .	36
3.2.1	Naming conventions and coordinate system . . . . .	36
3.2.2	Inner detector . . . . .	37
3.2.3	Calorimeter . . . . .	39
3.2.4	Muon Spectrometer . . . . .	41
3.2.5	Trigger system and data acquisition . . . . .	46
3.3	Object reconstruction . . . . .	46
3.3.1	Electron reconstruction . . . . .	46
3.3.2	Muon reconstruction . . . . .	48
3.3.3	Jet reconstruction . . . . .	49
3.3.4	Prospects for the Phase-1 ATLAS Upgrade . . . . .	49
<b>4</b>	<b>Upgrade of the ATLAS Muon Spectrometer</b>	<b>51</b>
4.1	Motivation for the Upgrade . . . . .	51
4.2	The New Small Wheel . . . . .	52
4.2.1	Small-strip Thin Gap Chambers . . . . .	56
4.2.2	Micromegas . . . . .	56
4.3	Production and characterisation of the Micromegas modules at Saclay . . . . .	59
4.3.1	Software framework for the characterisation . . . . .	60
4.3.2	Software validation . . . . .	61

4.4	Cavern background . . . . .	66
4.4.1	The MM detection efficiency for photons and neutrons . . . . .	67
4.4.2	Cavern background simulation . . . . .	70
<b>5</b>	<b>Heavy Higgs search in 4 lepton decay channel with 13 TeV data</b>	<b>73</b>
5.1	Analysis overview . . . . .	73
5.2	Data and simulated samples . . . . .	74
5.2.1	Data . . . . .	74
5.2.2	MC samples . . . . .	75
5.3	Event selection and categorisation . . . . .	76
5.3.1	Trigger . . . . .	76
5.3.2	Event selection . . . . .	77
5.3.3	Categorisation . . . . .	81
5.4	Background . . . . .	82
5.4.1	$\ell\ell + \mu\mu$ reducible background . . . . .	83
5.4.2	$\ell\ell + ee$ reducible background . . . . .	91
5.4.3	Control plots . . . . .	93
5.4.4	Background $m_{4\ell}$ shape modelling . . . . .	94
5.4.5	Background summary . . . . .	96
5.5	Signal modelling . . . . .	97
5.5.1	Acceptance . . . . .	97
5.5.2	Shape modeling . . . . .	98
5.6	Systematic uncertainties . . . . .	111
5.6.1	Experimental systematic uncertainties . . . . .	111
5.6.2	Theoretical systematic uncertainties . . . . .	114
5.7	Observed events with $14.8 \text{ fb}^{-1}$ of 13 TeV data . . . . .	116
5.8	Statistical procedure . . . . .	117
5.9	Upper limits on the heavy Higgs production cross section . . . . .	119
<b>6</b>	<b>Exploration of the large width hypothesis for heavy Higgs boson</b>	<b>121</b>
6.1	Overview . . . . .	121
6.2	MC samples . . . . .	121
6.3	Signal modelling . . . . .	122
6.4	Interference modeling . . . . .	127
6.4.1	Interference of the heavy Higgs with SM Higgs . . . . .	127
6.4.2	Interference of the heavy Higgs with the SM $gg \rightarrow ZZ$ . . . . .	128
6.4.3	Complete signal model including the interferences . . . . .	132
6.5	Results . . . . .	135
<b>7</b>	<b>Improvement of the narrow width heavy Higgs search using MELA kinematic discriminant</b>	<b>139</b>
7.1	Overview . . . . .	139
7.2	MELA discriminant . . . . .	140
7.3	Signal modelling . . . . .	144
7.4	Background modelling . . . . .	148
7.5	Results . . . . .	151
<b>8</b>	<b>Updated results of the search with <math>36.1 \text{ fb}^{-1}</math> of 13 TeV data</b>	<b>153</b>
8.1	Modifications of the analysis . . . . .	153
8.2	Observed events . . . . .	154
8.3	Cross section limits . . . . .	156
8.3.1	Narrow width . . . . .	156

---

8.3.2 Large width . . . . .	156
<b>9 Conclusions</b>	<b>159</b>
<b>Résumé</b>	<b>161</b>
<b>Bibliography</b>	<b>169</b>



# Introduction

---

Most of the processes in the high energy physics can be described by the Standard Model (SM) of particle physics. The Standard Model was tested with a great precision at various experiments at particle accelerators such as LEP or Tevatron. The last unobserved particle in the Standard Model, the Higgs boson, was observed around 125 GeV in 2012 at Large Hadron Collider by two experiments: ATLAS and CMS. Therefore, by 2012 this theory becomes a complete model that has spectacular agreement with experimental observations.

In spite of the great success of the Standard Model, it has several fundamental problems that are giving a hint of the new physics beyond the current formulation of the theory (BSM). Models that are aiming to describe new BSM physics are usually formulated in a way that does not break the SM predictions that are well compatible with experimental results. One of the popular scenarios is an extension of the Higgs sector. There are different possible ways to extend the Higgs sector, while it is common for all of them to have an additional neutral SM-like Higgs boson. An exhaustive search of the SM-like Higgs boson below 125 GeV was already carried out by LEP experiment, thus the additional boson is likely to be heavier than the SM one. Therefore, the heavy neutral Higgs boson is a good marker for the new physics search.

This thesis is focused on the heavy Higgs boson search in the four leptons decay channel with Run-2 data from the ATLAS detector at the Large Hadron Collider. The four leptons final state, where a lepton can be either a muon or an electron, benefits from a good detector resolution that makes it particularly sensitive to narrow resonances. It is one of the two decay channels that led to the SM Higgs boson discoveries in 2012. The heavy Higgs search is performed in a model independent way, e.g. without theoretical constraints on the parameters of the hypothetical new particle. This approach allows to produce a generic limit on the production rate of the particle that can be further interpreted in terms of various benchmark models.

The theoretical motivation of the analysis is discussed in Chapter 2, while the experimental facilities are described in Chapter 3. The heavy Higgs boson search in the narrow width approximation that was published at ICHEP 2016 conference, is discussed in details in Chapter 5. This part of the analysis is aiming to explore different Higgs production modes separately. Section 5.2.2 describes the MC samples used for the analysis, while mentioning a study of the generator level filters carried out by the author. The filter study allowed to significantly increase the statistics of the  $t\bar{t}$  MC samples without spending more computing resources. The event selection and cut optimisation done in the context of this thesis is discussed in Section 5.3. Background estimation and modelling is shown in Section 5.4, including the data-driven background estimate in  $\ell\ell + \mu\mu$  final state and  $ZZ$  background shape modelling proposed by the author. A signal model developed in the context of this thesis is described in Section 5.5. The new approaches of the signal and background modelling allows to reduce an effect of the statistical uncertainty in the MC samples, to propagate systematic uncertainties in more optimal way and finally to obtain a smooth transition of signal model for different signal hypothesis.

Another important part of the analysis that allows to extend the tested phase space of the BSM model, is the Higgs search under the large width assumption that is discussed in Chapter 6. In this case the signal has significant interference with the SM processes that has non trivial effects on the analysis sensitivity. Section 6.2 describes the additional MC samples that model the large



width signal and its interference, while the last ones are produced by the author. In the context of this thesis modelling of the large width signal and the interference was developed as it is described in Sections 6.3 and 6.4.

Sensitivity of the analysis can be significantly improved under the scalar signal assumption by adding an additional kinematic discrimination as presented in Chapter 7. Section 7.2 describes the matrix element based discriminant proposed and implemented by the author. This discriminant allows to improve the analysis sensitivity by 8-26% for different mass ranges.

Updated results that are based on the full 2015-2016 dataset ( $36.1 \text{ fb}^{-1}$  of  $\sqrt{s} = 13 \text{ TeV}$  data) are presented in Chapter 8. The conclusion on the current status of the heavy Higgs search is given in Chapter 9.

The upgrade of the ATLAS Muon Spectrometer (the New Small Wheel) is discussed in Chapter 4. The upgrade is required in order to ensure the detector performance under even more challenging operation conditions of the Large Hadron Collider in Run-3. In the context of this project, part of the Muon Spectrometer will be replaced with new modules based on Micromegas and small Thin Gap Chamber technologies. Section 4.3 describes the commissioning of the Micromegas chambers produced at Saclay for the New Small Wheel, while presenting the software framework for the data analysis developed by the author. Section 4.4 is dedicated to the simulation of the cavern background performed in the context of this thesis.

# Theory overview

This chapter contains a short overview of the relevant theoretical background. It covers a qualitative description of the Standard Model (SM), while paying more attention to the SM Higgs boson and its properties. Later part of the chapter discusses the Standard Model shortcomings that motivate to develop a theory beyond the current formulation. Possible extensions of the Higgs sector such as the real electroweak singlet model and the two-higgs-doublet model are described. The last two sections are discussing the heavy Higgs boson line shape and its interference with the SM background under the non negligible width assumption.

## 2.1 The Standard Model

### 2.1.1 General concept

Modern particle physics considers the Standard Model (SM) to be the most complete theoretical description of matter and energy. The SM was developing through out the 20th century and the actual formulation was finalised in the 1970s. The Standard Model describes all matter in terms of two types of particles: fermions and bosons. The fermions are  $\frac{1}{2}$  spin particles that play a role of elementary building blocks, while the bosons (integer spin) are mediators of interactions between all the particles. Each particle in the Standard Model is characterised by a unique set of quantum numbers, that defines particular properties of the particle. Interaction between particles is carried out by four fundamental forces: electromagnetic, weak, strong and gravitational, while the last one is considered to be very weak and therefore cannot be included into the SM. All the forces are mediated by a particular boson, or a set of bosons, as it will be described further. A final piece of the SM is the Higgs boson that has a unique role described in Section 2.1.3

Fermions are separated into two families: leptons and quarks. There are six leptons grouped into three generations as shown in Table 2.1. The leptons are classified according to following quantum numbers: charge ( $Q$ ), electron number ( $L_e$ ), muon number ( $L_\mu$ ) and tau number ( $L_\tau$ ). For each lepton there exist a corresponding antiparticle with identical properties but opposite quantum numbers. Similarly, there are six flavours of quarks grouped in three generations as shown in Table 2.2. The quarks are classified according to the following quantum numbers: charge ( $Q$ ), colour ( $C$ ), strangeness ( $S$ ), beauty ( $B$ ) and truth ( $T$ ). It is important to notice that quarks have fractional electrical charge. Again, there is a set of corresponding antiquarks with similar properties but opposite quantum numbers.

Table 2.1: Lepton classification.

Lepton		Mass	Electric Charge
electron	$e$	0.511 MeV	-1
$e$ -neutrino	$\nu_e$	<0.22 keV	0
muon	$\mu$	105.7 MeV	-1
$\mu$ -neutrino	$\nu_\mu$	<0.19 keV	0
tau	$\tau$	1.78 GeV	-1
$\tau$ -neutrino	$\nu_\tau$	<18.2 MeV	0

Table 2.2: Quark classification.

Quark		Mass	Electric Charge
up	$u$	1.8-3.0 MeV	+2/3
down	$d$	4.5-5.5 MeV	-1/3
charm	$c$	1.275 GeV	+2/3
strange	$s$	95 MeV	-1/3
top	$t$	173.5 GeV	+2/3
bottom	$b$	4.2 GeV	-1/3

Finally, every interaction is mediated by an exchange of a particular boson: a photon ( $\gamma$ ) for electromagnetic,  $Z$  and  $W^\pm$  bosons for weak, and gluon ( $g$ ) for strong (Table 2.3). Weak mediators interact with all the fermions, while photons and gluons interact only with particles that carry electrical or colour charge respectively.

Table 2.3: Properties of the gauge bosons and the Higgs boson.

Boson		Mass	Electric Charge	Associated interaction
photon	$\gamma$	0	0	electromagnetic
$Z$ -boson	$Z$	91.2 GeV	0	weak
$W$ -boson	$W$	80.4 GeV	$\pm 1$	
gluon	$g$	0	0	strong
Higgs boson	$h$	125 GeV	0	—

There is a specific theory related to each of fundamental forces that describes elementary particle dynamics: quantum electrodynamics (QED) and quantum chromodynamics (QCD) for electromagnetic and strong interactions respectively. While QED, weak interaction and a Higgs mechanism are further unified into common electroweak theory. The following section contains a qualitative description of the elementary particle dynamics.

### 2.1.2 Particle dynamics

#### Quantum electrodynamics

Quantum electrodynamics describes the electromagnetic interactions of elementary particles. The QED, similarly to other theories, is based on the idea that there are some fundamental symmetries in nature that should be preserved. In this particular case, the theory is developed around the local gauge symmetry of the U(1) group.

Free fermionic field (let's say electron field) can be described by the Dirac Lagrangian of a form:

$$\mathcal{L}_0 = i\bar{\psi}(x)\gamma^\mu\partial_\mu\psi(x) - m\bar{\psi}(x)\psi(x) \quad (2.1)$$

where  $\psi(x)$  is a 4-component spinor, that describes the fermion field,  $\gamma^\mu$  are Dirac matrices,  $\partial_\mu$  is a partial derivative and  $m$  is a fermion mass. The first term of the Lagrangian can be understood as kinematic energy of a particle, while the last one corresponds to its mass.

As it was stated before, there is a set of fundamental symmetries that should be preserved. For examples, it can be shown that this Lagrangian is invariant under global gauge transformation of the U(1) group:  $\psi(x) \rightarrow e^{i\alpha}\psi(x)$ . This symmetry can be mathematically developed into the current conservation law.

But the Lagrangian should be also invariant under local gauge transformation of the U(1) group:

$\psi(x) \rightarrow e^{i\alpha(x)}\psi(x)$ , which is not the case for the free fermionic field. This symmetry can be recovered by adding an extra term in the Dirac Lagrangian that will compensate the asymmetry:

$$\mathcal{L} = i\bar{\psi}(x)\gamma^\mu\partial_\mu\psi(x) - m\bar{\psi}(x)\psi(x) - qA_\mu(x)\bar{\psi}(x)\gamma^\mu\psi(x) \quad (2.2)$$

where  $q$  is a fermion's charge, and  $A_\mu(x)$  is a new field that transforms under local gauge transformation as

$$A_\mu(x) \rightarrow A_\mu(x) + \frac{1}{q}\partial_\mu\alpha(x) \quad (2.3)$$

This modified Lagrangian (2.2) is now invariant under local gauge transformation, by the price of an additional vector boson field that couples to the fermions through the last term. But this Lagrangian is not complete since it should also include a free term of a new vector field. This free term can be written as Proca Lagrangian for a massless field (since non zero mass would violate the symmetry), that mimics the classical Maxwell theory:

$$\mathcal{L} = -\frac{1}{4}F^{\mu\nu}F_{\mu\nu} \quad (2.4)$$

where  $F^{\mu\nu} = \partial_\mu A_\nu(x) - \partial_\nu A_\mu(x)$  is a field strength tensor. In such a way, the full local gauge invariant Lagrangian can be written as:

$$\mathcal{L} = i\bar{\psi}(x)\gamma^\mu\partial_\mu\psi(x) - m\bar{\psi}(x)\psi(x) - qA_\mu(x)\bar{\psi}(x)\gamma^\mu\psi(x) - \frac{1}{4}F^{\mu\nu}F_{\mu\nu} \quad (2.5)$$

It is important to notice that there is no extra terms that could be added while preserving the imposed symmetries, thus the mass term is not allowed for the bosonic field and the bosons (photons) are massless.

This Lagrangian formalism can be further transformed in a set of Feynman rules that can be used for quantitative description of electromagnetic processes as shown in Appendix ??.

### Electroweak theory

Weak interaction is responsible for such processes as muon and neutron decays or neutrino scattering. It can be added to the theory by imposing an extra local gauge symmetry of SU(2) group to the Lagrangian that is already U(1) invariant. From this approach it is possible to derive three new gauge bosons, one electrically neutral, and the others with electric charge  $\pm 1$ . New bosons are predicted to be massless within this theory.

On the other hand, mediators of the weak interaction are known to be massive due to experimental evidences, therefore it is clear that the formulated weak theory is not complete. Further, it was modified by imposing spontaneous symmetry breaking mechanism as described in Section 2.1.3, in order to describe massive bosons. Therefore, the actual unified electroweak theory is based on local U(1)⊗SU(2) gauge symmetry and spontaneous symmetry breaking mechanism, and it includes four gauge bosons: massless photon, massive  $Z$  and  $W^\pm$  bosons.

### Quantum chromodynamics

Quantum chromodynamics is a theory of the strong interaction. Similarly to the others, it is also developed on the concept of a gauge symmetry, but this time for the SU(3) group. This symmetry group has eight generators, that leads to eight new massless gauge bosons called gluons. Strong interaction is related to a colour change of a particle, for example quark can carry one

of three colours: red, green or blue, while antiquark: antired, antigreen or antiblue. Gluons can carry colour-anticolour charge, like red-antigreen or blue-antired. In fact eight gluons are the same particle with different colour configurations that form a complete basis of the symmetry. The gluons are also predicted to be massless, that is well in agreement with experimental observations.

Dynamics of the strong interaction is quite different from the others, namely the strong force grows at large distances between colour charged particles, that leads to the so called confinement effect: no free coloured objects can be observed, but only colour neutral structures. Another interesting feature of the strong interaction is called asymptotic freedom, that means that strong interaction is almost absent when interacting particles are very close.

### 2.1.3 Higgs boson as a consequence of spontaneous symmetry breaking

By now we have discussed three theories of elementary particle dynamics that are based on the local gauge symmetries. This approach is a real breakthrough for the description of the electromagnetic and strong interactions, since it precisely describes experimental observations. But there is a problem of a local gauge approach in the case of the weak interaction: the gauge principle predicts the gauge bosons that are mediating interaction to be massless (since the mass term of the Lagrangian is not local gauge invariant), but the  $W^\pm$  and  $Z$  bosons are known to be massive. The problem of  $W$  and  $Z$  boson mass can be solved by imposing spontaneous symmetry breaking mechanism, that will be discussed in this section.

Previously in the section we were considering the second order term of a Lagrangian as a mass term, which is not always correct. More precisely speaking, to identify a mass from a Lagrangian, one should first locate the ground state (the field configuration for which potential part of a Lagrangian is minimal) and rewrite the Lagrangian as a function of deviation from the minimum  $\eta$ ; after expanding in powers of  $\eta$ , one obtains the mass from the coefficient of the  $\eta^2$  term.

An idea of the spontaneous symmetry breaking is to add an extra sophisticated scalar field that would provide mass to mediators of the weak interaction. After construction of a specific massive scalar field, the usual local gauge SU(2) invariance is imposed to it. This requirement is exactly the same as in the case of weak interaction, therefore, it will require identical set of additional gauge bosons, but now with corresponding mass terms. In other words, in the most complete approach, the local gauge invariance should be imposed directly to a sum of fermion and scalar fields, but since it yields exactly the same conclusions we will assume only the scalar one for the moment.

Let's assume the scalar field with a Lagrangian:

$$\mathcal{L} = \frac{1}{2}(\partial_\mu \phi)(\partial^\mu \phi) + \frac{1}{2}\mu^2 \phi^2 - \frac{1}{4}\lambda^2 \phi^4 \quad (2.6)$$

This Lagrangian has a non trivial ground state, therefore the mass term can be defined only after rewriting the Lagrangian as a function of deviation from the ground state  $\eta \equiv \phi - \phi_{min}$ , where  $\phi_{min} = \pm\mu/\lambda$ . Then the Lagrangian of redefined field will be:

$$\mathcal{L} = \frac{1}{2}(\partial_\mu \eta)(\partial^\mu \eta) - \mu^2 \eta^2 \pm \mu\lambda \eta^3 - \frac{1}{4}\lambda^2 \eta^4 + \frac{1}{4}(\mu^2/\lambda)^2 \quad (2.7)$$

Here one can clearly see the mass term with a correct sign, while the last two terms describe self interaction of three or four scalars. It is important to notice that initial Lagrangian (2.6) was invariant under  $\phi \rightarrow -\phi$  transformation, but the later one (2.7) is not any more. This feature is called spontaneous symmetry breaking. The symmetry was broken when one ground states was

chosen from the two available. In principle, we could have chosen a ground state as a superposition of both, then the symmetry would be still there, but the Feynman formalism that is used for further computations is forcing us to chose one preferred minimum. Therefore, the symmetry breaking is quite artificial, and it would be more precise to say that the symmetry is hidden in a choice of the ground state, but not broken. The word spontaneous is used since there is no external agency responsible for the symmetry-breaking.

Now let's consider a complex scalar field

$$\phi \equiv \phi_1 + i\phi_2 \quad (2.8)$$

That will have a continuous set of ground states as shown in Figure 2.1. This field will have the following Lagrangian:

$$\mathcal{L} = \frac{1}{2}(\partial_\mu \phi) * (\partial^\mu \phi) + \frac{1}{2}\mu^2(\phi * \phi) - \frac{1}{4}\lambda^2(\phi * \phi)^2 \quad (2.9)$$

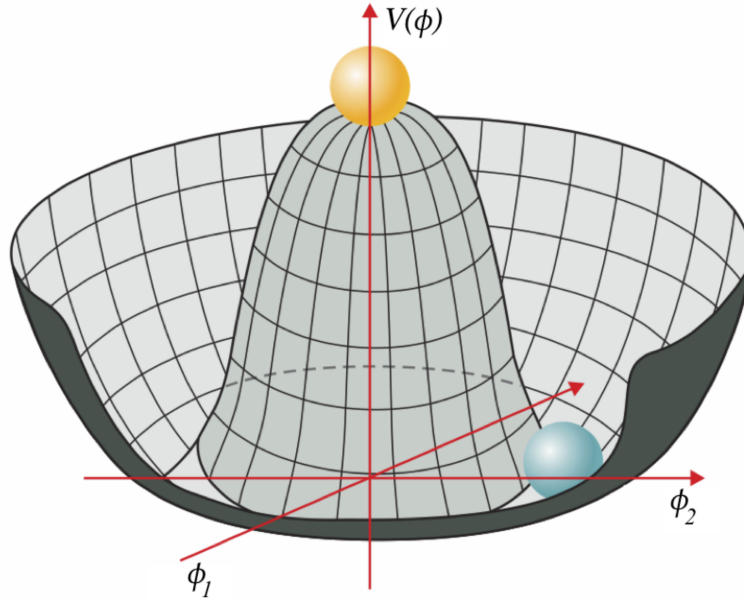


Figure 2.1: Potential of the scalar field considered in Equation (2.9). The potential is defined as  $V(\phi) \equiv -\frac{1}{2}\mu^2(\phi * \phi) + \frac{1}{4}\lambda^2(\phi * \phi)^2$ .

This complex scalar field is the one that will be used to assign masses to  $Z$  and  $W$  bosons. For this field, the analog of the spontaneously broken  $SO(2)$  symmetry becomes an invariance under  $U(1)$  phase transformation:

$$\phi \rightarrow e^{i\theta} \phi \quad (2.10)$$

After imposing local gauge invariance as for the weak interaction and going to a ground state

$$\phi \rightarrow e^{i\theta(x)} \phi \quad (2.11)$$

the Lagrangian looks as:

$$\begin{aligned} \mathcal{L} = & \left[ \frac{1}{2} (\partial_\mu \eta) (\partial^\mu \eta) - \mu^2 \eta^2 \right] + \left[ \frac{1}{2} (\partial_\mu \xi) (\partial^\mu \xi) \right] \\ & + \left[ \frac{1}{16\pi} F^{\mu\nu} F_{\mu\nu} + \frac{1}{2} \left( q \frac{\mu}{\lambda} \right)^2 A_\mu A^\mu \right] - 2i \left( q \frac{\mu}{\lambda} \right) (\partial_\mu \xi) A^\mu \\ & + \left\{ q [\eta \partial_\mu \xi - \xi \partial_\mu \eta] A^\mu + \frac{\mu}{\lambda} q^2 \eta A_\mu A^\mu + \frac{1}{2} q^2 (\xi^2 + \eta^2) A_\mu A^\mu - \lambda \mu (\eta^3 + \eta \xi^2) - \frac{1}{4} \lambda^2 (\eta^4 + 2\eta^2 \xi^2 + \xi^4) \right\} + \left( \frac{\mu^2}{2\lambda} \right)^2 \end{aligned}$$

The first line of the Lagrangian describes two scalar particles: a scalar  $\eta$  with a mass of  $m_\eta = \sqrt{\mu}$  and a massless Goldstone boson ( $\xi$ ). The second line describes a massive gauge field  $A^\mu$  with a mass of  $m_A = 2\sqrt{\pi}q\mu/\lambda$ , so the initial goal to assign masses to the gauge bosons is reached.

However, the additional massless Goldstone boson that pop up in the theory is a problem. There is no chance that such a massless particle that couples to the others exists, but is never observed experimentally. Moreover, there is a suspicious term in the Lagrangian:  $-2i \left( q \frac{\mu}{\lambda} \right) (\partial_\mu \xi) A^\mu$ , that is basically telling that the gauge boson can be converted to the Goldstone boson in flight, without any extra party involved. Such an unusual behaviour cannot be explained within the model. It looks like this representation of the scalar field does not identify fundamental particles of the theory. This issue can be solved by making use of local gauge invariance of the theory. We can entirely rotate away the Goldstone boson by fixing specific gauge. After performing the transformation  $\phi \rightarrow e^{-\tan^{-1}(\phi_1/\phi_2)i} \phi$ , the Lagrangian can be written as:

$$\begin{aligned} \mathcal{L} = & \left[ \frac{1}{2} (\partial_\mu \eta) (\partial^\mu \eta) - \mu^2 \eta^2 \right] + \left[ \frac{1}{16\pi} F^{\mu\nu} F_{\mu\nu} + \frac{1}{2} \left( q \frac{\mu}{\lambda} \right)^2 A_\mu A^\mu \right] \\ & + \left\{ \frac{\mu}{\lambda} q^2 \eta A_\mu A^\mu + \frac{1}{2} q^2 \eta^2 A_\mu A^\mu - \lambda \mu \eta^3 - \frac{1}{4} \lambda^2 \eta^4 \right\} + \left( \frac{\mu^2}{2\lambda} \right)^2 \end{aligned}$$

One left here with a single massive scalar particle  $\eta$  further called the Higgs boson, and a massive gauge field  $A^\mu$ .

The massive gauge field  $A^\mu$  still does not correspond to the well known  $Z$  and  $W$  bosons. These particles can be recovered after adding electromagnetism to the theory. Then, based on the superposition of local gauge  $U(1) \otimes SU(2)$  symmetries, it is possible to deduce 4 familiar particles: massless photon, electrically neutral massive  $Z$  boson and charged massive  $W^\pm$  bosons.

In the Standard Model, the Higgs field also provides masses to quarks and leptons through the Yukawa coupling. The Higgs mechanism completes the modern formulation of the Standard Model, that led to numerous predictions in particle physics. As it can be seen from above equations, the Higgs boson mass is a free parameter of the theory and, therefore, it was the last unobserved particle in the SM for a long time.

## 2.2 The Standard model Higgs boson at LHC

The Higgs boson search was a motivation of numerous experiments in high energy physics for a long time. The Large Hadron Collider is not an exception, the Higgs search was in a top priority of the project goals, that finally led to the discovery of a Higgs boson like particle in 2012.

This section will shortly overview the Higgs boson search at the LHC, including initial mass constraints, production and decay modes interesting for this particular case and finally the discovery of the new particle and its properties. A big part of this section will be also relevant for the heavy Higgs boson that is the subject of this thesis.

### 2.2.1 Mass constraints

Before the LHC started its Higgs search campaign, it was already more or less clear where to look for the new boson. Even if the Higgs boson mass is a free parameter of the SM, nevertheless there is a set of theoretical constraints on this quantity that are required to keep the model consistent. Moreover, by the LHC time there were already some large experiments such as LEP [1] and Tevatron [2], that had excluded the Higgs boson in a certain mass range.

#### 2.2.1.1 Theoretical constraints

It is important to notice that the following theoretical mass constraints are based on consistency of the SM as it is formulated now, however, the model consistency can be recovered for other values of the Higgs mass by adding extra components to the theory, such as, for example, new particles. Therefore, this mass constraint should not be understood as a region where there is no new scalar boson, but as a region where a potential new scalar could not be the SM Higgs boson.

An upper bound on the Higgs mass can be deduced from so called perturbative unitarity requirement. This requirement is telling that unitarity should be preserved in every process that involves the Higgs boson. The SM processes that involve heavy vector boson scattering have cross sections that increase with an interaction energy, that would lead to unitarity violation. This problem can be avoided at certain values of the Higgs boson mass, that would pull down the cross section to reasonable level. The perturbative unitarity constraint at tree level can be developed into an upper limit of the Higgs boson mass of 710 GeV, under assumption that the SM is still perturbative at this scale. [3]

Another upper bound is coming from the Higgs quartic coupling (Higgs self coupling term). Similarly to other parameters of the Standard Model, the quartic coupling is a function of the energy scale due to higher order loop corrections, namely, it grows with the energy scale. A requirement of the finite coupling at the Higgs mass scale leads to the mass upper bound of  $\sim 640$  GeV. On the other hand, if the quartic coupling is too small, at some scale it can be overkilled by fermion contributions in the loops that would make the coupling to be negative. In this case the Higgs mechanism is not working, and the vacuum is not stable anymore. It leads to a lower bound on the Higgs boson mass of about 70 GeV, depending on the assumed SM validity scale [3]. Theoretical limits on the SM Higgs boson mass are summarised in Figure 2.2, as a function of the SM validity scale.



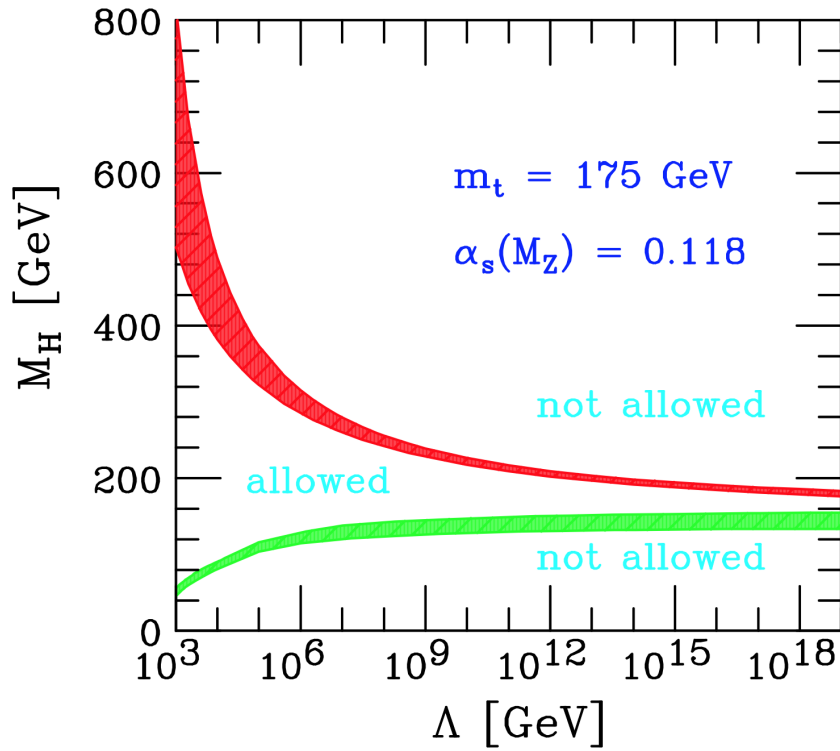


Figure 2.2: Theoretical limits on the mass of the Standard Model Higgs boson as a function of the Standard Model validity scale ( $\Lambda$ ). [4]

### 2.2.1.2 Experimental constraints

Direct search of the Higgs boson by the LHC time was already carried out by LEP and Tevatron experiments. Also indirect search was performed through the precision measurement of the SM quantities that are affected by the predicted particle.

#### LEP

The Higgs search at the Large Electron-Positron Collider (LEP) [1] has started in 1989. There are 2 processes that can produce the Higgs boson in electron positron collision:  $e^+e^- \rightarrow Z \rightarrow Z^*H$  and  $e^+e^- \rightarrow Z^* \rightarrow ZH$  (Figure 2.3). These two processes are quite similar with the only difference that the intermediate  $Z$  boson is on-shell in first case, and off-shell in the second case. The first process is of use when a tested Higgs mass is reasonably smaller than  $Z$  boson mass, while the second process allows to explore higher mass hypothesis.

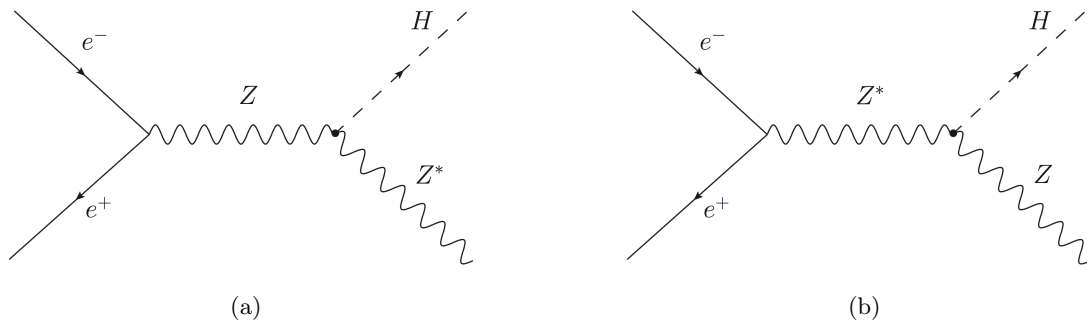


Figure 2.3: Dominant production modes for the Higgs boson at LEP.

During the first phase LEP was operating at the centre of mass energy of the  $Z$  resonance, targeting the first production mode. The best decay channel for the Higgs search at this conditions was the

$Z$  decaying leptonically and  $H$  decaying into a pair of  $b$  quarks ( $Z \rightarrow \ell\ell(\nu_\ell\nu_\ell)$ ,  $H \rightarrow b\bar{b}$ ).  $b$  decay of the Higgs boson allows to access the highest branching ratio, while leptonic decay of  $Z$  was providing a good discrimination from high multi-jet background. As a result of the first run, the Higgs boson was excluded at 95 % confidence level for masses below 65.2 GeV [5].

The second phase of LEP was targeting higher Higgs masses and therefore the second production mode. For this reason the centre of mass energy was raised to 209 GeV. The considered production mode implies the on-shell  $Z$  boson in a final state, that provide significant discrimination of signal with respect to background. This feature makes accessible other decay channels in addition to the ones explored at LEP1. This time the Higgs boson was excluded at 95 % confidence level for  $m_H < 114.4$  GeV [5]. The exclusion limits for the Standard Model Higgs boson at LEP are summarised in Figure 2.4.

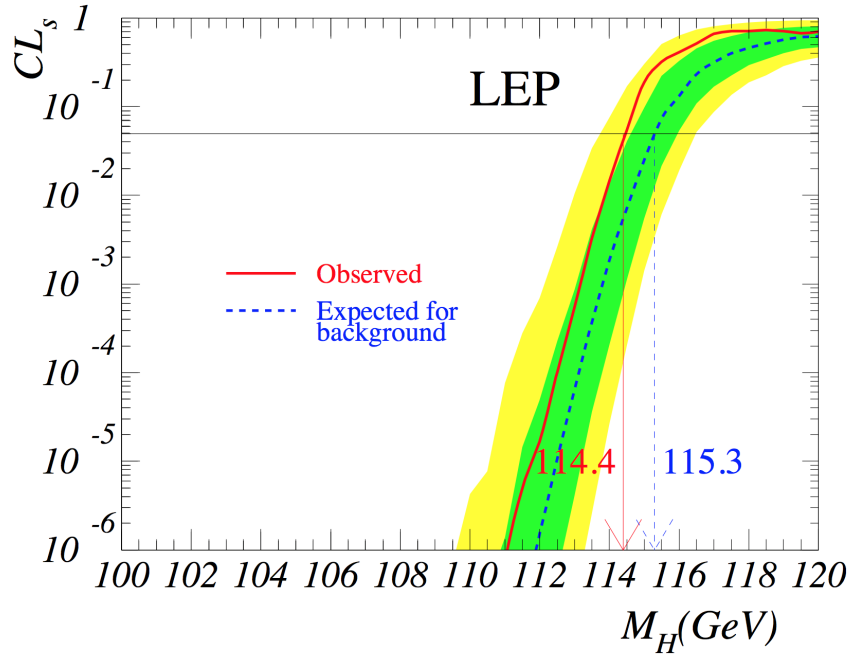


Figure 2.4: Exclusion limits for the SM Higgs boson at LEP [5].

### Tevatron

Tevatron [2] is a  $p - \bar{p}$  collider with a centre of mass energy of 1.96 GeV. It was hosting two large experiments: DØ and CDF, and both of them were targeting the SM Higgs search in a mass range of 100 – 200 GeV. Similarly to the LHC case, a dominant Higgs production mode here is gluon-gluon fusion, however, non negligible contribution is also coming from the associated production with a  $W$  or  $Z$  boson, and vector boson fusion. Corresponding Feynman diagrams are given in Figure 2.7. The Tevatron search was targeting the  $b\bar{b}$ ,  $WW$  and  $\gamma\gamma$  Higgs decay channels since the first two are the dominant ones at the tested masses, however the last one still could help to gain some sensitivity. Higgs decay modes are discussed in more details in Section 2.2.2.

During the 2011 and 2012 runs, there were almost  $10 \text{ fb}^{-1}$  of data collected at Tevatron, that allows to exclude the Higgs boson for masses  $100 < m_H < 103$  GeV and  $147 < m_H < 180$  GeV. Moreover, a significant excess of data were observed in the region of  $115 < m_H < 140$  GeV, that provides an evidence of a new particle but still not enough to claim the discovery. Results of the SM Higgs search at Tevatron are shown in Figure 2.5 [6].

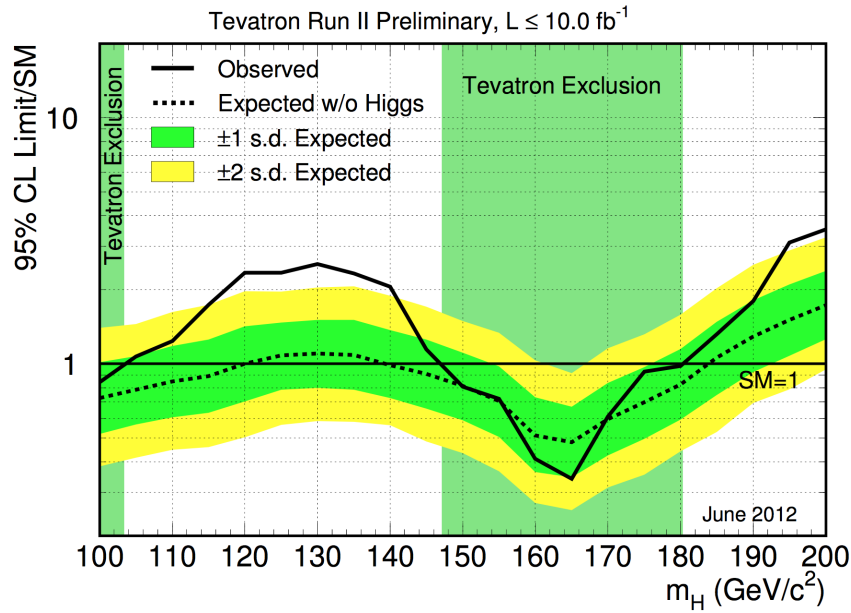


Figure 2.5: Exclusion limits for the SM Higgs boson at Tevatron [6].

### Indirect search

The Higgs boson has an influence on other Standard Model observables through the radiative corrections. Precise knowledge of these observables can lead to a non-trivial constraint on the Higgs mass. This indirect Higgs mass constraint was first performed by the LEP electroweak working group [7], and then by GFitter [8] too. These works were based on a global fit of various Standard Model observables such as  $W$  boson and top quark masses, that were measured by different experiments. The most recent results that do not include any LHC data were published in 2011 and both groups obtained similar best fit of  $m_H = 95^{+30}_{-24}$  GeV, that exclude the SM Higgs boson above 161 GeV at 95% confidence level. The fit result from the LEP electroweak working group is shown in Figure 2.6.

### 2.2.2 The SM Higgs production and decay modes at the LHC

From the last section it becomes clear that the most interesting region for the SM Higgs boson search at LHC starts at 100 GeV and should not go far beyond 200 GeV, however, it may happen that the current formulation of the SM is not complete or not precise enough that would make the upper bound for the Higgs mass to be not valid. For this reason the Higgs boson search at LHC was targeting the whole mass range above 100 GeV, that will be tested in 7-14 TeV centre of mass collision energy.

In this section different production and decay modes that are relevant for the LHC and the target mass range will be discussed. In addition, the most promising detection channels will be pointed out.

#### 2.2.2.1 Production modes

The Higgs boson can be produced in a  $p - p$  collisions mostly in four different ways: gluon fusion, vector boson fusion, associated production with a vector boson, associated production with  $t\bar{t}$  quark pair. Corresponding Feynman diagrams are shown in Figure 2.7. More details about each production mode are given further, while their cross sections as a function of the Higgs mass are shown in Figure 2.8.

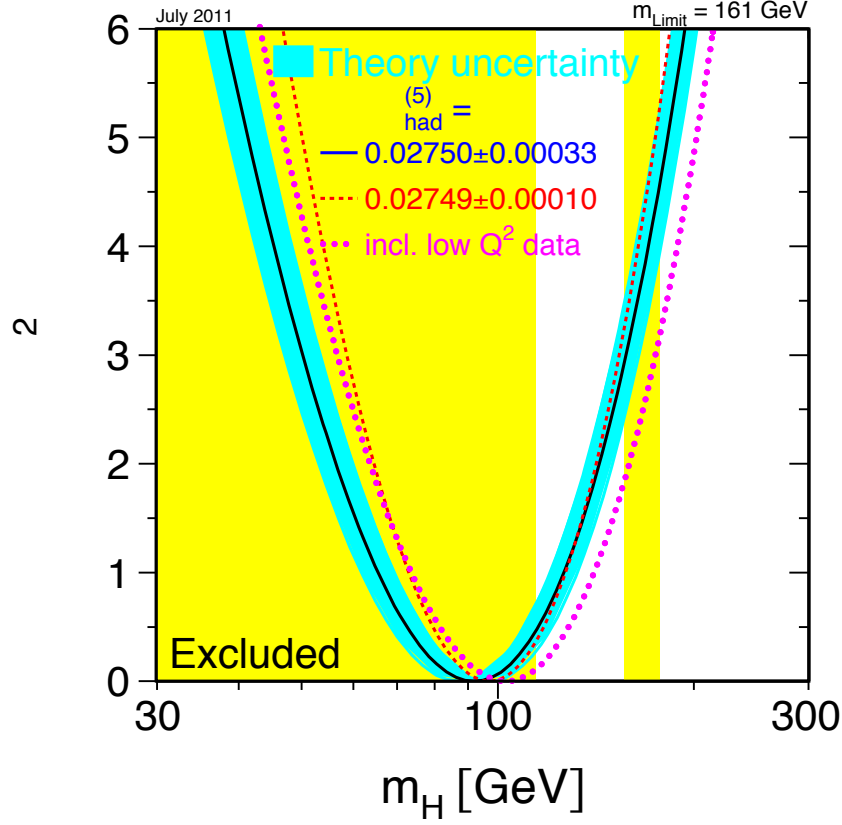


Figure 2.6: The  $\Delta\chi^2$  of the fit of the SM precision observables performed by the LEP electroweak working group in 2011 [7].

### Gluon fusion (ggF)

The SM Higgs boson is not directly coupled to gluons, therefore the gluon fusion can only happen through the quark loop as it is shown in Figure 2.7(a). Since the Higgs coupling to quarks is proportional to a quark mass, the dominant contribution in the loop is coming from the top quark. The ggF is a dominant production mode at the LHC in the full mass range of interest. It is possible due to high gluon contribution to a proton PDF (parton distribution function) at high collision energy. The ggF cross section is computed up to next-to-next-to-next-to-leading order (NNNLO) in QCD [9–11] with next-to-leading order (NLO) electroweak corrections [12, 13].

### Vector boson fusion (VBF)

In the VBF mode, two vector bosons, either  $Z$ s or opposite charge  $W$ s, are emitted by quarks in both of the protons. These vector bosons further produce the Higgs boson as shown in Figure 2.7(b). The Higgs boson will be accompanied by two hard forward jets, that are originated from recoil quarks that had emitted the vector bosons earlier. This feature can be used as a clear signature that allows to distinguish VBF mode from the others.

This process has the second dominant production rate at LHC, which relative contribution slowly grows with the Higgs mass. The VBF cross section is calculated with full NLO QCD and EW corrections [14–16], and approximate NNLO QCD corrections are available [17].

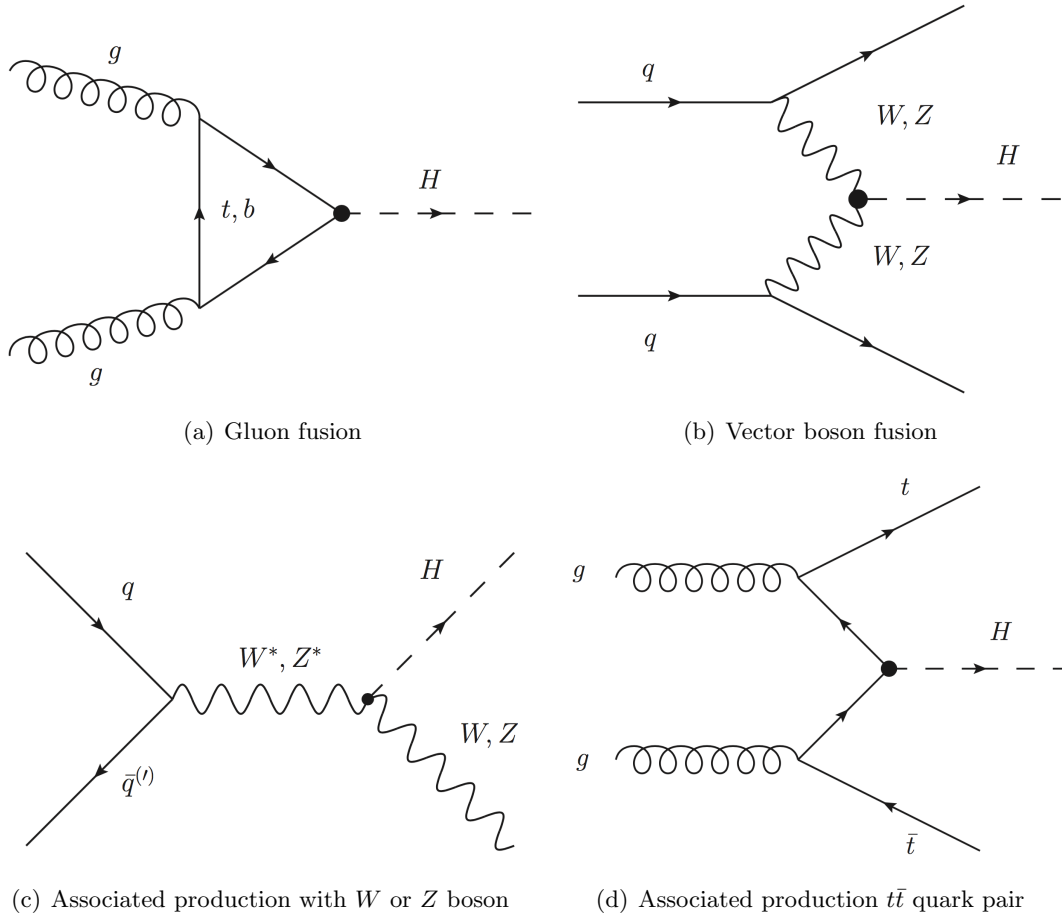


Figure 2.7: The Higgs boson production modes at LHC.

### Associated production with $W$ or $Z$ boson (VH)

This process (also known as a higgs-strahlung) is very similar to the dominant Higgs production mode at LEP. A primary off-shell vector boson is produced in a quark-quark interaction, and it is further emitting the Higgs boson in order to make a transition to the on-shell state. Therefore, in the final state of VH production mode, the Higgs boson is accompanied by an on-shell vector boson. This production mode has quite low cross section, however it can be useful to explore  $b\bar{b}$  Higgs decay channel due to extra separation signature in the final state. The cross section is known at NNLO in QCD [18, 19] with NLO EW corrections [20].

### Associated production with $t\bar{t}$ quark pair (ttH)

The Feynman diagram that illustrates the ttH Higgs production is shown in Figure 2.7(d). The cross section of this process is extremely small, however it is still interesting since it is the only process that gives direct access to the top-Higgs coupling.

#### 2.2.2.2 Decay Channels

The total decay width of the Higgs boson is shown in Figure 2.9(a). It is important to notice that the total width is rapidly growing with mass, therefore, the Higgs boson can be either a narrow peak with rather low mass or a broad heavy resonance. The branching ratios (BR) are shown in Figure 2.9(b). It has quite nontrivial dependence on the Higgs mass, that makes a search strategy dependent on the mass ranges.

$H \rightarrow gg$  and  $H \rightarrow c\bar{c}$  processes have quite high branching ratio at low mass, but they cannot be

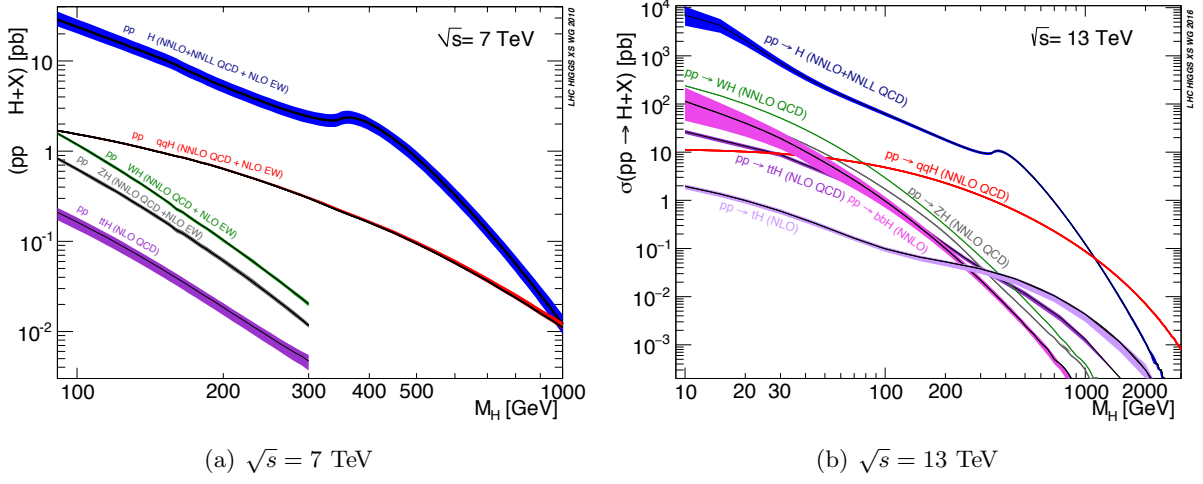


Figure 2.8: The Standard Model Higgs production cross section. [21]

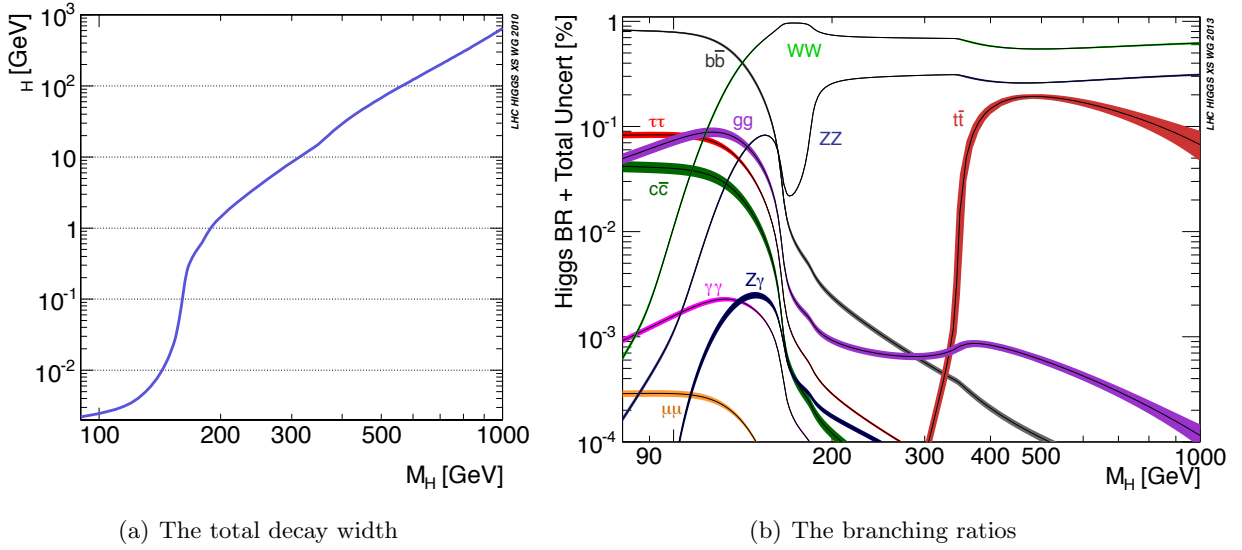


Figure 2.9: The total decay width and the branching ratios of the Standard Model Higgs boson. [21]

detected due to multi-jet background that has production rate higher by few orders of magnitude. The same reasoning is valid for  $H \rightarrow b\bar{b}$  decay channel, however its high BR in combination with VH production mode allows to build a signal region with relatively high signal rate that is not suffering from a huge background. Thus, the  $H \rightarrow b\bar{b}$  channel is promising for  $m_H < 130 \text{ GeV}$ .

Another channel that can be interesting at low mass is  $H \rightarrow \tau\tau$ . It can be used in combination with VBF production mode that would provide a rare signature in the final state: two forward jets accompanied by central lepton (in case of leptonic or semi-leptonic  $\tau$  decay).

$H \rightarrow WW$  is a dominant decay channel for masses above 130 GeV. However, fully hadronic decay of the  $W$  pair cannot be detected due to high multi-jet background, so the actual channels of interest are:  $H \rightarrow WW \rightarrow \ell\nu\ell\nu$  and  $H \rightarrow WW \rightarrow \ell\nu q\bar{q}$ . These channels do not have good mass resolution due to missing energy in both final states.

$H \rightarrow ZZ$  consists of a set of sub-channels that have quite different properties:  $H \rightarrow ZZ \rightarrow \ell\ell\ell\ell$ ,  $H \rightarrow ZZ \rightarrow \ell\ell\nu\nu$ ,  $H \rightarrow ZZ \rightarrow \ell\ell q\bar{q}$  and  $H \rightarrow ZZ \rightarrow q\bar{q}\nu\nu$ . The first one has quite small rate, however it can benefit from fully reconstructable final state with excellent resolution of a reconstructed Higgs mass. The  $H \rightarrow 4\ell$  channel provides good search capability for the Higgs mass above 115 GeV. Also this channel is the most promising one for the Higgs mass measurement

when it is already discovered. The other listed sub channels become important at the high masses where cross section of the 4 lepton channel is fairly small.

Another interesting channel is a Higgs decaying to a pair of photons. It has relatively high probability for low and intermediate masses. This process has two high energetic isolated photons in the final state, that can be rarely produced in the SM processes. The background yield can be precisely estimated with data driven method. It makes this decay channel particularly interesting for the mass range of interest, both in terms of search and mass measurement.

The  $t\bar{t}$  decay channel becomes important for the  $m_H > 350$  GeV, therefore it is another channel that should be considered for the heavy Higgs search.

### 2.2.3 Discovery of the SM Higgs boson

By summer of 2012, the LHC had collected about  $5 \text{ fb}^{-1}$  of  $\sqrt{s} = 7$  TeV and about  $5 \text{ fb}^{-1}$  of  $\sqrt{s} = 8$  TeV data, that provides suitable statistics for the Higgs boson search. On 4<sup>th</sup> July 2012, an observation of a new particle around 125 GeV compatible with the Standard Model Higgs boson was simultaneously announced by the two collaborations, ATLAS and CMS.

Combination of different decay channels in ATLAS provides an excess at 126.5 GeV with local significance of  $5.9 \sigma$  and global significance of  $5.3 \sigma$  [22]. While the CMS combined results observe the largest excess at 125 GeV with local significance of  $5.0 \sigma$  and  $4.6 \sigma$  global [23]. Local significance of the observations is shown in Figure 2.10 in terms of  $p$ -value, that quotes the probability of the experimental observation assuming background only hypothesis.

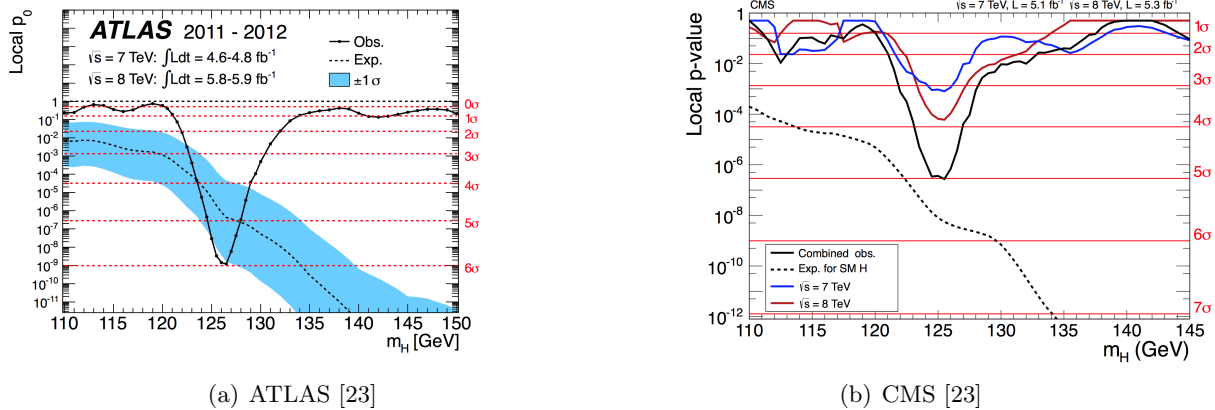


Figure 2.10: Local significance of the observations of the Higgs boson like particle for 7 TeV and 8 TeV data recorded at ATLAS (a) and CMS (b).

### 2.2.4 Properties of the new particle

After the new particle was discovered, the main question was either it is really the SM Higgs boson or any other particle. Therefore, an exhaustive campaign of particle properties determination was carried out by both experiments. The results based on full Run1 dataset from the ATLAS experiment will be shown in this section.

The SM Higgs search was performed in ATLAS exploiting various decay channel, while results from the most sensitive ones are shown in Figure 2.11 and Table 2.4. The highest sensitivity to the observed particle was provided by  $WW$ ,  $4\ell$  and  $\gamma\gamma$  final states, and the combined signal strength with respect to the SM prediction is  $\mu = 1.43 \pm 0.21$ . Combination of these decay channels

allows to determine the particle mass and put constraints on its spin, width and couplings to other particles.

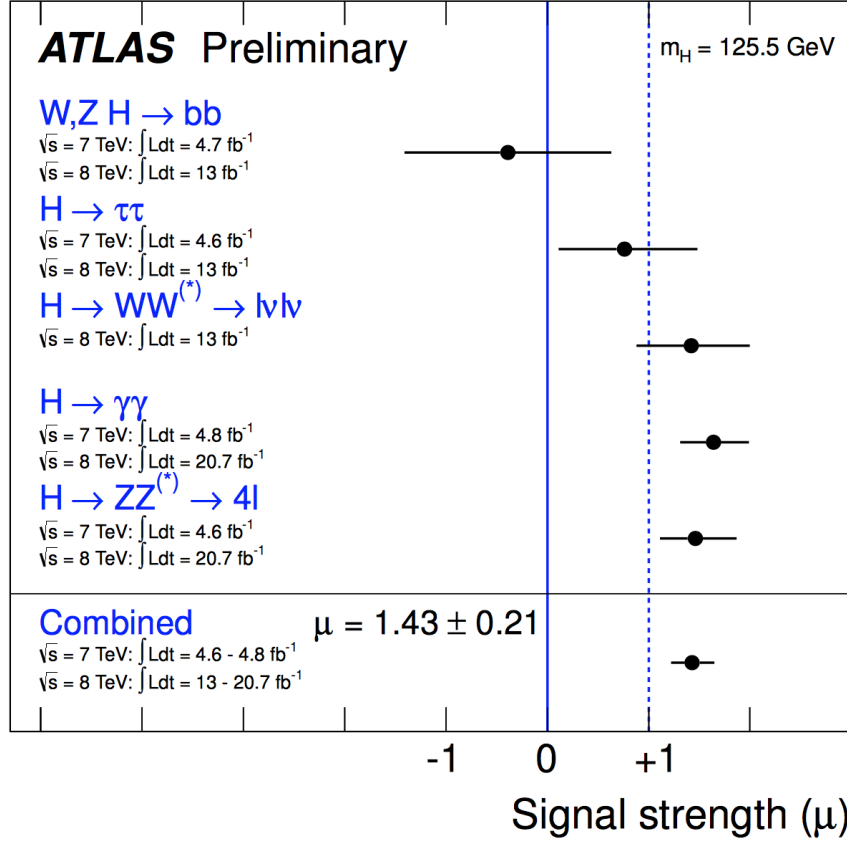


Figure 2.11: Measurements of the signal strength parameter  $\mu$  for  $m_H = 125.5 \text{ GeV}$  for the individual channels and for their combination. [24]

Table 2.4: Summary of the best-fit values and uncertainties for the signal strength  $\mu$  for the individual channels and their combination for  $m_H = 125.5 \text{ GeV}$ . [24]

Decay Channel	Signal Strength
$VH \rightarrow Vbb$	$-0.4 \pm 1.0$
$H \rightarrow \tau\tau$	$0.8 \pm 0.7$
$H \rightarrow WW^{(*)}$	$1.4 \pm 0.6$
$H \rightarrow \gamma\gamma$	$1.6 \pm 0.3$
$H \rightarrow ZZ^{(*)}$	$1.5 \pm 0.4$
Combined	$1.43 \pm 0.21$

## Mass

Fortunately, both of the most sensitive channels have rather high mass resolution, that allows to measure the particle mass with good precision. The best fit value for the mass in the four lepton decay channel is  $m_H^{4\ell} = 124.3^{+0.6}_{-0.5}(\text{stat.})^{+0.5}_{-0.3}(\text{syst.}) \text{ GeV}$ , while the two photon decay channel have reported  $m_H^{\gamma\gamma} = 126.8 \pm 0.2(\text{stat.}) \pm 0.7(\text{syst.}) \text{ GeV}$ . The difference of the measurements between the two channels is  $2.3^{+0.6}_{-0.7}(\text{stat.}) \pm 0.6(\text{syst.}) \text{ GeV}$ , corresponding to 2.4 standard deviations. Combination of these two measurements leads to  $m_H = 125.5 \pm 0.2(\text{stat.})^{+0.5}_{-0.6}(\text{syst.}) \text{ GeV}$ . Summary of the likelihood scans in the 2D plane of signal strength  $\mu$  versus Higgs boson mass  $m_H$  including full Run 1 dataset is shown in Figure 2.12. This plot includes the best fit result from each decay channel as well as the combination of the measurements. [24]



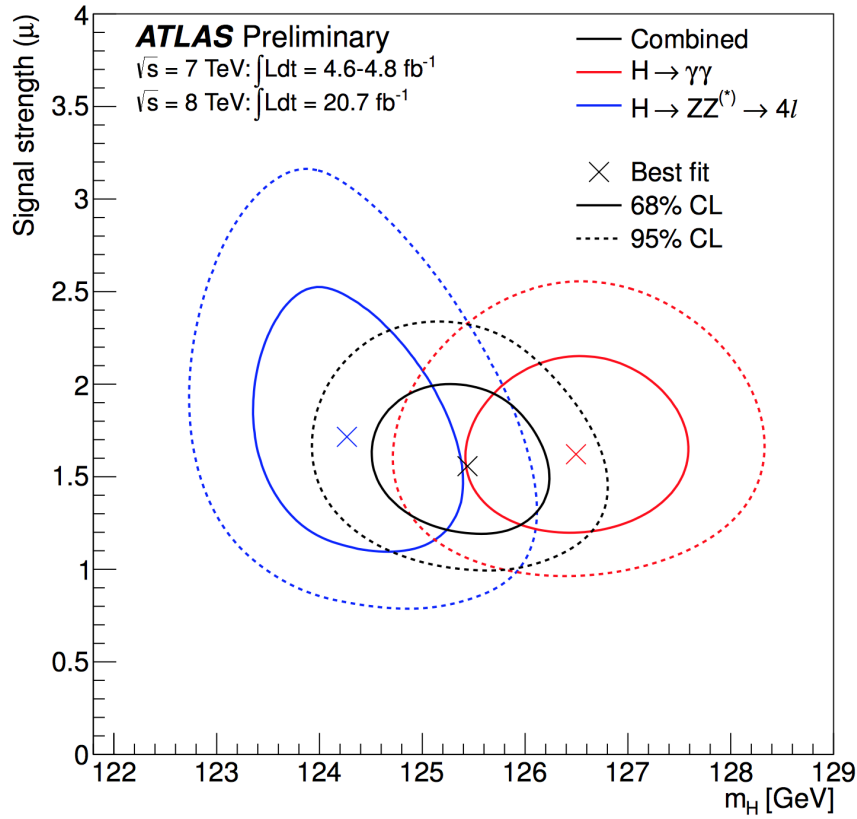


Figure 2.12: Confidence level intervals in the  $(\mu, m_H)$  plane for the  $H \rightarrow ZZ \rightarrow 4\ell$  and  $H \rightarrow \gamma\gamma$  channels and their combination, including all systematic uncertainties. [24]

### Spin and parity

One of the ways to test either the new particle is the SM Higgs boson, is to determine its spin and parity. The Standard Model expectation for the Higgs boson is  $0^+$  configuration. Spin of the particle can be measured experimentally through different kinematic variables specific to the final state. In ATLAS experiment the spin studies for the new particle are performed using three different decay channels:  $H \rightarrow ZZ^{(*)} \rightarrow 4\ell$  [25],  $H \rightarrow \gamma\gamma$  [26] and  $H \rightarrow WW^{(*)} \rightarrow e\nu\mu\nu$  [27].

The first channel is used for pairwise comparison of the SM predicted  $0^+$  hypothesis to  $0^-$ ,  $1^+$ ,  $1^-$ ,  $2^+$  and  $2^-$ , assuming purely ggF production mode. The  $4\ell$  channel is sensitive to the spin of the new particle mostly through the angular variables of the four leptons in centre of mass system. The Higgs-like boson is found to favour the SM expectation of  $0^+$  when compared pair-wise to other hypotheses. The  $0^-$  and  $1^+$  states are excluded at the 97.8% confidence level or higher using  $CL_S$  method in favour of  $0^+$ .

The other two channels are used to discriminate the SM spin- $0^+$  hypothesis with respect to the spin- $2^+$  graviton-like model. In the two-body decay  $H \rightarrow \gamma\gamma$ , the spin information is extracted from the distribution of the polar angle  $\theta^*$  of the photons with respect to the  $z$ -axis of the Collins-Soper frame [28] in combination with diphoton invariant mass  $m_{\gamma\gamma}$ . While in  $H \rightarrow WW^{(*)} \rightarrow e\nu\mu\nu$  case, the spin correlations between the decay products affect event topologies by shaping angular distributions of the leptons as well as the lepton momenta and missing transverse energy. Both decay channels have excluded  $2^+$  hypothesis in favour of a  $0^+$  at a  $CL_S$  confidence level which varies between 99% and 95% for different assumed ratio of gluon fusion and quark-antiquark annihilation production modes for the graviton.

## Width

The Standard Model Higgs boson with  $m_H = 125$  GeV is predicted to have a total width of 4 MeV. The current experimental mass resolution is of the order of few GeV, that is not enough to perform a direct measurement of the particle total width. However, it can be still probed indirectly in  $H \rightarrow ZZ$  and  $H \rightarrow WW$  decay channels through the off-shell production rate. The on-shell cross section of the Higgs boson is proportional to the ratio of the particle width and the SM predicted width  $(\Gamma_H/\Gamma_H^{SM})^{-1}$ , while the off-shell production rate does not have such dependency. Therefore the particle width can be constrained through the ratio of the off-shell and on-shell production rates. Unfortunately, the off-shell cross section measurement is strongly affected by the theoretical uncertainty on the  $gg \rightarrow ZZ$  background due to higher order corrections, therefore the off-shell limit is usually presented as a function of the unknown background k-factor. Combination of the Run1 width studies in the  $H \rightarrow ZZ \rightarrow 4\ell$  and  $H \rightarrow ZZ \rightarrow \ell\ell\nu\nu$  channels have excluded the total Higgs boson width above 4.8 – 7.7 times the SM width at 95% CL, depending on the assumed  $gg \rightarrow ZZ$  background k-factor. [29]

## Couplings

Another set of key parameter to understand the nature of the new boson is its couplings to the other SM particles. In order to determine the couplings of the Higgs like boson, all decay channels listed in Table 2.4 are used. The couplings are extracted from the global fit of the observed signal strength in different final states. Higgs coupling to a particle  $X$  is usually expressed in terms of the scale factor with respect to corresponding Standard Model Higgs coupling  $\kappa_X$ . Sometimes it is impossible to disentangle an effect of two different couplings, then a ratio  $\lambda_{XY} = \kappa_X/\kappa_Y$  or a product  $\kappa_{XY} = \kappa_X \cdot \kappa_Y/\kappa_H$  of couplings can be estimated. Since the available dataset provides quite limited access to the Higgs coupling, their measurement can be only performed assuming some specific scenario with additional theoretical constraints. The benchmark models considered for the Higgs couplings measurements in ATLAS are listed below, while their detailed description is given in Ref. [30]:

- Probing fermion versus vector (gauge) boson couplings
  - Only SM contributions to the total width
  - No assumption on the total width
  - No assumption on the total width and on the  $H \rightarrow \gamma\gamma$  loop content
- Probing the custodial symmetry of the  $W$  and  $Z$  couplings
  - Including the  $H \rightarrow \gamma\gamma$  channel
  - Independently of deviations in the  $H \rightarrow \gamma\gamma$  channel
- Probing beyond the SM contributions
  - Only SM contributions to the total width
  - No assumption on the total width

Results of the Higgs couplings measurements assuming these benchmark models are shown in Figure 2.13. For the different tested scenarios the compatibility with the SM Higgs expectation ranges between 5% and 10%; hence, no significant deviation from the SM prediction is observed in any of the benchmarks. Different scenarios are strongly correlated, as they are obtained from fits to the same experimental data, hence they should not be considered as independent measurements and an overall  $\chi^2$ -like compatibility test to the SM is not possible.

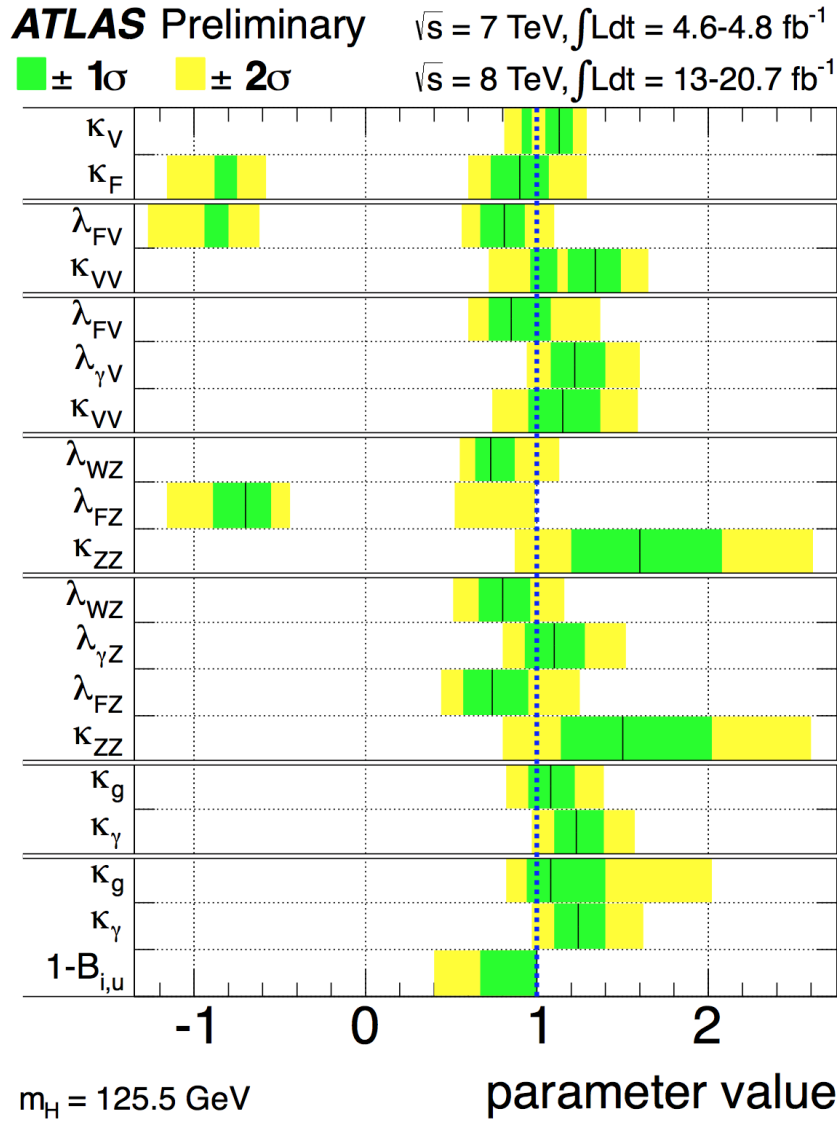


Figure 2.13: Summary of the coupling scale factor measurements for  $m_H = 125.5 \text{ GeV}$ . The best-fit values are represented by the solid black vertical lines. The measurements in the different benchmark models (ordered according to the list in the text), separated by double lines in the Figure. [30]

### 2.2.5 Summary

The new particle has been discovered around 125 GeV by the two experiments, ATLAS and CMS. The highest sensitivity is provided by the  $4\ell$  and the  $\gamma\gamma$  decay channels. The observed particle is compatible with the Standard Model Higgs boson within the experimental uncertainty on its properties, however, more data is needed to draw certain conclusions about the particle nature.

## 2.3 Higgs sector beyond the Standard Model

The Standard model is a spectacular theory that provides very precise calculations of different physics quantities that could be measured experimentally. The Higgs boson was the last missing piece, and its discovery confirms the theory in such a formulation as we currently know it.

However, the Standard model has some problems with its formulation, as well as it cannot explain

some experimental observations. For example, in the SM all fermions acquire their masses from the same Higgs field although their masses differ by six orders of magnitude. It would require quite a broad spectrum of the Higgs couplings to different particles. This fine tuning looks quite suspicious, and it can be explained in other more elegant ways, like fermions get their masses from several fields at different energy scales. Another problem is that the Standard Model cannot explain the baryon asymmetry of the universe, in other words, why there is much more matter than anti-matter in the universe. Also the SM is not able to describe the dark matter that is well known to be there from cosmology. Moreover, there is a problem with the particles that are already included in the theory. Experimental data have confirmed neutrino oscillations, that are possible only in case they are massive particles, but the SM predict them to be massless.

All these shortcomings give a hint that the Standard Model is an effective theory that is valid under certain conditions. Therefore, there is a big effort ongoing to develop more universal theory beyond the SM (BSM). The usual approach is to extend the SM with extra components that would solve some problems without ruining the SM itself. Such an extended model often has quite a lot of additional free parameters, that makes experimental probing rather challenging due to large available phase space. Moreover, there is a huge number of BSM theories on a market, that makes individual probing of each theory quite difficult.

One of the most popular BSM models is SuperSymmetry, in particular its minimal extension called MSSM. This theory is saying that all the SM particles have their supersymmetric partners, that would lead to a significant extension of the Higgs sector. In MSSM, instead of one SM Higgs boson, there are five of them, while the lightest is often similar to the SM one.

Since the BSM models are quite specific, on practice, experimentalists are trying to consider for testing not one certain scenario, but rather a benchmark model that would generalise a group of theories. Benchmark model for a BSM Higgs search are usually taking into account an extension of the Higgs sector while ignoring other additional particles. The most popular benchmark models are electroweak singlet (EWS) and two-Higgs-doublet model (2HDM) which are summarised in a comprehensive way in Ref. [31].

### 2.3.1 Real Electroweak singlet model (EWS)

The simplest extension of the SM Higgs sector that is still consistent with the SM Higgs boson is EWS [32–38]. It considers the existence of an additional electroweak singlet field that is mixing with the SM Higgs doublet. The additional heavy field is characterised by a nontrivial vacuum expectation value that leads to an extra neutral particle. There are two CP-even Higgs bosons as a result of spontaneous symmetry breaking of this model. Usually the lightest boson is denoted as  $h$ , while  $H$  is used for the heaviest one.

EWS model assumes that both scalars are quite similar to the SM Higgs boson, and their couplings to the SM fermions and vector bosons are scaled with a common factors  $\kappa$  and  $\kappa'$  for  $h$  and  $H$  respectively. In order to preserve unitarity under this assumption, the coupling scale factors should obey the following requirement:

$$\kappa^2 + \kappa'^2 = 1 \quad (2.12)$$

while the SM can be recovered at the limit  $\kappa' \rightarrow 0$ , where  $h$  would correspond to the SM Higgs boson.

This assumption for the coupling allows to get  $h$ , that is compatible with the 125 GeV particle observed at LHC. The branching ratios for  $h$  are exactly the same as for the SM Higgs since all

the couplings are scaled in the same way, while the production cross section and width are scaled with  $\kappa^2$ :

$$\begin{aligned}\sigma_h^i &= \kappa^2 \times \sigma_{SM}^i \\ \Gamma_h &= \kappa^2 \times \Gamma_{SM} \\ BR_h^j &= BR_{SM}^j\end{aligned}$$

where  $\sigma$  is a production cross section for  $i$ -th production mode allowed in the SM;  $\Gamma$  is a total decay width of the resonance; and BR is a decay branching ration with index  $j$  that runs over all decay channels allowed in the SM.

Similar statement is also valid for the heavier scalar  $H$ , however, it will have an extra decay channel  $H \rightarrow hh$  in addition to the Standard Model ones. Then the production and decay of  $H$  can be described as:

$$\begin{aligned}\sigma_H^i &= \kappa'^2 \times \sigma_{SM}^i \\ \Gamma_H &= \frac{\kappa'^2}{1 - BR_{H \rightarrow hh}} \times \Gamma_{SM} \\ BR_H^j &= (1 - BR_{H \rightarrow hh}) \times BR_{SM}^j\end{aligned}$$

In principle, the 125 GeV is compatible both with  $h$  and  $H$ , but if  $H$  would be at 125 GeV, than the second scalar would be lighter. As it was stated in the previous section, the lower mass range was exhaustively scanned at LEP without any scalar particle observed. Therefore, a preferred scenario considers  $h$  to have mass of 125 GeV, while the second scalar can be searched for in the high mass region.

According to the previously described properties, hypothetical heavy Higgs boson would have similar event kinematics at LHC as those in the SM Higgs search. Therefore, it makes sense to extend the SM Higgs search at LHC to higher masses.

EWS predicts the heavy Higgs with the width that differs from the SM one by a factor

$$C' \equiv \frac{\Gamma_H}{\Gamma_{SM}} = \frac{\kappa'^2}{1 - BR_{H \rightarrow hh}}$$

that allows the width to be either smaller or larger then the SM one. It means that the heavy Higgs search should be carried out both for the narrow width approximation (NWA) when the resonance width is significantly smaller than experimental resolution, and for the large width (LWA) hypothesis.

In case of the resonance with a large width, there will be a non-negligible interference between the signal and background processes that have the same initial and final states. This interference can significantly affect the phenomenology of the search in a big part of the tested phase space, therefore it be considered in large width searches. The interference is discussed in Section 2.6, while interference modelling for the  $H \rightarrow ZZ \rightarrow 4\ell$  case is developed in Section 6.4.

### 2.3.2 Two-Higgs-doublet model (2HDM)

The Higgs sector is constrained by the experimental observation:

$$\rho \equiv \frac{m_W}{m_Z \cos \theta_W} \approx 1$$

that is usually violated by an extension of the SM Higgs sector, but it can be resolved by a certain level of fine tuning of model parameters. However, if the Higgs sector is extended with additional  $SU_L(2)$  doublet, then  $\rho = 1$  at tree level by construction for entire model phase space. Such SM extension is called 2HDM, and it generalises a broad set of BSM models such as MSSM [39], axion models [40] and baryogenesis models [41]. 2HDM is another popular benchmark model for the heavy Higgs search.

2HDM is assuming two scalar Higgs doublet ( $\Phi_1$  and  $\Phi_2$ ) with nontrivial vacuum expectation values ( $v_1$  and  $v_2$ ), that after spontaneous symmetry breaking would result into five Higgs bosons: two CP-even neutral bosons  $h$  and  $H$  ( $m_H > m_h$  by notation), one CP-odd neutral boson  $A$ , and two charged bosons  $H^\pm$ . While the population of the Higgs sector is common between the 2HDM models, the couplings of the scalars are rather specific for assumed theory.

After imposing a set theoretical constraints (namely, absence of flavour changing neutral current and CP-symmetry conservation [31]), any 2HDM model can be described in terms of seven free parameters: masses of the bosons  $m_h$ ,  $m_H$ ,  $m_A$ ,  $m_{H^+}$  and  $m_{H^-}$ ; ratio of vacuum expectation values for two doublets  $\tan \beta \equiv v_1/v_2$ ; the mixing angle  $\alpha$  between CP-even bosons  $h$  and  $H$ . The SM can be recovered from any 2HDM model for the limit  $\sin(\beta - \alpha) \rightarrow 1$ , then  $h$  is fully consistent with the SM Higgs boson.

In case both doublets have SM like couplings, it would lead to a tree level flavour changing neutral current, that is not supported by experimental observation. This fact can be used to formulate a set of constraints on the Higgs couplings in 2HDM. The remaining allowed coupling configurations that do not initiate flavour changing neutral current, can be classified into 4 types.

The type-I 2HDM assumes that all fermions are coupled to  $\Phi_2$  only, while type-II is defined in such a way that up-type right- hander fermions couple to  $\Phi_2$  and down-type right-handed fermions to  $\Phi_1$ . For both types of 2HDM, the  $h$  coupling to the vector bosons is the SM coupling times  $\sin(\beta - \alpha)$ , and for the  $H$  coupling to vector bosons is the SM times  $\cos(\beta - \alpha)$ . Yukawa couplings of neutral Higgs bosons to fermions in 2HDM type-I and type-II are summarised in Table 2.5. Type-I and type-II models are the most relevant 2HDM models for the  $H$  search at LHC. 2HDM type-III and type-IV have equivalent structure to type-I and type-II respectively, but they are lepton specific.

Table 2.5: Yukawa couplings of neutral Higgs bosons to fermions in 2HDM type-I and type-II . [31]

	2HDM Type-I	2HDM Type-II
<i>h</i> coupling to		
Up quarks	$\sin(\beta - \alpha) + \cos(\beta - \alpha)/\tan \beta$	$\sin(\beta - \alpha) + \cos(\beta - \alpha)/\tan \beta$
Down quarks	$\sin(\beta - \alpha) + \cos(\beta - \alpha)/\tan \beta$	$\sin(\beta - \alpha) - \cos(\beta - \alpha)\tan \beta$
Charged lepton	$\sin(\beta - \alpha) + \cos(\beta - \alpha)/\tan \beta$	$\sin(\beta - \alpha) - \cos(\beta - \alpha)\tan \beta$
<i>H</i> coupling to		
Up quarks	$\cos(\beta - \alpha) - \sin(\beta - \alpha)/\tan \beta$	$\cos(\beta - \alpha) - \sin(\beta - \alpha)/\tan \beta$
Down quarks	$\cos(\beta - \alpha) - \sin(\beta - \alpha)/\tan \beta$	$\cos(\beta - \alpha) + \sin(\beta - \alpha)\tan \beta$
Charged lepton	$\cos(\beta - \alpha) - \sin(\beta - \alpha)/\tan \beta$	$\cos(\beta - \alpha) + \sin(\beta - \alpha)\tan \beta$
<i>A</i> coupling to		
Up quarks	$1/\tan \beta$	$1/\tan \beta$
Down quarks	$-1/\tan \beta$	$\tan \beta$
Charged lepton	$-1/\tan \beta$	$\tan \beta$

The Higgs production mechanism at LCH for 2HDM is quite similar to the SM Higgs case. The dominant production modes are still gluon fusion and vector boson fusion, however their relative

contribution depends on the considered phase space region. VBF becomes particularly important for low  $\tan\beta$  region of type-II model. Relative contribution of top and bottom quark in the quark loop of ggF production mode can change as well.

In practice, the 2HDM model can be probed by performing model independent search for the SM like heavy Higgs boson for ggF and VBF production modes separately. Both narrow and large width cases are interesting here. Later, the model independent result can be interpreted in the context of 2HDM type-I and type-II under some benchmark assumptions on other free parameters of the model [31]. Usually the model dependent result is presented as a function of  $m_H$ ,  $\tan\beta$  and  $\cos\beta$ .

### 2.3.3 Considerations of the heavy Higgs search

As it comes out from this section, it is quite inefficient to test each possible extension of the SM Higgs sector separately, due to the significant diversity of the models and available parameter phase space for each of them. Therefore, experimental search of the BSM Higgs boson is usually carried out in a model independent way that can be further interpreted in terms of a set of benchmark models.

In this thesis the model independent search of a neutral SM-like heavy Higgs boson will be performed. The considered Higgs boson is compatible with  $H$  in EWS and 2HDM.

The search will be carried out both for the narrow width (NWA) and large width (LWA) hypothesis. The NWA assumes that the total width of the Higgs boson is negligible compared to the experimental resolution. In this case the interference of the heavy Higgs boson with the SM Higgs boson and other SM background is negligible, that significantly simplifies the experimental search. However, the NWA does not cover the full phase space of the BSM models, therefore there is a strong motivation to explore large width hypothesis as well. The narrow width scenario will be considered for ggF and VBF production modes separately, while in large width case ggF production mode only will be considered in order to simplify the analysis. The LWA search will also include an interference of the signal with the 125 GeV Higgs and SM background that is discussed in Section 2.6. The model independent search result will be presented as a limit on the heavy Higgs boson production cross section scanned in  $m_H$  and  $\Gamma_H$ .

## 2.4 Heavy Higgs search with Run-1 data from ATLAS detector

After the SM Higgs boson like particle was discovered at LCH around 125 GeV, the Higgs search campaign was continued at higher masses in order to explore a BSM Higgs sector. In this section the ATLAS results will be discussed. The Run1 heavy Higgs search in ATLAS is performed in three decay channels:  $H \rightarrow ZZ$ ,  $H \rightarrow \gamma\gamma$  and  $H \rightarrow WW$ .

### $H \rightarrow ZZ$

This decay channel is represented by four final states:  $llll$ ,  $ll\nu\nu$ ,  $llqq$  and  $\nu\nu qq$ , that have different relative sensitivity at specific mass ranges. The four lepton final state provides the dominant sensitivity in the mass region below 450 GeV, while hadronic channels are more important at higher masses. This analysis is considering the NWA scenario only, that allows to neglect the interference with the SM processes. The limits are set on the production cross section for the ggF and VBF production modes separately. Combination of the search results in all  $ZZ$  final states in terms of 95% CL upper limits on  $\sigma \times BR(H \rightarrow ZZ)$  as a function of  $m_H$  is shown in Figure 2.14. No excess observed in the mass range from 140 to 1000 GeV.

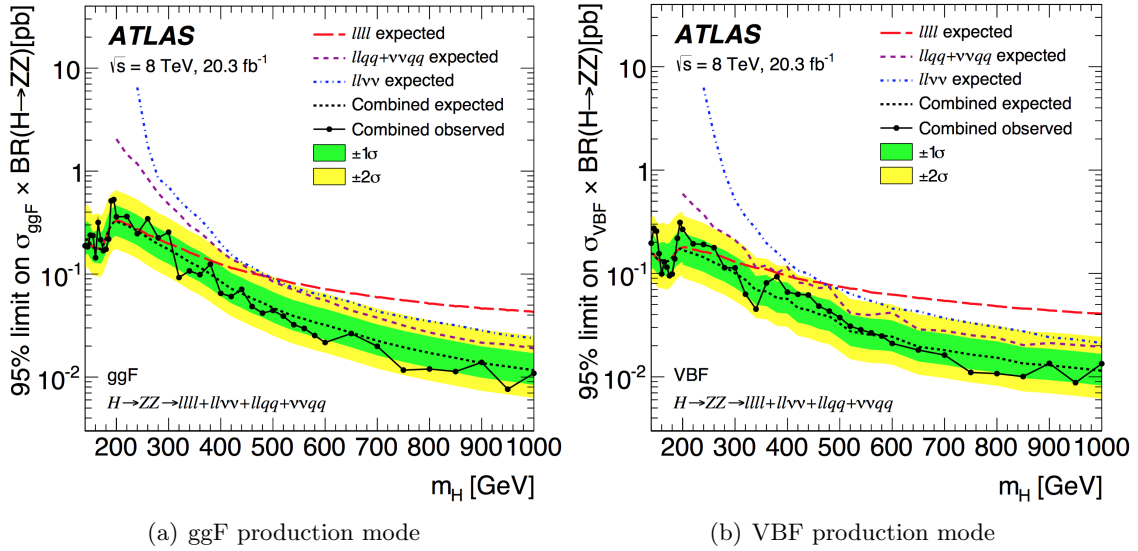


Figure 2.14: 95% CL upper limits on  $\sigma \times BR(H \rightarrow ZZ)$  as a function of  $m_H$ , resulting from the combination of all of the searches in the (a) ggF and (b) VBF channels. The solid black line and points indicate the observed limit. The dashed black line indicates the expected limit and the bands the  $1\text{-}\sigma$  and  $2\text{-}\sigma$  uncertainty ranges about the expected limit. The dashed coloured lines indicate the expected limits obtained from the individual searches; for the  $llqq$  and  $\nu\nu qq$  searches, only the combination of the two is shown as they share control regions. [42]

### $H \rightarrow \gamma\gamma$

In diphoton decay channel the search is performed in terms of the narrow width scalar without any assumptions on its production mode. The mass range from 65 to 600 GeV is explored, while the SM Higgs boson is treated as a background. The search results in terms of 95% CL upper limit on the fiducial cross section times  $BR(X \rightarrow \gamma\gamma)$  as a function of  $m_X$  is shown in Figure 2.15, while no significant excess observed.

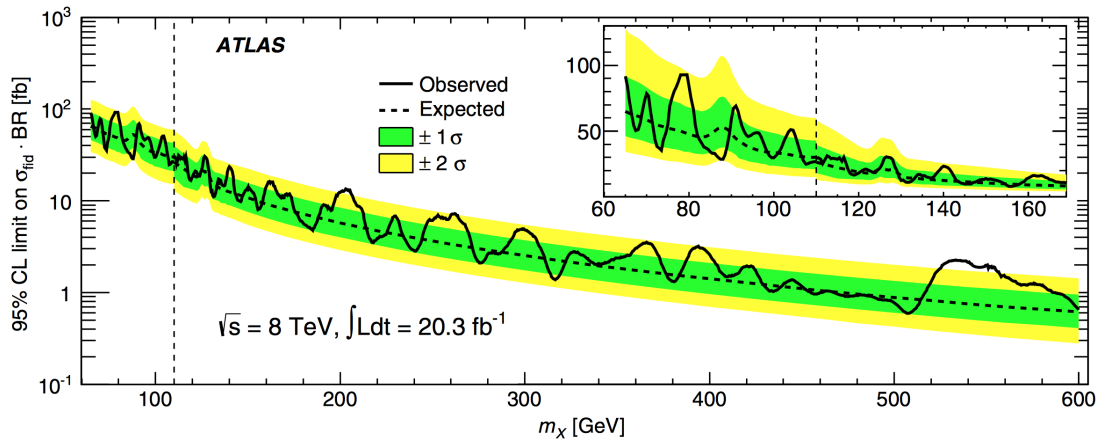


Figure 2.15: Observed and expected 95% CL upper limit on the fiducial cross section times  $BR(X \rightarrow \gamma\gamma)$  as a function of  $m_X$  in the range  $65 < m_X < 600$  GeV. The discontinuity in the limit at  $m_X = 110$  GeV (vertical dashed line) is due to the transition between the low-mass and high-mass analyses. The green and yellow bands show the  $1\text{-}\sigma$  and  $2\text{-}\sigma$  uncertainties on the expected limit. The inset shows a zoom around the transition point. [43]

### $H \rightarrow WW$

There Higgs boson search in  $WW$  decay channel can exploit two final states:  $\ell\nu\ell\nu$  that is more



sensitive at lower masses and  $\ell\nu qq$  that is more useful at higher mass range. This analysis is considering both narrow width approximation and the SM-like width scenario, when the total width is rapidly growing with mass (called CPS since the signal truth line shape is modelled by the complex-pole schema). The ggF and VBF production modes are considered separately. The search results are shown in Figures 2.16 and 2.17, while no significant excess observed in the mass range from 300 to 1500 GeV.

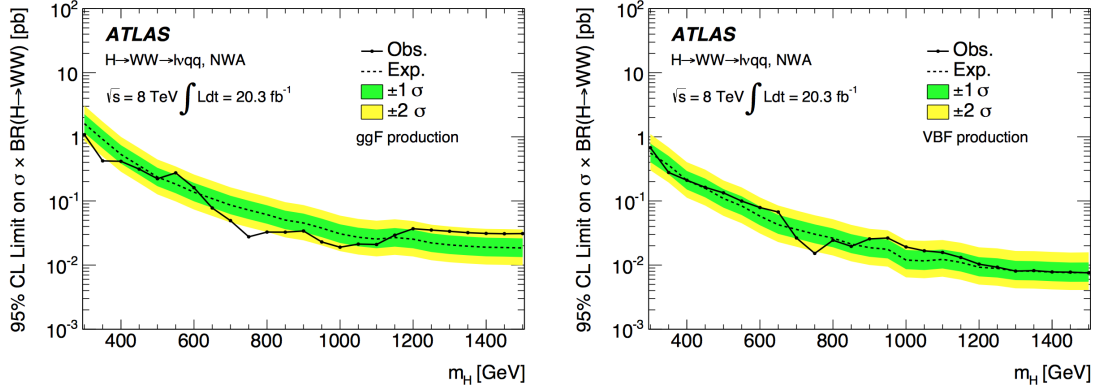


Figure 2.16: 95% CL upper limits on  $\sigma_H \times BR(H \rightarrow WW)$  for a signal with a narrow width from the combination of the  $H \rightarrow WW \rightarrow \ell\nu\ell\nu$  and  $H \rightarrow WW \rightarrow \ell\nu qq$  final states. Limits for ggF production (left) and VBF production (right) are shown. The green and yellow bands show the 1- $\sigma$  and 2- $\sigma$  uncertainties on the expected limit. [44]

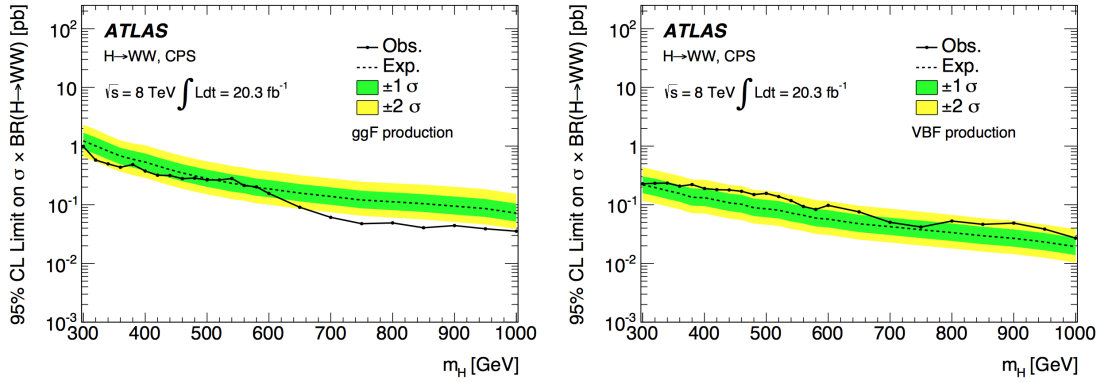


Figure 2.17: 95% CL upper limits on  $\sigma_H \times BR(H \rightarrow WW)$  for a signal with a SM-like width from the combination of the  $H \rightarrow WW \rightarrow \ell\nu\ell\nu$  and  $H \rightarrow WW \rightarrow \ell\nu qq$  final states. Limits for ggF production (left) and VBF production (right) are shown. The green and yellow bands show the 1- $\sigma$  and 2- $\sigma$  uncertainties on the expected limit. [44]

## Summary

Run1 Higgs search in the high mass region set limits on the production cross section of the BSM boson, mostly under the narrow width approximation. Further analyses are interesting not only in terms of including new data and improving the sensitivity, but also in terms of extension of the tested width hypothesis, that would allow to explore larger phase space of the BSM models. The large width assumption would require a proper treatment of the interference effect in the analyses.

## 2.5 Signal line shape in LWA

As stated in the previous section there is a strong motivation to explore the large width hypothesis for the heavy Higgs search. In this case, the natural width of the particle is of the same order or larger than the experimental mass resolution, therefore the truth line shape of the signal should be treated carefully. Moreover, the signal interference with the SM backgrounds have non negligible effect. The SM prediction both for the signal and interference line shapes for the  $H \rightarrow ZZ$  channel will be discussed in this section exploiting.

The SM was discussed in the Lagrangian formalism in Section 2.1, however it is not used directly for the computation of the physics observables. The Lagrangian formalism can be reinterpreted in terms of a set of Feynman rules that provides a convenient toolkit to compute different processes. A basic example of the transition from the Lagrangian to the set of Feynman rules and further cross section calculation is given in Appendix 2.5. Further in this section the Feynman diagrams will be used to estimate the questioned properties of the process.

For the simplicity, the ggF production mode is assumed to be the dominant one, and therefore the other production modes are neglected. Then the only tree level Feynman diagram contributing to the signal is Shown in Figure 2.18.

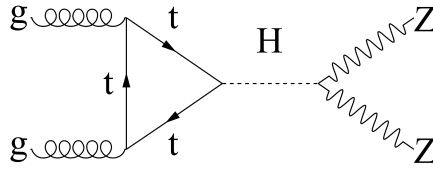


Figure 2.18: Feynman diagram of the ggF production of a heavy Higgs boson with subsequent decay to Z boson pair.

This diagram can be rewritten in terms of the process amplitude according to a set of Feynman rules, but at the end it would lead to a complicated mathematical expression that is not straightforward to compute. On the other hand, this diagram can be factorised into three parts that are interconnected by the single variable, energy in the centre of mass system  $s$ . Thus we can factorise the production amplitude  $A_{prod}^H$  that is on the left side from the propagator, the decay amplitude  $A_{decay}^H$  that is on the right, and a propagator itself. Then the process amplitude  $A^H$  can be written as:

$$A_H(s, \Omega, \Omega') = A_H^{prod}(s, \Omega) \cdot \frac{1}{s - s_H} \cdot A_H^{decay}(s, \Omega') \quad (2.13)$$

where  $\Omega$  and  $\Omega'$  represents different kinematic variables of the initial and final states of the process, and  $\frac{1}{s - s_H}$  is a general notation for the scalar propagator. This amplitude can be used to compute the differential cross section of the process:

$$\sigma_{gg \rightarrow H \rightarrow ZZ}(s) = \frac{1}{2s} \int d\Omega d\Omega' |A_H(s, \Omega, \Omega')|^2 = \frac{1}{2s} \int d\Omega d\Omega' |A_H^{prod}(s, \Omega)|^2 \frac{1}{|s - s_H|^2} |A_H^{decay}(s, \Omega')|^2 \quad (2.14)$$

One can further factorise the integral into three independent parts:

$$\sigma_{gg \rightarrow H \rightarrow ZZ}(s) = \frac{1}{2s} \times \frac{1}{|s - s_H|^2} \times \int |A_H^{prod}(s, \Omega)|^2 d\Omega \times \int |A_H^{decay}(s, \Omega')|^2 d\Omega' \quad (2.15)$$

The two last integrals have similar structure which is coherent with the definition of the particle partial width for the decay in a final state  $F$ :

$$\Gamma_{H \rightarrow F}(s) = \frac{1}{2\sqrt{s}} \int d\Omega |A_{H \rightarrow F}(s, \Omega)|^2 \quad (2.16)$$

In this case the decay component can be replaced by the partial width of the Higgs boson decaying to  $Z$  boson pair, while the production part corresponds to the partial width in case of the decay to  $gg$  final state, because the amplitude is invariant under inversion of time. Therefore, differential cross section can be rewritten as:

$$\sigma_{gg \rightarrow H \rightarrow ZZ}(s) = 2 \frac{1}{|s - s_H|^2} \times \Gamma_{H \rightarrow gg}(s) \times \Gamma_{H \rightarrow ZZ}(s) \quad (2.17)$$

According to the signal definition, it has the same partial widths as the Standard Model Higgs boson ( $\Gamma_{H \rightarrow F} = \Gamma_{h \rightarrow F}$ ). Therefore, one can use analytical expressions for  $\Gamma_{H \rightarrow gg}(s)$  and  $\Gamma_{H \rightarrow ZZ}(s)$  computed in Ref. [45], [46]:

$$\Gamma_{h \rightarrow ZZ}(s) = C \cdot s^{\frac{3}{2}} \cdot \left[ 1 - \frac{4m_Z^2}{s} + \frac{3}{4} \left( \frac{4m_Z^2}{s} \right)^2 \right] \cdot \left[ 1 - \frac{4m_Z^2}{s} \right]^{\frac{1}{2}} \quad (2.18)$$

$$\begin{aligned} \Gamma_{h \rightarrow gg}(s) &= C \cdot s^{\frac{3}{2}} \cdot |A_t(\tau_t)|^2 \\ A_t(\tau) &= 2 \frac{\tau + (\tau - 1)f(\tau)}{\tau^2} \\ \tau_t &= \frac{s}{4m_t^2} \\ f(\tau) &= \begin{cases} \arcsin^2(\sqrt{\tau}), & \tau \leq 1 \\ -\frac{1}{4} \left[ \log \frac{1+\sqrt{1-\tau^{-1}}}{1-\sqrt{1-\tau^{-1}}} - i\pi \right]^2, & \tau > 1 \end{cases} \end{aligned} \quad (2.19)$$

The last missing component in the cross section formula is the scalar propagator. It can be written according to the Bar-schema (rewritten complex-pole schema) described in more details in Ref. [47]. The propagator is given below:

$$\begin{aligned} \frac{1}{s - s_H} &= \frac{1 + i \cdot \bar{\Gamma}_H / \bar{m}_H}{s - \bar{m}_H^2 + i \cdot s \cdot \bar{\Gamma}_H / \bar{m}_H} \\ \bar{m}_H &= \sqrt{\Gamma_H^2 + m_H^2} \\ \bar{\Gamma}_H &= \bar{m}_H \cdot \frac{\Gamma_H}{m_H} \end{aligned} \quad (2.20)$$

where  $m_H$  and  $\Gamma_H$  are assumed heavy Higgs mass and total width. Therefore, the combination of the Equations (2.18)-(2.20), provides a fully analytical expression for the differential parton production cross section.

This differential cross section after the change of variable from  $s$  to  $m_{ZZ} = \sqrt{s}$ , determines the

truth signal line shape, however in case of hadron colliders it should be further corrected by parton luminosity function since it has non trivial dependency on the  $m_{ZZ}$ . The parton luminosity describes the probability of parton interaction in hadron-hadron collisions, and it is precisely defined in Ref. [48]. After adding gluon-gluon luminosity for the 13TeV  $p - p$  collisions, the LWA line shape can be described by the following function:

$$\sigma_{pp \rightarrow H \rightarrow ZZ}(m_{4\ell}) = 2 \cdot m_{4\ell} \cdot \mathcal{L}_{gg} \cdot \frac{1}{|s - s_H|^2} \cdot \Gamma_{h \rightarrow gg}(m_{4\ell}) \cdot \Gamma_{h \rightarrow ZZ}(m_{4\ell}) \quad (2.21)$$

Further validation and experimental implement of the LWA line shape is shown in Section 6.3.

## 2.6 Interference

Except of the signal there are two other SM processes that share  $gg$  initial and  $ZZ$  final states: the SM  $gg \rightarrow ZZ$  (with an amplitude  $A_B$ ) and the ggF production of the SM Higgs boson ( $A_h$ ), that are shown in Figure 2.19.

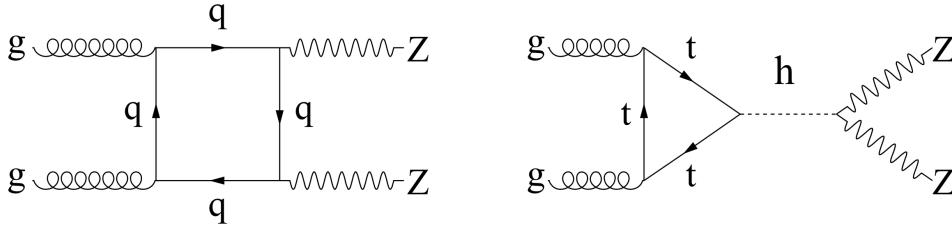


Figure 2.19: Feynman diagram of the SM  $gg \rightarrow ZZ$  process (left) and the ggF production of the SM Higgs boson with a subsequent decay to  $Z$  boson pair (right).

Since all the processes have the same initial and final states, they will interfere with each other. Full parton cross section for the sum of the processes can be written as:

$$\begin{aligned} \sigma_{gg \rightarrow (X) \rightarrow ZZ}(s) &= \frac{1}{2s} \int d\Omega d\Omega' |A_H + A_h + A_B|^2 = \\ &= \frac{1}{2s} \int d\Omega d\Omega' \left( |A_H|^2 + |A_h|^2 + |A_B|^2 \right) + \\ &+ \frac{1}{s} \int d\Omega d\Omega' \left( \text{Re} [A_h \cdot A_B^*] + \text{Re} [A_H \cdot A_h^*] + \text{Re} [A_H \cdot A_B^*] \right) \end{aligned} \quad (2.22)$$

The first term in the equation above corresponds to the heavy Higgs signal, while the further tree are the SM background that is well under control in the search. Finally, the last two terms describe the interference of heavy Higgs boson with the SM Higgs boson and the SM  $gg \rightarrow ZZ$  background respectively. The interference treatment in the experimental search is quite complicated since it will have a non trivial effect both on the signal shape and normalisation depending on the tested hypothesis and analysis sensitivity. Contribution from these terms becomes significant if the heavy Higgs boson is assumed to have Large width, therefore it should be carefully included into the LWA searches.

The interference of the the heavy Higgs with SM Higgs boson is discussed in Section 2.6.1, while The interference with SM  $gg \rightarrow ZZ$  background is discussed in Section 2.6.2.

### 2.6.1 Interference of the heavy Higgs with the SM Higgs

The interference of the two Higgs bosons can be computed according to the following formula:

$$\sigma_{hH}(s) = \frac{1}{s} \int d\Omega d\Omega' \text{Re} [A_H(s, \Omega, \Omega') \cdot A_h^*(s, \Omega, \Omega')] \quad (2.23)$$

while the SM Higgs amplitude can be factorised similar to Equation 2.13:

$$A_h(s, \Omega, \Omega') = A_h^{prod}(s, \Omega) \cdot \frac{1}{s - s_h} \cdot A_h^{decay}(s, \Omega') \quad (2.24)$$

where the production and decay amplitudes are the same as in heavy Higgs case by definition, and the propagator can be written in the complex-pole schema as well. Then the parton cross section for the interference become very similar to the signal cross section, with the only difference in the propagator term:

$$\sigma_{hH}(s) = \frac{1}{s} \times \text{Re} \left[ \frac{1}{s - s_H} \cdot \frac{1}{(s - s_h)^*} \right] \times \int |A_h^{prod}(s, \Omega)|^2 d\Omega \times \int |A_h^{decay}(s, \Omega')|^2 d\Omega' \quad (2.25)$$

Further development of the expression that completely follows the logic of Section 2.5, can be concluded in the cross section for the interference of two Higgs bosons given below:

$$\sigma_{pp}(m_{4\ell}) = 4 \cdot m_{4\ell} \cdot \mathcal{L}_{gg} \cdot \text{Re} \left[ \frac{1}{s - s_H} \cdot \frac{1}{(s - s_h)^*} \right] \cdot \Gamma_{H \rightarrow gg}(m_{4\ell}) \cdot \Gamma_{H \rightarrow ZZ}(m_{4\ell}) \quad (2.26)$$

This expression is fully analytical and can be explicitly computed using Equations (2.18)-(2.20). It is interesting that the interference cross section is equivalent to the heavy Higgs boson cross section (Equation (2.21)) up to the propagator term. However, the propagator term does not affect the event final state kinematics. It means that both the signal and the interference of the two Higgs bosons are expected to have exactly the same acceptance and detector resolution. This feature allows to build the interference pseudo-MC samples by reweighting the LWA signal samples, that significantly reduce computing resources needed for the analysis. Moreover, precise analytical line shape can be directly used for the interference modelling in the LWA search.

### 2.6.2 Interference of the heavy Higgs with the SM $gg \rightarrow ZZ$

The interference of the heavy Higgs bosons and the SM  $gg \rightarrow ZZ$  is defined as:

$$\sigma_{HB}(s) = \frac{1}{s} \int d\Omega d\Omega' \text{Re} [A_H(s, \Omega, \Omega') \cdot A_B^*(s, \Omega, \Omega')] \quad (2.27)$$

While after factorisation of the Higgs propagator it can be rewritten as:

$$\sigma_{HB}(s) = \frac{1}{s} \text{Re} \left[ \frac{1}{s - s_H} \int d\Omega d\Omega' \cdot A_H^P(s, \Omega) \cdot A_H^D(s, \Omega') \cdot A_B^*(s, \Omega, \Omega') \right] \quad (2.28)$$

Unfortunately, the integral in the upper equation is not analytical, therefore it is not easy to perform pure theoretical calculation of the interference differential cross section. However, the interference modelling still can be developed in a bit more sophisticated way. One can treat the

integral as an unknown complex function of  $s$ . Under assumption that this function has a smooth behaviour across the full mass range, one can try to replace it with a complex polynomial of a certain order.

$$\int d\Omega d\Omega' \cdot A_H^P(s, \Omega) \cdot A_H^D(s, \Omega') \cdot A_B^*(s, \Omega, \Omega') \approx (a_0 + a_1 \cdot \sqrt{s} + \dots) + i \cdot (b_0 + b_1 \cdot \sqrt{s} + \dots) \quad (2.29)$$

The introduced polynomial is still an unknown function, however it is described by a certain number of parameters ( $a_i$  and  $b_i$ ) that can be fitted to the MC samples of the interference. These parameters are independent from the Higgs mass and width, therefore they should have the same values for every tested signal hypothesis. After changing the mass variable and adding the gluon-gluon luminosity effect, the interference line shape can be expressed as:

$$\sigma_{pp}(m_{4\ell}) = \mathcal{L}_{gg} \cdot \frac{1}{m_{4\ell}} \cdot \text{Re} \left[ \frac{1}{s - s_H} \cdot ((a_0 + a_1 \cdot m_{4\ell} + \dots) + i \cdot (b_0 + b_1 \cdot m_{4\ell} + \dots)) \right] \quad (2.30)$$

This derivation does not allow to estimate the interference of the heavy Higgs and the SM background, however it provides a reliable modelling of both the shape and the normalisation. Experimental implementation of the method is shown in Chapter 6.



# The Large Hadron Collider and the ATLAS detector

## 3.1 The Large Hadron Collider

The Large Hadron Collider (LHC) [49] is a 26.7 km long circular proton-proton collider constructed at the European Organisation for Nuclear Research (CERN). The LHC was designed to collide proton beams with an unprecedented centre of mass energy up to 14 TeV at designed luminosity of  $10^{34} \text{ cm}^{-2}\text{s}^{-1}$ . It is also aiming to collide heavy ions at 5.5 TeV per nucleon pair at luminosity of  $10^{27} \text{ cm}^{-2}\text{s}^{-1}$ . Four large experiments analyse data from the LHC in order to explore broad physics program never accessible before. The LHC benefits from the existing infrastructure maintained for the Large Electron-Positron collider, so it was installed in the already existing tunnel.

### 3.1.1 The accelerator complex

Proton beams in the LHC are accelerated to the appropriate energy in multiple steps in the CERN accelerator complex, illustrated in Figure 3.1.

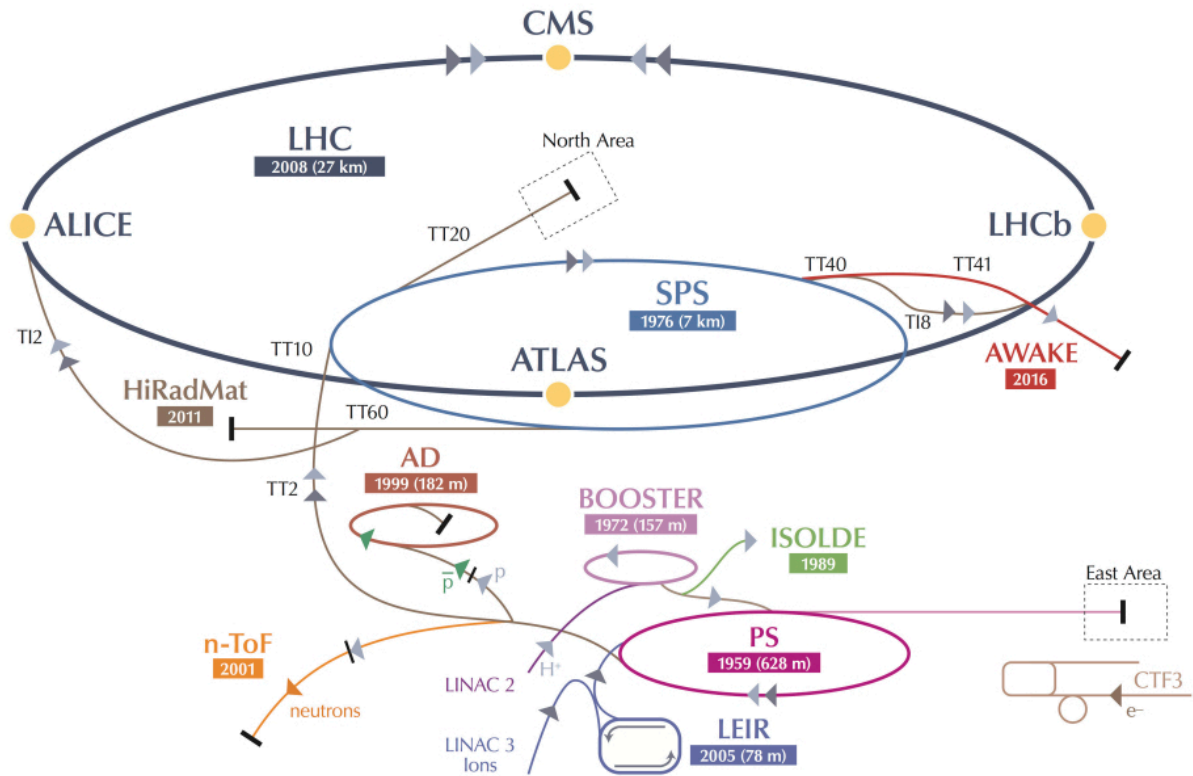


Figure 3.1: Overview of the CERN accelerator complex.



Protons are initially extracted from hydrogen atoms using an electrical field, then they are accelerated to an energy of 50 MeV by the linear accelerator Linac 2. Subsequently, the beam is injected to the Proton Synchrotron Booster (PSB), which accelerates the protons to 1.4 GeV and feeds them to the Proton Synchrotron (PS). The PS increases the energy to 25 GeV and passes the beam on to the Super Proton Synchrotron (SPS), which is the last step before injection to the LHC. The SPS accelerates protons to the energy of 450 GeV and further injects them to the LHC both in clockwise and counter-clockwise directions.

In the LHC, two beams are contained in separate pipes, which intersect at four points where the detectors are based. Further proton acceleration is provided by 8 superconducting radio frequency cavities operated at 400 MHz, located at a single point on the LHC ring. The beam steering is carried out by superconducting dipole magnets that can provide magnetic field of the order of 8 T, with opposite orientation for each of 2 beam pipes. A total of 1232 dipole magnets are installed in the LHC ring. 540 superconducting quadruplet magnets are used to focus the beam.

### 3.1.2 The LCH experiments

Four large experiments are based on the LCH ring: A Toroidal LHC ApparatuS (ATLAS) [50], Compact Muon Solenoid (CMS) [51], A Large Ion Collider Experiment (ALICE) [52] and LHC-beauty (LHCb) [53]. These experiments are located at the four LHC interaction points illustrated in Figure 3.1 and are dedicated to different physics programmes. ATLAS and CMS are designed for a broad variety of the SM measurements and searches of the SM Higgs boson and new physics in proton-proton collisions. The LHCb is dedicated to b-physics, and in particular, to the CP symmetry violation in this sector, while the ALICE experiment is focused on heavy-ion physics. In addition to previously mentioned experiments, there are three smaller ones: TOTEM [54], MoEDAL [55] and LHCf [56], that are focused on specific physics measurements.

This thesis is related to the ATLAS experiment, which is described in details in Section 3.2.

### 3.1.3 Luminosity and operation

One of the most important characteristics of a particle collider performance is an instantaneous luminosity, which is a measure of the data production rate. It is defined according to the following formula:

$$L_{inst} = \frac{f_{rev} \cdot n_b \cdot N_b^2}{2\pi\sigma_x\sigma_y} \cdot F(\phi, \sigma_{x,y}, \sigma_s) \quad (3.1)$$

Here  $f_{rev}$  is the revolution frequency of the accelerated protons (11245 Hz);  $n_b$  is the number of bunches per beam;  $N_b$  is the number of particles per bunch;  $\sigma_x$  and  $\sigma_y$  are the transverse RMS beam dimensions at an interaction point (IP). The  $F$  is the geometrical correction factor and  $\phi$  is an angle between two beams. Usually, the transverse beam size is expressed in terms of the normalised transversed emittance  $\varepsilon_n$ , the betatron function  $\beta^*$  and relativistic gamma factor  $\gamma_r$  as  $\sigma_{x,y} = \sqrt{\varepsilon_n\beta_{x,y}/\gamma_r}$  [57]. Therefore, the expression for luminosity can be rewritten as:

$$L_{inst} = \frac{f_{rev} \cdot n_b \cdot N_b^2 \cdot \gamma_r}{2\pi\varepsilon_n\beta^*} \cdot F(\phi, \sigma_{x,y}, \sigma_s) \quad (3.2)$$

The integrated luminosity  $L$  is the instantaneous luminosity integrated over machine operation time, therefore, it is useful measure to quantify size of a given data sample. Produced number of

events  $N$  from a given process can be determined as a product of the integrated luminosity and a corresponding production cross section:

$$N = L \times \sigma \quad (3.3)$$

The LHC is an outstanding particle collider with pioneering specifications. It had exceeded performance of all previously built colliders, both in terms of interaction energy and luminosity. The LHC started its operation in 2008, and the first two years were required for the machine commissioning and tuning. The first data taking period called Run-1 took place in 2010-2012, while there was delivered  $5.5 \text{ fb}^{-1}$  of 7 TeV proton-proton data in 2011 and  $23 \text{ fb}^{-1}$  of 8 TeV proton-proton data in 2012 [58]. This data set allowed to perform numerous spectacular physics measurements, and in particular it led to the Higgs boson discovery. Run-1 was followed by two years long shutdown, that was needed for accelerator and detectors development in order to get to the designed performance. The data taking was resumed in 2015, that was a beginning of so called Run-2. There was  $4.2 \text{ fb}^{-1}$  of 13 TeV data delivered for ATLAS in 2015, and  $38.5 \text{ fb}^{-1}$  at 13 TeV in 2016 [59]. The Run-2 data set is used in the physics analyses presented further in this thesis. A summary of the luminosity delivered for ATLAS experiment by the end of 2016 is shown in Figure 3.2. In total the LHC is planned to deliver  $350 \text{ fb}^{-1}$  of 14 TeV data by 2021 [60].

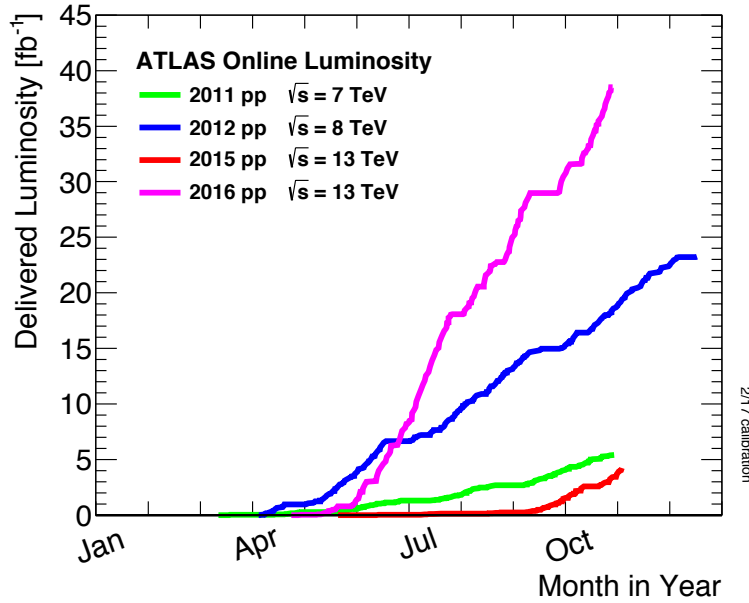


Figure 3.2: The total integrated luminosity delivered ATLAS experiment during 2011-2012 and 2015-2016 data-taking periods. [59]

High instantaneous luminosity of the LCH give an opportunity to record more data, but unfortunately, it results into some serious complication for the data analysis. While operating in high luminosity mode, there will be typically few tens of proton-proton collisions per bunch crossing. At most one of the collisions can contain interesting physics while the others will produce a significant background that complicates reconstruction of the final state. This problem is called pile-up, and it is one of the limiting factors for the high luminosity machines. In some physics analysis, the pile-up background can be rejected by precise determination of the primary vertex, however it is not an absolute solution since the pile-up also affects the trigger.

## 3.2 The ATLAS detector

ATLAS is a multi-purpose particle detector of typical  $4\pi$  geometry that is shown in Figure 3.3. In order to target a diverse physics programme, the detector should be capable to efficiently trigger and reconstruct a broad variety of final states. Therefore, three detector sub-systems can be distinguished in ATLAS: the Inner Detector, the Calorimeters and the Muon Spectrometer. Design requirements to the performance of these systems are summarised in Table 3.1.

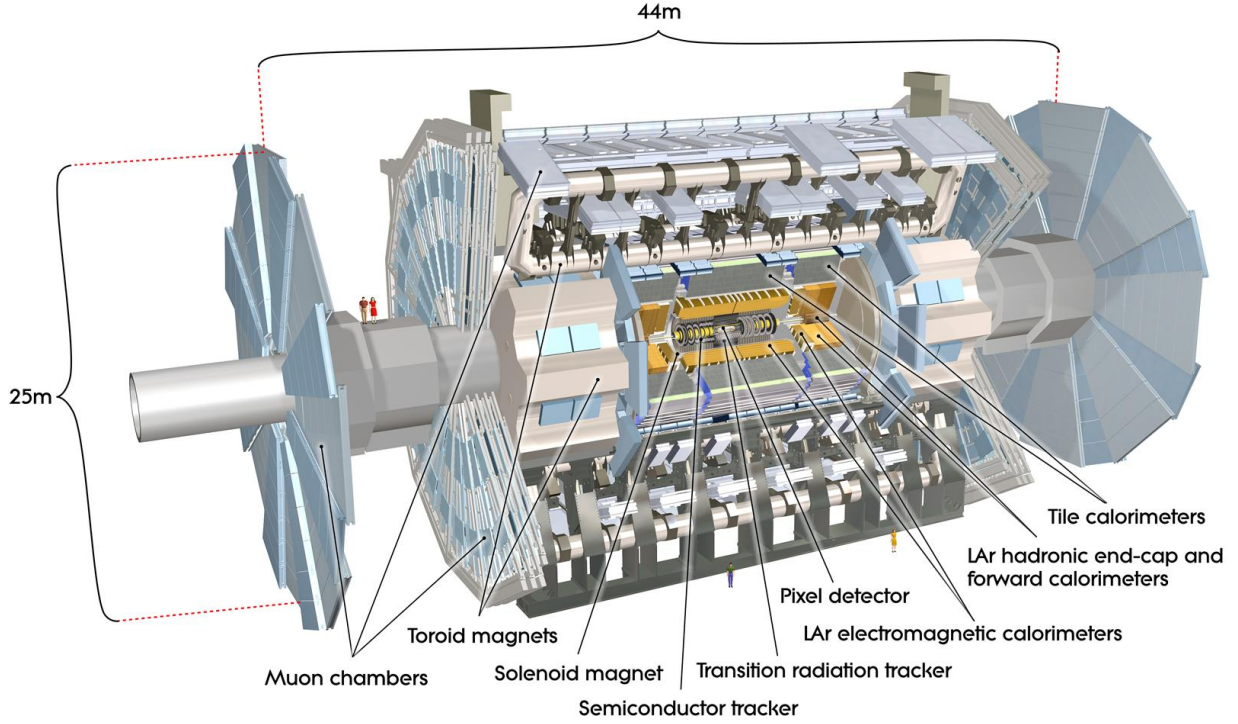


Figure 3.3: Cut-away view of the ATLAS detector, with different sub-systems identified. [50]

Detector component	Required resolution	$\eta$ coverage	
		Measurement	Trigger
Tracking	$\sigma_{p_T}/p_T = 0.05\% \text{ } p_T \oplus 1\%$	$ \eta  < 2.5$	
EM calorimetry	$\sigma_E/E = 10\%/\sqrt{E} \oplus 0.7\%$	$ \eta  < 3.2$	$ \eta  < 2.5$
Hadronic calorimetry			
barrel and end-cap	$\sigma_E/E = 50\%/\sqrt{E} \oplus 3\%$	$ \eta  < 3.2$	$ \eta  < 3.2$
forward	$\sigma_E/E = 100\%/\sqrt{E} \oplus 10\%$	$3.1 <  \eta  < 4.9$	$3.1 <  \eta  < 4.9$
Muon spectrometer	$\sigma_{p_T}/p_T = 10\% \text{ at } p_T = 1 \text{ TeV}$	$ \eta  < 2.7$	$ \eta  < 2.4$

Table 3.1: Performance requirements for the ATLAS detector.  $E$  and  $p_T$  are given in GeV units. [50]

This section describes the detector sub-systems and the trigger system, as well as discusses plans for the further upgrade.

### 3.2.1 Naming conventions and coordinate system

The coordinate system and nomenclature used to describe the ATLAS detector and the particles emerging from the proton-proton collisions are briefly summarised here, since they will be used

repeatedly. The nominal interaction point is defined as the origin of the coordinate system, while the beam direction defines the  $z$ -axis and the  $x$ - $y$  plane is transverse to the beam direction. The positive  $x$ -axis is defined as pointing from the interaction point to the centre of the LHC ring and the positive  $y$ -axis is defined as pointing upwards. The side-A of the detector is defined as that with positive  $z$  and side-C is that with negative  $z$ . The azimuthal angle  $\phi$  is measured as usual around the beam axis, and the polar angle  $\theta$  is the angle from the beam axis. The pseudorapidity is defined as:

$$\eta = -\ln[\tan(\theta/2)]. \quad (3.4)$$

The transverse momentum  $p_T$  and the transverse energy  $E_T$  are defined in the  $x$ - $y$  plane unless stated otherwise. The distance  $\delta R$  in the pseudorapidity-azimuthal angle space is defined as:

$$\Delta R = \sqrt{\Delta\eta^2 + \Delta\phi^2} \quad (3.5)$$

### 3.2.2 Inner detector

The ATLAS Inner Detector (ID) [61] is designed to provide hermetic and robust pattern recognition, excellent momentum resolution and both primary and secondary vertex measurements for charged tracks above approximately 0.5 GeV. Its acceptance covers the pseudorapidity range  $|\eta| < 2.5$ . It also provides electron identification over  $|\eta| < 2.0$ . One of the main requirements on the ID is to be capable to operate at very large track density environment, without degrading the resolution, therefore, this detector has very fine granularity. The ID consists of three types of tracking components listed from innermost one: Silicon Pixel Detector (PIX), SemiConductor Tracker (SCT) and Transition Radiation Tracker (TRT). The ID layout is shown in Figures 3.4 and 3.5, while the specification of each of detector components is given in Table 3.2.

Detector	Coverage	Composition	Resolution [ $\mu m$ ]
Pixel	$ \eta  < 2.5$		
Barrel		3 layers + IBL	10 $R - \phi \times 115(z)$
End-cap		2×3 disks	10 $R - \phi \times 115(R)$
SCT	$ \eta  < 2.5$		
Barrel		4 layers	17 $R - \phi \times 580(z)$
End-cap		2×9 disks	17 $R - \phi \times 580(R)$
TRT	$ \eta  < 2.0$		
Barrel		73 straw panels	130 $R - \phi$
End-cap		160 straw panels	130 $R - \phi$

Table 3.2: Specification of the ID detector [50], [62], [63].

The ID is tracking particles with energies above 0.5 GeV, and each track is defined by 5 variables: azimuthal and polar angle ( $\eta$  and  $\phi$ ), the charge of the particle divided by its momentum ( $q/p$ ) determined from the track curvature, and its coordinate of origin specified by transverse and longitudinal impact parameter ( $d_0$  and  $z_0$ ). In order to perform the momentum measurement, the inner detector is placed into magnetic field of 2 T, provided by a solenoid inserted between the ID and the EM calorimeter.

**The semi-conductor pixel detector** is positioned the closest to the beryllium beam-pipe and has the highest granularity. The main limitation of the pixel detector is the radiation hardness as the expected fluence is at the tolerable limit. Wide ( $400 \times 50 \mu m$ )  $n^+/n$  silicon sensors of  $250 \mu m$  thickness are used here. The silicon pixel detector consists of three layers in the barrel region at  $R = 50.5, 88.5$  and  $122.5$  mm, and three discs in the end-cap regions on each side positioned at  $|z| = 495, 580$  and  $650$  mm. In total there are about 80 million readout channels in the whole

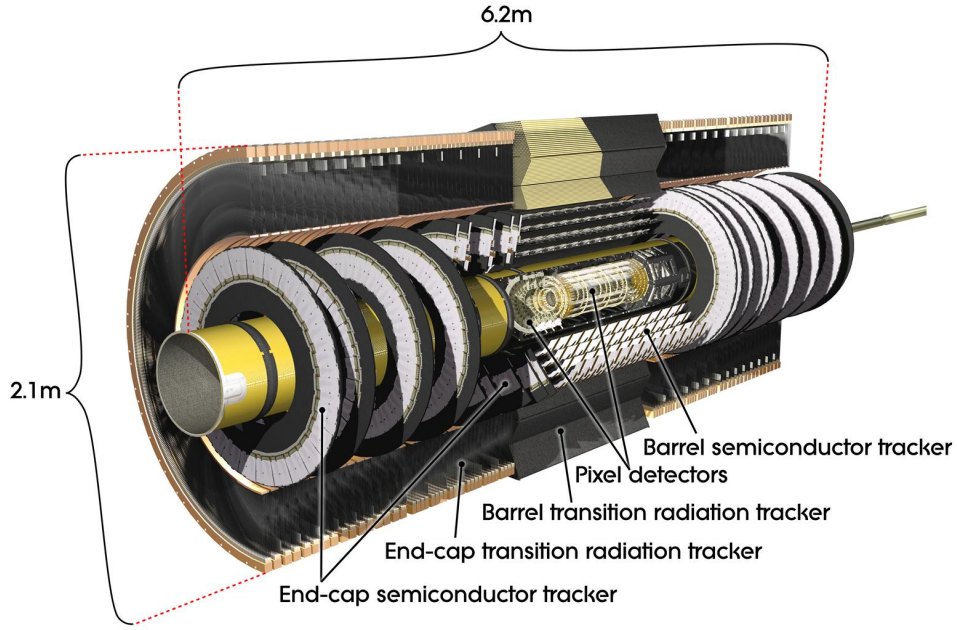


Figure 3.4: Cut-away view of the ATLAS inner detector. [50]

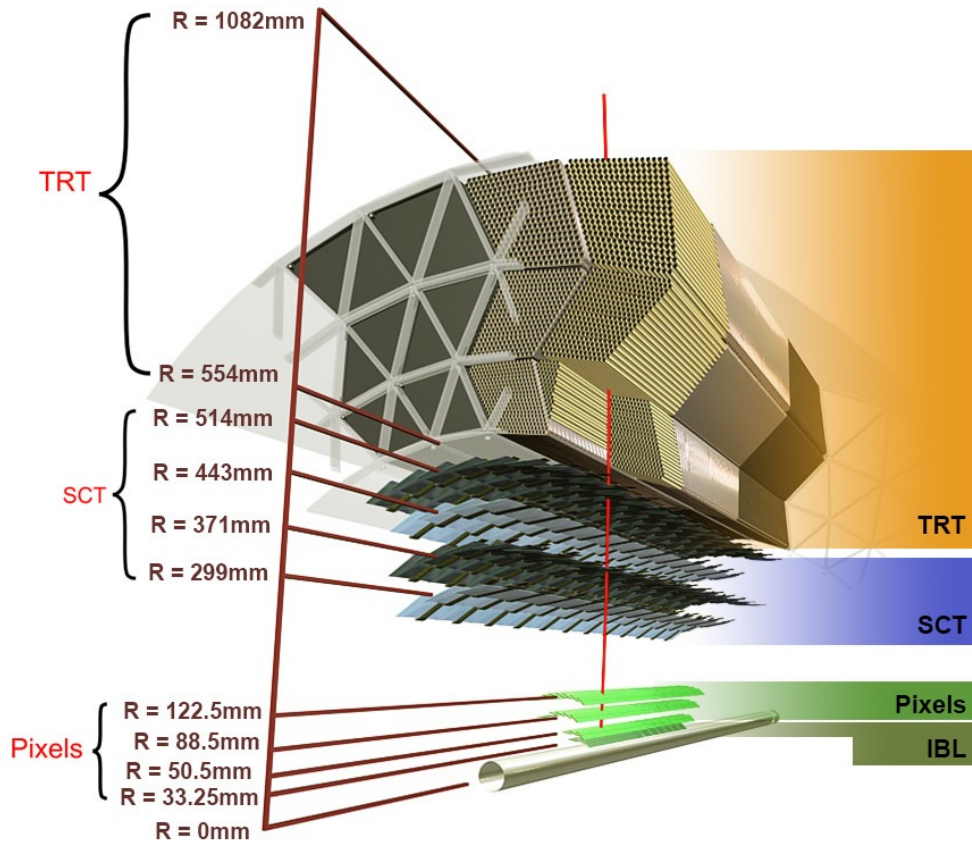


Figure 3.5: Illustration of a track traversing the three detectors in the ID. [64]

Pixel Detector. The intrinsic spatial resolution of individual Pixel Detector modules is  $10 \mu\text{m}$  in  $R\phi$  and  $115 \mu\text{m}$  in  $z$ .

In order to maintain adequate performance at an instantaneous luminosity greater than  $10^{34} \text{ cm}^{-2}\text{s}^{-1}$ , a fourth layer, the so called insertable B-layer (IBL), was integrated before the start of Run-2. The

IBL is positioned at radial distance  $R = 33$  mm, and is constructed with the same geometry and detecting medium as the existing three layers. The IBL pixels have dimensions of  $50 \times 250 \mu\text{m}^2$  (in  $\phi \times z$ ), that allows to deal with higher occupancy than in the original layers. Moreover, the IBL allows to increase precision of the primary vertex position determination, that leads to reduction of the uncertainty on the transverse impact parameter. This parameter is important since it is widely used for background rejection in physics analysis [64].

**The SCT**, similarly to the PIX, is a silicon detector, but it exploits  $80 \mu\text{m}$  wide 12 cm long microstrips rather than pixel sensors. Single layer of the strips provides spatial resolution of  $16 \mu\text{m}$  in  $R - \phi$  and  $580 \mu\text{m}$  in  $z$  ( $R$ ) in barrel (end-cap). Barrel part of the SCT consists of 4 layers, while the forward modules are represented by nine end-cap wheels on each side. There are 6.3 millions readout channels for the SCT in total.

**The TRT** is composed of multiple layers of gaseous straw tubes inserted in a material that initiates transition radiation. The TRT provides more tracking points comparing to the PIX and the SCT, however, precision of these measurements is less accurate. In addition to its tracking capability, the TRT also provides particle identification. Transition radiation measurements allow to distinguish electrons from pions, that is rather important feature for electron identification procedure.

### 3.2.3 Calorimeter

The calorimeter surrounds the ID as shown in Figure 3.6, and it is aiming to absorb all the high energetic particles except of muons and neutrinos, while measuring their energy. The calorimeter consists of two parts: the electromagnetic calorimeter that exploits the liquid argon (LAr) technology and absorbs electromagnetic particles such as electrons and photons; the hadron calorimeter is used to detect the rest of particles and it exploits both LAr and tile technologies. It is important that the calorimeter absorbs all the particles coming from the IP, otherwise prompt particles will penetrate to the Muon Spectrometer and affect the muon reconstruction. The calorimeter material depth in units of interaction length as a function of  $\eta$  is displayed in Figure 3.7. Specification of the ATLAS calorimeter is shown in Table 3.3.

Detector	Absorber	Active material	Coverage
Presampler			
Barrel		Liquid Argon	$ \eta  < 1.52$
End-cap		Liquid Argon	$1.5 <  \eta  < 1.8$
Electromagnetic			
Barrel	Lead	Liquid Argon	$ \eta  < 1.48$
End-cap	Lead	Liquid Argon	$1.38 <  \eta  < 3.2$
Forward	Copper	Liquid Argon	$3.1 <  \eta  < 4.9$
Hadronic			
Barrel	Steel	Scintillating tiles	$ \eta  < 1.7$
End-cap	Copper	Liquid Argon	$1.5 <  \eta  < 3.2$
Forward	Tungsten	Liquid Argon	$3.1 <  \eta  < 4.9$

Table 3.3: Specification of the ATLAS calorimeter [50], [65].

**The Liquid Argon Calorimeters** cover four different components of the detector: the electromagnetic barrel calorimeter (EMB), electromagnetic end-cap calorimeter (EMEC), the hadronic end-cap calorimeter (HEC) and the forward calorimeter (FCal). The liquid argon is widely used in calorimetry due to its unique properties such as radiation-hardness, stability, linear response and low cost. However, it should be kept at rather low temperature (88.5 K) during the operation [65].



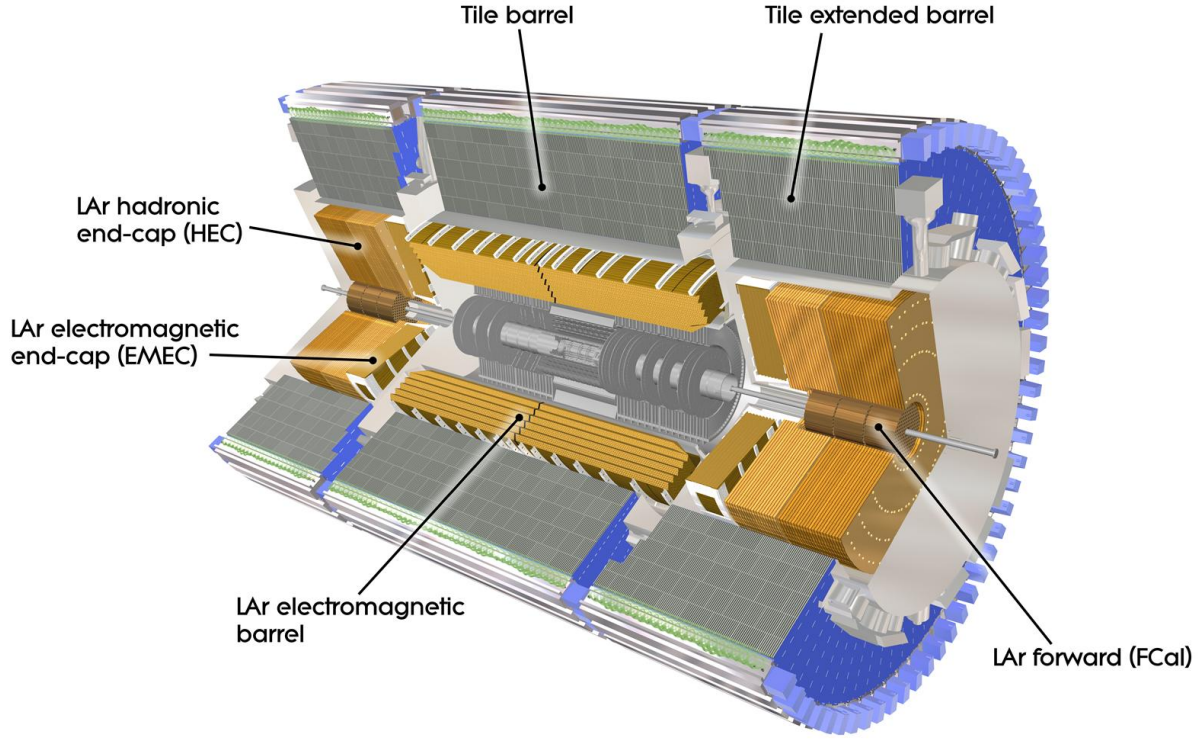


Figure 3.6: The ATLAS calorimeter with highlighted components. [50]

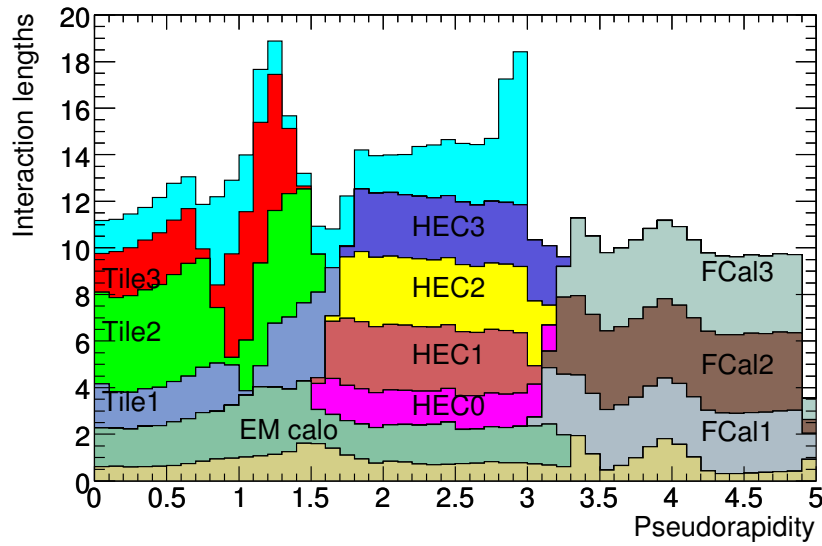


Figure 3.7: Cumulative amount of material in the ATLAS calorimeter components in units of interaction length as a function of  $\eta$ . [50]

Big part of the LAr calorimeter (EMB and EMEC) is a sampling calorimeter with a lead absorber of accordion-like shape. Both liquid argon and the read out electrodes are repeating the shape in the gaps between layers of the absorber. This specific geometry is advantageous because it naturally provides full coverage in  $\phi$  without any cracks. In the EMB, the accordion waves are axial and arranged in  $\phi$ , whereas in the EMEC, they are rotated by  $90^\circ$  to ensure full coverage. Both EMEC and EMB have three separate layers, while the granularity of the detector is decreasing for outer layers. The front layer is targeting a finely segmented description of the shower profile,

the middle layer provides a precise energy measurement, while the last one captures shower's tail. HEC calorimeter has similar structure, but instead of lead accordion-like absorber, the flat copper one is used.

The FCal has quite different design due to other operation conditions. It is located in very forward region close to the beam pipe, where the particle flux is much higher than in other regions of the detector. The FCal works both like electromagnetic and hadronic calorimeters. The absorber has a shape of three cylinders aligned along the beam pipe. The first cylinder is made of copper while the other two are made of tungsten. Liquid argon together with the read out electrodes is placed in holes that are drilled along the beam direction.

Moreover, the LAr is used for the presampler, which is an individual component that has been added to detect showers initiated by interactions with material before the calorimeters. This detector is covering  $|\eta| < 1.8$  range.

**The Tile Calorimeter** is positioned behind the EMB, and it is meant to absorb hadrons and to measure their energy, in the barrel region of the detector. This calorimeter has steel absorber, while the active material is represented by scintillating tiles. The tiles are arranged in radial direction, perpendicular to the beam pipe. Similarly to other parts of the detector, read-out of the Tile Calorimeter is segmented according to depth, with granularity decreasing with radial distance [66].

### 3.2.4 Muon Spectrometer

The muon spectrometer (MS) forms the outer part of the ATLAS detector, defining its overall dimensions. It is a combination of large superconducting air-core toroid magnets and a system of gaseous detectors that are used both for precision measurements and trigger purpose, as shown in Figure 3.8. It is designed to detect charged particles, namely muons, exiting the calorimeter and to measure their momentum in the pseudorapidity range of  $|\eta| < 2.7$ . It is also meant to provide triggering capability based on the muon signal in a region of  $|\eta| < 2.4$ . The designed performance goal is a stand-alone transverse momentum resolution of approximately 10% for 1 TeV tracks, which translates to a resolution of 50  $\mu\text{m}$  for a single point measurement.

Cost, performance requirements and the radiation tolerance led to implementation of four different technologies for the muon chambers. Over most of the pseudorapidity range, a precision measurement in the track bending direction is carried out by the Monitored Drift Tubes, while in the very forward region close to the beam pipe the Cathode Strip Chambers with higher granularity are used to treat demanding hit rate and background conditions. The trigger system is represented by the Resistive Plate Chambers in the barrel and the Thin Gap Chambers in the end-cap regions. Both trigger chambers also provide a measurement of the  $\phi$  coordinate. Specification for all the chambers is given in Table 3.4 and each of them will be discussed further in this section. More detailed information about the muon spectrometer can be found in Ref. [50, 67].

Technology	Coverage	Resolution
Precision		
MDT	$ \eta  < 2.7$	35 $\mu\text{m}$ ( $z$ )
CSC	$2.0 <  \eta  < 2.7$	40 $\mu\text{m}$ ( $R$ ) $\times$ 5 mm ( $\phi$ )
Trigger		
RPC	$ \eta  < 1.05$	10 mm ( $z$ ) $\times$ 10 mm ( $\phi$ )
TGC	$1.05 <  \eta  < 2.7$	2-6 mm ( $R$ ) $\times$ 3-7 mm ( $\phi$ )

Table 3.4: Specification of the ATLAS Muon Spectrometer [50], [50].



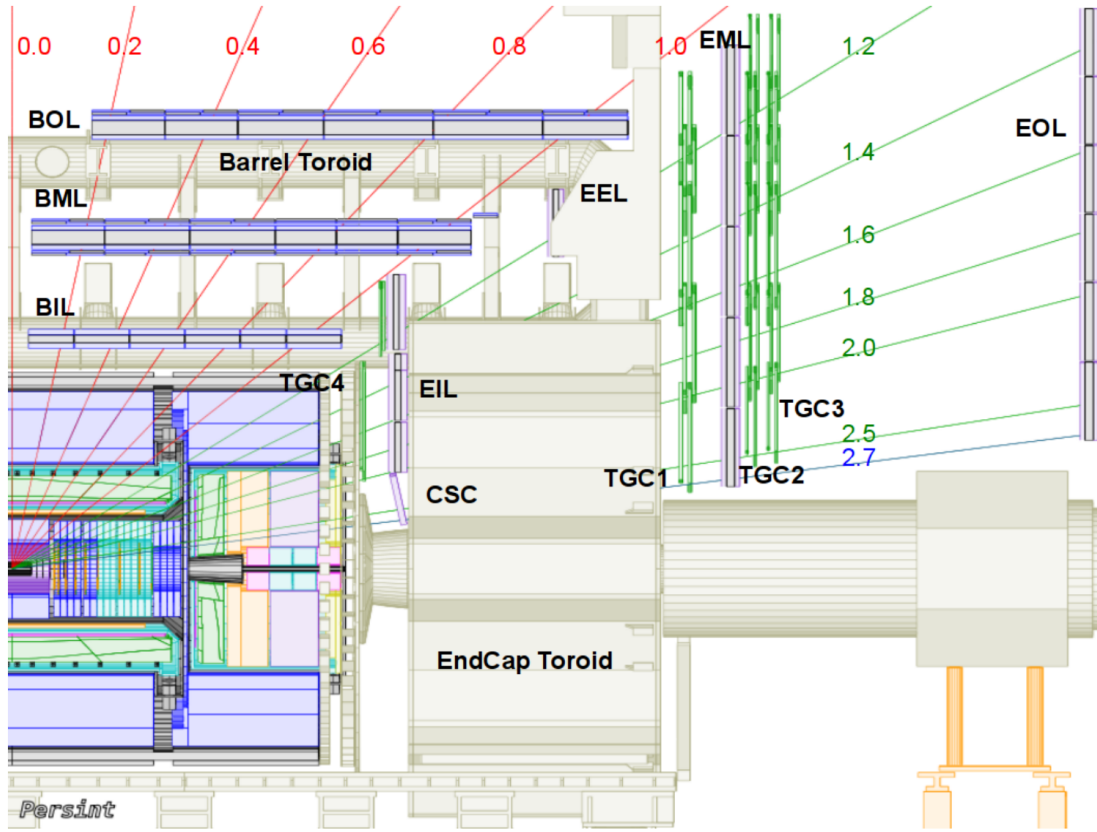


Figure 3.8:  $z$ - $y$  cut view of the MS and the toroid magnet. [50]

### The toroidal magnets

Measurement of a particle momentum in the MS is possible due to magnetic field bending its trajectory in the  $\eta$ -plane. This magnetic field is provided by a set of three toroidal magnets: a barrel toroid, and two smaller end-cap toroids. The barrel one provides magnetic field of the 0.5 T, while 1 T field is reached in the end-cap. Each of the three magnets has eight coils arranged around the beam pipe, as shown in Figure 3.9. They exploit superconducting technology based on NbTi/Cu material at the operation energy of 4.7 K [68]. Magnetic field in the barrel region ( $|\eta| < 1.4$ ) is fully provided by the big toroid, while magnetic field of the end-cap region ( $1.6 < |\eta| < 2.7$ ) is caused by the smaller toroids. In the transition region of  $1.4 < |\eta| < 1.6$  the fields from both barrel and end-cap toroids contribute.

The magnetic field provides typical bending powers  $\int Bdl$  of 3 Tm in the barrel and 6 Tm in the end-cap regions that is shown in Figure 3.10.

### The Monitored Drift Tubes (MDT)

The Monitored Drift Tubes are aluminium tubes of 29.970 mm diameter filled with Ar/CO<sub>2</sub> gas (93% / 7%) at a pressure of 3 bar. A tungsten-rhenium wire of 50  $\mu\text{m}$  diameter that acts as an anode is placed in the centre of the tube. The tube wall plays a role of a cathode with a nominal difference of potentials of 3080 V. Two end-plugs hold the wire at a precise and stable position with respect to the tube.

An ionising particle traversing the MDT tube left a trace of ionisation electrons that drift in the electric field to the anode, while creating an avalanche close to the wire. The arrival time of the signal can be interpreted as a drift-radius. Single-wire resolution of the order of 80  $\mu\text{m}$  is achieved with a detection efficiency around 96%. Single-wire resolution as a function of the drift distance is shown in Figure 3.12. In ATLAS there are 380,000 MDTs grouped in 1194 chambers, covering a

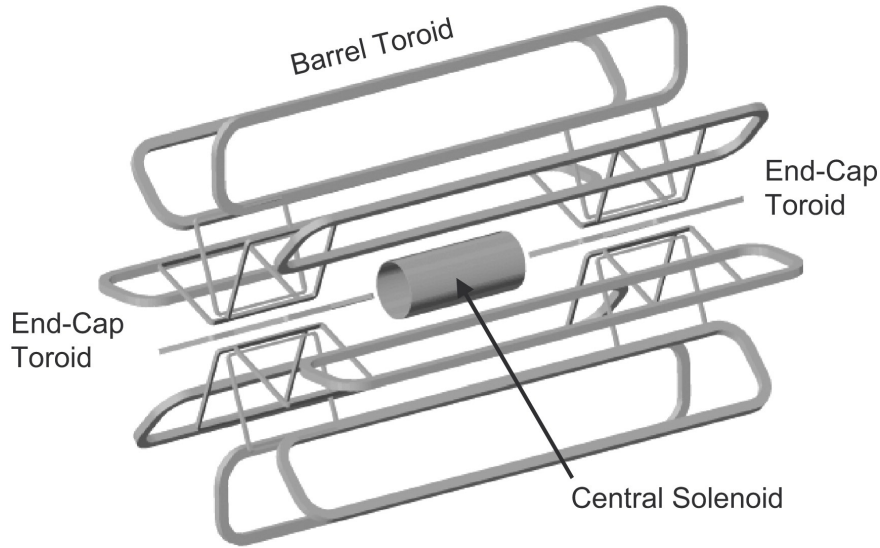


Figure 3.9: Schematic view of the solenoidal and toroidal magnets in the ATLAS detector. [50]

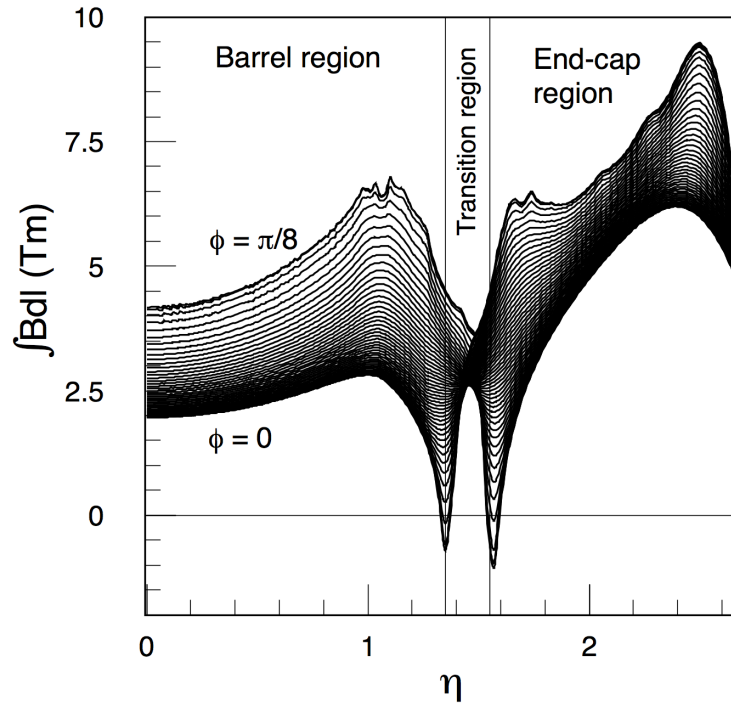


Figure 3.10: Toroid bending power  $\int Bdl$  of the azimuthal field component, integrated between the first and last muon chamber, as a function of pseudorapidity. The curves correspond to azimuthal angles equally spaced between the BT and ECT coil planes. [67]

total area of 5500 m<sup>2</sup>. Every chamber consists of two multi-layers, as shown in Figure 3.11. In the middle and outer stations each multi-layers host three layers of drift tubes, while there are four layer structures in the inner station. The overall precision of a chamber in the plane transverse to the anode wires is 40 μm. [69]

### The Cathode Strip Chambers (CSC)

The Cathode Strip Chambers are multi-wire proportional chambers with a cathode strip readout. Each chamber is composed of 4 layers with 5 mm gaps filled with Ar / CO<sub>2</sub> (80% / 20%). The wire plane is located at the centre of each gap, with a wire pitch of 2.5 mm, equal to the anode-cathode

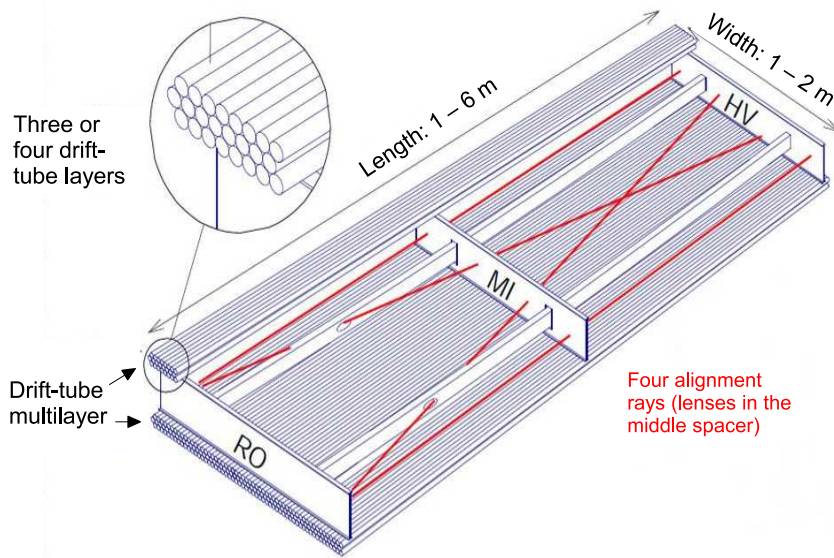


Figure 3.11: Structure of a MDT chamber. An aluminium frame carries two multi-layers of three or four drift tube layers. The internal geometry of the chamber is monitored by two parallel and two diagonal optical alignment rays.

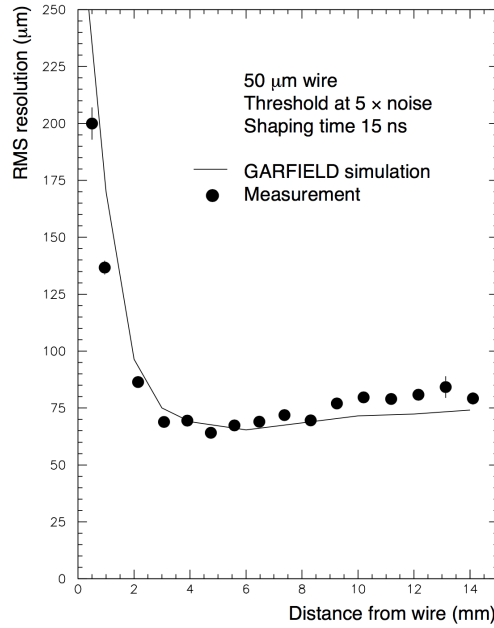


Figure 3.12: MDT single-wire resolution as a function of the drift distance. Note that this plot was produced for a different gas mixture (91% Ar, 4% N<sub>2</sub>, 5% CH<sub>4</sub>) with respect to the one currently used in ATLAS MDT. [67]

spacing, as illustrated in Figure 3.13(a). The CSC is installed in the inner-most end-cap muon station that covers a pseudorapidity range of  $2 < |\eta| < 2.7$ . It has been selected for high counting rate capability, good spatial resolution and short electron drift time of less than 40 ns, that allow to operate at high background conditions.

The precision coordinate is determined in the CSC from a charge distribution measured on the cathode strips. The second coordinate is readout using another set of strips which are parallel to the anode wires (orthogonal to the cathode strips). The spatial resolution on the precision coordinate per measurement plane is 60 μm, while for the second coordinate the resolution is around 5 mm. [69]

### The Resistive Plane Chambers (RPC)

The RPC are gaseous detectors which provide the trigger and a second coordinate measurement in the barrel. They are made of two parallel resistive electrode-plates of phenolic-melaminic plastic laminate which are separated from each other by insulating spacers forming a gas gap of 2 mm. The gap is filled with a mixture of  $\text{C}_2\text{H}_2\text{F}_4$  / Iso- $\text{C}_4\text{H}_{10}$ /SF<sub>6</sub> (94.7/5/0.3). Electric field, which is created between the plates, is about 4.9 kV/mm, it's suitable to produce electron avalanches along the ionising tracks towards the anode. Signal is read out from metallic strips, which are mounted on outer faces of the two resistive plates, two sets of strips are perpendicular to each other. These are called  $\eta$ - and  $\phi$ -strips,  $\eta$ -strips are parallel to the MDT wires and provide  $\eta$  coordinate measurement, while  $\phi$ -strips are orthogonal to the MDTs wire and give the second coordinate. The spatial resolution is roughly 1 cm, while timing resolution is 2 ns. [69]

### The Thin Gap Chambers (TGC)

The TGC have the same function as the RPC, to provide trigger and second coordinate measurement in the end-cap region. Each chamber is a multi-wire proportional chamber filled with a highly quenching gas mixture of CO<sub>2</sub> and n-pentane, the TGC layout is shown in Figure 3.13(b). It operates in a quasi-saturated mode, preventing an occurrence of streamers in all operating conditions. Wire-to-cathode distance of 1.4 mm and wire-to-wire distance of 1.8 mm lead to very good time resolution.

Including variation of the propagation time, signal arrives with 99% probability inside a time window of 25 ns. Such a timing fully corresponds to the needs of the trigger system. The radial, bending coordinate is measured by the TGC wire groups, while the azimuthal coordinate is determined by the radial strips. [69]

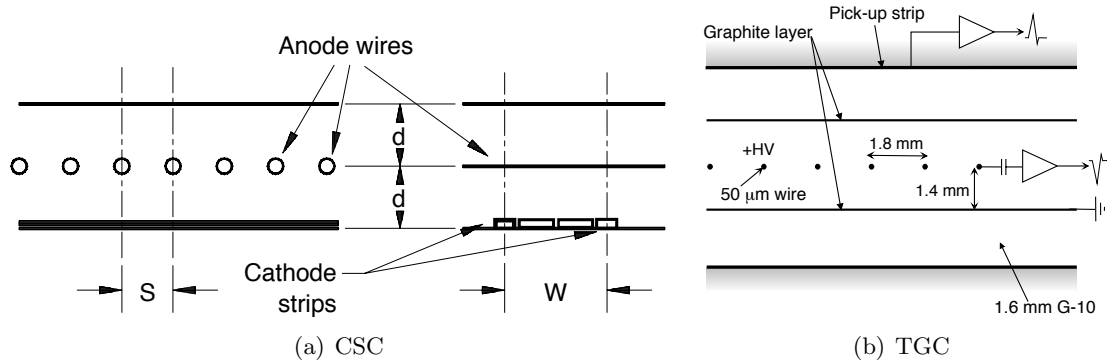


Figure 3.13: Structure of Cathode Strip Chambers (a) and Thin Gap Chambers (b).

### Precision chamber alignment

Accurate measurement of the muon tracks in the Muon Spectrometer requires ultimate precision in the relative positioning of individual detector elements (drift tubes). Although the construction and mounting quality ensures precise initial position of the detector, it does not account for dynamic chamber deformation due to temperature or magnetic field variation or gravity effect. Therefore, chamber deformations and positions are continuously monitored by the optical alignment system and displacements of up to  $\sim 1$  cm can be corrected for in the offline analysis.

The ATLAS muon alignment system consist of about 12 000 precisely mounted optical sensors that monitor both the internal chamber deformation and their relative positions within projective towers, and a set of thermal sensors that monitor global thermal expansion. In the barrel MS the optical sensors are placed directly on the MDT chambers, while in the end-cap the sensors sit on a set of precision bars that are attached to the chambers.

The alignment system includes two types of optical sensors: a 3-point alignment device RASNIK

(Read Alignment System of NIKhef) [70] and a camera system SACAM / BCAM (SAclay CAMera in the barrel and a Boston Ccd Angle Monitor in the end-cap).

In addition to the optical alignment system, the global position determination of the barrel and end-cap muon-chamber systems with respect to each other and to the Inner Detector is performed by track-based alignment algorithms. This algorithm exploits nearly straight tracks in order to determine relative position of the detectors. It can make use either of high energy muons or dedicated alignment runs without toroidal field. The desired accuracy in the sagitta measurement of  $50\text{ }\mu\text{m}$  can only be achieved with the combination of both alignment technics.

### 3.2.5 Trigger system and data acquisition

The trigger system is used to reduce a rate of recorded events. The LHC produce data with the rate of 40 MHz (rate of the bunch crossing) that should be reduced at least to 20 Hz that can be actually recorded. The ATLAS trigger system consists of three consequent parts: Level-1 (L1), Level-2 (L2) and the Event Filter (EF).

L1 is the fastest hardware based trigger that uses raw information from the Muon Spectrometer and the calorimeters. The L1 decision should be made within  $2.5\text{ }\mu\text{s}$  after a collision occurred. The decision is usually based on a track-like set of hits in a sub detector. The output of the Level-1 trigger should be limited to 75 kHz.

Further data processing is done by the Level-2 trigger and the Event Filter, both of them are software base procedures that exploit information from all sub-detectors. Here the trigger decision is based on presence of a signature of a reconstructed physics objects such as muons, electrons, jets, missing energy, etc. The typical processing time for this step is about few seconds, and the final recording rate is a few hundred events per second.

## 3.3 Object reconstruction

### 3.3.1 Electron reconstruction

Electron candidates are reconstructed from energy deposits in the EM calorimeter that are matched to a good ID track. In order to recover electron energy loss due to bremsstrahlung, the track associated to a cluster is refitted using a Gaussian-Sum Filter [71].

Electron candidate can be faked by another object such as a hadronic jet. A robust electron identification is achieved by exploiting a set of 17 quality variables, that summarise the longitudinal and transverse shapes of the electromagnetic showers in the calorimeters, properties of tracks in the inner detector and track-cluster matching [71]. A full list of the variables is given in Table 3.3.1. These variables are further combined into a single discriminant that uses probability density model for signal and background electrons in MC [72]. Electron quality is defined as a cut on the discriminant. This cut value depends on the  $|\eta|$  and  $E_T$  of the electron and it is corrected for the number of interaction points in the event [72]. Moreover, a simple cut is applied on the track hits, as every electron should have a high quality track to allow for a robust momentum measurement. Particular configurations of electron quality cut are called working points (WP) and they are associated to a certain target reconstruction efficiency. Physics analysis described in this thesis is using Loose WP that allows to reach  $> 95\%$  signal efficiency for every considered final state.

Type	Description	Name
Hadronic leakage	Ratio of $E_T$ in the first layer of the hadronic calorimeter to $E_T$ of the EM cluster (used over the range $ \eta  < 0.8$ or $ \eta  > 1.37$ )	$R_{\text{Had1}}$
	Ratio of $E_T$ in the hadronic calorimeter to $E_T$ of the EM cluster (used over the range $0.8 <  \eta  < 1.37$ )	$R_{\text{Had}}$
Back layer of EM calorimeter	Ratio of the energy in the back layer to the total energy in the EM accordion calorimeter	$f_3$
Middle layer of EM calorimeter	Lateral shower width, $\sqrt{(\sum E_i \eta_i^2)/(\sum E_i) - ((\sum E_i \eta_i)/(\sum E_i))^2}$ , where $E_i$ is the energy and $\eta_i$ is the pseudorapidity of cell $i$ and the sum is calculated within a window of $3 \times 5$ cells	$W_{\eta_2}$
	Ratio of the energy in $3 \times 3$ cells over the energy in $3 \times 7$ cells centered at the electron cluster position	$R_\phi$
	Ratio of the energy in $3 \times 7$ cells over the energy in $7 \times 7$ cells centered at the electron cluster position	$R_\eta$
Strip layer of EM calorimeter	Ratio of the energy difference between the largest and second largest energy deposits in the cluster over the sum of these energies	$E_{\text{ratio}}$
	Ratio of the energy in the strip layer to the total energy in the EM accordion calorimeter	$f_1$
Track quality	Number of hits in the innermost pixel layer (the newly added B layer), discriminates against photon conversions	$n_{\text{Blayer}}$
	Number of hits in the pixel detector	$n_{\text{Pixel}}$
	Number of total hits in the pixel and SCT detectors	$n_{\text{Si}}$
	Transverse impact parameter with respect to the beamspot	$d_0$
	Significance of transverse impact parameter defined as the ratio of $d_0$ and its uncertainty	$\sigma d_0$
	Momentum lost by the track between the perigee and the last measurement point divided by the original momentum	$\Delta p/p$
TRT	Likelihood probability based on transition radiation in the TRT	TRTPID
Track-cluster matching	$\Delta\eta$ between the cluster position in the strip layer and the extrapolated track	$\Delta\eta_1$
	$\Delta\phi$ between the cluster position in the middle layer and the extrapolated track, where the track momentum is rescaled to the cluster energy before extrapolating the track to the middle layer of the calorimeter	$\Delta\phi_{\text{Res}}$

Table 3.5: Definition of electron discriminating variables. [71]

### 3.3.2 Muon reconstruction

There are several muon reconstruction algorithms that are based on available information from the MS, the ID and the calorimeter [73]. Depending on the applied algorithm there can be five types of muon candidates:

- **Combined (CB):** Starting from tracks reconstructed in the MS and extrapolating to the interaction point (ME tracks), this algorithm searches for an ID track within a cone around the ME track. Then a combined fit using the hits of the inner detector track, the energy loss in the calorimeter and the hits of the track in the muon system is performed.
- **Segment tagged (ST):** A track in the ID is identified as a muon if the trajectory extrapolated to the MS can be associated with track segments in the precision muon chambers. ST muons adopt the measured parameters of the associated ID track.
- **Calorimeter tagged (CT):** A trajectory in the ID is identified as a muon if the associated energy depositions in the calorimeters are compatible with the hypothesis of a minimum ionising particle. They are used in the analyses to cover the region of  $|\eta| < 0.1$  which is not equipped with muon chambers. The calorimeter muon identification algorithm is optimised for muons with  $p_T > 15$  GeV.
- **Silicon-associated forward (SiAF):** In the  $2.5 < |\eta| < 2.7$  region, where the ID provides no coverage, tracks are reconstructed in the MS and are extrapolated back to the interaction point. If a very forward ID tracklet formed by Silicon hits is found within a cone around the ME track, a combined fit is performed including the hits of the ID tracklet.
- **Standalone (SA):** ME tracks in the  $2.5 < |\eta| < 2.7$  region that could not be associated with a forward ID tracklet are extrapolated back to the interaction point and refitted with a loose interaction point constraint taking into account the energy loss in the calorimeter.

Muon candidates can be faked by pion or kaon decay. These fakes are rejected by applying a set of quality requirements based upon the specific features of each of the muon types described above [73]. The analysis described in this thesis is using **Loose** working point that allows CB muons at any  $\eta$  range, while CT and ST muons are restricted to  $|\eta| < 0.1$ , SiAF and SA to  $2.5 < |\eta| < 2.7$  regions. The quality requirements applied for the **Loose** working point are described below.

A set of quality requirements related to the ID tracks are designed to ensure a minimum number of hits in each of the ID sub-systems, therefore selecting only reasonably well-reconstructed tracks. They are applied to all muon types except the SA muons, since they do not have an associated ID track. The requirements consist of:

- at least 1 Pixel hit;
- at least 5 SCT hits;
- less than 3 Pixel or SCT holes;
- at most 10% of the total number of TRT hits flagged as outliers (abandoned since summer 2016).

A hole consists of an active sensor traversed by the track containing no hits. If some inefficiency is expected for a given sensor, the requirements on the number of Pixel and SCT hits are reduced accordingly. The requirements for the forward ID tracklets of the SiAF muons that are used in the  $|\eta| > 2.5$  region are relaxed, consisting of at least 1 Pixel hit and at least 3 SCT hits.

MS hit requirements are also applied. SA and SiAF muons are required to have at least three hits in each of the three stations of MDT or CSC and are employed only in the  $2.5 < |\eta| < 2.7$

region. Combined muons are required to have  $\geq 3$  hits in at least two layers of MDT, except for the  $|\eta| < 0.1$  region where tracks with at least three hits in one single MDT layer are allowed.

Muon fakes originating from in-flight decays of hadrons, are rejected by a requirement on the compatibility between the measured momentum in the ID and the MS [73]. A cut of  $< 7$  is applied to  $q/p$  significance defined below:

$$\frac{|q/p_{\text{ID}} - q/p_{\text{MS}}|}{\sqrt{\sigma_{\text{ID}}^2 + \sigma_{\text{ME}}^2}} \quad (3.6)$$

### 3.3.3 Jet reconstruction

Jets in the ATLAS calorimeters are reconstructed using the anti-kt algorithm [74] with radius parameter  $R = 0.4$ , using as an input positive-energy topological clusters (topoclusters) [75] of calorimeter cell energies. Jet calibration procedure used in Run-2 is similar to the one used in 2012 [76], but it has been updated to take into account the IBL detector, the new beam conditions, changes in LAr pulse shape reconstruction and sampling points, improved track reconstruction and muon track segment reconstruction [77].

Different processes such as  $p-p$  collision remnants, cosmic-ray showers and high coherent calorimeter noise can fake a jet candidate. To reject those, jets are required to fulfil the **BadLoose** set of quality criteria described in Ref. [78]. Moreover, in order to suppress pile-up jets a recently developed discriminant called jet-vertex-tagger (JVT) is used. The JVT discriminant is described in Ref. [79] and in current analysis the JVT score is required to be greater than 0.64 in case of jet with  $p_T < 50$  GeV.

### 3.3.4 Prospects for the Phase-1 ATLAS Upgrade

The closest upgrade of the ATLAS detector is planed for 2019-2020, it is called the Phase-1 upgrade. The main focus of the Phase-I ATLAS upgrade is on the Level-1 trigger. Starting from 2020 the LHC will operate at higher instant luminosity regime, that would lead to much higher event rate, beam induced background and pile-up. An objective of the upgrade is to keep the Level-1 rate at a manageable level without increasing the threshold requirements for each individual lepton, that would cause the loss of a big part of a phase space interesting for numerous analyses. Upgrades are planned both for the muon and the calorimeter trigger systems. [80]

Within the Phase-1 ATLAS upgrade the inner stations of the end-cap muon system will be replaced with a new muon detector, the New Small Wheel (NSW) [81]. This upgrade is aiming to increase the efficiency of the muon L-1 trigger, as well as to improve momentum resolution of the system. The NSW will be based on two detector technologies, the MicroMegas (MM) and the small-strip Thin Gap Chambers (sTGC). The NSW is discussed in more details in Section 4.2.

The LAr calorimeter upgrade will be focused on modification of the L-1 trigger concept, without replacing the detector it self. The existing calorimeter trigger information is based on a concept of “Trigger Towers” that sum energy deposition across the longitudinal layers of the calorimeters in an area of  $\Delta\eta \times \Delta\phi = 0.1 \times 0.1$ . The Trigger Tower is created through several stages of on-detector analog electronics. This approach will be changed to a new finer granularity scheme based on so-called “Super Cells”, which provide information for each calorimeter layer in full  $\eta$  range. The LAr upgrade is essential to treat the high pile-up operation conditions expected in Run-3. [82]

Moreover, a new hardware-based Fast Tracker (FTK) will be added to process data from the silicon tracking detectors. The FTK is aiming to reconstruct charged particle tracks with a latency



suitable for the high level trigger. [82]

# Upgrade of the ATLAS Muon Spectrometer

## 4.1 Motivation for the Upgrade

Starting from Run-3, the LHC will be operating at high luminosity regime, that will require corresponding detector performance. For the MS it means not only more interesting muon tracks, but also it will cause a significant increase of the cavern background up to  $15 \text{ kHz/cm}^2$  [81], that can degrade the MS performance. These problems mostly affect the inner station of the end-cap Muon Spectrometer called the Small Wheel, since it is placed in a very forward region close to the IP and the beam-pipe as shown in Figure 4.1. The effect of the new operation conditions can be separated into precision measurement and trigger related aspects that are discussed below.

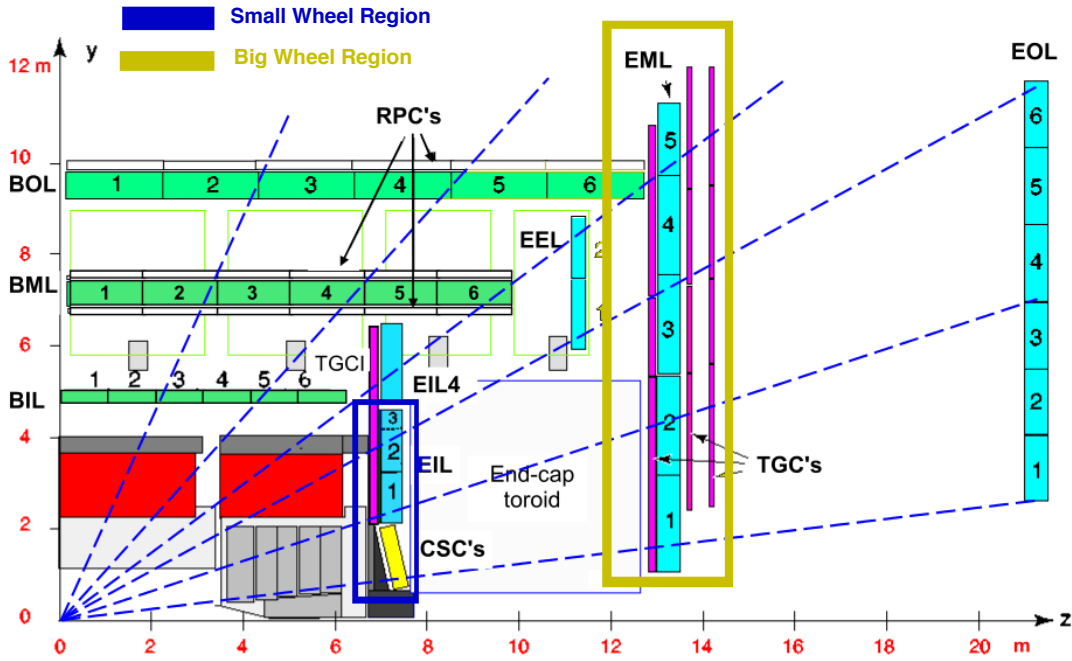


Figure 4.1: A  $z$ - $y$  view of quarter of the ATLAS detector. The MS Small Wheel is highlighter in blue at  $z \approx 7 \text{ m}$ . [81]

Performance of the existing muon tracking chambers (in particular in the end-cap region) degrades with the expected increase of cavern background rate. This effect was estimated using extrapolation from the observed rates at the lower luminosity conditions of 2012 to higher luminosity and energy. Substantial degradation of tracking performance, both in terms of efficiency and resolution in the inner end-cap station was indicated. Given that the momentum measurement precision crucially depends on the measured points at the Small Wheel (i.e. in front of the end-cap toroid magnet), this degradation is detrimental for the performance of the ATLAS detector. Therefore the Small Wheel requires an upgrade to match a set of precision requirements summarised below.

**Precision measurement requirements [81]:**

- Reconstruct track segments with a position resolution in the bending plane better than  $50\ \mu\text{m}$ , that is translated into better than  $100\ \mu\text{m}$  segment position resolution per plane for the planned 4-layer multi-plane detector that may replace the Small Wheel
- Segment finding efficiency better than 97% for muons with  $p_T$  greater than 10 GeV
- Efficiency and resolution should not degrade at very high momentum (due to  $\delta$ -rays, showers)
- The second coordinate measurement with a resolution of 1-2 mm to facilitate good linking between the MS and the ID track for the combined muon reconstruction

The Level-1 muon trigger in the end-cap region is based on TGC track segments of the middle muon station located after the end-cap toroidal magnet. The transverse momentum of the muon is determined by the segment angle with respect to the direction pointing to the interaction point. A significant part of the muon trigger rate in the end-caps is originated by background caused fakes. Low energy particles, generated far from the IP, produce fake triggers by hitting the end-cap chambers at angles similar to that of real high  $p_T$  muons. An analysis of 2012 data demonstrates that approximately 90% of the muon triggers in the end-caps are fakes [81]. As a consequence the rate of Level-1 muon trigger in the end-cap is eight to nine times higher than the rate in the barrel region. One of the possible way to improve the trigger performance is to include the Small Wheel in the Level-1 trigger together with the Big Wheel. The requirements on the trigger part of the Small Wheel are summarised below.

**Level-1 Trigger requirements [81]:**

- Track segment information should arrive at the trigger logic module not later than  $1.088\ \mu\text{s}$  after a collision
- Track segment reconstruction for triggering should have an angular resolution of 1 mrad or better
- Track segments should have a granularity better than  $0.04 \times 0.04$  in the  $\eta$ - $\phi$  plane
- Track segments should be reconstructed online with high efficiency in the full  $\eta$  coverage of the detector ( $1.3 < |\eta| < 2.5$ )
- Online track segment reconstruction efficiency should be more than 95%

These issues represent serious limitation on the ATLAS Muon Spectrometer performance beyond Run-2, it can cause a reduction of muon tracking acceptance, and an unacceptable rate of fake Level-1 muon triggers. It was proposed to solve the problem by replacing the present muon Small Wheels with the New Small Wheels (NSW), a new muon station that is able to operate at high rates with excellent real-time spatial and time resolution. The NSW will be included into the muon Level-1 trigger system together with the Big Wheel, that will lead to a significant improvement of the trigger efficiency.

## 4.2 The New Small Wheel

The New Small Wheel will replace the current inner station of the end-cap muon spectrometer in order to insure required precision of muon  $p_T$  measurement and to improve an efficiency of the muon Level-1 trigger in future runs. It will exploit two chamber technologies: small-strip Thin Gap Chambers (sTGC) [83] and Micromegas detectors (MM) [84]. The sTGC are primarily deployed for triggering given their single bunch crossing identification capability, while the MM detectors have exceptional precision tracking capabilities due to their small gap (5 mm) and strip

pitch (approximately  $450 \mu\text{m}$ ). Another interesting feature of the MM is a capability to confirm the existence of track segments found by the muon end-cap middle station (Big Wheels) on-line within the time interval suitable for the Level-1 trigger. This feature provides further possibility to include the MM into the Level-1 trigger system (in addition to sTGC). Moreover, the sTGC are also capable to measure off-line muon tracks with good precision. Therefore, the combination of both sTGC and MM technologies forms a fully redundant detector both for triggering and tracking. Potential of such a redundant detector will provide an excellent performance not only at the Run-3, but also at even more challenging operation conditions of the high luminosity LHC.

The NSW should replace the current Small Wheel, that is placed on the supporting structure of the JD shielding as shown in Figure 4.2, therefore spacial dimensions and total weight of the new detector have tight constraints. Moreover, the new inner station should be compatible with current muon spectrometer alignment system.

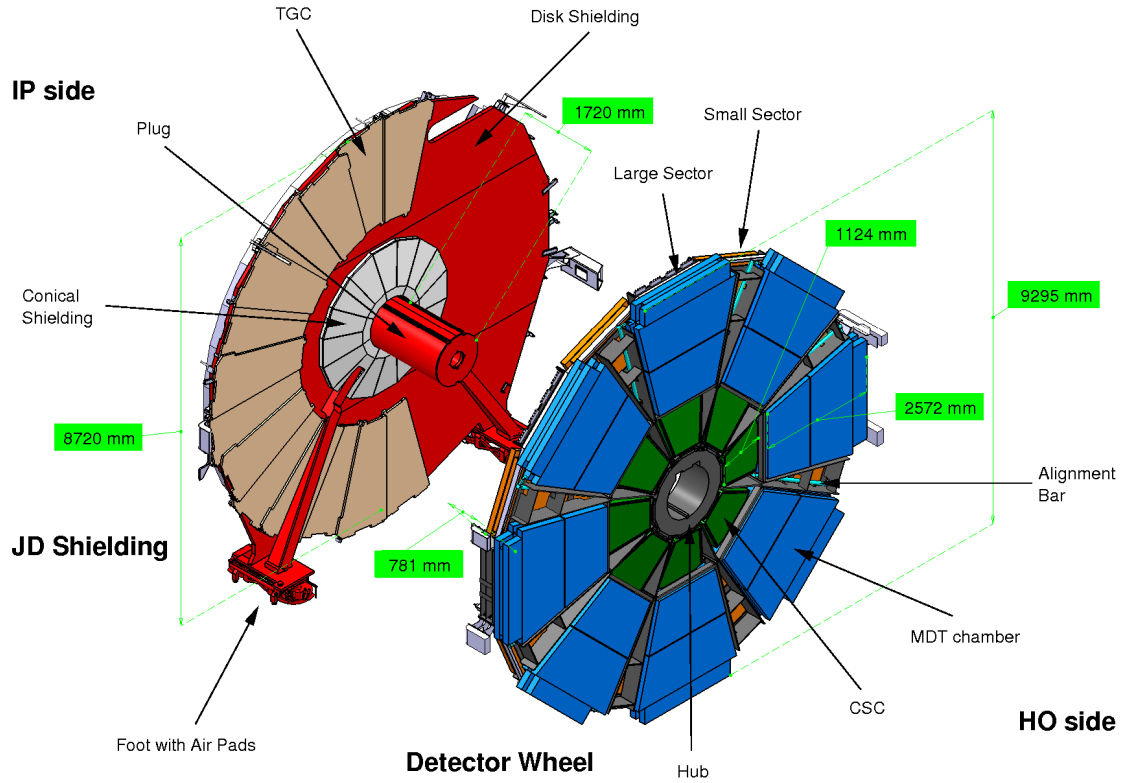
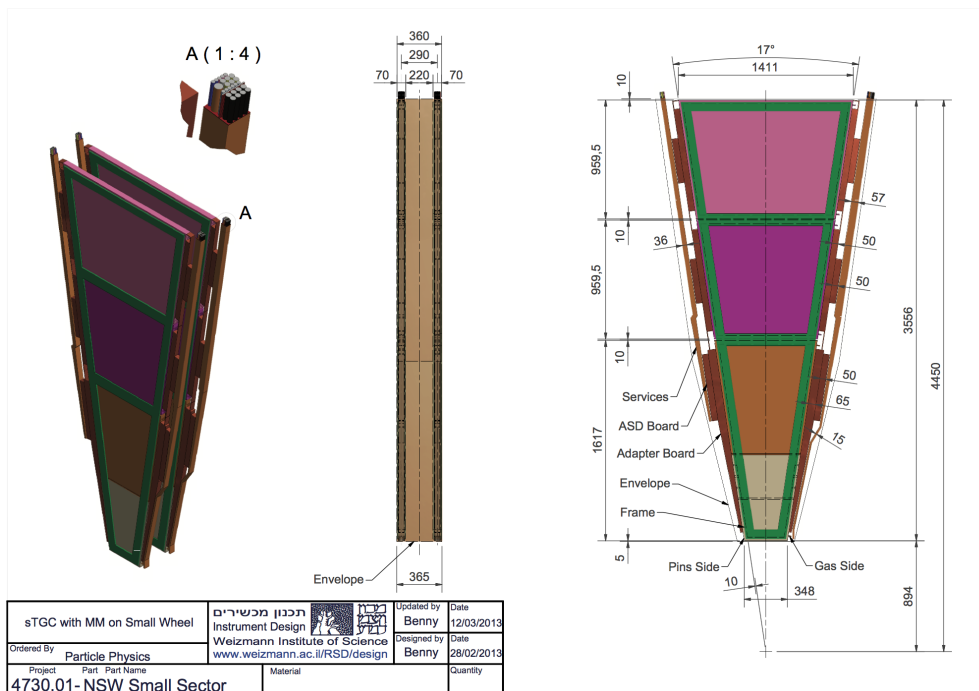


Figure 4.2: Components and layout of the present Small Wheel. [81]

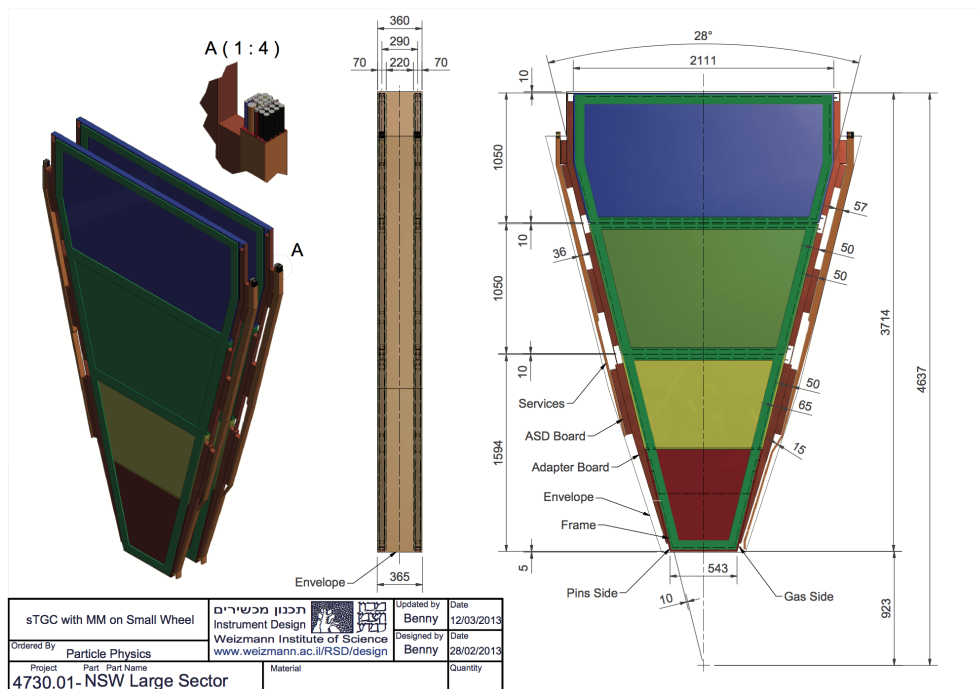
The upgraded muon station similarly to the old one will consist of eight big and eight small sectors as shown in Figure 4.2. The wheel will have common supporting structure for the MM and the sTGC detectors, that will be put on a new JD shielding plug. Each sector of the NSW will consist of multiplets of the detectors ordered in  $z$  direction as sTGC-MM-MM-sTGC, and each multiplet will have 4 independent detecting planes.

The sTGC detectors of each sector will be pre-assembled into wedges, consisting of three modules in the  $r$  direction, as it is shown in Figure 4.3. The modules in two sTGC wedges of each sector are arranged in such a way that there is no dead regions in projective geometry with respect to the IP, however a small region of reduced detection efficiency is expected in front of the frame.

The MM detectors of each sector will be combined into a MM chamber with four detector planes. Each chamber will consist of two modules in  $r$  direction. The MM layout and dimensions are shown in Figure 4.4.

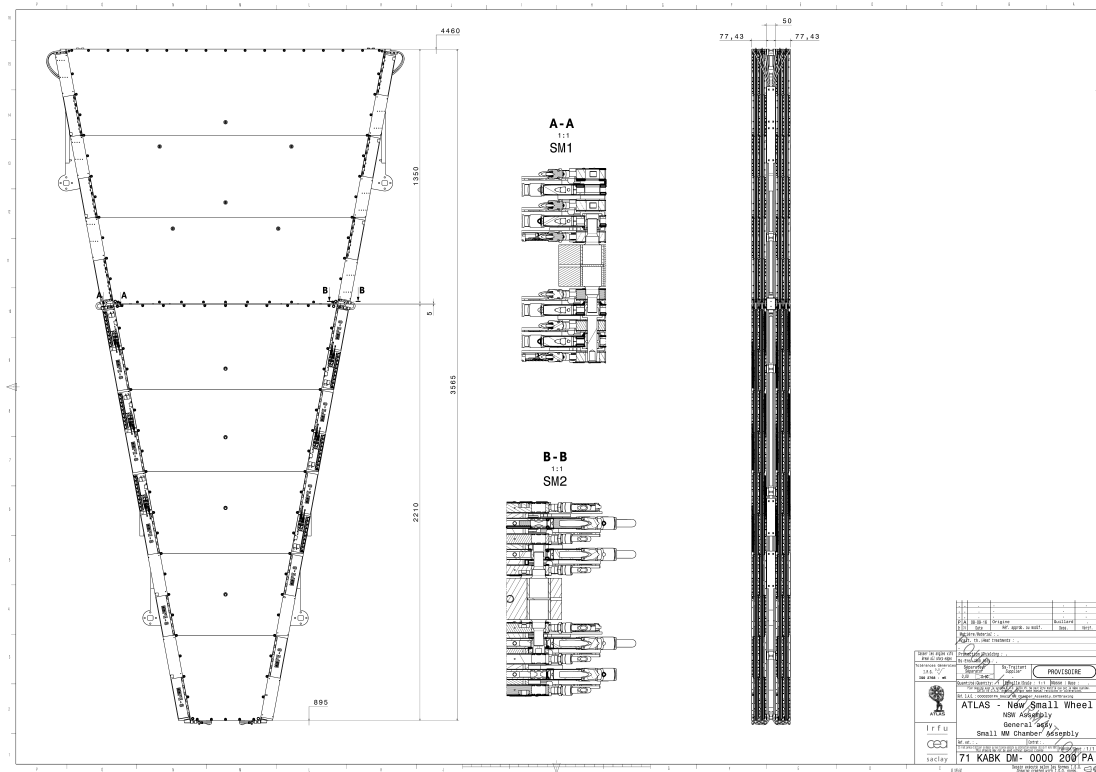


(a) Small sector.

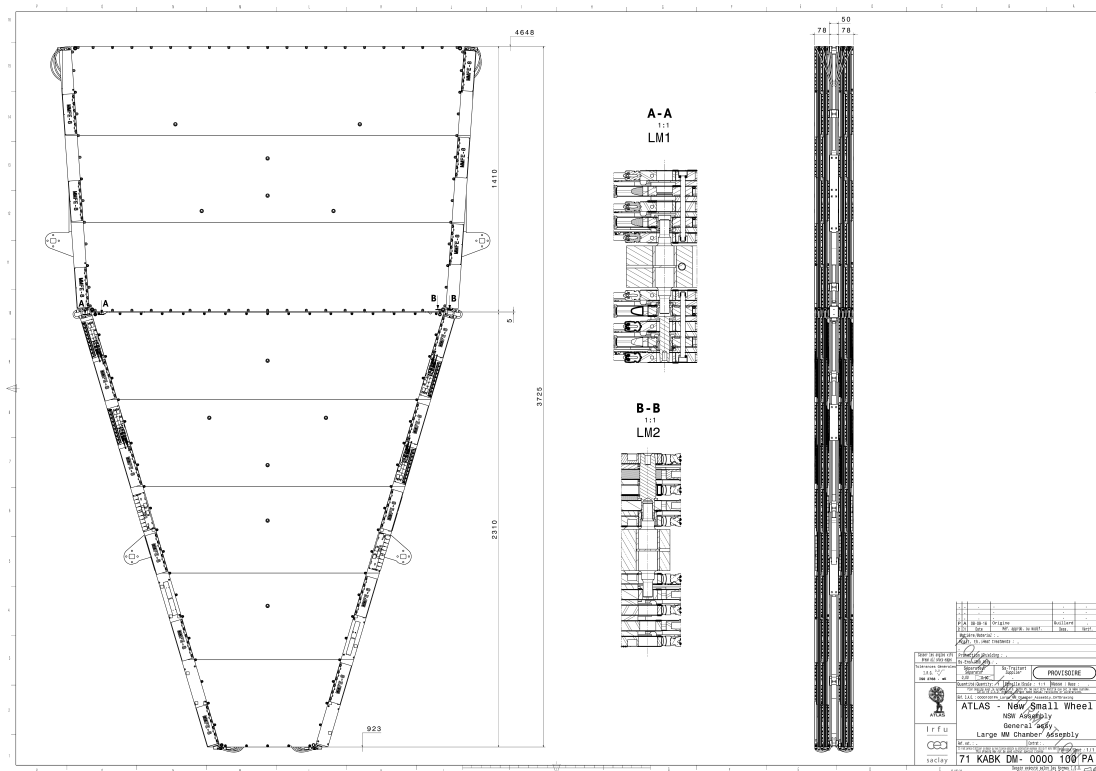


(b) Large sector.

Figure 4.3: Layout of the sTGC detectors. [81]



(a) Small sector.



(b) Large sector.

Figure 4.4: Layout of the MM detectors. [81]

### 4.2.1 Small-strip Thin Gap Chambers

The small-strip TGC has similar structure to the TGC described in Section 3.2.4. It consists of a grid of gold-plated tungsten wires with  $50\ \mu\text{m}$  diameter and  $1.8\ \text{mm}$  pitch sandwiched between two cathode planes at a distance of  $1.4\ \text{mm}$  from the wire plane, as shown in Figure 4.5. One of the cathode planes consists of strips with  $3.2\ \text{mm}$  pitch that are covered with resistive layer, while the second one is formed by pads. Since the wires and the strips are aligned in perpendicular direction, the sTGC is capable to measure two space coordinates while the third one is fixed by the detector position.

This technology is currently used for the ATLAS trigger, as well as for other experiments such as OPAL [85], therefore the (s)TGC has already gone through a long phase of R&D and testing.

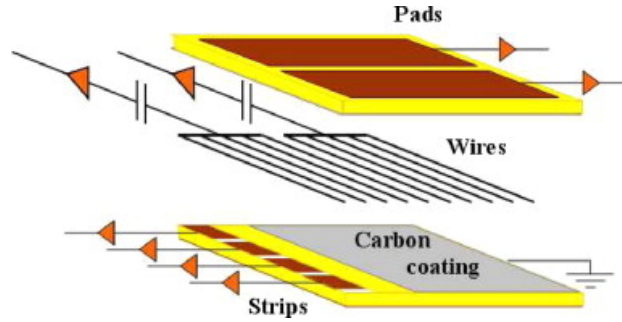


Figure 4.5: The sTGC internal structure. [81]

### 4.2.2 Micromegas

The Micromegas is a gaseous detector that was developed in middle 1990's at IRFU [84]. The detector consists of two gas gaps that are separated by a thin metallic mesh. The first gap, usually few millimetre thick, is referred to as the drift volume, where primary ionisation occurs. The ionised electrons drift towards the mesh in a weak electric field between the drift electrode and the mesh itself. After reaching the mesh, 95% of electrons get into the second gas gap called amplification volume. Its thickness is about  $128\ \mu\text{m}$  and there is a strong electric field applied in between the mesh and the readout strips, therefore, primary electrons create avalanches that are collected at the readout electrodes.

The structure of the MM detector is shown in Figure 4.6. The detector is confined in between two PCB (Printed Circuit Board) planes, the first one has the drift electrode on it, while the second one holds the readout strips. On top of the readout strips there are pillars made of insulator, that act as a support for the mesh dividing the gas gap into two sub-volumes. The drift gap usually has an electric field of few hundred  $\text{V/cm}$ , while  $40\text{-}50\ \text{kV/cm}$  field is applied to the amplification gap.

Electron drift in the conversion gap is a relatively slow process. Depending on the drift gas, field and distance it typically takes several tens of nanoseconds. On the other hand the amplification process happens within few nanoseconds, resulting in a fast electrical pulse on the readout strip. Ions that are produced in the avalanche process, move in the opposite direction of the electrons, back to the amplification mesh. Most of the ions are produced in the last avalanche step, and, therefore, close to the readout strip. Given the relatively low drift velocity of ions, it takes them about  $100\ \text{ns}$  to reach the mesh, still very fast compared to the other detectors. Such a fast evacuation of the positive ions makes the MM particularly suited to operate at a very high particle flux.

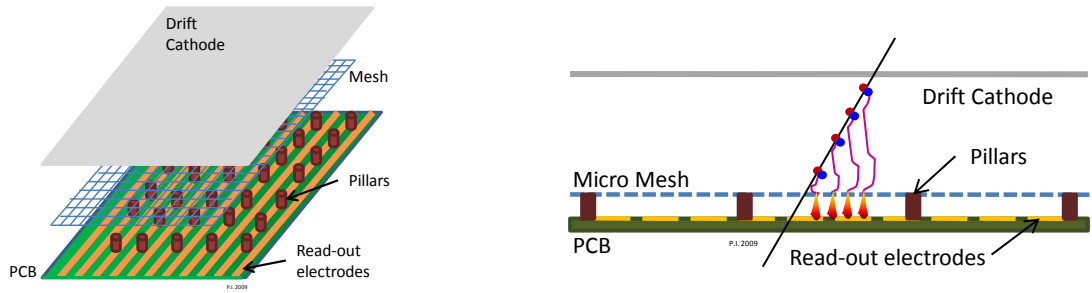


Figure 4.6: Sketch of the layout and operating principle of a MM detector. [81]

### Resistive Micromegas

A weak point of the original design of the MM is a probability to get a spark in the amplification gap, when the avalanche reach electron multiplicity of  $10^7$  [86]. Taking into account an average MM amplification factor of  $10^4$ , a spark can be caused by low energetic proton or  $\alpha$ -particle in the detector. Such an incident can lead to large dead time due to HV breakdown or even damage of the detector and readout electronics. This risk is not acceptable for the ATLAS detector.

For the MM detectors to be installed on the New Small Wheel a spark protection system has been invented [87]. The readout strips are covered with a thin insulating layer. Resistive strips are added on top of the insulator directly above the readout strips. In this case the avalanche does not reach the readout directly, but it is slowly propagating to ground through the resistive layer. The readout electrodes are capacitively coupled to the resistive strips. This mechanism allows to reduce the spark probability by three orders of magnitude while keeping the detector sensitivity relatively unchanged. The MM design with the spark protection is called resistive, and it is sketched in Figure 4.7.

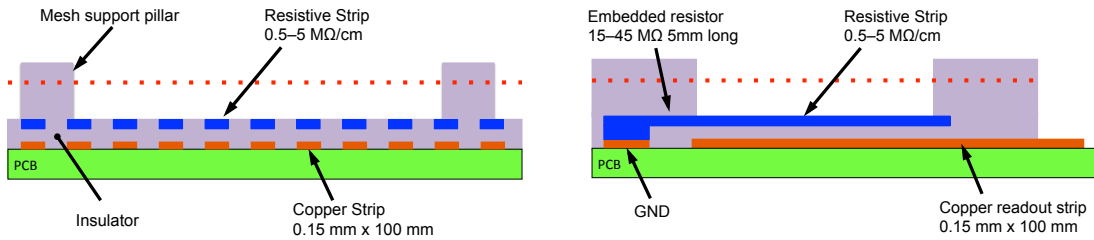


Figure 4.7: Sketch of the resistive MM design, with resistive strips placed in parallel to the readout strips. [81]

The resistive MM has been extensively tested in hadron and neutron test beams. Moreover, since the beginning of 2011 four small MM detectors have operated faultlessly on the Small Wheel in the ATLAS cavern. Two small prototypes were tested in the high rate environment in front of the electromagnetic end-cap calorimeter.

### Micro TPC mode ( $\mu$ TPC)

Another interesting feature of the MM detector is the so called  $\mu$ TPC operation mode [88].  $\mu$ TPC is a capability of the detector to operate as a very small Time Projection Chamber [89]. In this mode the MM can reconstruct a small track of an ionising particle within the drift volume. This option is possible due to the fine time of fit arrival measurement and a high segmentation of the readout electrodes. Position of each primary ionisation can be reconstructed by analysing space-time structure of the avalanche signal.  $x$  coordinate of a primary ionisation corresponds to a position of a fired strip, while  $z$  coordinate (perpendicular to the strip plane) can be reconstructed from



the time of arrival measurement, given a known electron drift velocity. Naturally, this operation mode has better performance for more inclined tracks, when the avalanche is distributed between reasonable amount of strips, since this method allows to consider information from all strips in a cluster, but not only the ones on the cluster borders. The micro TPC principle is illustrated in Figure 4.8. This feature is used for precision measurement of the tracks with incident angle greater than  $10^\circ$ . Comparison of the spacial resolution using  $\mu$ TPC and common Centroid methods is shown in Figure 4.9.

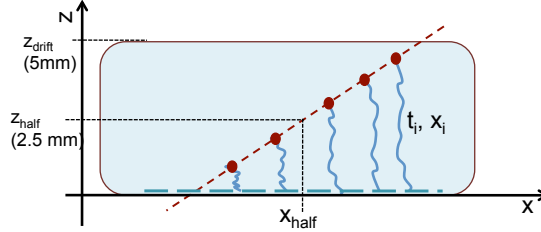


Figure 4.8: Illustration of the MM  $\mu$ TPC operating mode principle. [81]

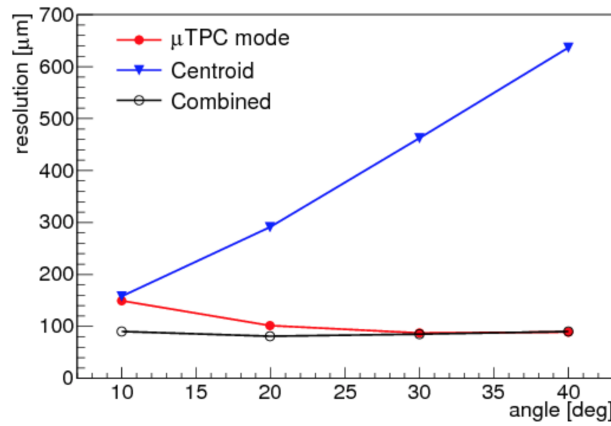


Figure 4.9: Comparison of the spatial resolution using different reconstruction methods. [81]

### MM layout in the NSW

Each NSW sector contains eight MM detection layers, grouped into two multiplets of four layers each, separated by a 40 mm thick spacer. Figure 4.10(a) shows schematically the arrangement of the detectors in a sector. Each multiplet contains two pairs of detection planes mounted back-to-back on common PCB, as shown in Figure 4.10(b).

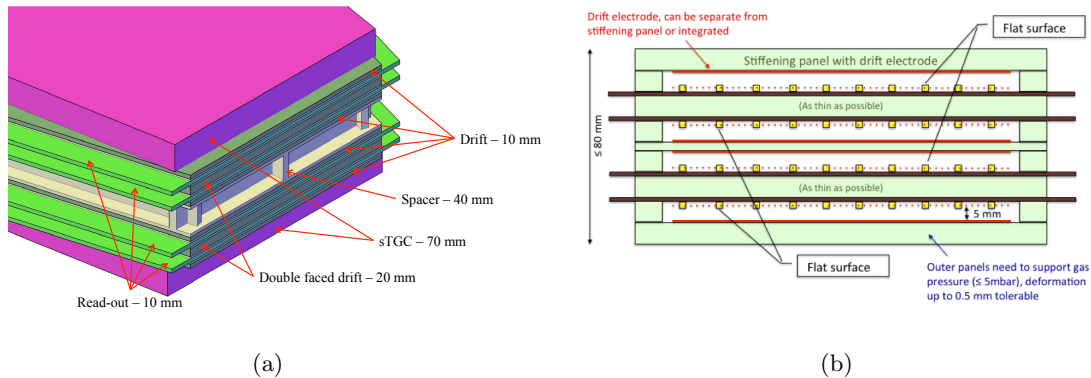


Figure 4.10: (a) Arrangement of the MM detector in the NSW sector. (b) Cross section view of the MM multiplet.

Each MM detection plane will have 1D strip readout with a pitch of 400-450  $\mu\text{m}$ . In order to provide a measure of the second coordinate, the readout strips in each second detector layer will be inclined by  $1.5^\circ$ .

### 4.3 Production and characterisation of the Micromegas modules at Saclay

The CEA-Saclay laboratory is involved in production of the Micromegas modules for the New Small Wheel project. The laboratory is responsible of the production of the inner parts of the big sectors that are called LM1. The layout of the LM1 module is shown in Figure 4.11. 32 modules should be produced by the NSW installation time in 2019.

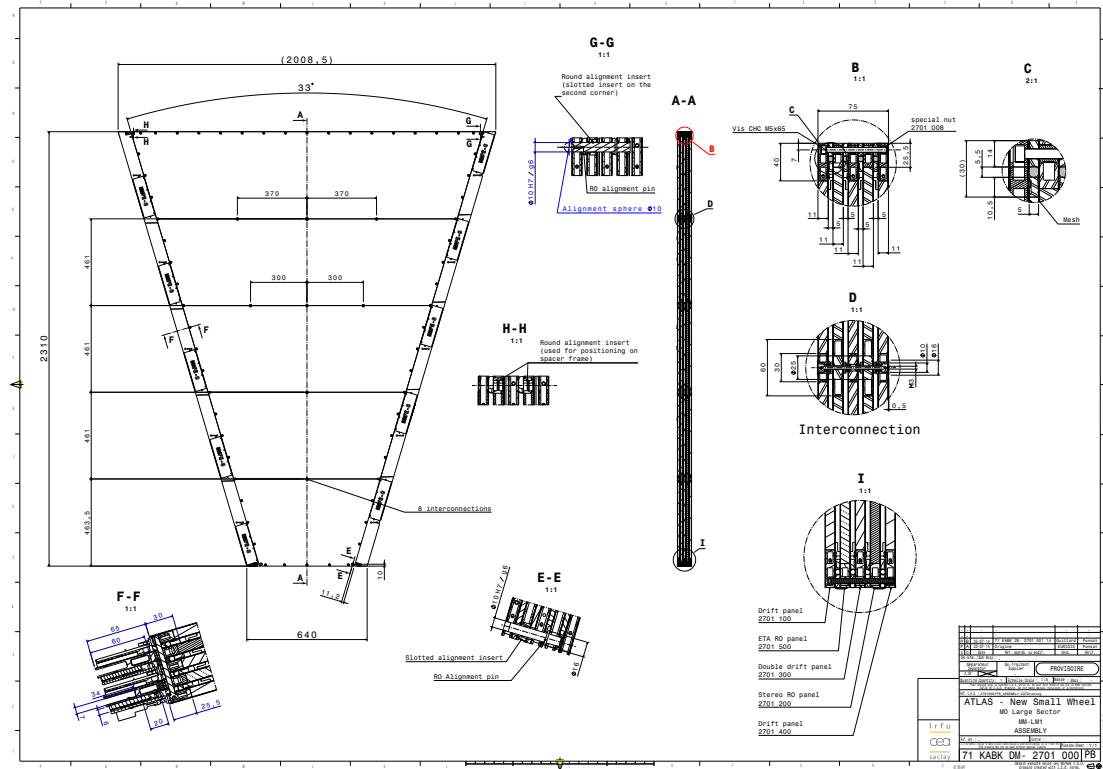


Figure 4.11: LM1 Micromegas modules for the New Small Wheel.

After the modules are produced, they should be characterised before being sent to CERN for the test-beam commissioning and installation. The production site has to provide a set of metrological specification of the modules, and moreover, study the detector performance in terms of:

- detection efficiency for minimum ionising particles
- detector gain
- spacial resolution

The characterisation can be performed by exploiting cosmic rays. In case of detector efficiency and the spacial resolution, the tested module should be incorporated in a cosmic bench with a precise external tracker that allow to determine a particle flux. It is planned to use the cosmic bench facilities of the  $M^3$  experiment that is hosted at Saclay [90]. For the gain studies, an external tracker is not needed, however it is crucial to have another reference Micromegas detector with known detector gain, in order to determine the gain of the electronics that will be used for the

test. It is planned to use the R17 prototype as a reference detector. The R17 detector is described further in this section.

Tested modules do not have the final read out electronics that will be used in ATLAS detector, therefore some other electronics should be used for the characterisation. The DREAM [91] electronics was favoured with respect to commonly used APV [92] electronics, because it has broader trigger capabilities and there is a team of experts that can provide a continuous support for the DREAM electronics.

#### 4.3.1 Software framework for the characterisation

For the commissioning task, it is essential to develop a software framework capable to process raw data from the DREAM electronics and perform the data analysis up to production of the characterisation plots. It is also important that the framework contains the capability of online monitoring of data acquisition. Finally, the software framework should have user friendly interface that is suitable to be used by a diverse team involved into production and characterisation process.

The software should read raw binary data from the DREAM electronics, and perform pedestal and common noise subtraction. Further, the data should be cleaned from not fired channels and converted to a readable *Root* format. The next steps for the data processing is detector geometry decoding, clustering and tracking in case of multiple detector planes. At each step it should be possible to write out data in a *Root* format. The framework should also include a set of scripts that produce certain characterisation plots. Moreover, the software should include an online monitoring capability, namely it should perform a full processing of a fraction of recorded events in live time. The Software functionality is sketched in Figure 4.12.

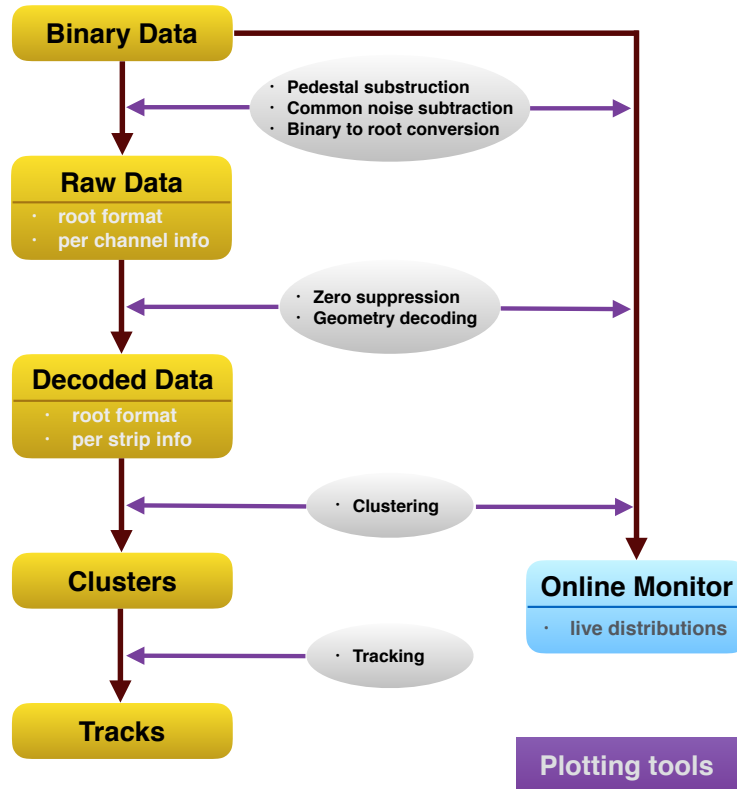


Figure 4.12: A sketch of the software framework functionality. Yellow rounded rectangles represent different data states while the grey blocs corresponds to actions on data.

The software framework should be ready by the arrival time of the first full scale Micromegas prototype that is expected in Summer 2017. Currently most parts of the software are ready and their validation is discussed in the following section. However there are some components such as decoding of the multiplexing, tracking and online monitoring that are still under development.

### 4.3.2 Software validation

Since there is no full scale Micromegas module for the NSW, the software can be validated with several smaller prototypes: R17 and M0, both are resistive Micromegas detectors. Further detectors description is given below.

#### R17

R17 is a small Micromegas prototype that has dimensions of  $10 \times 10$  cm. It has two planes of perpendicular readout strips and one plane of resistive strips. Both readout and resistive strips have a pitch of  $250 \mu\text{m}$ . The R17 detector is shown in Figure 4.13. This detector was initially aimed for studies of radiation hardness of the resistive Micromegas technology, and currently available as one of the operational prototypes.

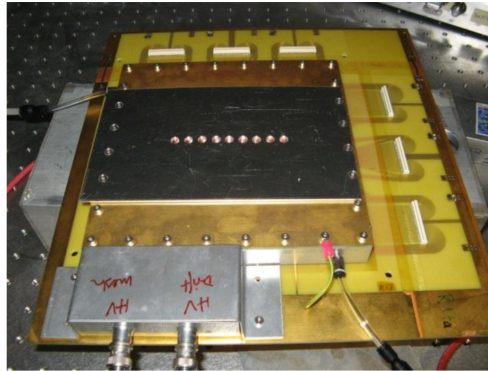


Figure 4.13: R17 prototype.

#### MLO

Operational Multi-Layer (MLO) is a first multilayer resistive Micromegas prototype built at Saclay within the NSW project. This detector was manufactured in order to check feasibility of the production technique. The MLO is a doublet of two detectors sitting back-to-back on a single PCB. One detector of the MLO doublet is shown in Figure 4.14, while the second one is placed symmetrically on the bottom side of the PCB. Each detector contains two planes of perpendicular readout strips and a plane of resistive strips. Both readout and resistive strips have a pitch of  $450 \mu\text{m}$ . The prototype contains two detection planes with an active area of  $0.4 \times 0.6 \text{ m}^2$ .

#### R17 gain studies

In order to validate the software framework the gain of the R17 detector with the DREAM electronics was studied. The gain as a function of the high voltage (HV) applied to the detector is deduced in two different experiments: using  $\text{Fe}^{55}$  radioactive source, and using cosmic rays. This test is important not only for the purpose of the software validation, but also for validation of the gain characterisation procedure of the NSW modules.

Few data taking runs are performed with  $\text{Fe}^{55}$  source with the different high voltage applied to the detector: 570, 580, 590, 600, 605 V. In order to study the gain in the most simple way, the signal is integrated over the all strips of a detector Y plane (this variable is further called EventCharge).  $\text{Fe}^{55}$  radiates x-rays with an energy of about 5.9 keV that correspond to in average 221 primary

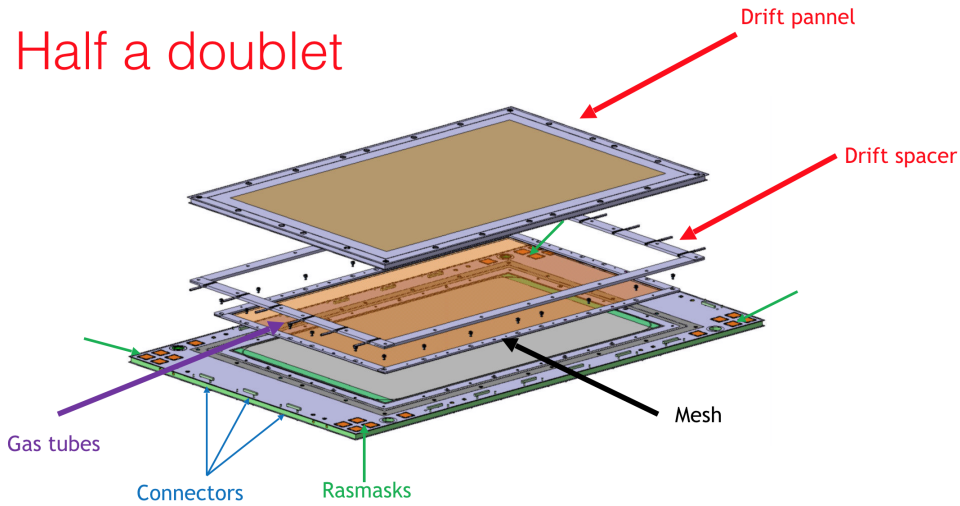


Figure 4.14: One of the two detectors in the MLO prototype.

ionised electrons in the detection volume. There is also other radiation coming from  $\text{Fe}^{55}$  source, but its relative yield is minor. Therefore, a clear gaussian peak that corresponds to 221 primary electrons is expected in the EventCharge distribution. The EventCharge distribution for the runs with different HV is shown in Figure 4.15. Position of the peak is defined as a mean value of the gaussian function fitted to the observed peak. The detector plus electronics gain can be defined as the position of the signal peak normalised to the number of primary electrons. The gain is shown as a function of the HV in Figure 4.17(a). The obtained gain function has an expected exponential behaviour, that confirms good operation both of the detector and of the low level software.

Another test of the R17 gain is performed using cosmic rays. In this case the detector is mostly irradiated by minimum ionising particles, and their energy deposition follows the Landau distribution with the most probable value of about 0.75 keV, that corresponds to 28 primary ionised electrons. Thus the gain can be determined by fitting the EventCharge distribution with the Landau distribution, and further normalising its median to the number of primary electrons. The fitted EventCharge distribution for the cosmic runs with HV of 580, 590, 600, 610 V is shown in Figure 4.17, while the deduced gain as a function of HV is shown in Figure 4.17(b).

Comparison of the gain curves obtained from the two experiments is shown in Figure 4.17(c). The two curves are well compatible, that confirms that the detector gain can be studied with cosmic rays, but not only with monochromatic source. It is an important conclusion, since the first approach will be not applicable for the NSW modules since the low energy radiation is absorbed in the detector walls.

### Validation of MLO mapping

In order to validate the geometry decoding implemented in the software framework, some data is collected with MLO detector in a self-trigger mode with cosmic rays. Only one layer of the MLO detector is used in the test. A cluster map reconstructed with the software framework is shown in Figure 4.18. Due to manufacturing problems, the detector has some area where the mesh is not attached to the pillars that should cause reduction of detector sensitivity in this region. Successful reconstruction of the insensitive area that is compatible with the expectation from mechanical commissioning, confirms proper decoding of the detector geometry in the software framework.

### Conclusions

The software framework for the commissioning of the NSW Micromegas modules is well advanced.

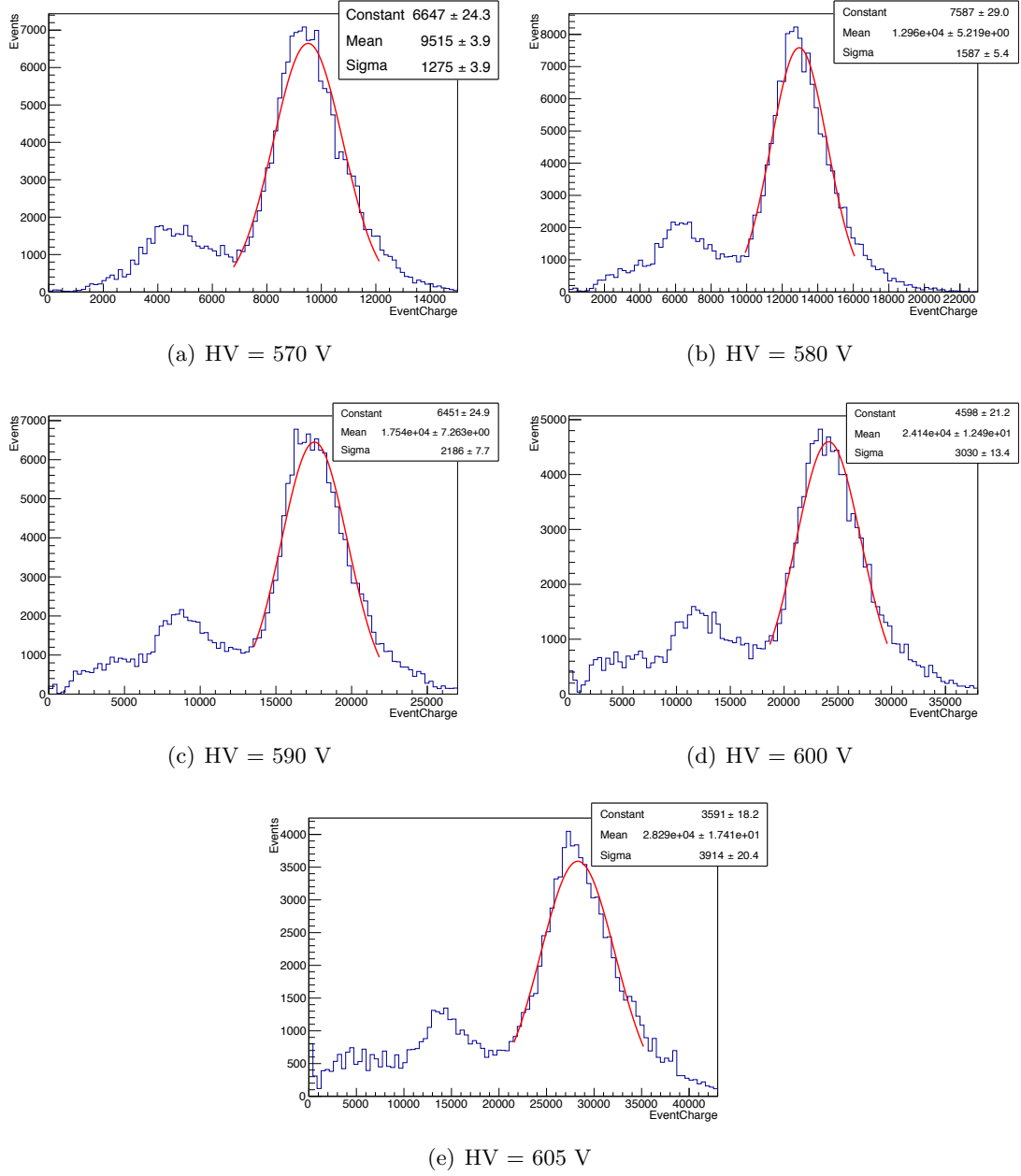


Figure 4.15: Distribution of the signal integrated over the Y strips of R17 for different high voltage applied to the detector in the  $\text{Fe}^{55}$  runs. The peak is fitted with a gaussian distribution.

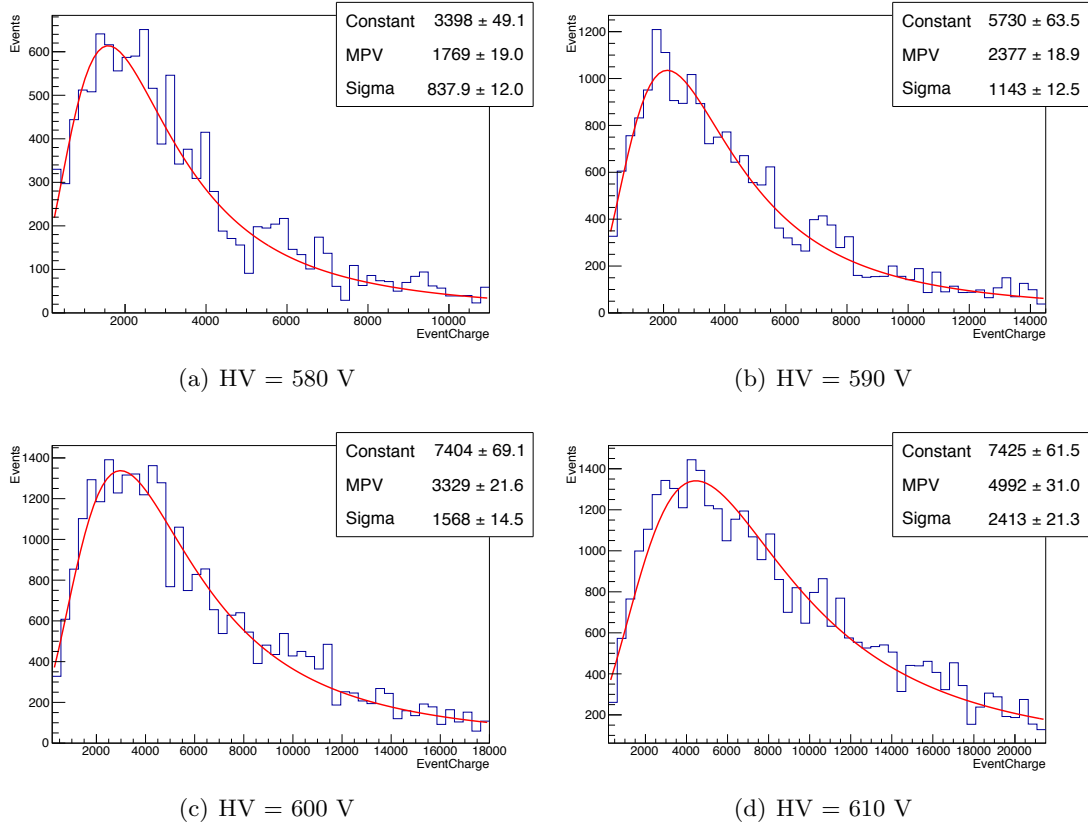


Figure 4.16: Distribution of the signal integrated over the Y strips of R17 for different high voltage applied to the detector in the cosmic runs. The peak is fitted with a Landau distribution.

Most of the functionalities are already implemented, while several important features like tracking, demultiplexing and online monitoring capabilities are still under development. Basic validation of the software framework using small scale Micromegas prototypes is performed.

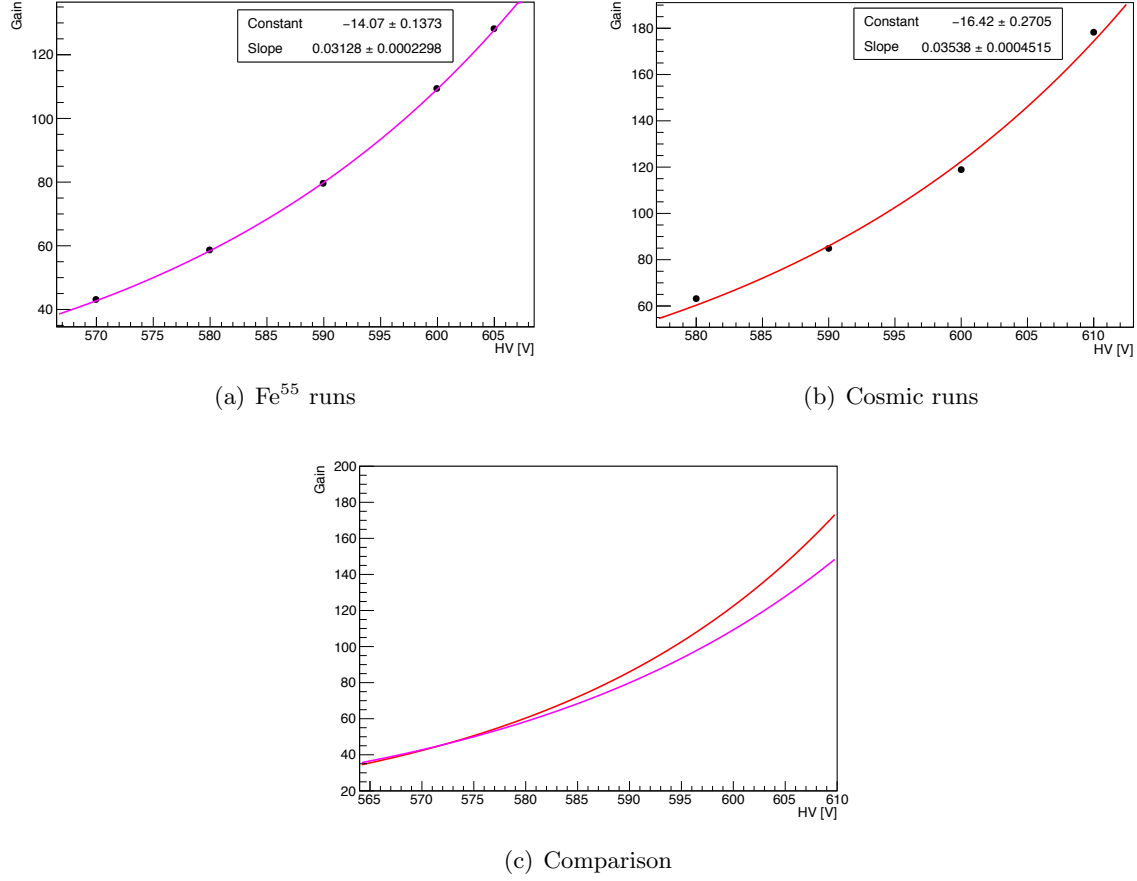


Figure 4.17: R17 gain as a function of the high voltage deduced from the  $\text{Fe}^{55}$  runs (a) and from cosmic runs (b). The gain is fitted with an exponential function. Also a comparison of the R17 gain function deduced from two experiments is shown (c).

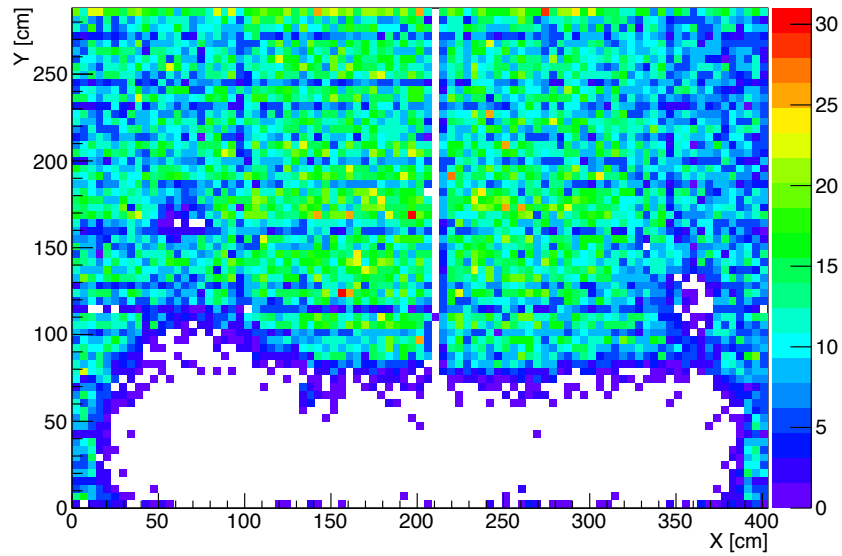


Figure 4.18: MLO hit map reconstructed by the software framework from the cosmic ray run in a self trigger mode. The insensitive detection area corresponds to the manufacturing problem.



## 4.4 Cavern background

As it was mentioned in Section 4.1, one of the main motivations of the NSW project is a degradation of the MS performance with expected increase of the cavern background rate. An extrapolation from the observed rates at the lower luminosity conditions in 2012 to higher luminosity and energy indicates a substantial degradation of the tracking performance, both in terms of efficiency and resolution in the existing inner end-cap station [81]. Therefore, it is crucial to estimate the effect of the cavern background on the upgraded NSW detector systems. The effect of the cavern background on the MM detector performance, will be discussed in this section.

### Description of the cavern background

The cavern background is defined as an incoherent background originated from induced cavern radiation. The cavern radiation is mostly composed of long-lived low energy neutrons and other particles produced in nuclear reactions with these neutrons.

Neutrons are produced due to the spallation reactions of proton debris with the medium. The main radiation sources are close to the beam-line and they are the IP, the FCAL, the beam-pipe and the TAS (Target Absorber Secondaries) collimator on the external side of the detector. The Run-1 simulation of the cavern background flux is shown in Figure 4.19.

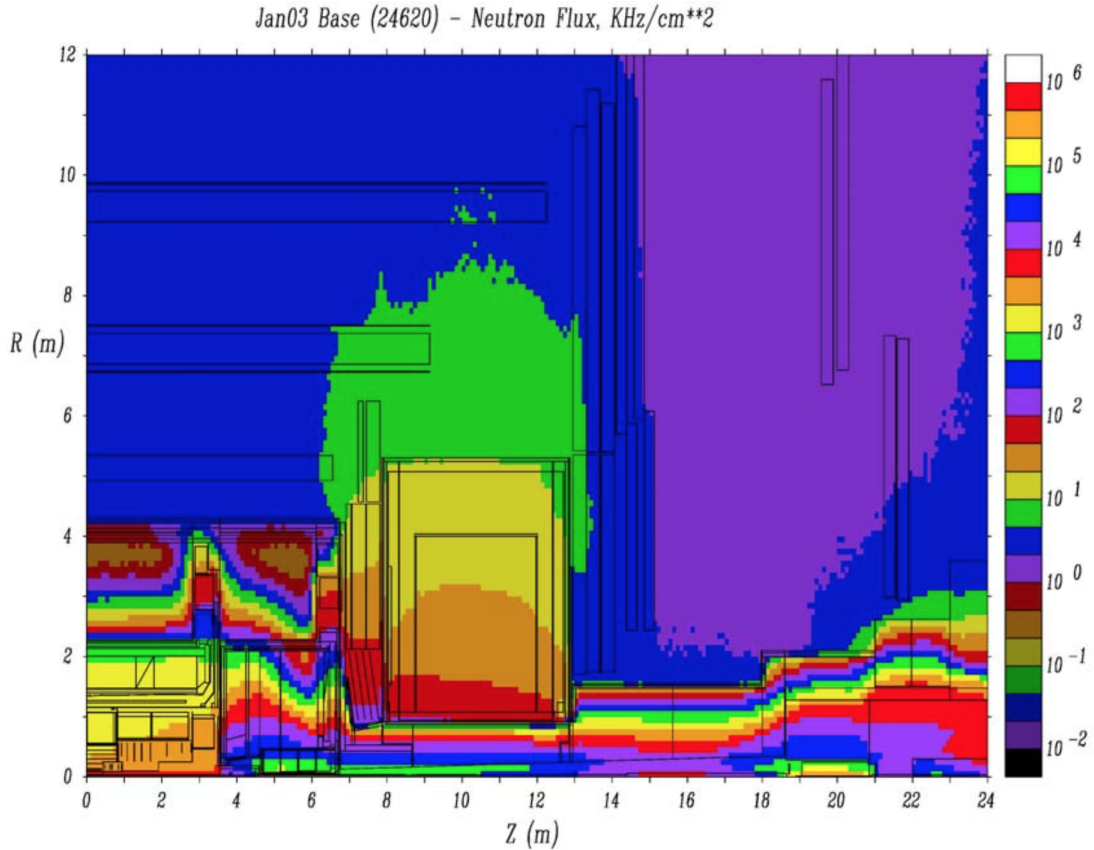


Figure 4.19: Neutron flux in the ATLAS detector simulated with GCALOR software, assuming Run-1 operation conditions. [93]

The neutrons are produced at high energies and further slowed down while interacting with medium, therefore, they have a broad energy spectrum starting from several GeV down to thermal energies. The simulated energy spectrum of the background neutrons and neutron induced photons is shown in Figure 4.20.

Neutrons can produce hits in the detector in several ways. It can be an elastic scattering of neutrons

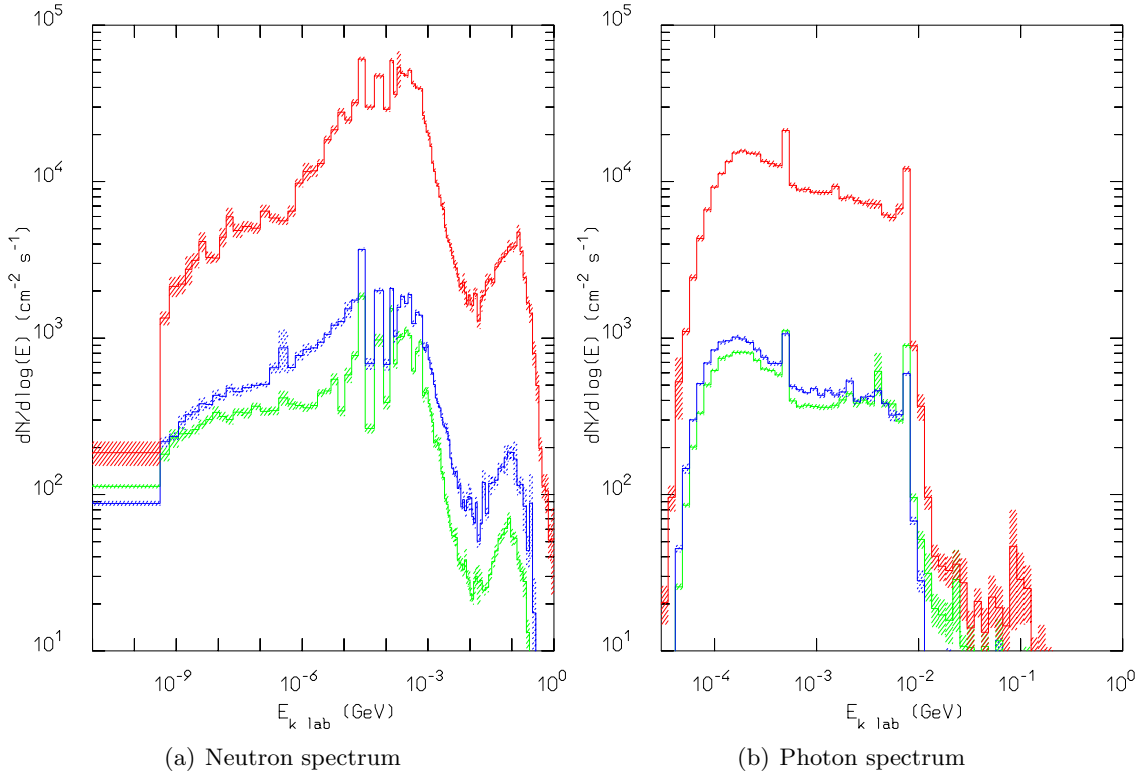


Figure 4.20: Simulated spectrum of neutrons and neutron induced photons in the Muon Spectrometer, assuming Run-1 operation conditions. Red line corresponds to the spectrum averaged in  $2.3 < |\eta| < 2.7$  region; blue -  $1.4 < |\eta| < 2.3$ ; green -  $|\eta| < 1.4$ . Thermal neutrons are not included. [67]

with light nucleus in detector material,  $(n, \gamma)$  reactions or material activation. This interaction will mostly produce single hit in one detector plane, but there is also non negligible probability that the ionising particle will produce a small track segment. Therefore, it is important to produce a detailed simulation of the cavern background effects on the MS detectors, in order to explore possible impacts on the detector and trigger performance.

#### 4.4.1 The MM detection efficiency for photons and neutrons

The detector sensitivity to the cavern background is proportional to its neutron/photon detection efficiency. Therefore, this efficiency can be used to compare relative sensitivity to cavern background for different detector technologies.

Neutron and photon detection efficiencies of the resistive micromegas were never studied in details before. Therefore, the NSW like MM was simulated using Geant4, in the context of this thesis work, in order to determine the efficiencies. The simulated sample is a single plane of the resistive micromegas described in Section 4.2.2, including supporting structure made of aluminium honeycomb as shown in Figure 4.21. The simulated detector sample has a shape of a  $40 \times 80$  cm rectangular. More details on the simulated detector geometry are given in Table 4.1.

The photon and neutron sensitivity of the MM detector were derived from the Geant4 simulation using QGSP\_BERT\_LIV and QGSP\_BERT\_HP physics list respectively (each of the physics lists is aiming for better description of particular particle interactions [94]). More details on the simulation runs performed for the efficiency determination are given in Table 4.2. The estimated efficiencies as a function of the particle energy are shown in Figure 4.22.

The detection efficiency has nontrivial dependency on the particle energy, that can be understood

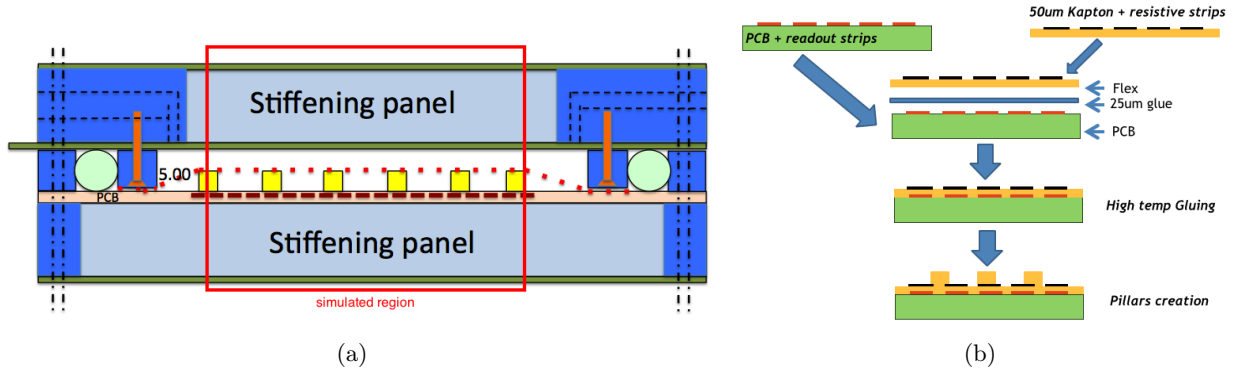


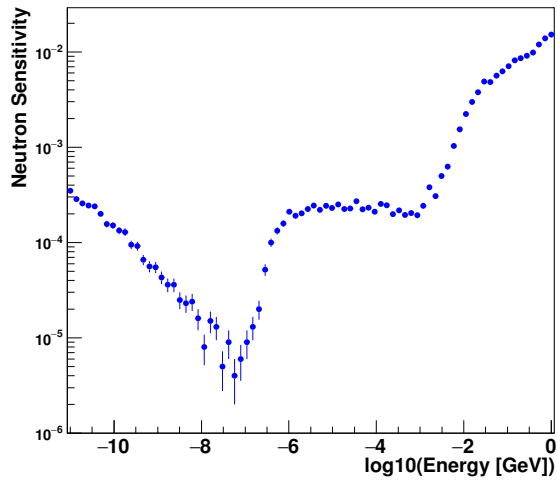
Figure 4.21: (a) Illustration of the resistive micromegas detector sample simulated in Geant4. (b) Detailed structure of the readout PCB.

Structure unit	Material	Thikness ( $\mu m$ )	Simulation details
Honeycomb	Aluminium, $\rho = 0.08 \text{ g/cm}^3$	$10^4$	uniform density is assumed
PCB	FR4 / G10	500	according to FR4 specification
Drift cathode	Copper	17	natural isotope composition
Readout strips	Copper	thickness=17 pitch=450, width=250	full geometry, natural isotope composition
Glue	Akaflex CDF25	25	simulated as epoxy
Insulator	Pyralux PC1025	64	simulated as Polyimide: $\text{H}_{12}\text{N}_2\text{C}_{16}\text{O}_4$ , $\rho = 1.4 \text{ g/cm}^3$
Resistive strips	Carbon filled Kapton	thickness=50 pitch=450, width=250	full geometry, simulated as Polyimide
Pilars	Pyralux PC1025	thickness=128 pitch=7000, diam.=400	full geometry, simulated as Polyimide
Mesh	Stainless steel	pitch=18, diam.=40	stainless steel plane of 22.6 $\mu m$ thickness
Gas	93% Ar + 7% $\text{CO}_2$	drift gap: 5000, ampl. gap: 128	natural isotope composition

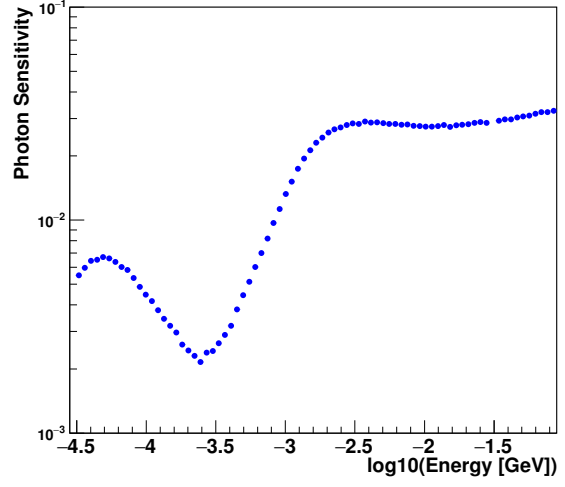
Table 4.1: Specification of the MM detector simulated with Geant4.

due to different interaction processes that dominates at a certain energy range. In case of neutrons, detection in the low energy region mostly happen due to neutron capture with further photon emission ( $n, \gamma$ ), while the sub-keV range is dominated by neutron elastic scattering with gas nucleus, and neutrons with higher energies are mostly detected through direct neutron reactions such as ( $n, p$ ). Low energy photons are mostly detected through the photoelectric effect which is happening on the material with hight nucleus charge, a intermediate energies the detection is dominated by the Compton scattering. The high energy plateau in the detection efficiency corresponds to a mixture of the Compton scattering and  $e^+e^-$  pair production. It is also possible to notice a decrease of detection efficiency for photons with very low energy, that happens due to absorption in detector walls.

The estimated MM detection efficiencies can be compared to similar characteristics of MDT detectors that are currently used instead of the MM. The MDT detection efficiencies for neutrons and photons are shown in Figure 4.23. From the efficiency plots, it is possible to conclude that the MM is less sensitive to neutron and has similar sensitivity to photon (taking into account energy spectrums from Figure 4.20) comparing to MDT detectors.

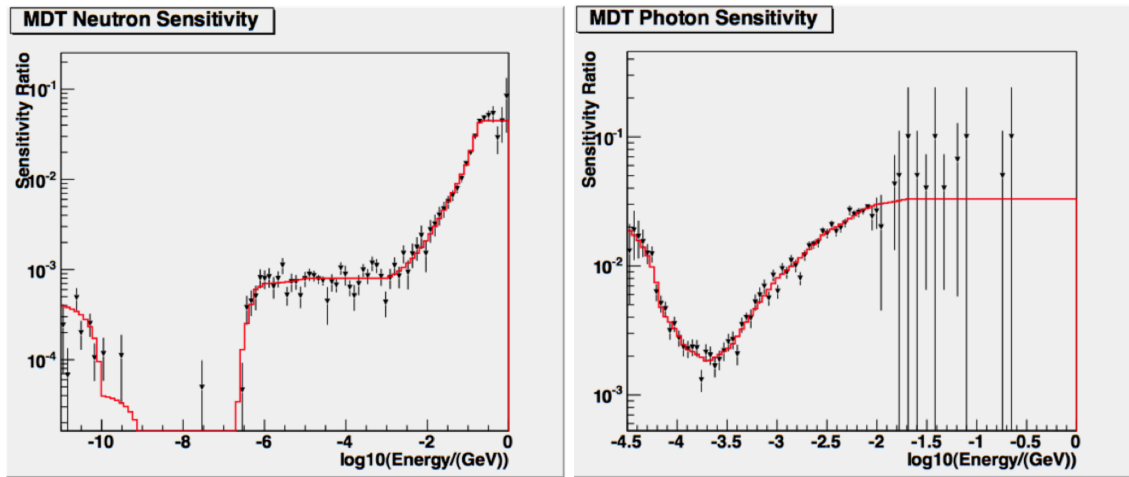


(a) MM Neutron sensitivity



(b) MM Photon sensitivity

Figure 4.22: Neutron and photon sensitivity of the MM detector obtained from the Geant4 simulation.



(a) MDT Neutron sensitivity

(b) MDT Photon sensitivity

Figure 4.23: Measured neutron and photon sensitivity of the MDT detector. [95]

	Photon runs	Neutron runs
Particle source	Two plane sources at the top and bottom borders of the detector that emit particles uniformly in $2\pi$ (in detector direction). Source plane is 70% of linear detector dimensions	
Energy range	$[10^{-4.5}, 10^{-1}]$ GeV	$[10^{-11}, 1]$ GeV
Runs	80 mono energetic runs with $10^6$ events per each	
G4 physics list	QGSP_BERT_LIV	QGSP_BERT_HP
Detection criteria	Particle is considered to be detected if ionisation energy deposit to the drift volume is above 25 eV (1 primary ionised electrons)	

Table 4.2: Description of the simulation runs performed for the efficiency determination.

#### 4.4.2 Cavern background simulation

At an early stage of the ATLAS experiment, the cavern background was simulated with standalone application based on FLUKA [96]. FLUKA was assumed to provide the most reliable simulation of neutron and photon physics involved, since it is commonly used for simulation of radiation shielding. In this standalone application, the cavern background fluxes were derived, and the detector response was deduced using simplified detector models.

Recent studies [97] have shown a good compatibility of standalone cavern background simulations with FLUKA and Geant4 [98] using High Precision (HP) neutron model [99]. It leads to the conclusion that the cavern background can be reliably simulated using Geant4 within the common ATLAS framework called ATHENA [100]. This approach allows to insure precise and complete description of full ATLAS geometry, and, moreover, to exploit full simulation of the MS detectors including electronics.

##### Cavern background simulation within ATHENA framework

The concept and implementation of the cavern background simulation within ATHENA framework was developed in 2011 [101]. So called minimum bias events that does not imply any specific physics, and correspond to the most commonly occurring inelastic  $p - p$  scattering, are used for cavern background simulation. The simulation is performed in two steps. First, the minimum bias event is fully simulated in the ATLAS detector, while all the neutrons with energies below 5 MeV are recorded when enter the MS logic volume. The neutron record is implemented as a separate root ntuple of a specific ATHENA type called `TrackRecordCollection`, that can be further re-used as an input for the second step of the cavern background simulation. Later, the recorded neutron collection is used for a precise simulation of the MS response. This two step approach is convenient to test different MS configurations in relatively fast way, without redoing the full simulation. The output of the second step can be directly interfaced to the ATHENA digitisation and reconstruction algorithms that produce realistic detector response to the simulated event. The described cavern background chain is illustrated in Figure 4.24

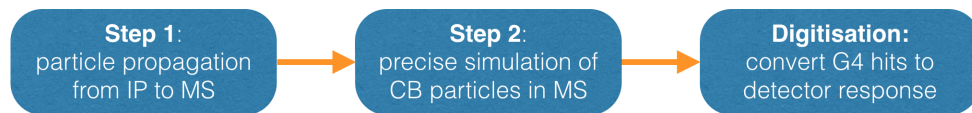


Figure 4.24: Illustration of the two step cavern background simulation within ATHENA frameworks.

In order to correctly simulate the neutron gas in the detector cavern, several modifications to a standard ATLAS simulation setup are needed. The standard cut on primary particle pseudorapidity ( $|\eta| < 6.0$ ) is removed, because a large fraction of the neutron flux comes from particles

striking the forward shielding. The default lifetime cut for neutrons (150 ns) is removed as well. The High Precision neutron physics list from Geant4 (called `QGSP_BERT_HP`) is used for the purpose of cavern background simulation. Its current implementation occasionally produces very low energy ( $< 1$  eV) photons, that are asked to be automatically killed since they cannot produce any detector hits. Additionally, the ATLAS cavern and surrounding bedrock were added to the simulation geometry in order to allow the neutrons to scatter in realistic environment outside the ATLAS detector.

These configurations (HP physics model, no lifetime cut-off for neutrons, geometry modifications) has a CPU time penalty of a factor of 6-7 and a memory penalty of  $\sim 800$  MB relative to the standard simulation configuration. Therefore, the cavern background production is extremely resource consuming task.

Because of the very long time signature of the cavern background energy deposition, a single signal event is in time with 25 ns pieces of thousands of simulated cavern background events. An event of interest in a bunch crossing  $N$  will overlap with the cavern background hits of bunch crossing  $N - 1$  within relative time window 25-50 ns, as well as with the hits of bunch crossing  $N - 2$  within 50-75 ns, and so on. It is impractical to overlay thousands of cavern background events in order to emulate one signal event, particularly when using such a small portion of each background event. This issue is resolved in the simulation using so called *time wrapping* technic. In cavern background output files, any energy deposition in a time window of  $[n \times 25, (n + 1) \times 25)$  ns, where  $n$  is a positive integer, was shifted by  $-n \times 25$  ns to have a complete time profile within a window of  $[0, 25)$  ns. By wrapping energy deposits in this way, a single cavern background event can then be overlaid for an event of interest.

In the context of this thesis (as an authorship qualification task), the implementation of the cavern background simulation was adapted to the new ATLAS software framework that will be used for the Phase-1 upgrade. A cavern background samples of  $5 \times 10^5$  events was generated. This sample is planed to be used for the MM and sTGC trigger and performance studies, when the description of these detectors is fully implemented into the ATLAS framework.

This simulated sample is also required, in order to add the cavern background effect to the ATLAS MC production tasks. The cavern background is added to a simulated physics event at the digitisation level, by overlaying Geant4 hits recorded in caver background event. Detailed description of the procedure is given in Ref. [101].



# Heavy Higgs search in 4 lepton decay channel with 13 TeV data

In 2012, the ATLAS and the CMS collaborations had announced a discovery of a new particle consistent with the Standard Model Higgs boson with a mass around 125 GeV [22, 23]. The four leptons decay channel (Figure 5.1) played a key role in this discovery and in the determination of properties of the new particle [25]. The discovered particle can be the last missing piece of the Standard Model, however there are other theoretical models that predict it to be a component of a larger Higgs sector. The BSM scenarios can be tested by performing a search for other predicted particles. This chapter describes the search for an additional neutral heavy Higgs boson in the  $H \rightarrow ZZ \rightarrow 4\ell$  decay channel with  $14.8 \text{ fb}^{-1}$  of  $\sqrt{s} = 13 \text{ TeV}$  data recorded by ATLAS in Run-2 (2015 - June 2016) [59]. Results of this analysis were presented at ICHEP 2016 conference. This round of the search benefits from higher centre of mass collision energy compared to Run-1, that gives a rise of production cross section for the potential heavy Higgs boson, leading to better sensitivity of the analysis.

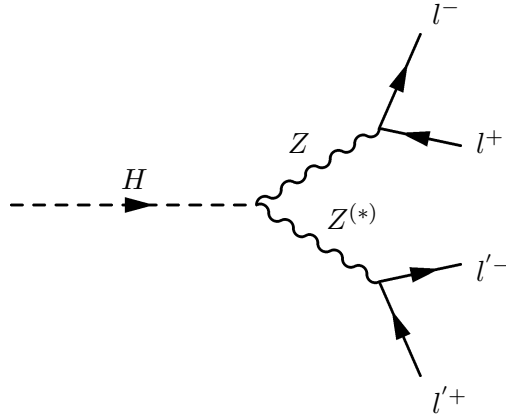


Figure 5.1: The Feynman diagram of the Higgs boson decaying to four leptons.

## 5.1 Analysis overview

Current analysis searches for a Higgs boson decaying into a pair of  $Z$  bosons with a subsequent decay into pairs of opposite charge electrons or muons. This event topology provides a clean final state, since it cannot be mimicked by multi-jet background that has extremely high cross section at hadron colliders. The  $4\ell$ -decay channel has a fully reconstructable kinematics and benefits from the excellent performance of the ATLAS inner tracker, calorimeters and muon spectrometer, that leads to a remarkable resolution of  $4\ell$ -invariant mass measurement. This variable is the main signal to background discriminant, that makes the search particularly sensitive to the narrow resonance. The most significant background is coming from the SM production of two  $Z$  bosons,  $qq \rightarrow ZZ$  and  $gg \rightarrow ZZ$ , while other processes such as SM production of three vector bosons and  $Z + jet$  have a small contribution to the background as well.

This analysis is based on a simple event selection, that insure presence of four well-reconstructed



leptons (electrons/muons) in the final state. The search is performed by carrying out an un-binned fit to the  $m_{4l}$  distribution for the signal mass hypotheses in  $200 \leq m_H \leq 1000$  GeV range. The lower bound was chosen to avoid any overlap with the SM Higgs, and the upper one is limited by available data and MC statistics. The search result is expressed as an upper limit on the heavy Higgs production cross-section times its branching-ratio of four lepton decay, where leptons can be either electrons or muons.

This analysis is aiming to put a cross section limits for different production modes of the additional heavy Higgs boson in narrow width approximation (NWA). The gluon fusion (ggF) and vector-boson fusion (VBF) processes are assumed to be the dominant production modes in a proton-proton collisions. Other production modes are assumed to be minor and therefore not included into the analysis. Selected events are separated into two categories as described in Section 5.3.3, in order to discriminate ggF and VBF production modes.

## 5.2 Data and simulated samples

### 5.2.1 Data

For this analysis, both 2015 and early 2016 data is used. Both datasets were produced in proton-proton collisions of  $\sqrt{s} = 13$  TeV centre of mass energy with a 25 ns bunch spacing configuration. Early 2015 data with 50 ns bunch spacing was dropped from the analysis due to very low statistics ( $0.13 \text{ fb}^{-1}$ ). The ATLAS experiment has recorded  $3.9 \text{ fb}^{-1}$  in 2015 and  $12.8 \text{ fb}^{-1}$  in 2016. A small fraction of this data was rejected due to quality problems such as subdetector or magnet failure. The resulting integrated luminosity considered here is equal to  $14.8 \text{ fb}^{-1}$ . Further data recorded by ATLAS since July 2016 will be included in the updated results shown in Chapter 8.

There are some differences between the 2015 and 2016 datasets, that were carefully taken into account while combining them. The second one has significantly higher number of proton-proton interactions per bunch crossing (higher pile-up profile) that can be clearly seen from Figure 5.2. Another difference is coming from the change of TRT gas mixture performed in-between 2015 and 2016 operation periods, that is taken into account as described in Section 5.2.2.

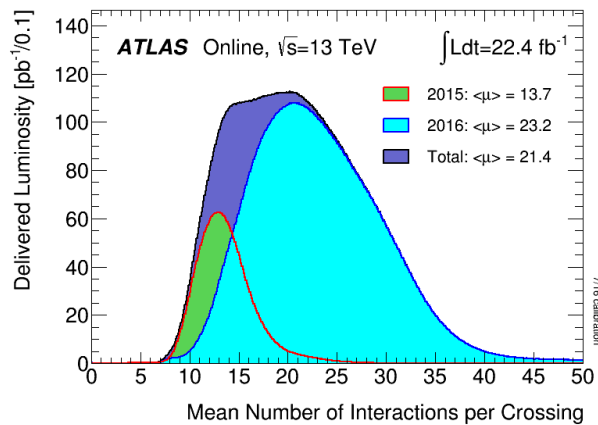


Figure 5.2: The distribution of the mean number of interactions per bunch crossing is shown for the 2015 and 2016 proton-proton collision data.

This analysis uses specific reduced data format that includes basic preselection of events. At least two leptons (electrons or muons) with the di-lepton mass greater than 5 GeV are required, while one of them should fire single lepton trigger. The leading lepton should have  $p_T > 15$  GeV and in case it is muon (electron) it should pass the Loose (LHVeryLoose) quality criteria described

in Section 3.3. The subleading muon is required to have suitable number of hits (as in case of Loose quality) in the Inner Detector, while there is no additional requirement for the subleading electron.

### 5.2.2 MC samples

Different processes that are important for the analysis are simulated using Monte Carlo (MC) technic. Production of the events is carried out by various generators that are based on perturbative theoretical calculations. Interaction of the generated particles with the detector is simulated using the full ATLAS simulation [102] within Geant4 [98]. The simulated detector response is further digitised and reconstructed within ATHENA framework [100]. The additional  $p$ - $p$  interactions (pile-up) and cavern background effects are included into the simulation at digitisation step. To simulate the pile-up, minimum bias events, which were previously simulated, are superimposed with the signal event. Cavern background simulation is described in Section 4.4

For simulating both the 2015 and 2016 data-taking conditions, only one MC set is used. The pile-up profile is reweighed according to the combined 2015 and 2016 dataset. For the TRT gas mixtures, the current MC campaign contains the 2015 configuration, hence, extra uncertainty is added for the 2016 scale factors.

The  $H \rightarrow ZZ \rightarrow 4\ell$  signal is modelled using the POWHEG Monte Carlo event generator [103,104], which calculates separately the gluon fusion and the vector-boson fusion production mechanisms with matrix elements up to next-to-leading order (NLO). POWHEG is interfaced to PYTHIA 8 [105] for showering and hadronisation, which in turn is interfaced to EvtGen [106] for the simulation of B-hadrons decay. Both ggF and VBF samples for NWA are simulated for the mass hypotheses from 200 to 1000 GeV in a step of 100 GeV.

The  $ZZ$  continuum background is modelled using POWHEG for quark-antiquark annihilation ( $q\bar{q} \rightarrow ZZ$ ) and Sherpa [107] for gluon fusion ( $gg \rightarrow ZZ$ ). POWHEG here is also interfaced to PYTHIA 8 for parton shower and hadronisation, and to EvtGen for the simulation of  $B$ -hadron decays. Simulation of the  $gg \rightarrow ZZ$  process includes an interference with the SM Higgs boson gluon fusion production. More details on the  $ZZ$  background simulation are given in Section 5.4.

$Z$  boson production in association with extra jets ( $Z + jets$ ) is modelled using Sherpa at NLO for 0 to 2 jets and at LO for 3 and 4 jets. The  $t\bar{t}$  background is modelled using POWHEG interfaced to PYTHIA 6 [108] for parton shower and hadronisation, to PHOTOS [109] for quantum electrodynamics (QED) radiative corrections, to Tauola [110,111] for the simulation of  $\tau$  lepton decays and to EvtGen for the simulation of  $B$ -hadron decays. The  $WZ$  background is modelled using POWHEG interfaced to PYTHIA 8 for parton shower and hadronization and to EvtGen for the simulation of B-hadron decays. The tribosons backgrounds  $ZZZ$ ,  $WZZ$ , and  $WWZ$  with four or more genuine leptons are modelled using Sherpa. For the all-leptonic  $t\bar{t} + Z$  the MadGraph+PYTHIA 8 is used.

#### Generator level filters

In order to get suitable statistics for the  $Z + jets$  MC sample,  $4\ell$  and  $3\ell$ -filters are applied at the generator level. An effect of this lepton filters on the final composition of the MC sample was studied using truth information. As it can be seen in Figure 5.3, more then 99% of events that pass both the filter and the analysis selection, have at least one lepton originated from a hadron containing  $c$  or  $b$  quark. Therefore such samples are supposed to be enhanced in the heavy flavour originated component, while the missing light flavour contribution is recovered by data driven technique described in Section 5.4.

Study of generator level filters for  $t\bar{t}$  production was performed in the context of this thesis. The

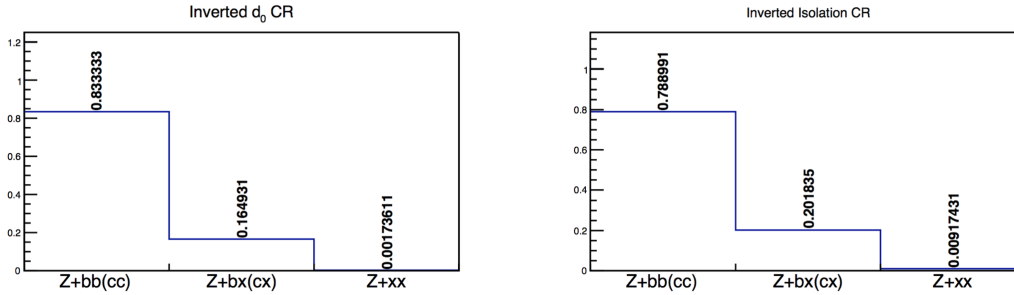


Figure 5.3: Origine of the leptons in the  $Z + jets$  MC samples produced with  $4\ell$  and  $3\ell$ -filters. The distributions are shown for two control regions (defined in Section 5.4) that have close event selection to the signal region, but are enriched in  $Z + jets$  events. The first bin of the histogram shows a fraction of events that have two leptons originated from  $Z$  decay and two leptons originated from decay of a hadron with  $c$  or  $b$  quark. The second bin: two leptons from  $Z$ , one lepton from a hadron with  $c$  or  $b$  quark, and one lepton with different origin. The last bin: two leptons from  $Z$  and two leptons with an origin other then a hadron with  $c$  or  $b$  quark.

aim was to find a suitable filter that allows to increase statistics for the MC samples without consuming more resources. Different filters were checked in terms of filter efficiency (fraction of events that pass the filter) and loss of the acceptance in the control regions used for the background estimation. The filter efficiency shows how many events are reject before performing the full detector simulation, therefore this number can be considered as a reduction factor for the consumed computing resources. Acceptance loss describes a fraction of events that are cut away by filter, but they could pass the control region selection. The best filter can be chosen by minimising both quantities, however usually reduction of one of the quantities cause an increase of another one. As an outcome of this study it was decided to use three different filters with an overlap removal applied: 1 lepton, 2 lepton and 4 lepton filters. This approach allows to obtain high MC statistics for a large part of the phase space without missing events in other parts of the phase space. Specific information for the MC samples with each of the filters applied is given in Table 5.1.

Table 5.1: Detailed information about the  $t\bar{t}$  MC samples with different generator level filters is shown. The number of generated events in the sample, filter efficiency and acceptance loss in the CRs due to the filter is shown. All three samples are used with the overlap removal among them. The CRs definitions are given in Section 5.4

Filter:	1 lepton	2 lepton	4 lepton
Generated events	$2.0 \cdot 10^7$	$1.8 \cdot 10^7$	$1.0 \cdot 10^7$
Filter efficiency	1/2	1/10	1/220
Acceptance loss in the CRs			
Inv. $d_0$	0%	4%	15%
Inv. Iso.	0%	4%	24%
$e\mu + \mu\mu$	0%	4%	18%
Relaxed	0%	4%	17%

## 5.3 Event selection and categorisation

### 5.3.1 Trigger

Data is recorded using single lepton, di-lepton and tri-lepton triggers. A summary of the triggers used in 2015 is shown in Table 5.2, while the trigger set used in 2016 is shown in Table 5.3. The

combined efficiencies for these triggers are  $0.9941 \pm 0.0027$  ( $4e$ ),  $0.9921 \pm 0.0023$  ( $4\mu$ ),  $0.9996 \pm 0.0003$  ( $2e2\mu$ ) and  $0.9889 \pm 0.0035$  ( $2\mu2e$ ) for the 2015 data, and  $0.9951 \pm 0.0004$  ( $4e$ ),  $0.9859 \pm 0.0006$  ( $4\mu$ ),  $0.9952 \pm 0.0004$  ( $2e2\mu$ ) and  $0.9684 \pm 0.0011$  ( $2\mu2e$ ) for the 2016 data. Explicit trigger information can be found in Ref. [112].

Table 5.2: Summary of the HLT triggers that are used during the 2015 data taking for the three analysis channels. When multiple chains are indicated, it is intended that the OR among them is requested.

Channel	Single-lepton	Di-lepton	Tri-lepton
$4e$	e24_lhmedium_L1EM18VH (Period D) e24_lhmedium_L1EM20VH (Period E-J) e60_lhmedium e120_lhloose	2e12_lhloose_L12EM10VH	e17_lhloose_2e9_lhloose
$4\mu$	mu20_loose_L1MU15 mu40 mu60_0eta105_msonly	2mu10 mu18_mu8noL1	3mu6 3mu6_msonly mu18_2mu4noL1
$2e2\mu$	$4e$ OR $4\mu$	$4e$ OR $4\mu$ OR e17_lhloose_mu14 e24_medium_L1EM20VH_mu8noL1 e7_medium_mu24	$4e$ OR $4\mu$ OR 2e12_lhloose_mu10 e12_lhloose_2mu10

Table 5.3: Summary of the HLT triggers that are used during the 2016 data taking for the three analysis channels. When multiple chains are indicated, it is intended that the OR among them is requested.

Channel	Single-lepton	Di-lepton	Tri-lepton
$4e$	e24_lhmedium_ivarloose (Period A-D3) e26_lhtight_nod0_ivarloose (Period D4-F) e60_lhmedium_nod0 e60_lhmedium e140_lhloose_nod0	2e15_lhvloose_nod0_L12EM13VH (Period A-D3) 2e17_lhvloose_nod0 (Period D4-F)	e17_lhloose_nod0_2e9_lhloose_nod0 (Period A-D3) e17_lhmedium_nod0_2e9_lhmedium_nod0 (Period D4-F)
$4\mu$	mu24_ivarloose_L1MU15 (Period A) mu24_loose_L1MU15 (Period A) mu24_ivarmedium (Period B-D3, D4-E) mu24_imedium (Period B-D3, D4-E) mu26_ivarmedium (Period D4-F) mu26_imedium (Period D4-F) mu50	2mu10 (Period A) 2mu10_nomucomb (Period A) mu20_mu8noL1 (Period A-E) mu20_nomucomb_mu6noL1_nscan03 (Period A-D3) 2mu14 (Period D-F) 2mu14_nomucomb mu22_mu8noL1 (Period D4-F)	3mu4 (Period A) 3mu6 (Period B-F) 3mu6_msonly (Period D4-F) mu20_2mu4noL1 mu11_nomucomb_2mu4noL1_nscan03_L1MU11_2MU6 (Period B-D3) mu20_msonly_mu10noL1_msonly_nscan05_noComb (Period B-D3)
$2e2\mu$	$4e$ OR $4\mu$	$4e$ OR $4\mu$ OR e17_lhloose_nod0_mu14 (Period A-D3) e24_lhmedium_nod0_L1EM20VH_mu8noL1 (Period A-D3) e7_lhmedium_nod0_mu24 (Period A-D3) e17_lhloose_mu14 (Period D4-F) e24_lhmedium_L1EM20VH_mu8noL1 (Period D4-F) e7_lhmedium_mu24 (Period D4-F)	$4e$ OR $4\mu$ OR 2e12_lhloose_nod0_mu10 (Period A-D3) e12_lhloose_nod0_2mu10 (Period A-D3) 2e12_lhloose_mu10 (Period D4-F) e12_lhloose_2mu10 (Period D4-F)

### 5.3.2 Event selection

Electrons and muons are used for reconstruction of the event kinematics, while jets are used for separation of the events into two categories enriched in different production modes. Both leptons and jets are used in the analysis only if they pass a set of quality requirements given in Section 3.3. Electrons are required to have  $E_T > 7$  GeV and  $|\eta| < 2.47$  while muons are required to have  $p_T > 15$  GeV in case of CT muon, or  $p_T > 5$  GeV for the other types. The  $\eta$  cut for muons has been incorporated into the quality requirements, as described in Section 3.3.2. Jets are required to have  $p_T > 30$  GeV and  $|\eta| < 4.5$ .

After the selection of leptons and jets, the object overlap removal is applied according to recommendations from combined performance group [113]. Due to this procedure an electron is removed

in case it has a track close to ID track of a selected muon. Calorimeter tagged muon is removed in case it shares ID track with a good electron. Moreover, an additional  $e$ - $e$  overlap removal is performed, which keeps the electron with the highest  $E_T$  if multiple electrons share an ID track or have overlapping EM clusters. Lepton-jet overlap removal with lepton removed is not applied to prevent any acceptance loss.

A primary vertex is defined as one with the largest  $p_T$  sum in the event. Each good event is required to have at least four leptons pointing to a primary vertex, which is ensured by asking a distance from the primary vertex along the proton beam axis to be  $|z_0 \cdot \sin \theta| < 0.5 \text{ mm}$ . Transverse impact parameter cut  $|d_0| < 1 \text{ mm}$  is applied to muons in order to reduce the cosmic background.

When the event has at least four good leptons, a candidate quadruplet is formed by selecting two opposite sign same flavour di-lepton pairs. The leptons in the quadruplet are required to have  $p_T > 20, 15, 10 \text{ GeV}$  starting from the most energetic one, while they also should be well separated from each other,  $\Delta R = \sqrt{\Delta\eta^2 + \Delta\phi^2} > 0.10$  for same flavour leptons and  $\Delta R > 0.20$  for different flavour leptons. In order to reject leptons from  $J/\psi$ , alternative same-flavour opposite-charge di-lepton pairs are required to have  $m_{\ell\ell} > 5 \text{ GeV}$ .

Since both di-leptons should originate from (virtual)  $Z$  boson decay, there is a mass window cut applied to di-lepton invariant mass. A di-lepton that has a mass  $m_{12}$  closer to  $Z$  is called a leading one. It is required that  $50 < m_{12} < 106 \text{ GeV}$ . Invariant mass of the second di-lepton should satisfy  $m_{\text{threshold}} < m_{12} < 106 \text{ GeV}$ , where  $m_{\text{threshold}}$  is dependent on the quadruplet invariant mass  $m_{4\ell}$ . The value of  $m_{\text{threshold}}$  is 12 GeV for  $m_{4\ell} < 140 \text{ GeV}$ , rises linearly to 50 GeV with  $m_{4\ell}$  in the interval  $m_{4\ell} \in [140 \text{ GeV}, 190 \text{ GeV}]$  and stays at 50 GeV for  $m_{4\ell} > 190 \text{ GeV}$ . In case if after this kinematic selection there are still more than one quadruplet candidate, the one with  $m_{12}$  and  $m_{34}$  closest the  $m_Z$  mass is retained.

The next step is to apply isolation and  $d_0$  significance (transverse impact parameter normalised to its uncertainty) cuts to each lepton in the quadruplet. These lepton quality cuts are applied at the end of selection for several reasons. First, an overlap removal is performed to remove a contribution to the isolation variables of nearby leptons chosen in the quadruplet. Moreover, these cuts will be further relaxed/inverted to build control regions for data driven estimate of the reducible background. Isolation and  $d_0$  significance cut optimisation is described in [114]. The calorimeter isolation for a lepton is defined as a sum transverse energy of all topo-clusters in the  $\Delta R < 0.20$  cone around the object of interest:  $E_T^{\text{topocone20}}$ . The Inner Detector isolation is a sum of transverse momentum of all the tracks within given  $\Delta R$  cone:  $p_T^{\text{varcone20}}$  for  $\Delta R < 0.20$  or  $p_T^{\text{varcone30}}$  for  $\Delta R < 0.30$ . In case of muons the isolation cuts of  $p_T^{\text{varcone30}}/p_T < 0.15$  and  $E_T^{\text{topocone20}}/E_T < 0.30$  are applied, while electrons are required to satisfy  $p_T^{\text{varcone20}}/p_T < 0.15$  and  $E_T^{\text{topocone20}}/E_T < 0.20$ . For the transverse impact parameter significance, electrons are required to satisfy  $d_0/\sigma_{d_0} < 5$ , while for muons the cut value is  $d_0/\sigma_{d_0} < 3$ , where  $\sigma_{d_0}$  is an uncertainty on the reconstructed transverse impact parameter  $d_0$ .

To further reject reducible background events, another cut is introduced. It is based on the fit quality ( $\chi^2/N_{\text{dof}}$ ) of the vertex formed by the tracks of the quadruplet [115]. The applied cut is  $\chi^2/N_{\text{dof}} < 5$  for  $4\mu$  candidates and  $\chi^2/N_{\text{dof}} < 9$  for the rest. The event selection summary is shown in Table 5.4.

The mass resolution is further improved by applying final state radiation correction (FSR) and  $Z$  mass constraint. FSR is the procedure that allows to recover energy loss by the lepton due to final state photon radiation. The  $Z$  mass constraint allows to improve precision of the invariant di-lepton (originated from  $Z$  boson decay) mass by exploiting a priori information of  $Z$  boson line shape and detector resolution. It is applied to both di-leptons of the selected quadruplet. A detailed description of these two technics is given in Ref. [115].

### Z-mass Constraint

Table 5.4: Summary of the event selection requirements. The two lepton pairs are denoted as  $m_{12}$  and  $m_{34}$ . (The choice of the threshold value  $m_{\text{threshold}}$  for  $m_{34}$  can be found in the text.) [115]

Physics Objects	
ELECTRONS	
Loose Likelihood quality electrons with hit in innermost layer, $E_T > 7$ GeV and $ \eta  < 2.47$	
MUONS	
Loose identification	
Calo-tagged muons with $p_T > 15$ GeV and $ \eta  < 0.1$	
Combined, stand-alone (with ID hits if available) and segment tagged muons with $p_T > 5$ GeV	
JETS	
anti- $k_T$ jets with $p_T > 30$ GeV, $ \eta  < 4.5$ and passing pile-up jet rejection requirements	
Event Selection	
QUADRUPLET SELECTION	Require at least one quadruplet of leptons consisting of two pairs of same-flavour opposite-charge leptons fulfilling the following requirements: $p_T$ thresholds for three leading leptons in the quadruplet - 20, 15 and 10 GeV Maximum one calo-tagged or standalone muon per quadruplet Select best quadruplet to be the one with the (sub)leading dilepton mass (second) closest the $Z$ mass Leading di-lepton mass requirement: $50 \text{ GeV} < m_{12} < 106 \text{ GeV}$ Sub-leading di-lepton mass requirement: $m_{\text{threshold}} < m_{34} < 115 \text{ GeV}$ Remove quadruplet if alternative same-flavour opposite-charge di-lepton gives $m_{\ell\ell} < 5 \text{ GeV}$ $\Delta R(\ell, \ell') > 0.10(0.20)$ for all same(different) flavour leptons in the quadruplet
ISOLATION	Contribution from the other leptons of the quadruplet is subtracted Muon track isolation ( $\Delta R \leq 0.30$ ): $\Sigma p_T/p_T < 0.15$ Muon calorimeter isolation ( $\Delta R = 0.20$ ): $\Sigma E_T/p_T < 0.30$ Electron track isolation ( $\Delta R \leq 0.20$ ): $\Sigma E_T/E_T < 0.15$ Electron calorimeter isolation ( $\Delta R = 0.20$ ): $\Sigma E_T/E_T < 0.20$
IMPACT PARAMETER SIGNIFICANCE	Apply impact parameter significance cut to all leptons of the quadruplet. For electrons : $d_0/\sigma_{d_0} < 5$ For muons : $d_0/\sigma_{d_0} < 3$
VERTEX SELECTION	Require a common vertex for the leptons $\chi^2/\text{ndof} < 6$ for $4\mu$ and $< 9$ for others.

The leptons in the final state are predominately produced in a decay of on-shell  $Z$  bosons. It allows to improve the di-lepton mass resolution exploiting prior information about the  $Z$  line shape and the lepton momentum measurement uncertainty. The probability to observe a  $Z$  boson with a true mass  $\mu_{12}$  decaying to two leptons with true 4-momenta  $\mathbf{p}_{1,2}^{true}$ , while measuring the 4-momenta  $\mathbf{p}_{1,2}^{rec}$  can be factorised as:

$$L(\mathbf{p}_1^{true}, \mathbf{p}_2^{true}, \mathbf{p}_1^{rec}, \mathbf{p}_2^{rec}) = B(\mathbf{p}_1^{true}, \mathbf{p}_2^{true}) \cdot R_1(\mathbf{p}_1^{true}, \mathbf{p}_1^{rec}) \cdot R_2(\mathbf{p}_2^{true}, \mathbf{p}_2^{rec}), \quad (5.1)$$

where  $B$  is a probability of a  $Z$  boson to decay into two leptons with given momentums, and  $R$  is a lepton resolution function. Function  $B$  depends only on the true value of the di-lepton invariant mass  $\mu_{12}$ , that can be expressed in terms of true lepton energy  $\varepsilon$  and the opening angle between the two decay leptons  $\theta$ :

$$\mu_{12}^2 = 2 \cdot \varepsilon_1 \varepsilon_2 (1 - \cos \theta), \quad (5.2)$$

It is important to notice that the angles are measured with very high precision, therefore the reconstructed angle value can be assumed to be equal to the true one. In this case the lepton resolution function becomes dependent only on reconstructed 4-momenta and true energy of a lepton.

$$R_l(\mathbf{p}_l^{true}, \mathbf{p}_l^{rec}) = R_l(\varepsilon_{l2} | \mathbf{p}_l^{rec}). \quad (5.3)$$

In summary, the only uncertain variables in Equation (5.1) are the measured lepton energies  $E$ . Knowing the true  $Z$  boson mass, these measurements can be constrained using the relations in Equations (5.2) and (5.3). To this end, the likelihood  $L$  is maximised for a given event with measured lepton 4-momenta over the true lepton energies. The maximised likelihood gives the maximum likely 4-momenta,  $\mathbf{p}_l^{ml}$ , which are composed from the maximum likely energies and the measured angles. This procedure will be called  $Z$  mass constraint from now on. Since the natural width of the  $Z$  boson is at the same order as the experimental di-lepton mass resolution, an improvement in the latter is expected. In the present implementation,  $B$  is modelled with a relativistic Breit-Wigner function, while the single lepton response functions are approximated by gaussian distribution.

### Cut optimisation

A cut optimisation and harmonisation task force was carried out in order to optimise the analysis selection and harmonise it with the analysis that is measuring the Standard Model production cross section of a  $Z$  boson pair (SM ZZ group). It was found that an increase of the lepton  $p_T$  thresholds does not lead to a sizeable improvement of signal to background ratio, therefore it was chosen to keep the current values of the cuts. The lepton pairing procedure described in this section was compared to another algorithm used by the SM ZZ group. This algorithm is choosing the best lepton quadruplet by minimising a deviation of the two di-lepton masses from twice the mass of  $Z$  boson:  $\Delta m = |m_{12} + m_{34} - 2m_Z|$ . The currently used pairing procedure was found to have better performance, and therefore it is further used in the analysis. All the other cut were found to be compatible between the two analyses.

As the outcome, both analyses, the heavy Higgs and the SM ZZ ones, are using similar event selections with few minor differences that allow to keep the analyses optimal:

- the Standard Model group has a bit tighter lepton  $p_T$  cuts, that is required by their method of the background estimate;
- different pairing algorithms are used.

In the previous round of the analysis the  $Z$  mass constrain was applied to the leading lepton pair

only, however, as it can be seen from Figure 5.4 applying  $Z$  mass constraint to both lepton pairs can improve the  $m_{4\ell}$  resolution even more. It was found that by applying  $Z$  mass constrain to both lepton pairs in the quadruplet, it is possible to gain up to 5% in analysis sensitivity at high mass. This gain is mostly coming from resolution improvement for high  $p_T$  muons. Therefore  $Z$  mass constrain will be applied to both lepton pairs in this analysis, as it was mentioned before.

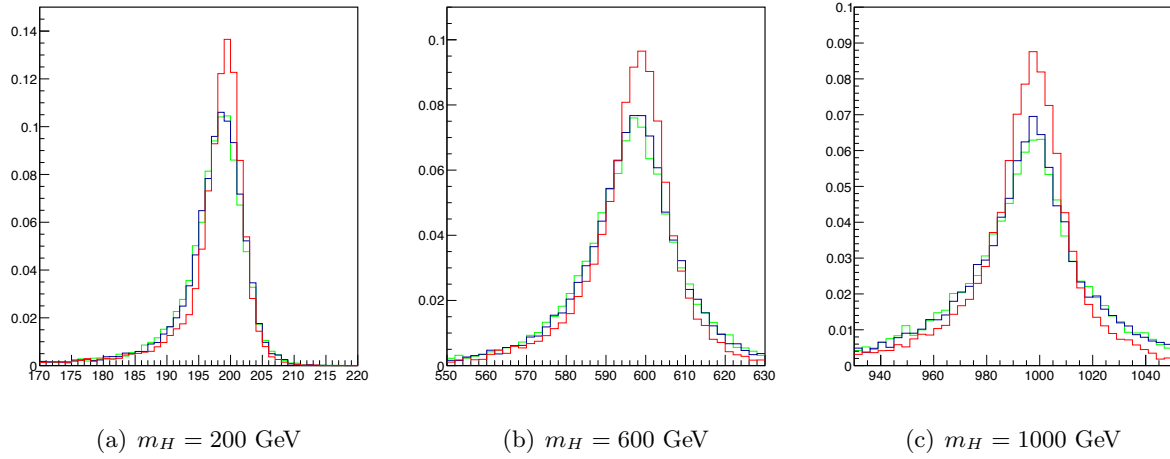


Figure 5.4: The reconstructed signal mass spectrum for three signal mass hypothesis. Green line corresponds to the  $m_{4\ell}$  variable without  $Z$  mass constraint, blue - single  $Z$  mass constraint, red - double  $Z$  mass constraint.

The double  $Z$  mass constrained was not used previously due to a problem reported in Ref. [116]. There the idea was to apply single  $Z$  mass constraint below  $ZZ$  on-shell threshold, while applying double  $Z$  mass constraint above the threshold. This approach caused a dip around the threshold in the background distribution, which is originated from bin-to-bin migrations due to  $Z$  mass constraint applied. This problem can be avoided by applying double  $Z$  mass constraint for the full mass range without introducing a threshold. In this case the double  $Z$  mass constraint is not physics motivated in the low mass region since one  $Z$  candidate is off-shell, so this algorithm just introduce some minor random modification of  $m_{4\ell}$  below 180 GeV. In practice, the  $m_{4\ell}$  variable with double  $Z$  mass constraint below in the low mass region where one of  $Z$  bosons is off-shell has the same distribution as the  $m_{4\ell}$  with single  $Z$  mass constraint, because the  $m_{34}$  is simply not modified. By applying double  $Z$  mass constraint to the full mass range it is possible to achieve a smooth background distribution that is shown in Figure 5.5.

### 5.3.3 Categorisation

Events passing the signal region selection are further separated into ggF and VBF like categories. Signal categorisation is based on the fact that VBF production mode usually has two forward back-to-back jets. Signal candidate is falling into VBF-like category in case there are at least two jets with  $p_T > 30$  GeV in the event, and they have significant  $\eta$  separation  $\Delta\eta > 3.3$  as well as high invariant mass of the di-jet system  $m_{jj} > 400$  GeV. All the other events that do not satisfy this criteria, are falling into ggF like category. Such a categorisation allows to separate a very clean VBF signal region, while in the ggF like one there is still noticeable contamination from potential VBF production mode.



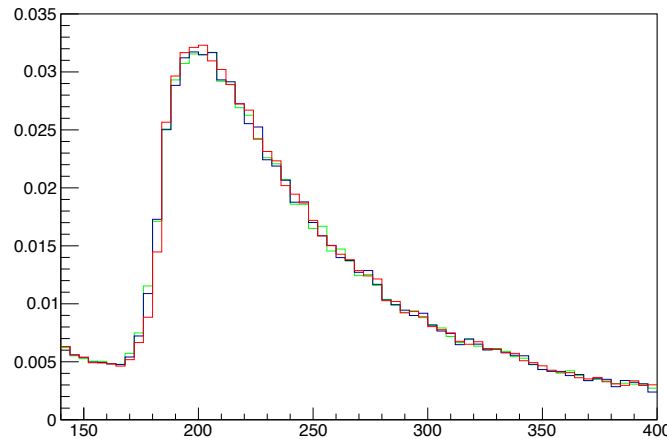


Figure 5.5: The reconstructed  $qq \rightarrow ZZ$  mass spectrum. Green line corresponds to the  $m_{4\ell}$  variable without  $Z$  mass constraint, blue - single  $Z$  mass constraint, red - double  $Z$  mass constraint.

## 5.4 Background

The main background is coming from the Standard Model production of  $Z$  boson pair with further decay to four leptons. This process has exactly the same final state topology as the signal (further called irreducible), namely four well isolated leptons are produced. Therefore, it is hard to construct a signal region (SR) that is not contaminated by this background, but fortunately this process can be simulated with reasonable accuracy. This final state can be produced in two reactions:  $qq \rightarrow ZZ$  and  $gg \rightarrow ZZ$  (Figure 5.6), while the production rate of the first one is about ten times higher than the second. Since these two production modes involved quite different physics, they are simulated separately with POWHEG and SHERPA accordingly. Quark-antiquark annihilation has up to NNLO QCD and NLO EW corrections applied [117], while the gluon-gluon channel is known only at leading order precision and has conservative 60% uncertainty due to higher order corrections.

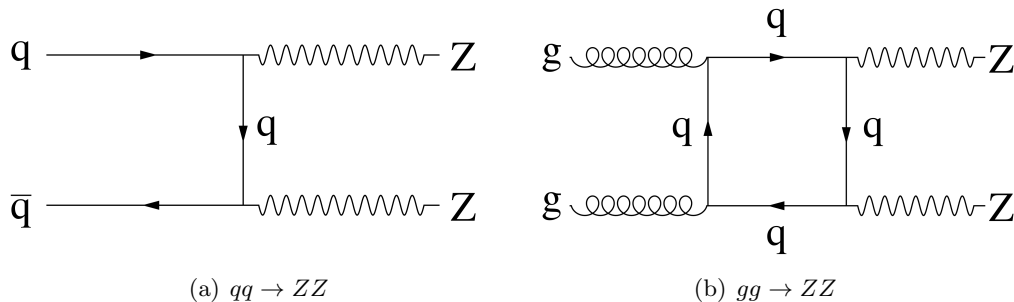


Figure 5.6: The lowest order Feynman diagram of the SM  $qq \rightarrow ZZ$  (a) and  $gg \rightarrow ZZ$  (b) processes in a  $p$ - $p$  collider.

Another source of irreducible background is the standard model production of three vector bosons ( $ZZZ$ ,  $WZZ$ ,  $WWZ$ ) and fully leptonic decay of a top quark pair produced in association with a  $Z$  boson ( $t\bar{t}+Z$ ). These processes have minor contribution and they are also estimated from MC simulation.

Another type of background is coming from lepton misidentification. In this case the reconstructed event contains two or three real leptons in the final state as well as one or more objects misidentified as good lepton and selected to the quadruplet. The simulation of such a process has quite poor

accuracy, therefore, a data driven approach is applied to estimate reducible backgrounds such as  $t\bar{t}$  and  $Z$ +jets. A detailed description of the method is given in Sections 5.4.1 and 5.4.2. Usually in the case of reducible background there are at least two real leptons that form a leading di-lepton in the event, while the subleading di-lepton contains one or two fake leptons. The origin of electron and muon fakes is quite different, therefore the reducible background is estimated separately for events with two muons ( $\ell\ell + \mu\mu$ ) or two electrons ( $\ell\ell + ee$ ) in the subleading dilepton. The reducible background is quite small comparing to  $ZZ$  one, and its contribution is almost negligible above 300 GeV. Nevertheless, it is important to discuss this data driven estimate since it is shared both by the heavy Higgs and the Standard Model Higgs analyses.  $WZ$  production has a small contribution to the background as well and it is estimated from MC simulation.

Further break down of the background to different categories is based on MC simulation for all the processes. Final estimate of the expected background yields for  $14.8 \text{ fb}^{-1}$  of data can be found in Table 5.19.

#### 5.4.1 $\ell\ell + \mu\mu$ reducible background

In the  $\ell\ell + \mu\mu$  final state, there are several sources of reducible background. The dominant contribution is from  $Z$  boson production accompanied by leptons from semi-leptonic decays of heavy flavour hadrons. There is a smaller contribution from  $Z$  production accompanied by leptons from in-flight decays of  $\pi/K$  in light-flavour jets. The sum of these two components is denoted as  $Z$ +jets. Another contribution is coming from a top quark pair production  $t\bar{t}$  and diboson production  $WZ$ .

MC simulation of  $Z$ +jets background requires huge statistics due to low probability for the jets to fake a good lepton or even two leptons simultaneously. Such a MC statistics is not available due to limited computing resources. The problem was solved by applying three and four-lepton filters at the generator level, that allow to cut a big part of the events, that will not be selected as good ones, even before passing them through the whole simulation chain. This filter does not cut any interesting events from the first component since the heavy flavour hadron decay is treated inside the generator, thus all “fake” leptons are present already at the filter level. In contrary, the second component will be highly suppressed because  $\pi/K$  decay is treated within GEANT4 at the level of detector simulation, thus the “fake” leptons do not exist at the filter level. Therefore, the simulated component was denoted as the heavy flavour one  $Z$ +HF and the missing component is denoted as light flavour originated  $Z$ +LF and the later one will be estimated from data.

Since we have the MC simulation for  $Z$ +HF and  $t\bar{t}$  components, but we know that they have poor precision, the idea is to rescale their normalisation according to data yields in dedicated control regions (CR) that are orthogonal to the signal region (SR) and among each other. After this two components are fixed to data driven yields,  $Z$ +LF component will be estimated from an extra control region. Moreover, dedicated  $Z$ + $X$  control region will be used to estimate a systematic uncertainty of the method, that corresponds to different cut efficiency for data and MC.  $WZ$  contribution to the SR is estimated from MC.

#### Definition of the Control Regions

A brief description of the control regions used for the data driven estimate is given below:

- *Inverted  $d_0$  CR* (enhanced in  $Z$ +HF)  
The standard four-lepton analysis selection is applied to the leading dilepton and the vertex cut is not applied to the quadruplet. The subleading dilepton pair has the  $d_0$  significance selection inverted for at least one lepton in the pair and the isolation

selection is not applied. This control region is enhanced in  $Z+\text{HF}$  and  $t\bar{t}$  since leptons from heavy-flavour hadrons are characterised by large  $d_0$  significance. It will be used for a simultaneous fit of  $Z+\text{HF}$  and  $t\bar{t}$  together with the  $e\mu+\mu\mu$  CR.

- $e\mu+\mu\mu$  CR (enhanced in  $t\bar{t}$ )

In this control region an opposite-charge different-flavour leading dilepton is required, and it must pass the standard four-lepton analysis selections. In this way leading lepton pair cannot be originated from  $Z$  boson decay, that guarantees clean  $t\bar{t}$  CR. The vertex cut is not applied to the quadruplet. The subleading dilepton has neither the impact parameter significance nor the isolation selection applied, while both same and opposite charge leptons are accepted. This control region is dominated by the  $t\bar{t}$  component, and will be also used for the simultaneous fit.

- *Relaxed CR* (high statistics CR used for normalisation)

The standard four-lepton analysis selection is applied to the quadruplet, but  $d_0$  significance and isolation are not applied to the subleading lepton pair. Vertex cuts is neither applied. This CR is not orthogonal to the others and to the SR, therefore it cannot be included into the fit. Nevertheless it has high statistics of all types of the reducible background and it is used for normalisation of the components during the fit.

- *Inverted isolation CR* (enhanced in light-flavour jets)

The standard four-lepton analysis selection is applied to the leading dilepton. The subleading dilepton pair is required to pass the  $d_0$  significance selection but has at least one lepton failing the standard isolation cut. The vertex cut is applied. This control region aims to enhance the  $Z+\text{LF}$  over the  $Z+\text{HF}$  component by imposing the  $d_0$  significance selection. It will be used for the estimate of  $Z+\text{LF}$  after two other components are fixed to the values estimated from the simultaneous fit.

### Simultaneous fit of the $Z+\text{HF}$ and $t\bar{t}$ components

In this method, an unbinned maximum likelihood fit is performed simultaneously to inverted  $d_0$  and  $e\mu+\mu\mu$  control regions in order to estimate  $Z+\text{HF}$  and  $t\bar{t}$  yields. The fit is performed on the leading dilepton mass distribution  $m_{12}$  which provides good separation of the two components, as the  $m_{12}$  distribution of the first one forms  $Z$  peak while the later one is non-resonant. The CRs used for the fit are chosen to be orthogonal both to each other and to the SR. They should have no or minimal contamination from irreducible background such as  $ZZ$  and practically no contamination from the Higgs signal. The  $e\mu+\mu\mu$  is extremely clean  $t\bar{t}$  CR, while the Inverted  $d_0$  one contains both  $Z+\text{HF}$  and  $t\bar{t}$  which are well separated by  $m_{12}$  shape. A complementary relaxed CR contains high statistics of the all reducible background sources. It is meant to be used as the normalisation of the components in the simultaneous fit by expressing the fit results in terms of number of events in this region. Finally, the number of background events in the relaxed CR is extrapolated to the SR using MC based transfer factor. Additional uncertainties on the transfer factor are discussed later in this section.

The  $m_{12}$  distributions in the inverted  $d_0$  and  $e\mu+\mu\mu$  control regions for data and MC simulation of the various backgrounds are shown in Figure 5.7. The corresponding yields are detailed in Table 5.5. From Figure 5.7 it is possible to see a significant mismatch between data and MC, as well as good separation of  $Z+\text{HF}$  and  $t\bar{t}$  contributions.

The  $t\bar{t}$  background shape is modelled by a 2<sup>nd</sup> order Chebyshev polynomial (parameters  $c_0$ ,  $c_1$ ) and has the same shape in all CRs. The parameters of the shape are fitted to  $t\bar{t}$  MC

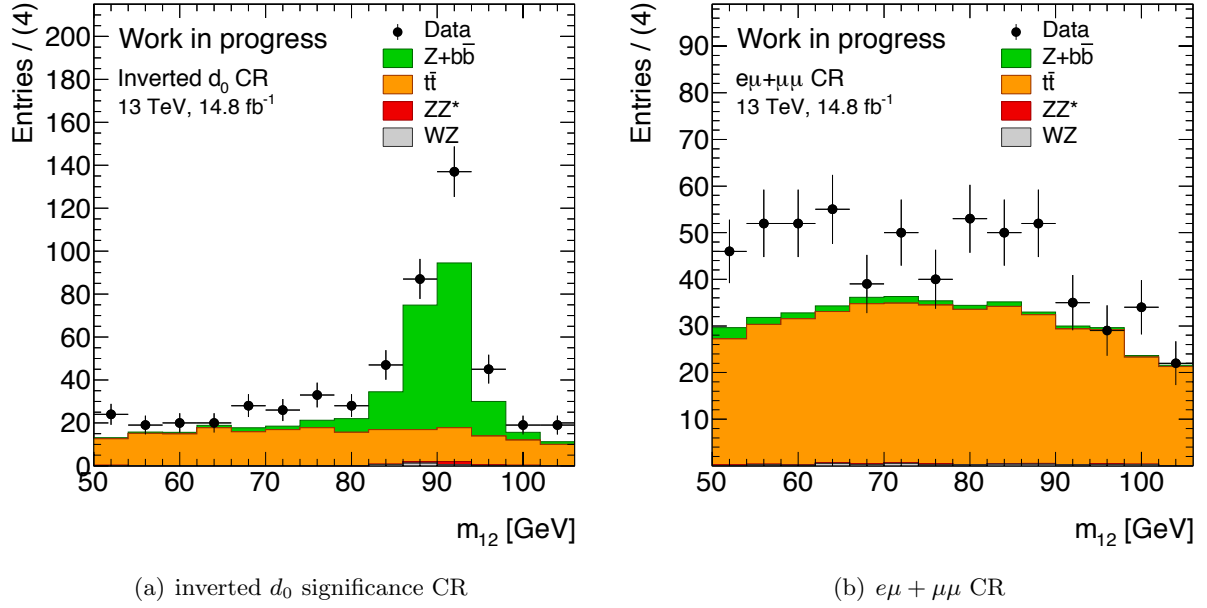


Figure 5.7: The  $m_{12}$  distributions for data and MC-simulated events for different processes for the control regions enhanced in  $Z$ +heavy-flavour jets (left) and  $t\bar{t}$  (right).

Table 5.5: Expected contributions of the various backgrounds (statistical error only) compared to observed yields in data for the control regions used for the simultaneous fit.

Source	inv- $d_0$ CR	$e\mu + \mu\mu$ CR
$Z$ +jets (HF)	$189.9 \pm 3.4$	$14.3 \pm 0.9$
$t\bar{t}$	$207.5 \pm 2.1$	$424.6 \pm 3.2$
$WZ$	$2.6 \pm 0.6$	$3.3 \pm 0.7$
$ZZ$	$3.3 \pm 0.3$	$1.7 \pm 0.2$
Total	$403.3 \pm 4.1$	$443.9 \pm 3.4$
Data	552	609

distributions in the involved CRs. During the data fit the parameters are constrained to MC fitted values using gaussian constraints within a fit error. For  $Z$ +jets shape, a Breit-Wigner function convolved with a Crystal Ball function (parameters  $\mu$ ,  $\alpha$ ,  $\eta_{CB}$ ,  $\sigma_{CB}$  and  $m_Z$ ) is used in the inverted  $d_0$  CR. While in the  $e\mu + \mu\mu$  CR, the  $Z$ +jets component cannot share the same pdf since the leading dilepton cannot be originated from a  $Z$  decay but is instead formed by random opposite-flavour leptons in the event. The  $m_{12}$  distribution for  $Z$ +jets in this CR is therefore non-resonant and is modelled with a first order polynomial.  $Z$ +HF resonant shape parameters are similarly fitted to the MC distribution and constrained during the data fit. The flat  $Z$ +HF shape is fitted to MC distribution and is fixed during the data fit. The shape parameters are shown in Table 5.6

Table 5.6: Shape parameters for the Chebyshev ( $c_0$ ,  $c_1$ ) and Crystal Ball convoluted with a Breit-Wigner ( $\mu_{CB}$ ,  $\alpha_{CB}$ ,  $\eta_{CB}$ ,  $\sigma_{CB}$  and  $m_Z$ ) shapes as estimated from the fit to MC-simulated events. The parameters are used for the data fit with gaussian constraints in their uncertainties.

Shape Parameter	MC fit estimated value
$c_0$	$-0.13 \pm 0.03$
$c_1$	$-0.20 \pm 0.03$
$\mu_{CB}$	$-0.71 \pm 0.12$
$\alpha_{CB}$	$1.3 \pm 1.7$
$\eta_{CB}$	$2.42$ (const.)
$\sigma_{CB}$	$1.87 \pm 0.13$
$m_Z$	$91.18 \pm 0.10$

The contributions from  $WZ$  and  $ZZ$  events that fail the nominal selections and end up in the background control regions are small. Their shapes are chosen to be the same as the one for  $Z$ +HF, since all are originated from  $Z$  boson decay. Their contributions are constrained in the fit to their expected values from MC simulation within their statistical errors.

$Z$ +HF and  $t\bar{t}$  normalisation in each of the two fitted CRs is expressed in terms of the number of events for the given component in the relaxed CR. For each fit CR, the pdf used in the simultaneous fit is defined as:

$$\mathcal{F}_{CR} = \sum_i N_i \cdot f_i^{CR} \cdot \mathcal{M}_i^{CR}, \quad (5.4)$$

where  $i$  is an index running for the various components considered in the fit ( $Z$ +HF,  $t\bar{t}$ ,  $WZ$ ,  $ZZ$ );  $f_i^{CR}$  is the ratio of the contribution for the  $i$ -th background in the given control region over its contribution in the relaxed CR (further called as fraction); and  $\mathcal{M}_i^{CR}$  is the shape model of the  $i$ -th background component that was described before.

The fractions  $f_i^{CR}$ , are obtained from the MC simulation and they are shown in Table 5.7. During the data fit the fractions are constrained to MC based values within statistical uncertainty.

Table 5.7: Fractions of the reducible background of the fit CR with respect to the relaxed CR, estimated with MC simulation and quoted with their statistical errors.

Background	$f = N(\text{inv-}d_0)/N_{OS}$	$f = N(e\mu + \mu\mu)/N_{OS}$
$Z$ +jets (HF)	$0.74 \pm 0.02$	$0.055 \pm 0.004$
$t\bar{t}$	$0.82 \pm 0.01$	$1.68 \pm 0.02$

## MC closure test

The method performance is tested by applying the same simultaneous fit procedure to the MC simulated data that includes all relevant processes. In case the estimated value will be compatible with the simulated ones within the error, it will prove the reliability of the method. The after-fit  $m_{12}$  distributions in the used CR are shown in Figure 5.8. The results from the fit are compared to the MC yield for each fitted background component in the relaxed CR in Table 5.8. The table shows good compatibility of the estimated and the expected yields.

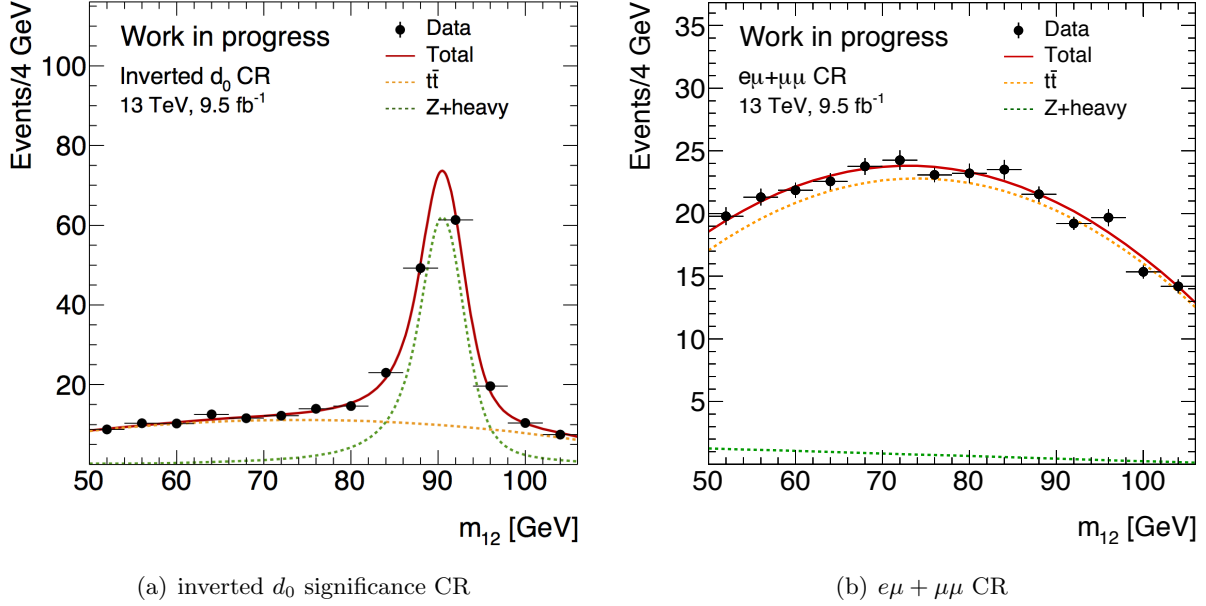


Figure 5.8: Distributions of  $m_{12}$  for MC-simulated data in the two simultaneously fitted control regions, used for the closure test of the fit method. Points with error bars are MC simulated data with statistical uncertainties. The continuous line is the result of the simultaneous fit. The dashed lines denote the components of the fit used to describe the  $Z$ +HF and  $t\bar{t}$  contributions.

Table 5.8: Results of the closure test of the simultaneous fit to the inverted  $d_0$  and  $e\mu + \mu\mu$  CRs using MC-simulated data. The MC yields of the  $Z$ +HF and  $t\bar{t}$  components in the relaxed CR are quoted with their statistical uncertainties and compared to the fit results, quoted also with their fit uncertainties.

Reducible background	MC yield	MC fit estimation
$Z$ +jets (HF)	$169 \pm 3$	$168 \pm 6$
$t\bar{t}$	$167 \pm 2$	$167 \pm 2$
total	$336 \pm 3$	$335 \pm 6$

### Data fit result

Figure 5.9 shows data yield to the CRs as well as the simultaneous fit results. Estimated number of events in the relaxed CR are extrapolated to the SR using MC based transfer factors. The transfer factor is defined as a ratio of the SR and relaxed CR MC yields for the relevant background process. The fit results together with the transfer factors and final SR estimates for  $Z$ +FH and  $t\bar{t}$  are shown in Table 5.9.

### Estimation $Z$ +LF component

$Z$ +LF contribution is estimated from the inverted isolation control region. This control region has significant contribution of the  $Z$ +LF background but also it is contaminated

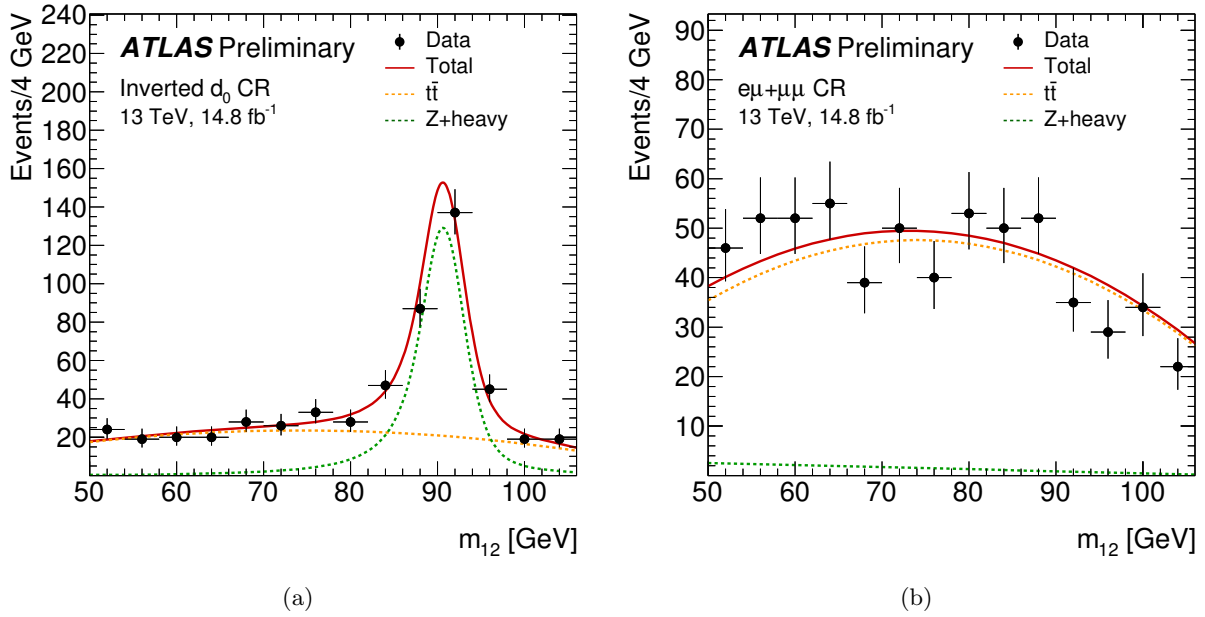


Figure 5.9: Distributions of  $m_{12}$  for data (points with error bars) in two control regions. The data are fitted simultaneously in the the inverted  $d_0$  (a) and the  $e\mu+\mu\mu$  (b) CRs and the result of the fit is shown with the continuous line. The dashed lines correspond to the  $Z$ +HF and  $t\bar{t}$  components of the fit.

with  $Z$ +HF,  $t\bar{t}$ ,  $ZZ$  and  $WZ$ , as it can be seen in Figure 5.10(a). Since there is no MC simulation of the  $Z$ +LF process, we estimate it as a missing component in inverted isolation CR. A fitting procedure is applied to extract this missing component.

$ZZ$  and  $WZ$  yields in the CR are taken from MC simulation, and the shape is assumed to be the same as  $Z$ +HF in the inverted  $d_0$  CR, since both are basically describing  $Z$  resonance.  $Z$ +HF and  $t\bar{t}$  components are rescaled to the data driven estimate, and their shapes are the same as described earlier in this section. All the shape and normalisation parameters except of  $Z$ +LF ones are constrained to their mean values within the errors.

$Z$ +LF is also assumed to share the common  $Z$  peak shape, while its normalisation is a free parameter of interest in the fit. The result of the fit is shown in Figure 5.10(b).

After the fit the estimate in the inverted isolation CR is extrapolated to the SR using  $Z$ +HF MC based transfer factor. The transfer factor derived from different type of the background can be used, since the isolation cut efficiency is similar for these two processes, however an extra systematic uncertainty is taken into account here. The final result of the  $Z$ +LF estimate is shown in Table 5.9.

### Systematic uncertainties

$Z$ +HF and  $t\bar{t}$  estimates in the relaxed CR are extrapolated to the SR using MC based transfer factors, that are basically the  $d_0$ -significance and isolation cut efficiencies. A potential error can arise due to different cut efficiency in data and MC. Another error comes from the  $Z$ +LF transfer factor used for extrapolation from the inverted isolation CR to the SR. In this case  $Z$ +HF MC based transfer factor is used.

These uncertainties can be estimated by the efficiency studies made in dedicated  $Z+\mu$  CR. This CR has rather close topology to the SR, but contains much higher statistics since only 3 leptons are required. It allows to use inclusive  $Z$ +jets Sherpa MC sample that does not have a flavour bias. The  $m_{12}$  distribution in the  $Z+\mu$  CR is shown in Figure 5.11 defined

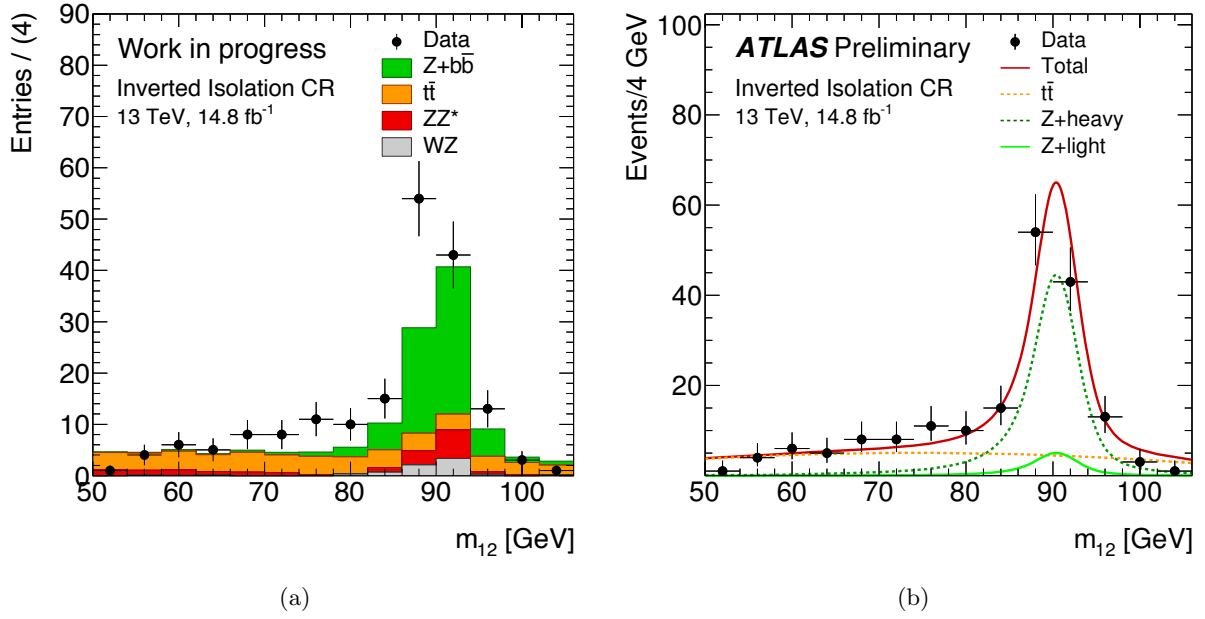


Figure 5.10: The  $m_{12}$  distributions for data and MC-simulated events for different processes for the inverted isolation control region (a), and after fit  $m_{12}$  distribution in this CR (b).

Table 5.9: Final  $\ell\ell + \mu\mu$  background estimate is shown. Second column is showing estimated background yield to relaxed CR for  $Z$ +HF and  $t\bar{t}$ , while showing yield estimate in the inverted isolation CR for  $Z$ +LF. The second column shows the corresponding transfer factors from the corresponding CRs to the SR with MC statistical uncertainty. The last column shows the estimate of the SR yields for the reducible  $\ell\ell + \mu\mu$  background with both statistical and systematical uncertainties.

Background type	Data fit	Extrapolation factor [%]	SR yield
$Z$ +jets (HF)	$348 \pm 29$	$0.60 \pm 0.04$	$2.1 \pm 0.17 \pm 0.13$
$t\bar{t}$	$351 \pm 14$	$0.21 \pm 0.03$	$0.74 \pm 0.03 \pm 0.09$
$Z$ +jets (LF)	$10 \pm 15$	$2.3 \pm 0.3$	$0.24 \pm 0.35 \pm 0.03$
$WZ$	(MC-based estimation)		$0.63 \pm 0.31$

below:

- $Z+\mu$  CR (used to estimate the systematics)

The selection requires a reconstructed  $Z$  candidate that fulfils selection criteria as for the leading  $Z$  candidate in the SR. An event is asked to contain an addition muon with  $p_T > 5$  GeV that is well separated from the leptons in the  $Z$  candidate.  $J/\psi$  cut is applied similarly as for the SR. Trilepton trigger is not used for this CR in order not to bias the quality of the third lepton. Events passing the SR selection are vetoed.

The light-flavour component in the CR can be enhanced by applying a cut on the momentum balance between the  $p_T$  measurements in the inner detector and the muon spectrometer ( $\Delta p_T/p_T = (p_T^{\text{ID}} - p_T^{\text{MS}})/p_T^{\text{ID}}$ ). The momentum balance distribution for the third lepton before the isolation and impact parameter cut is shown in Figure 5.12(a). The shoulder that appears at large values of the momentum balance variable is mainly coming from in-flight decays of light-flavour mesons (i.e. muons from  $\pi$  and  $K$  decays). By applying a  $\Delta p_T/p_T > 0.1$  cut it is possible to build the CR where 71% of the events are coming from light-flavour jets and 29% from heavy-flavour jets. Contributions from  $WZ$  and  $ZZ$  are below 1% and are subtracted from the efficiency calculations using MC simulation.



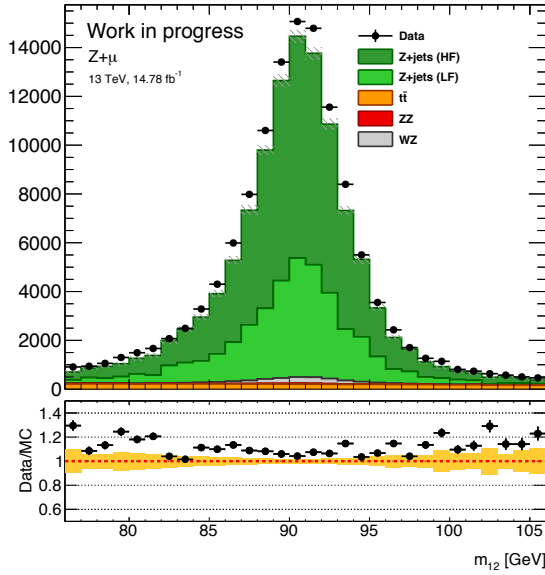


Figure 5.11: Invariant mass of  $Z$  candidates in selected  $Z+\mu$  events in data (points with errors) and MC-simulated background samples (stacked histograms). The uncertainty shown for the MC samples is statistical only.

The heavy-flavour component can be enhanced by inverting the  $d_0$ -significance cut on the additional muons in  $Z+\mu$  events (Figure 5.12(b)). In such a CR the fraction of the heavy flavour events is 90% while the other 10% are coming from the light-flavour events. The expected contribution of leptons from dibosons is negligible and is subtracted with MC simulation from the efficiency calculations.

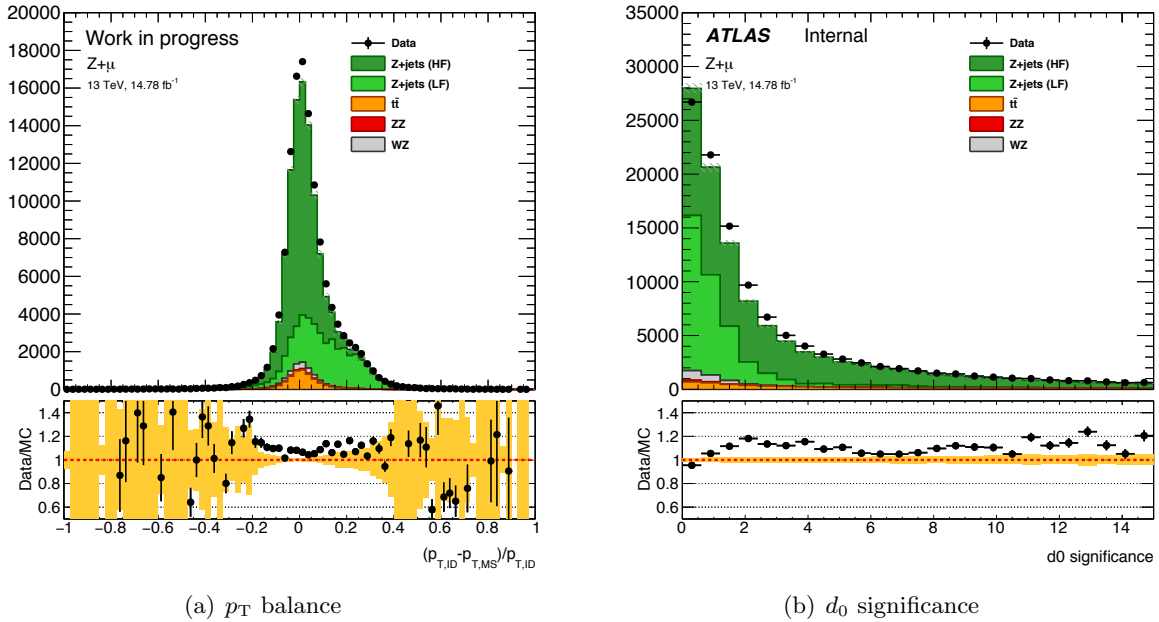


Figure 5.12: Distribution of the  $p_T$  balance (a) and the  $d_0$  significance (b) for additional muons in  $Z+\mu$  events for data and MC simulation.

The CR enhanced in heavy flavour component is used to define the isolation efficiency for the MC and data for the heavy flavour fakes, while the  $d_0$ -significance efficiency is determined from the nominal  $Z+\mu$  CR. The cut efficiencies are shown in Table 5.10. Both the isolation and the  $d_0$  significance cut efficiencies are found to be compatible within one

sigma of statistical uncertainty in data and MC, therefore no additional systematics due to cut mismodelling in MC were assigned for the  $Z$ +HF estimate in the SR. The same conclusion is drawn for the  $t\bar{t}$  background since it has a composition similar to  $Z$ +HF final state:: two real leptons and heavy flavour fakes. The uncertainty on the  $Z$ +LF estimate in the SR can be deduced by comparing the isolation efficiencies for the  $Z$ +HF MC events and data events in the light flavour CR. These efficiency for the last one can be also found in Table 5.10. The difference between the efficiencies is 10%, and this value is assumed as a systematic uncertainty on  $Z$ +LF estimate in the SR.

Table 5.10: Efficiency of isolation and impact parameter selections for background muons selected in  $Z+\mu$  events.

Cut efficiency	Data [%]	MC [%]
$Z+\mu$ inclusive		
$d_0$ significance	$63.5 \pm 0.4$	$64.9 \pm 1.3$
$Z+\mu$ enhanced in HF		
isolation	$16.6 \pm 0.2$	$15.9 \pm 0.5$
$Z+\mu$ enhanced in LF		
isolation	$14.3 \pm 0.4$	—

#### 5.4.2 $\ell\ell + ee$ reducible background

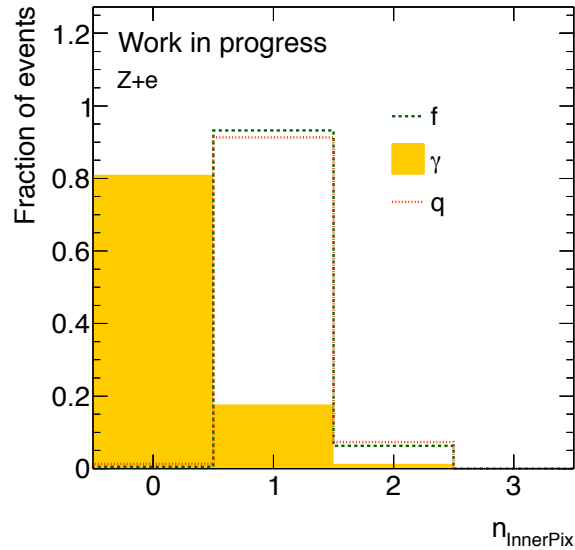
The estimate of the  $\ell\ell+ee$  reducible background is obtained using a  $3\ell+X$  control region with three leptons passing the full analysis selection, while for the lepton candidate that completes the quadruplet the  $d_0$ -significance, the isolation and the vertex cuts are not applied.

The electron background is originating from three processes and it is classified accordingly in the method. The major fake contribution is coming from light jets with energy deposit in the calorimeter ( $f$ ). Electrons coming from photon conversions or FSR ( $\gamma$ ) and from semileptonic decays of heavy quarks ( $q$ ) are contributing a considerable amount fakes as well. The last process is assumed to be reliably simulated in MC, therefore it is not rescaled with data driven approach. Each background type has different cut efficiency, therefore, the method is targeting to disentangle these three components with suitable discriminating variable. In MC simulation, the actual origin of the fake can be extracted from truth information. For data, the components can be distinguished using the  $n_{InnerPix}$  variable that shows a number of innermost (or next-to-innermost in case of dead area for the first detector) pixel hits. The  $n_{InnerPix}$  variable provides discrimination for  $\gamma$  over  $f$  and  $q$ , since photons mostly populate  $n_{InnerPix} = 0$  while it is not the case for the other types. Since  $q$  component is taken from MC simulation and is not scaled in the data driven estimate,  $n_{InnerPix}$  variable provides reasonable discrimination of the all components. Different processes are scaled to data using template hit of  $n_{InnerPix}$  variable in the  $3\ell+X$  CR.

A complementary control region denoted as  $Z+X$  is used to estimate an efficiency needed to extrapolate the yields from the relaxed electron requirements of “X” for each of the background components to the full electron identification and the isolation cuts used in the signal region. The description of the efficiency estimation is given in Ref. [115]. The same CR is used to extract the  $n_{InnerPix}$  templates (Figure 5.13) for each process.

#### Control Regions definition

A brief description of the control regions used for the data driven estimate is given be-



(a)

Figure 5.13: Templates used in the  $3\ell+X$  fit to  $n_{InnerPix}$  for the different sources of background ( $\gamma$ ,  $f$ ), extracted from MC simulation in the  $Z+X$  control sample. The  $q$  component (real electrons from heavy-flavour decays) is extracted from  $3\ell+X$  events.

low:

- $3\ell+X$  CR (used for the fit)

All the cuts are applied to the three leptons of the quadruplet, while the lowest  $E_T$  electron in the subleading lepton pair is only passing relaxed identification criteria. In specific, a modified *Loose* working point is used in which the likelihood identification cut and the  $n_{InnerPix}$  requirement are removed so that only track quality cuts are applied. The lepton  $d_0$ -significance and the  $4\ell$  vertex cut are applied too but the isolation selection is not.

- $Z+X$  CR (used for template and efficiency extraction)

The selection requires a reconstructed  $Z$  candidate that fulfils selection criteria as for the leading  $Z$  candidate in the SR. Moreover, an additional “ $X$ ” electron with similar properties as in  $3\ell+X$  CR is required. Trilepton trigger is not used for this CR.

## Data fit result

The result of the template fit of  $n_{InnerPix}$  data distribution in the  $3\ell+X$  CR is shown in Figure 5.14. The final SR estimate of the  $\ell\ell+ee$  background is shown in Table 5.11.

Table 5.11: Final  $\ell\ell+ee$  background estimate is shown. The SR yields for the  $f$  and  $\gamma$  components are quoted with statistical uncertainty as returned from the data fit and systematic uncertainty of the efficiency and the fit. For the  $q$  component that is not fitted in the data, the SR yield is taken directly from MC simulation and is quoted with its total uncertainty.

Background type	SR yield
$f$	$2.62 \pm 0.08 \pm 0.36$
$\gamma$	$0.55 \pm 0.08 \pm 0.04$
$q$ (MC-based)	$2.50 \pm 0.77$

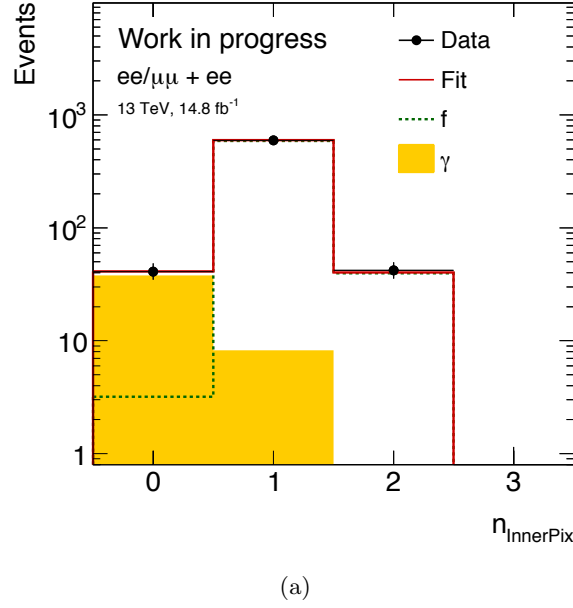


Figure 5.14: Data  $n_{InnerPix}$  distribution in the  $3\ell+X$  CR and result of the template fit.

### 5.4.3 Control plots

In order to validate the background estimate an extra CR was used. The CR definition is similar to the Relaxed CR described in Section 5.4.1 but with subleading lepton pair allowed to have either same or opposite signs. The MC distribution after data driven scaling shows good compatibility with data, as it can be seen from Figure 5.15.

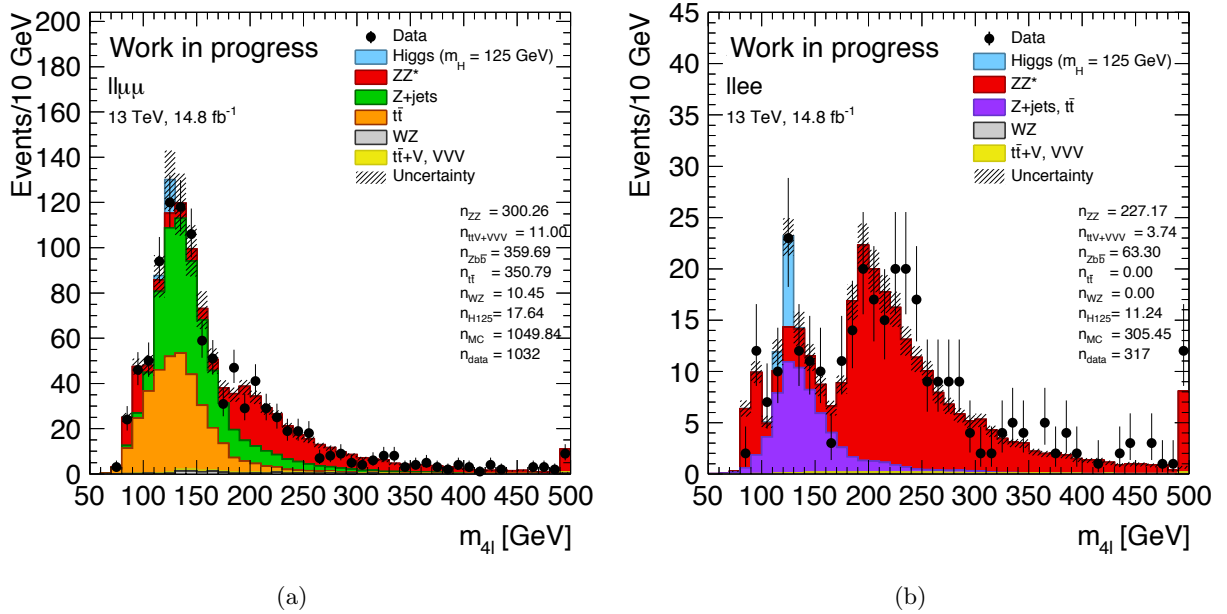


Figure 5.15: Invariant mass distributions of the lepton pairs in the control sample defined by a  $Z$  boson candidate and an additional same-flavour lepton pair. The sample is divided according to the flavour of the additional lepton pair. In (a), the  $m_{4l}$  distributions is presented for  $\ell\ell(\mu^+\mu^-/e^+e^-) + \mu\mu$  events. In (b), the  $m_{4l}$  distributions is presented for  $\ell\ell(\mu^+\mu^-/e^+e^-) + ee$  events. Isolation requirements are applied to the first lepton pair only. The MC distributions are normalised to the data-driven background estimations. The last bin contains the integral of the overflow.

#### 5.4.4 Background $m_{4\ell}$ shape modelling

The Standard Model  $ZZ$  production is going through two processes  $qq \rightarrow ZZ$  and  $gg \rightarrow ZZ$ , that are treated separately. In both cases the  $m_{4\ell}$  shape is taken from MC. This background has a slowly dropping high mass tail that suffers from limited statistics of the MC samples. A smooth shape of the high mass background tail can be achieved by using an analytical background model fitted to the MC distribution. Moreover, an advantage of this method comparing to the previously used smoothing approach is a possibility to incorporate the shape uncertainty due to MC statistics as a single nuisance parameter in the background model.

Both  $qq \rightarrow ZZ$  and  $gg \rightarrow ZZ$  shapes can be described by the same empirical analytical function in all final states ( $4\mu$ ,  $4e$ ,  $2\mu 2e$  and VBF):

$$f_{qqZZ/ggZZ}(m_{4\ell}) = (f_1(m_{4\ell}) + f_2(m_{4\ell})) \times H(m_{4\ell} - m_0) \times C_0 + f_3(m_{4\ell}) \times H(m_0 - m_{4\ell}) \quad (5.5)$$

where:

$$\begin{aligned} f_1(m_{4\ell}) &= \exp(a_1 + a_2 \cdot m_{4\ell}) \\ f_2(m_{4\ell}) &= \left(\frac{1}{2} + \frac{1}{2} \operatorname{erf}\left(\frac{m_{4\ell} - b_1}{b_2}\right)\right) \times \frac{1}{1 + \exp\left(\frac{m_{4\ell} - b_1}{b_3}\right)} \\ f_3(m_{4\ell}) &= \exp(c_1 + c_2 \cdot m_{4\ell} + c_3 \cdot m_{4\ell}^2 + c_4 \cdot m_{4\ell}^{2.7}) \\ C_0 &= \frac{f_3(m_0)}{f_1(m_0) + f_2(m_0)} \end{aligned} \quad (5.6)$$

The first part of the function  $f_1$  takes care of the flat low mass part of the spectrum where one of  $Z$  bosons is off-shell, while  $f_2$  models  $ZZ$  threshold around  $2 \times m_Z$  and  $f_3$  describes the high mass tail. Transition between low mass and high mass parts of the function is done by the Heaviside step function  $H(x)$  around  $m_0 = 240$  GeV for  $qq \rightarrow ZZ$  and  $m_0 = 265$  GeV for  $gg \rightarrow ZZ$ . Continuity of the function around  $m_0$  is ensured by normalisation factor  $C_0$  that is applied to the low mass part.  $a_i$ ,  $b_i$  and  $c_i$  are the shape parameters that will be fixed from MC fit for each final state. Four-lepton invariant mass distributions with projected shape model for  $qq \rightarrow ZZ$  and  $gg \rightarrow ZZ$  are shown in Figures 5.16 and 5.17. The quality of the background shape fit is controlled in terms of  $\chi^2/NDF$ . For all the categories the  $\chi^2/NDF$  varies from 0.8 to 1.2, that shows good compatibility of the model and the MC distribution. Additional systematics on the background shape due to MC statistical error is taken in to account as described in Section 5.6.

The reducible background consists of three components:  $Z+HF$ ,  $t\bar{t}$  and  $Z+LF$ . The  $m_{4\ell}$  shape for the first two is taken from MC in the signal region. Since there is no available MC statistics for the last one, it's shape was deduced from data distribution in the  $3\ell+X$  CR for  $\ell\ell + ee$  and in the same-sign CR (standard SR selection, without requiring isolation and  $d_0$ -significance cuts for subleading lepton pair, and the subleading lepton pair should have same sign leptons) for  $\ell\ell + \mu\mu$ , that are highly populated with  $Z+LF$  background. All three shapes are smoothed using kernel estimation (RooKeysPDF [118]), and further added according to relative fractions measured in data. Systematic uncertainty due to reducible background composition is estimated by varying the fractions of different components. The resulting shape is shown in Figure 5.18. It can be seen that the reducible background is contributing only to a low mass part of the  $m_{4\ell}$  spectrum.

The  $m_{4\ell}$  shapes of other irreducible background such as tri-boson and  $t\bar{t}+V$  is obtained

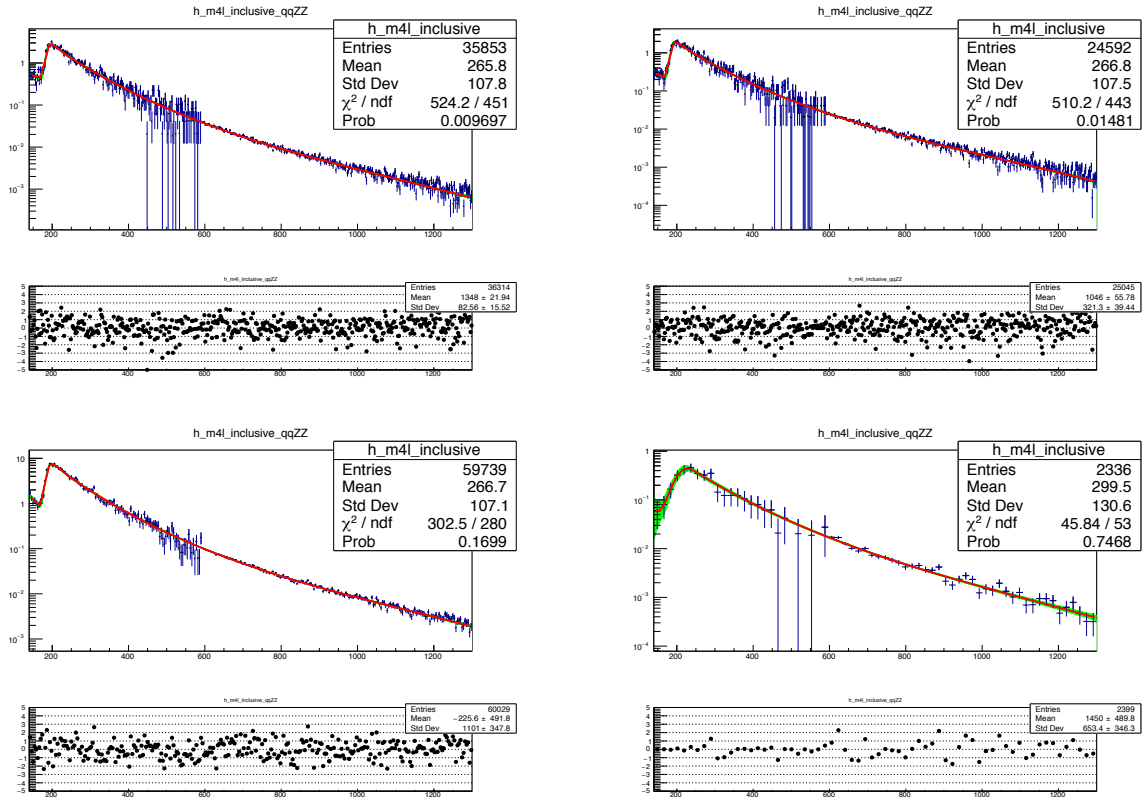


Figure 5.16: Distributions of  $m_{4\mu}$  invariant mass fit projection of the  $qq \rightarrow ZZ$  background samples in four categories ( $4\mu$ ,  $4e$ ,  $2\mu 2e$  and  $VBF$ ). The green band shows fit uncertainty.

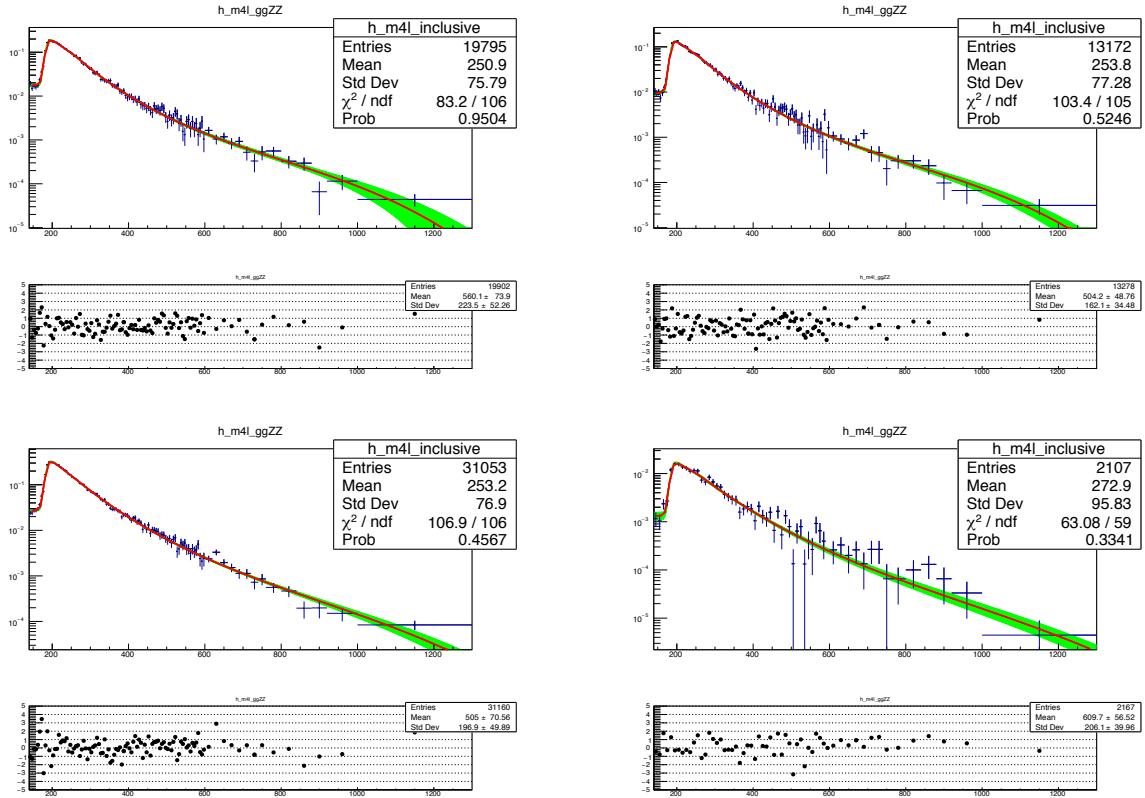


Figure 5.17: Distributions of  $m_{4\mu}$  invariant mass fit projection of the  $gg \rightarrow ZZ$  background samples in four categories ( $4\mu$ ,  $4e$ ,  $2\mu 2e$  and  $VBF$ ). Green band shows fit uncertainty.

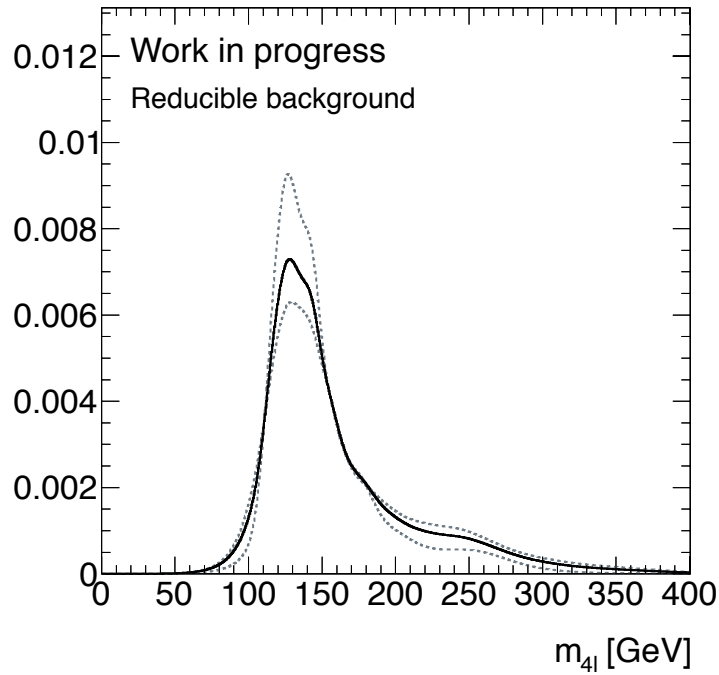


Figure 5.18: Invariant mass shape of reducible backgrounds ( $Z$ +jets,  $t\bar{t}$ ) after smoothing, shown in the full mass range for all channels combined. The solid line is for the nominal shape and the dashed lines show the variations obtained by varying the contributions of  $t\bar{t}$  and light-flavour jet background. The distributions are normalised to unit area.

from MC simulation. This shape is shown in Figure 5.19. Both for the reducible and the tri-boson backgrounds, a big part of the yield is falling below the lower bound of the mass range of interest, therefore only the yield above 140 GeV is taken into account.

#### 5.4.5 Background summary

The dominant source of the background is the SM  $ZZ$  production, for which both the normalisation and the shape are taken from MC. An analytical model used for the  $ZZ$  shape allows to reduce the effect of the statistical fluctuations in the high mass tail of the MC distribution and to propagate the corresponding uncertainty into a single nuisance parameter. The second largest contribution is coming from tri-boson background. The tri-boson normalisation is taken from MC, while the shape is modelled with smoothed MC distribution. The reducible background is quite small, and its normalisation is estimated using data driven methods. The shape is modelled by smoothed MC distribution in the SR or the CR for different processes.

Both the tri-boson and the reducible backgrounds were estimated in a mass region that goes below the mass range interesting for the heavy Higgs search. It is done in order to have a common estimate of these background between the heavy Higgs and the SM Higgs analyses. Besides the heavy Higgs search, this background estimate was also used for the measurement of the SM Higgs boson properties using the same dataset [119].

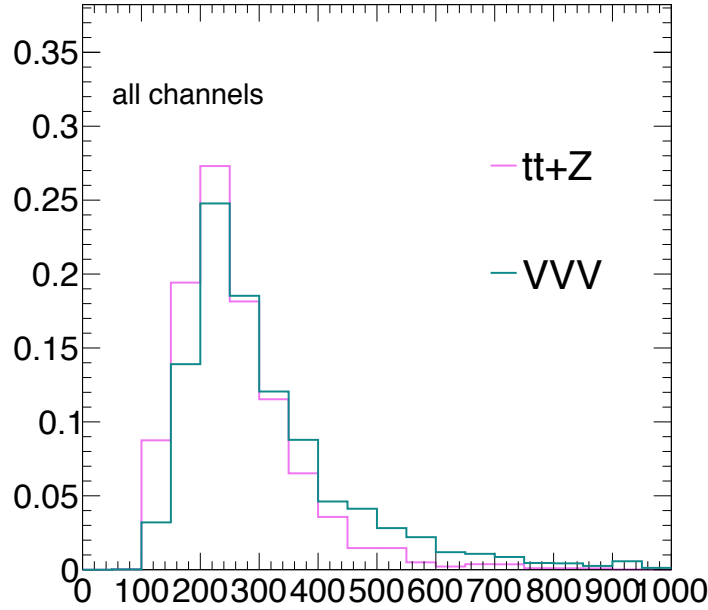


Figure 5.19:  $m_{4\ell}$  shape for the tribosons and  $t\bar{t}+V$  background. Distributions are normalised to unit area.

## 5.5 Signal modelling

This analysis explores the hypothesis of an additional heavy Higgs boson with narrow width. Within the narrow width approximation (NWA) the heavy Higgs boson is modelled by a Breit-Wigner resonance with a fixed width of 4.07 MeV. The choice of the width is arbitrary, since a precise value is not of great importance as long as the width is significantly smaller than the experimental resolution. The narrow width assumption is favoured since it covers significant phase space of the tested BSM theoretical models, while the interference of the heavy Higgs ( $H$ ) with the  $gg$ -initiated  $ZZ$  continuum is negligible in this scenario.

The MC samples used to model the signal are described in Section 5.2.2. There are the samples simulated for signal masses from 200 to 1000 GeV in a step of 100 GeV both for ggF and VBF production modes. The signal acceptance is calculated for available MC samples and interpolated for other mass values, as described in Section 5.5.1.

The NWA signal  $m_{4\ell}$  shapes are described with an analytical function that is a sum of a Crystal Ball and a Gaussian distributions, while the shape parameters are fitted to the MC distribution. The description of the signal shape model is given in Section 5.5.2.

### 5.5.1 Acceptance

The signal acceptance is defined as the fraction of generated  $H \rightarrow ZZ \rightarrow 4\ell$  signal events (where  $\ell = \mu, e$  only, taus are not considered since they are mostly cut away by the event selection) that are passing the reconstruction-level event selection for each analysis category, as defined in Section 5.3. By definition this includes both the phase space acceptance and the detector efficiencies. The acceptance is defined separately for each production mode and category. It is calculated for the mass points where the MC simulation is available



and parametrised by a  $2^{nd}$  order polynomial in  $m_H$  in order to interpolate for other mass hypotheses. The degree of the polynomial was chosen to ensure a smooth shape across the full  $m_H$  range, which well describes the simulated points but does not overfit statistical fluctuations.

The acceptance functions for ggF and VBF production modes is shown in Figure 5.20, while the parameters are given in Table 5.12. A systematic uncertainty of approximately 1% was assigned based on the deviation of the individual mass points from the best fit line in each channel.

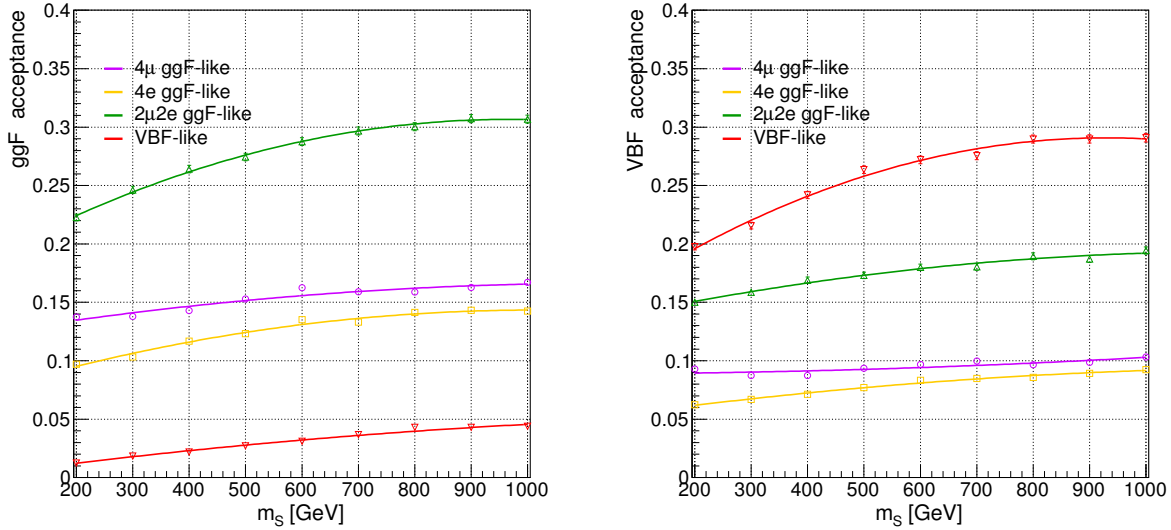


Figure 5.20: The signal acceptance vs  $m_S$  for the ggF (left) and VBF (right) production. For each production mode, acceptance into the four categories (ggF-like  $4\mu$ , ggF-like  $4e$ , ggF-like  $2\mu 2e$ , VBF) are parameterized and fit separately. The fit parameters are shown in Table 5.12.

Table 5.12: The polynomial parameters for signal acceptance for each production mode and each category.

Category	$a_0$	$a_1[/math>]/GeV]$	$a_2[/math>]/GeV2]$
ggF production mode			
ggF-like $4\mu$	1.279e-01	7.335e-05	-2.668e-08
ggF-like $4e$	7.088e-02	1.489e-04	-7.659e-08
ggF-like $2\mu 2e$	1.839e-01	2.705e-04	-1.428e-07
VBF-like	2.056e-03	7.462e-05	-2.687e-08
VBF production mode			
ggF-like $4\mu$	9.472e-02	-2.041e-06	1.300e-08
ggF-like $4e$	5.005e-02	6.893e-05	-2.764e-08
ggF-like $2\mu 2e$	1.354e-01	1.139e-04	-5.280e-08
VBF-like	1.466e-01	3.220e-04	-1.703e-07

### 5.5.2 Shape modeling

The  $m_{4\ell}$  shape of the signal in NWA is described with an empirical analytical function. It is given by the sum of Crystal Ball (CB) and Gaussian (Gauss) distributions that share the same mean value. This function was found to be the simplest one which can describe the  $m_{4\ell}$  shape in all the decay channels within the interesting mass range.

An equation for the signal shape model is given as:

$$f_{\text{signal}}(m_{4\ell}) = f_{CB} \cdot CB(m_{4\ell}; \mu, \sigma_{CB}, \alpha_{CB}, n_{CB}) + (1 - f_{CB}) \cdot \text{Gauss}(m_{4\ell}; \mu, \sigma_{\text{Gauss}}) \quad (5.7)$$

where  $f_{CB}$  is a parameter that controls relative normalisation of CB and Gaussian;  $\mu$  is a common mean value that is shared by both distributions;  $\sigma_{\text{Gauss}}$ ,  $\sigma_{CB}$ ,  $\alpha_{CB}$  and  $n_{CB}$  are standard parameters of the distributions.

All the parameters of the shape except the  $n_{CB}$  are fitted to the MC distribution, while the  $n_{CB}$  is fixed during the fit since it is highly correlated with  $\alpha_{CB}$ . The fixed value for  $n_{CB}$  is obtained from raw fit with all parameters free by averaging  $n_{CB}$  for different mass points within a decay channel.

The shape parameters are extracted from the MC fit for all simulated mass points (from 200 to 1000 GeV with a step of 100 GeV). The shape is estimated separately for each lepton flavour decay channel:  $4\mu$ ,  $4e$  and  $2\mu 2e + 2e 2\mu$ . The channels  $2\mu 2e$  and  $2e 2\mu$  are combined, considering that for  $m_{4\ell}$  above 180 GeV, both  $Z$  bosons coming from the Higgs decay are mostly on-shell, therefore, separation of this two channels would be artificial.

The distributions of the four-lepton invariant mass  $m_{4\mu}$ ,  $m_{4e}$  and  $m_{2\mu 2e + 2e 2\mu}$ , together with the shapes extracted from the fit for the available mass points are presented in Figures 5.21, 5.22 and 5.23. The quality of the fit is estimated by computing the Pearson's  $\chi^2$  [120], which values are summarised in Table 5.13. Overall, a good fit quality is obtained in the whole mass range.

The signal model parameters extracted from the fit of the signal MC samples for all the channels can be found in Figures 5.24, 5.25 and 5.26 for each mass point. All the parameters show a dependence on the  $m_{4\ell}$  invariant mass. This dependence is described using different order polynomial functions for each of the parameters.

In order to validate the procedure, the analytical shape with interpolated parameters is compared to the MC distribution for all mass points previously used in the fit. The result of the comparison can be found in Figures 5.29, 5.30, and 5.31, while the numerical estimate of the shape compatibility is given in Table 5.14 in terms of Pearson's  $\chi^2$ . The test shows that the analytical shape with interpolated parameters precisely describes the MC  $m_{4\ell}$  distribution.

Possible bias on the extracted signal yield due to the signal parametrisation with respect to the yield in simulation was studied. A yield closure test was performed by comparing signal yield extracted from the fit and from a simple count. Figure 5.27 shows  $\frac{N_{\text{Rec}} - N_{\text{Fitted}}}{N_{\text{Fitted}}}$ , where  $N_{\text{Rec}}$  is the number of reconstructed events and  $N_{\text{Fitted}}$  is the number of events obtained from the fit. The errors shown in the fit are statistical only. The extracted bias on the signal yield is below 1% for all channels, therefore, the bias was considered as negligible. The effect of the experimental systematic uncertainties on the signal shape is discussed in Section 5.6.1.

In Figure 5.28 the signal template distributions are shown for  $4\mu$ ,  $4e$  and  $2e 2\mu + 2\mu 2e$  final states. The shapes shown are obtained by interpolating the Crystal-Ball and Gaussian parameters between the available MC mass points, as described above.

The VBF category is inclusive in lepton flavour decay channels. It was found that each separate flavour decay channel has the same signal shape both in ggF and VBF categories.

Therefore, the signal shape in the VBF category is given as a sum of the three previously described shapes  $m_{4\mu}$ ,  $m_{4e}$  and  $m_{2\mu 2e+2e2\mu}$  with proper relative normalisation.

The signal shape in each categories was found to be independent from the production mode [121], therefore, the same shape is used for ggF and VBF production modes. Moreover, this signal modelling provides a good description of the  $m_{4\ell}$  shape of the SM Higgs boson as well, therefore it can be used for the SM Higgs boson mass measurement.

Table 5.13: Summary of the Pearson's  $\chi^2$  values obtained when estimating the parameters of Equation 1 with analytical fits to ggF MC distributions in ggF category.

$\chi^2$	$4\mu$	$4e$	$2\mu 2e$
200 GeV	1.2	1.2	1.3
300 GeV	1.8	1.0	1.1
400 GeV	1.5	1.1	1.5
500 GeV	0.9	1.4	0.9
600 GeV	1.6	1.0	1.2
700 GeV	1.4	1.1	1.6
800 GeV	1.2	1.3	1.0
900 GeV	1.5	1.0	1.3
1000 GeV	1.2	0.7	1.2

Table 5.14: Quality of the MC  $m_{4\ell}$  distribution description by the analytical signal shape with interpolated parameters, expressed in terms of Pearson's  $\chi^2$ .

$\chi^2$	$4\mu$	$4e$	$2\mu 2e$
200 GeV	1.2	1.3	1.4
300 GeV	1.8	1.2	1.3
400 GeV	1.0	1.4	1.5
500 GeV	1.9	1.5	1.2
600 GeV	1.2	1.2	1.3
700 GeV	1.6	1.4	1.7
800 GeV	1.5	1.6	1.3
900 GeV	1.3	1.3	1.5
1000 GeV	1.5	1.2	1.4

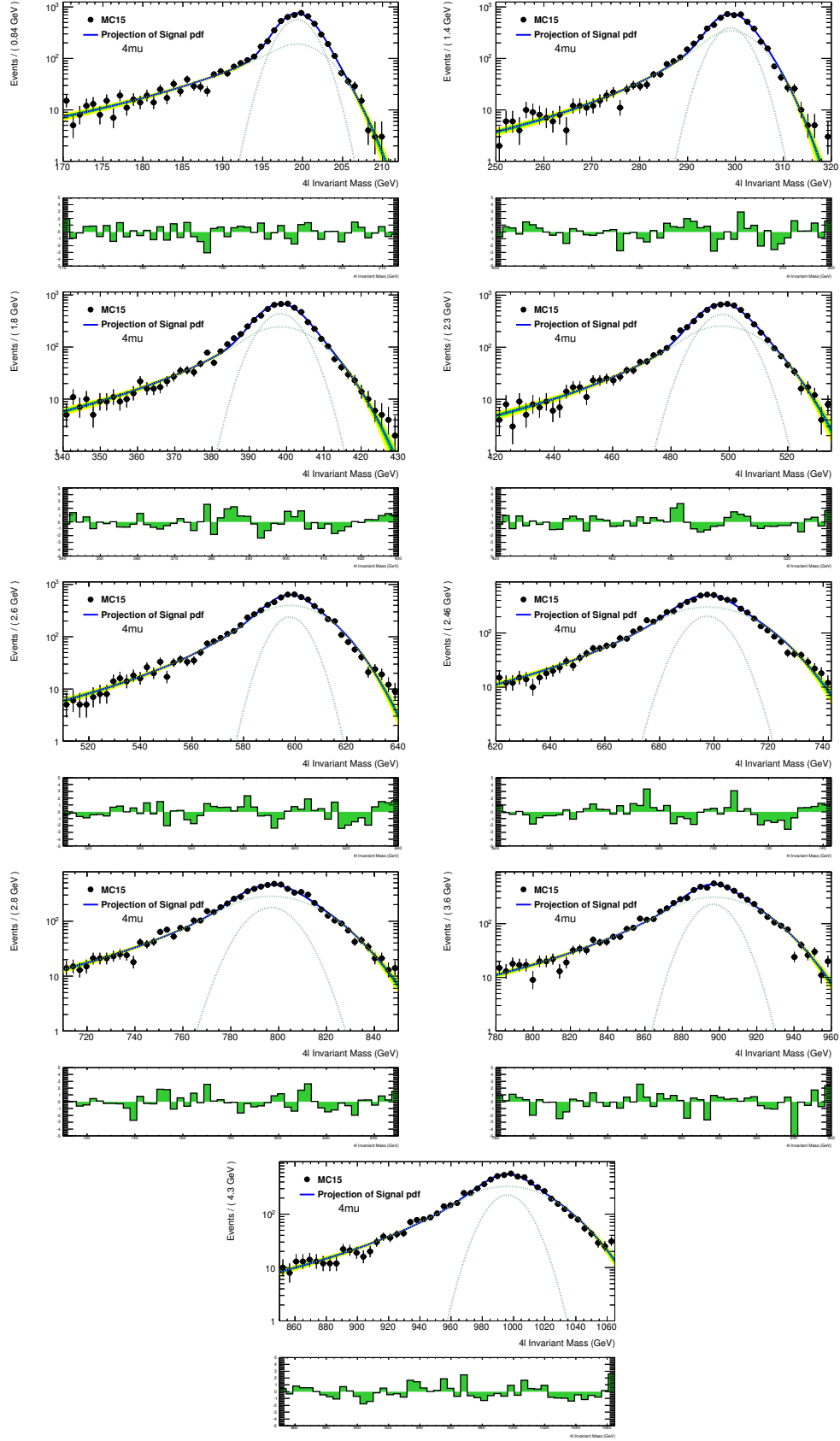


Figure 5.21: Distributions of  $m_{4\mu}$  invariant mass fit projection of the signal samples from mass of 200 to 1000 GeV in steps of 100 GeV.

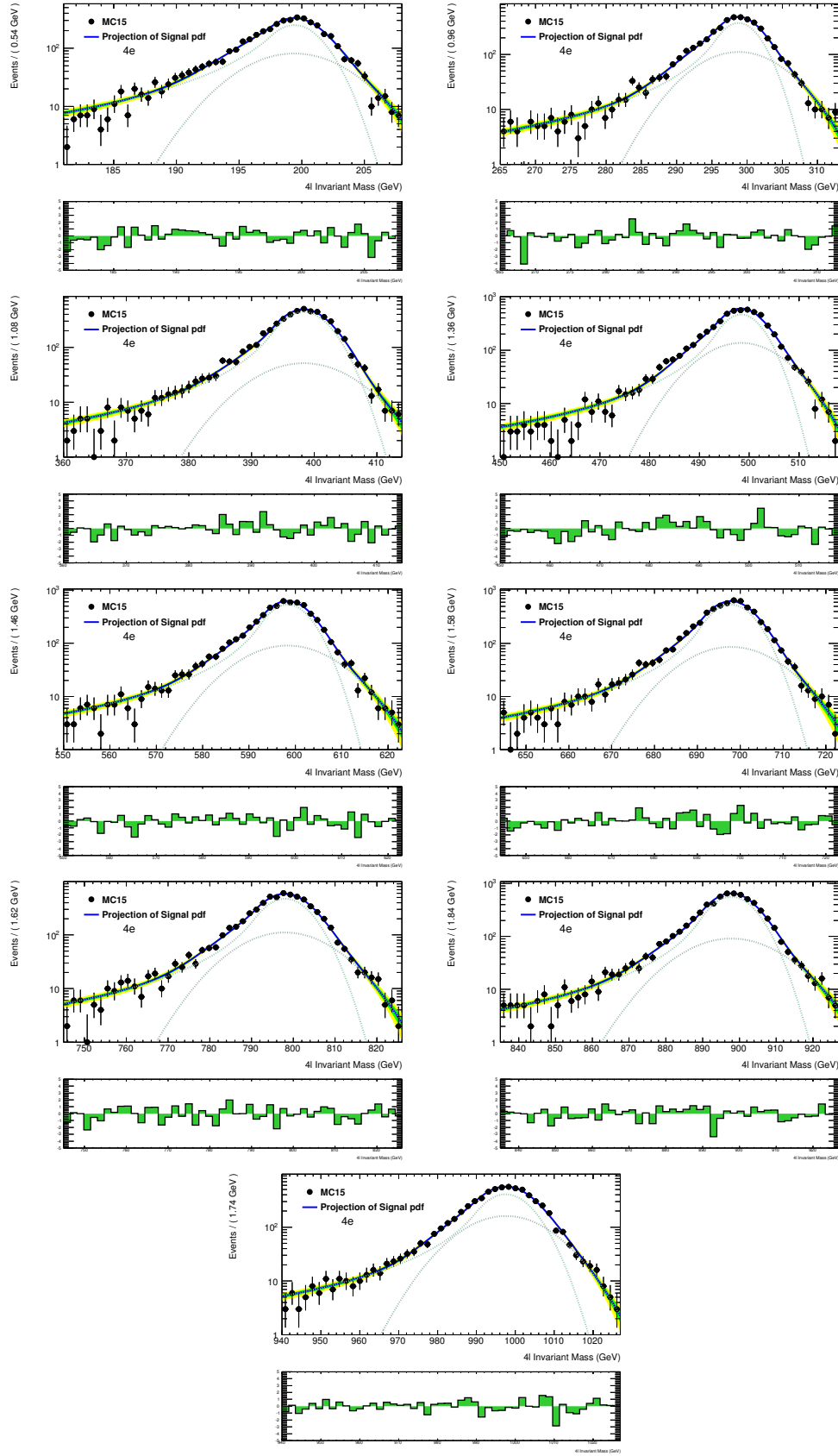


Figure 5.22: Distributions of  $m_{4e}$  invariant mass fit projection of the signal samples from mass of 200 to 1000 GeV in steps of 100 GeV.

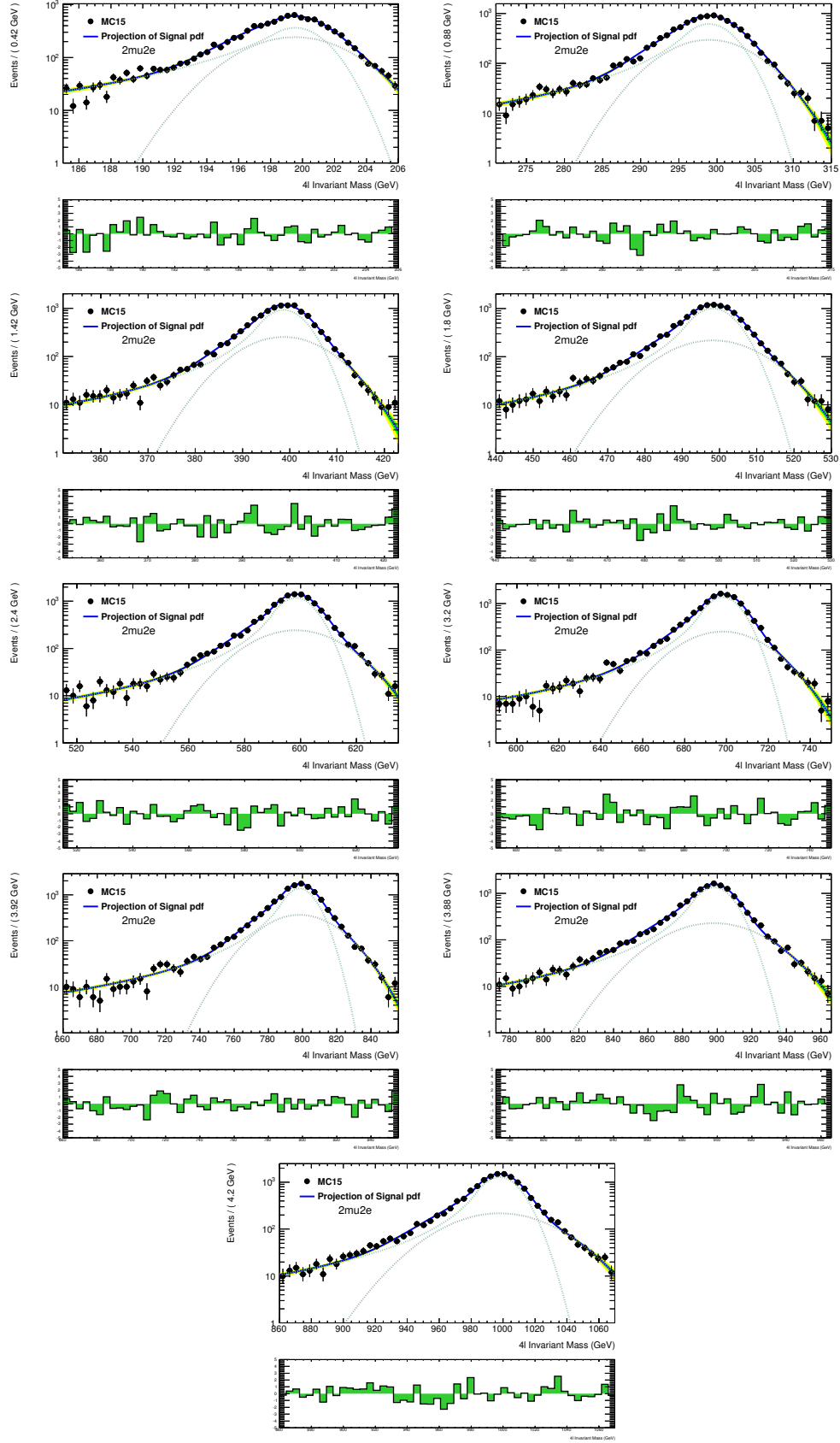


Figure 5.23: Distributions of  $m_{2\mu 2e}$  invariant mass fit projection of the signal samples from mass of 200 to 1000 GeV in steps of 100 GeV.

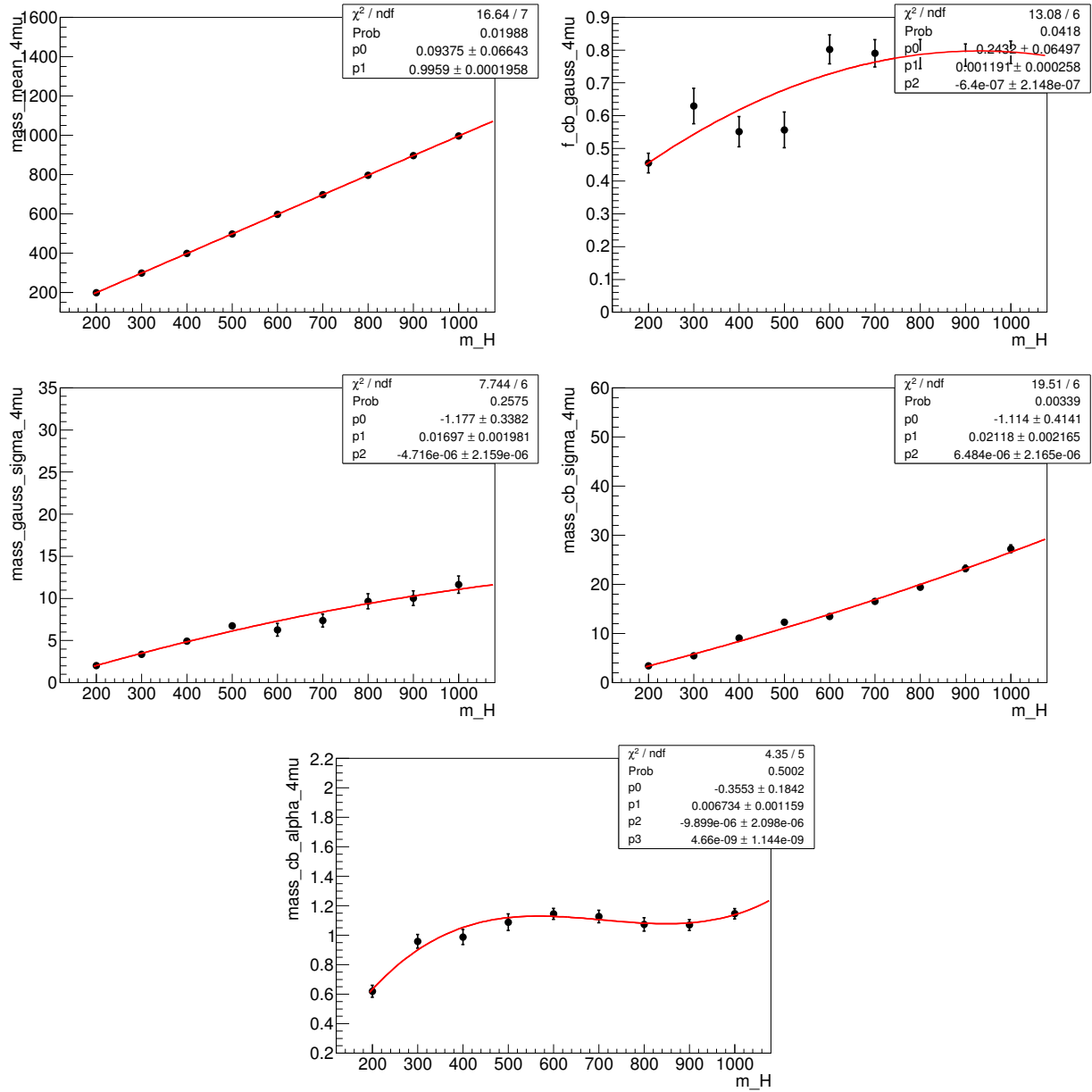


Figure 5.24: Interpolation of the parameters  $\mu$ ,  $f_{CB}$ ,  $\sigma_{Gauss}$ ,  $\sigma_{CB}$  and  $\alpha_{CB}$  of the signal model in the  $4\mu$  channel as a function of the mass.

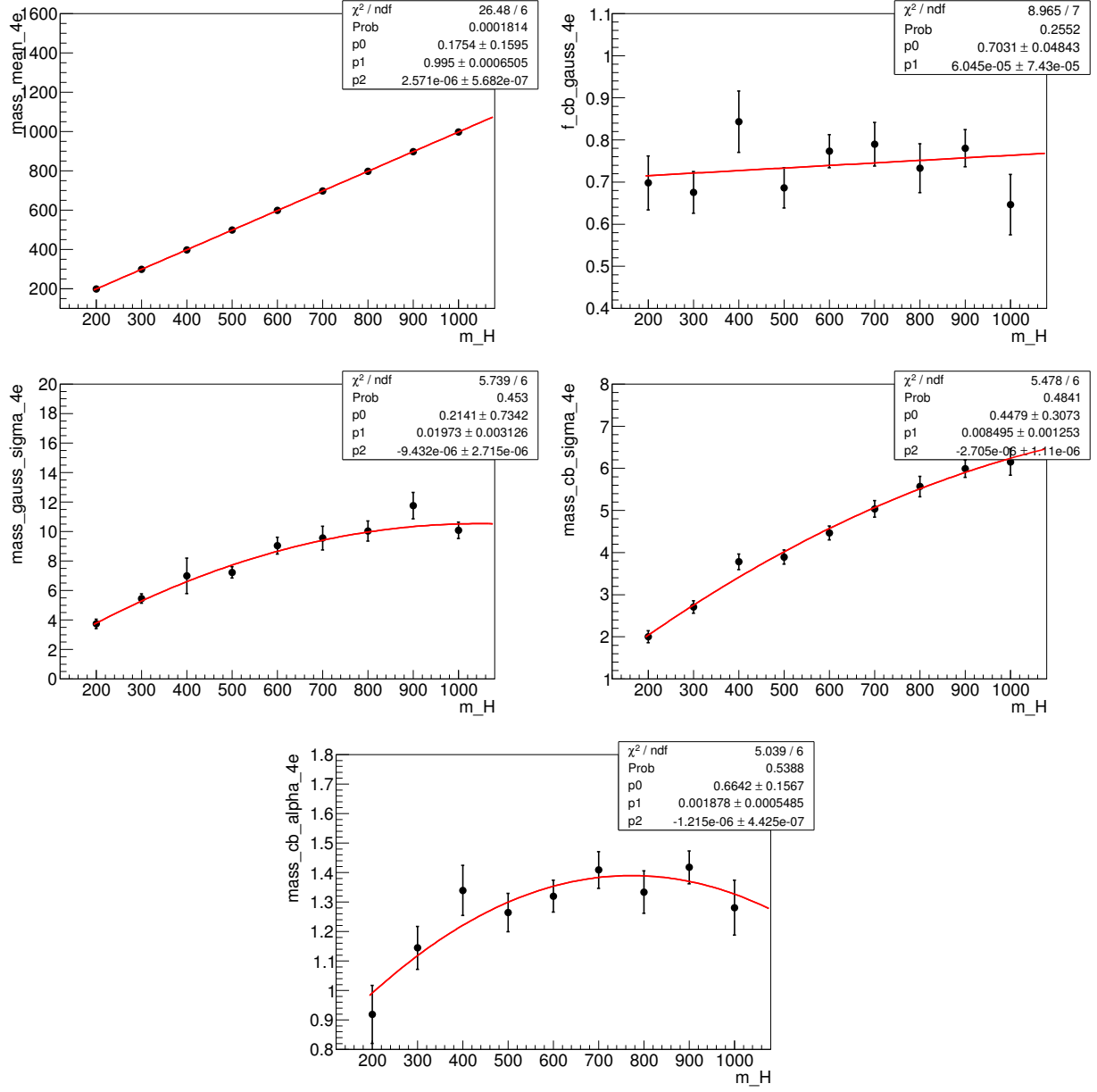


Figure 5.25: Interpolation of the parameters  $\mu$ ,  $f_{CB}$ ,  $\sigma_{Gauss}$ ,  $\sigma_{CB}$  and  $\alpha_{CB}$  of the signal model in the 4e channel as a function of the mass.



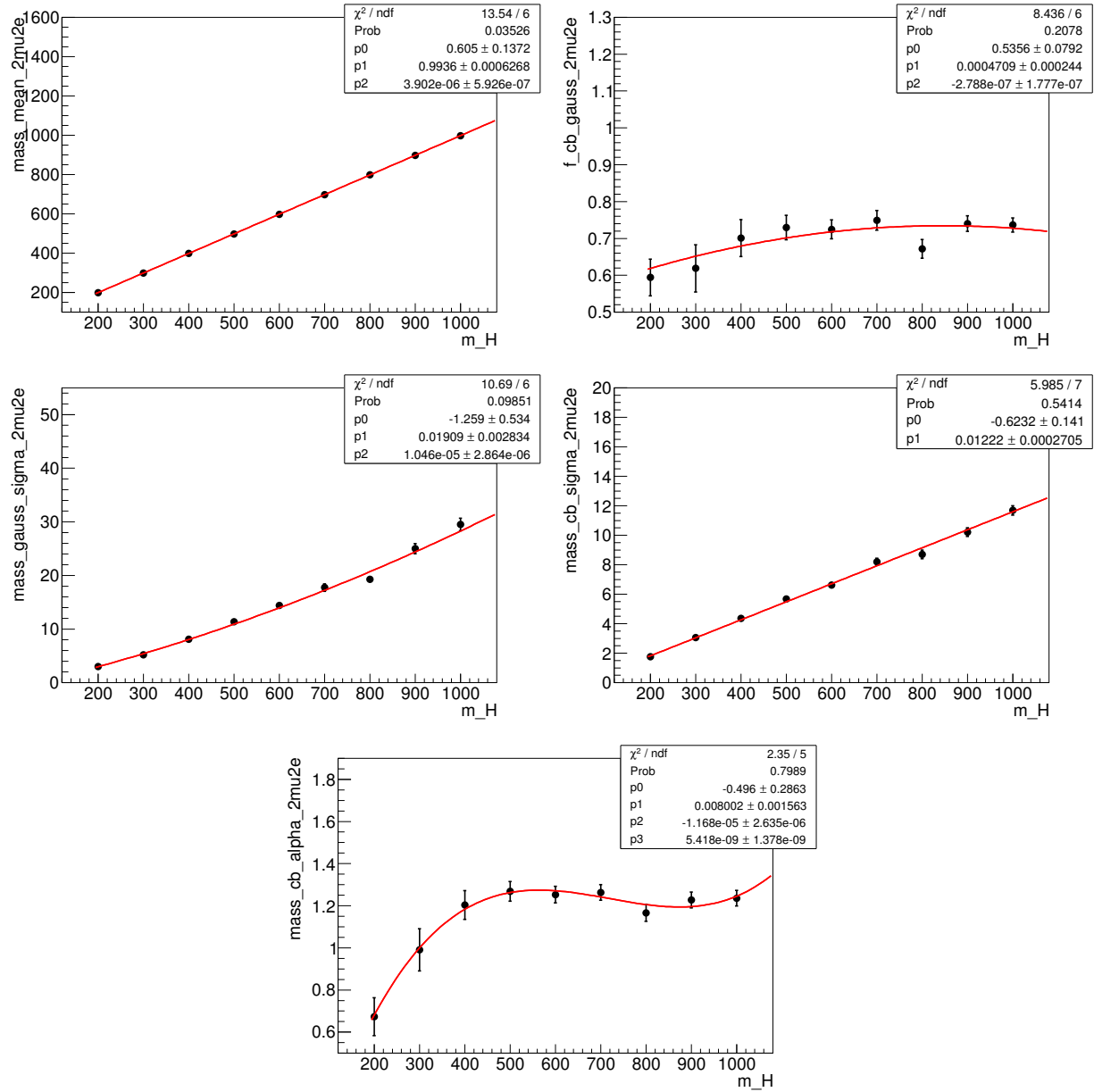


Figure 5.26: Interpolation of the parameters  $\mu$ ,  $f_{CB}$ ,  $\sigma_{Gauss}$ ,  $\sigma_{CB}$  and  $\alpha_{CB}$  of the signal model in the mixed channels  $2\mu 2e$  and  $2e 2\mu$  as a function of the mass.

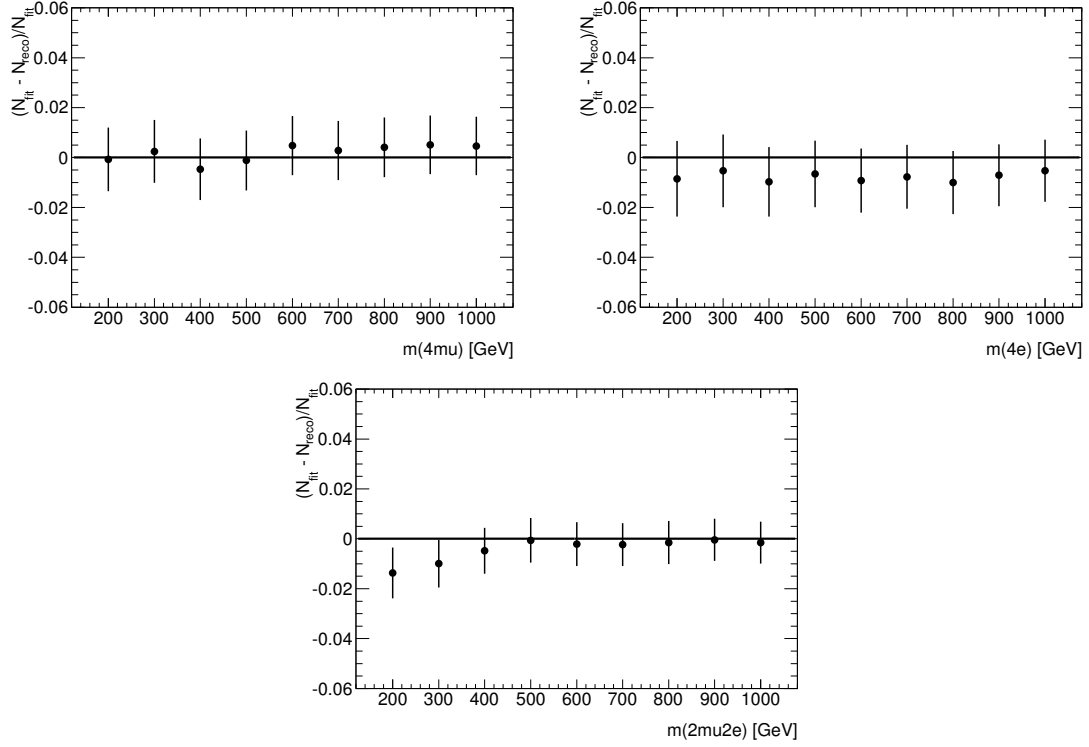


Figure 5.27: The bias introduced by the signal extraction is estimated as  $\frac{N_{\text{Rec}} - N_{\text{Fitted}}}{N_{\text{Fitted}}}$ , where  $N_{\text{Rec}}$  is the number of reconstructed events and  $N_{\text{Fitted}}$  is the number of events obtained from the fit.  $4\mu$  (left),  $4e$  (right) and mixed channels  $2\mu 2e$  and  $2e 2\mu$  (bottom).

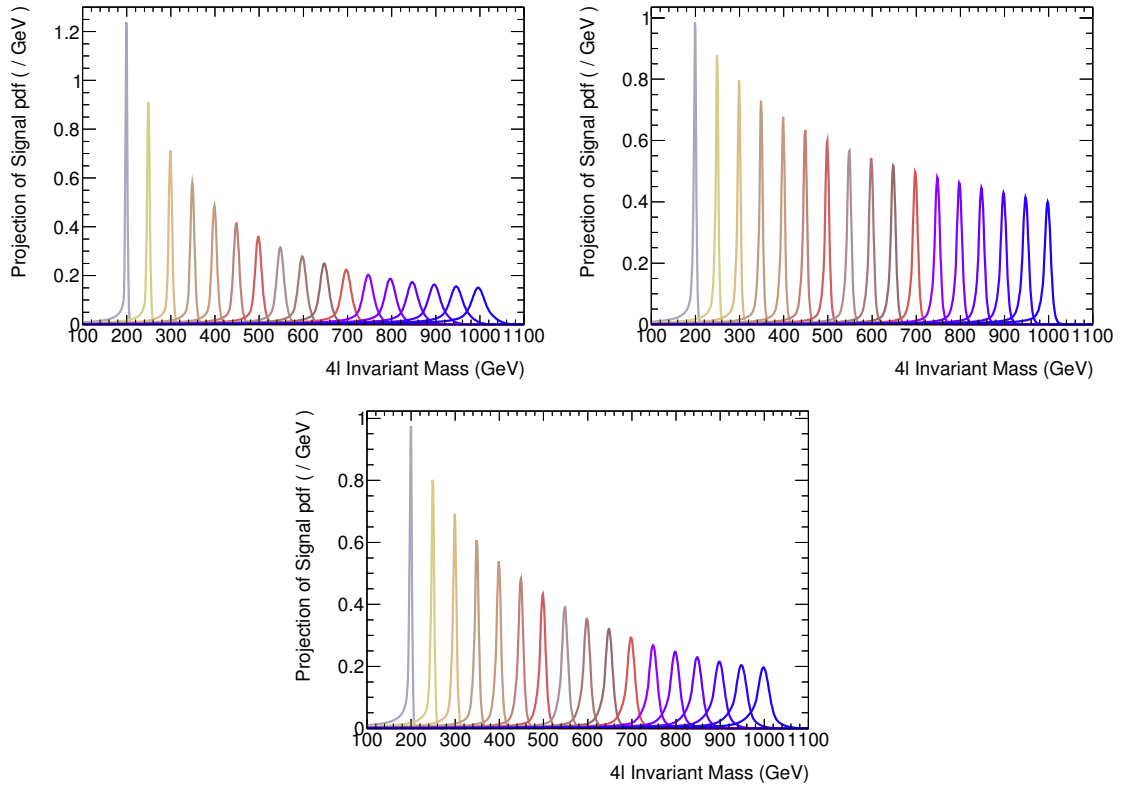


Figure 5.28: Signal template for  $4\mu$  (left),  $4e$  (right) and mixed channels  $2\mu 2e$  and  $2e 2\mu$  (bottom).

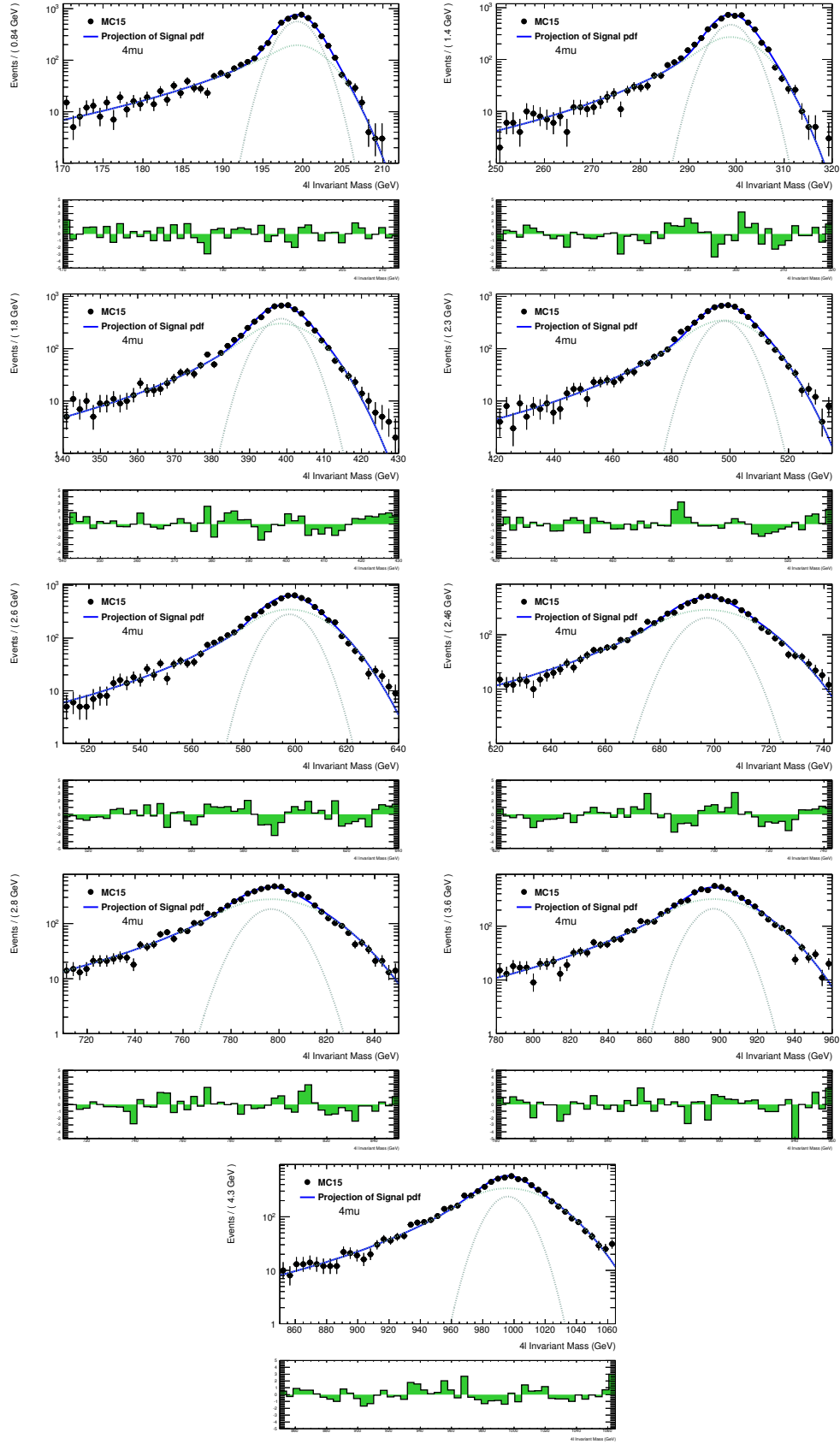


Figure 5.29: Distributions of  $m_{4\mu}$  invariant, mass compared to the analytical shape with interpolated parameters, of 200 to 1000 GeV in steps of 100 GeV.

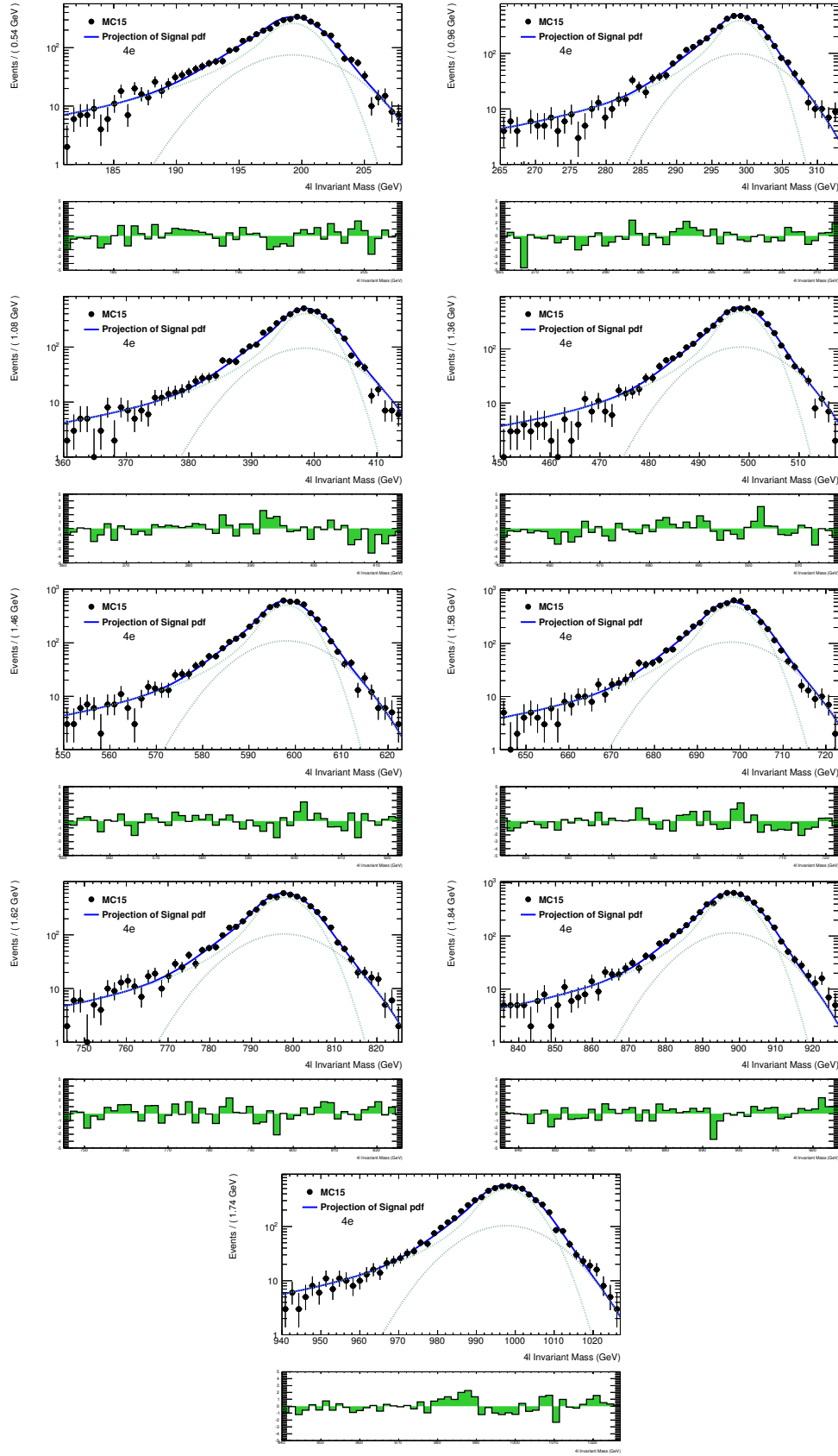


Figure 5.30: Distributions of  $m_{4e}$  invariant mass, compared to the analytical shape with interpolated parameters, of 200 to 1000 GeV in steps of 100 GeV.

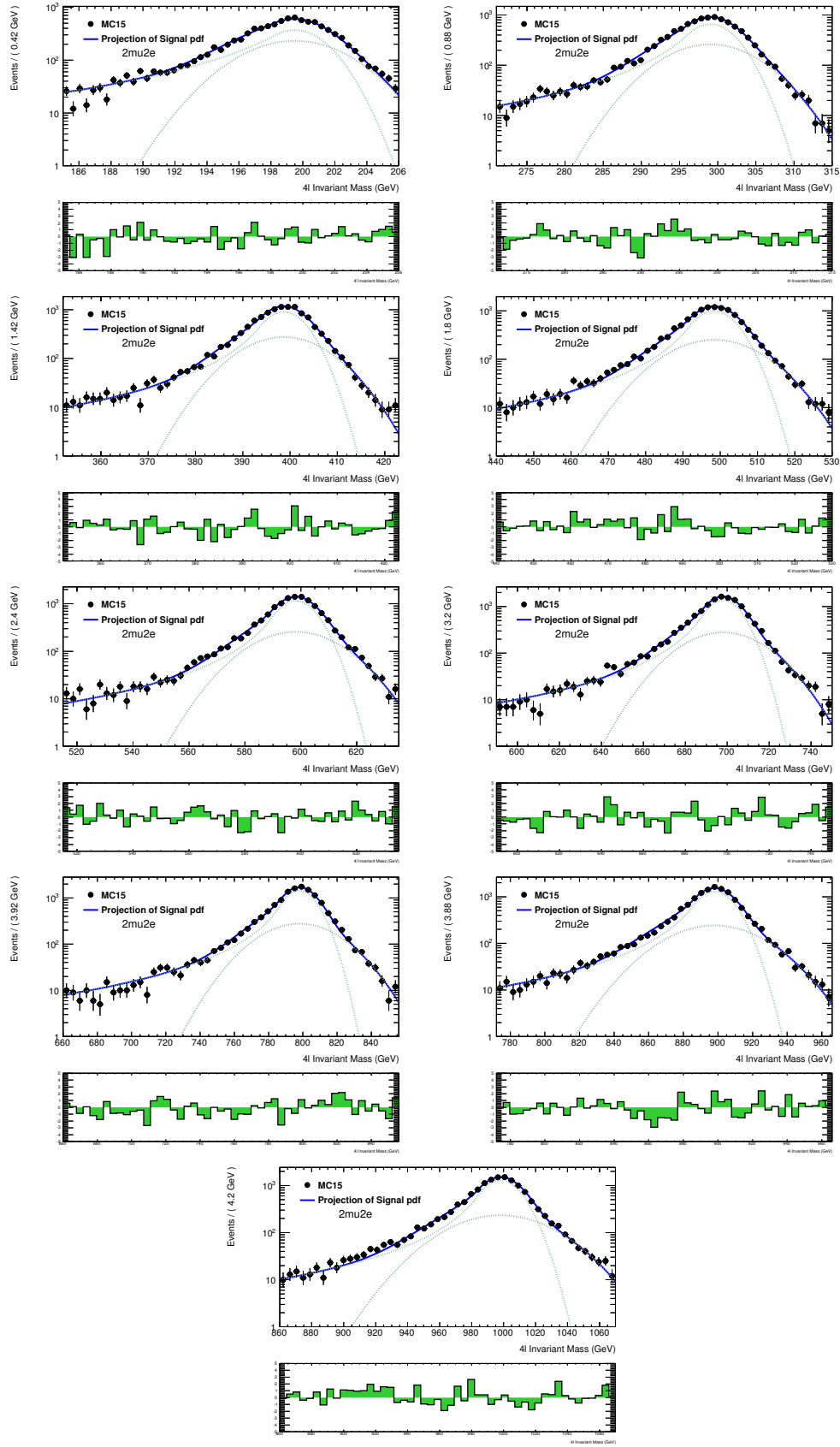


Figure 5.31: Distributions of  $m_{2\mu 2e}$  invariant mass, mass compared to the analytical shape with interpolated parameters, of 200 to 1000 GeV in steps of 100 GeV.

## 5.6 Systematic uncertainties

### 5.6.1 Experimental systematic uncertainties

This section describes the experimental systematic uncertainties associated to the detector effects. These uncertainties are estimated according to the recommendations from the Combined Performance (CP) groups. A systematic effect is evaluated by comparing the nominal MC sample with the one after having modified the interested quantity by applying weights, provided by the CP groups.

The main sources of the experimental uncertainties considered in the analysis are: object reconstruction and identification, object energy scale and resolution, object isolation, muon track-to-vertex-association, pile-up rescaling, integrated luminosity. 5% uncertainty on the integrated luminosity is used here.

### Background uncertainties

Experimental uncertainty on the reducible background was not included since it is negligible comparing to the statistical uncertainty and to the error associated to the method, which are described in Section 5.4. An effect of the experimental systematics on the tri-boson background is assumed to be negligible due to relatively low yield of this background.

Detector originated systematic effect on the  $m_{4\ell}$  distribution of the  $ZZ$  background was studied by comparing the parametrical shape described in Section 5.4.4 to the MC distribution with  $1\sigma$  systematic variation. As it can be seen from Table 5.15, this effect was found to be negligible both for  $qq \rightarrow ZZ$  and  $gg \rightarrow ZZ$ .

There is an extra uncertainty on the  $ZZ$  shape, that is originated from limited statistics of the MC samples in the high mass tail. This shape uncertainty is shown in Figure 5.32 in grey colour. This uncertainty is originally given as an error on all the parameters of the background shape described by Equation (5.5). Propagation of such an error to the statistical model of the analysis is quite challenging due to high correlation of the shape parameters, however, the uncertainty can be redefined as an error of a single shape parameter. It can be done by refitting the MC distribution with all parameters fixed, but the one most sensitive to the high mass tail (parameter  $b_4$  in Equation (5.5)). The single parameter uncertainty is shown in Figure 5.32 in green. The single parameter uncertainty is well covering the total uncertainty for the most of decay channel, while in case of  $gg \rightarrow ZZ$  background in the  $4\mu$  and  $2\mu 2e$  channels, the single parameter uncertainty can be enlarged by factor of two in order to ensure a conservative estimate. The single parameter uncertainty values are shown in Table 5.16.

The effect of the experimental systematics on the background normalisation is studied using the same MC samples with one sigma systematic variations. For the ggF-like categories the uncertainties are dominated by electron and muon identification efficiencies with a total effect  $< 2\%$  for each decay channel. The second largest uncertainty coming from pile-up rescaling is of the order of 1%. The uncertainties in the VBF-like category are dominated by the jet related uncertainties with a total effect about 24%, with the second largest contribution of the order of 8% is coming from pile-up rescaling. Although, the experimental uncertainty in the VBF category seems to be large, it is still minor compared to the theoretical uncertainty shown in Section 5.6.2

### Signal uncertainties

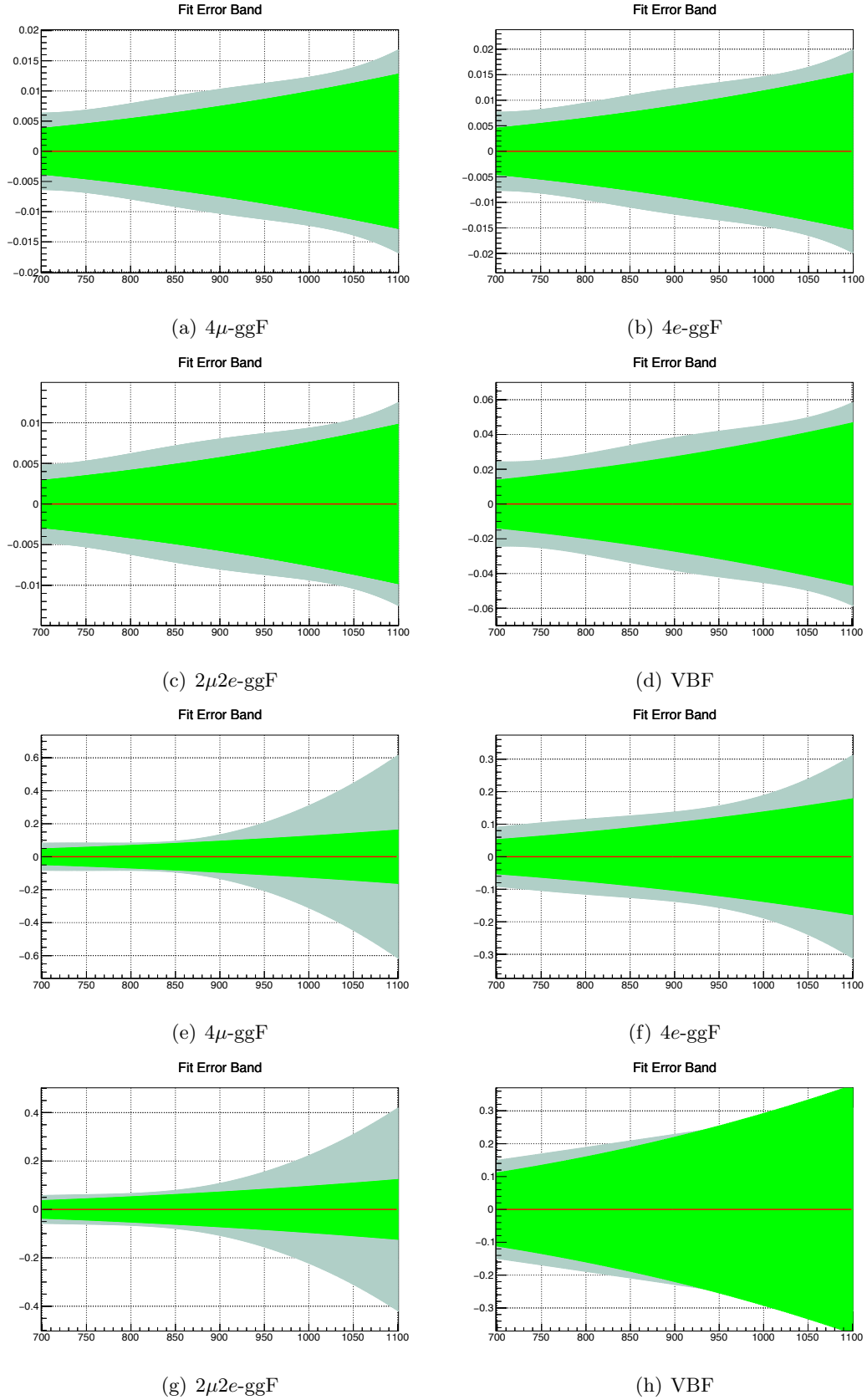


Figure 5.32: The fit error band of the analytical background shape fit to the MC distribution is shown for  $qq \rightarrow ZZ$  (top) and  $gg \rightarrow ZZ$  (bottom). The uncertainty is originating from the MC statistic error. Grey colour corresponds to the total fit uncertainty in all parameters free fit, while the green band shows the fit uncertainty in case of all parameters but the parameter  $b_4$  are fixed to the best fit values. It can be seen that green band is well compatible to the grey one in the high mass region. Therefore, the total fit error can be replaced by uncertainty on the parameter  $b_4$ . For the  $gg \rightarrow ZZ$   $4\mu$  and  $2\mu 2e$  the fitted error value was scaled by 2 in order to reach reasonable uncertainty level.

Table 5.15: Comparison of the nominal background ( $qq \rightarrow ZZ$  and  $gg \rightarrow ZZ$ ) shape to the MC distribution in the samples with systematic variations.  $\chi^2$  of the fit with all the shape parameters fixed, is showing how well the shape is compatible with the MC distribution. All the values are close to 1, therefore it was concluded that the experimental systematic affects do not affect neither  $qq \rightarrow ZZ$  nor  $gg \rightarrow ZZ$  shape. The check is done without separation into ggF and VBF like categories.

	$\chi^2$	$e$ resolution		$e$ scale		$\mu$ -ID resol.		$\mu$ -MS resol.		$\mu$ scale	
		Up	Down	Up	Down	Up	Down	Up	Down	Up	Down
$qqZZ$	$4\mu$	1.0	1.0	1.0	1.0	1.1	1.2	0.9	1.1	0.9	1.0
	$4e$	1.1	1.1	1.2	1.1	1.1	1.1	1.1	1.1	1.1	1.1
	$2\mu 2e$	1.1	1.0	1.1	1.1	1.0	1.0	1.2	1.0	1.0	1.0
$ggZZ$	$4\mu$	1.0	1.0	1.0	1.0	1.0	1.1	1.0	1.4	1.0	1.0
	$4e$	1.0	1.3	1.0	1.1	0.9	0.9	0.9	0.9	0.9	0.9
	$2\mu 2e$	1.0	1.0	1.0	1.0	1.0	1.0	1.2	1.2	1.2	1.0

Table 5.16: Additional systematic uncertainty on the background shape originating from MC statistic of the background samples. It is implemented into the  $b_4$  parameter of the analytical shape function, as described in the text.

Uncertainty	$qq \rightarrow ZZ$				$gg \rightarrow ZZ$			
	ggF- $4\mu$	ggF- $4e$	ggF- $2\mu 2e$	VBF	ggF- $4\mu$	ggF- $4e$	ggF- $2\mu 2e$	VBF
$b_4$ (%)	0.2	0.2	0.1	1.1	$2 \cdot 0.6$	0.9	$2 \cdot 0.7$	3.5

Signal experimental uncertainties are estimated using weighted MC samples from the CP groups as well. The  $m_{4\ell}$  distribution feels the effect in terms of the effective resolution change and shift of the signal peak, and it is taken into account as extra errors on the  $\mu$ ,  $\sigma_{CB}$  and  $\sigma_{Gauss}$  parameters of the analytical shape. The systematic uncertainty on  $\mu$  was estimated by comparing mean value of the  $m_{4\ell}$  distribution in the nominal MC sample to another one with  $1\sigma$  systematic variation. A difference in corresponding RMS values was considered as an uncertainty on the  $\sigma_{CB}$  and  $\sigma_{Gauss}$  parameters. These effects are estimated for every available MC mass point and interpolated to other mass values using B-Spline [122]. A summary of the signal shape systematic uncertainties for 500 GeV mass point is given in Table 5.17.

Table 5.17: Summary of the effects of the experimental systematic uncertainties on the parameters  $\mu$  and on  $\sigma_{CB}$  and  $\sigma_{Gauss}$  of the analytical signal shape at  $m_S = 500\text{GeV}$ .

Effect on $\mu$ (%)	ggF- $2\mu 2e$	ggF- $4\mu$	ggF- $4e$	VBF
MUON_SCALE	0.02	0.03	0.00	0.01
EG_SCALE	0.2	0.00	0.4	0.2
Effect on $\sigma_{CB}$ and $\sigma_{Gauss}$ (%)	ggF- $2\mu 2e$	ggF- $4\mu$	ggF- $4e$	VBF
MUON_ID	0.7	1.2	0.00	1.1
MUON_MS	0.6	0.5	0.00	1.0
EG_RESOLUTION	1.9	0.00	3.0	0.9

Experimental uncertainty on the signal acceptance is dominated by muon (1-5% in  $4\mu$  decay channel) and electron (1-3% in  $4e$  decay channel) identification efficiencies in ggF enriched categories, while in VBF-like category jet related uncertainties dominate (4-6%). The systematic effects are estimated for available MC mass points, and then a B-Spline [122] is



used to interpolate the effect at intermediate mass values. The experimental uncertainty on the signal acceptance for ggF and VBF production modes is shown in Figures 5.33 and 5.34 respectively.

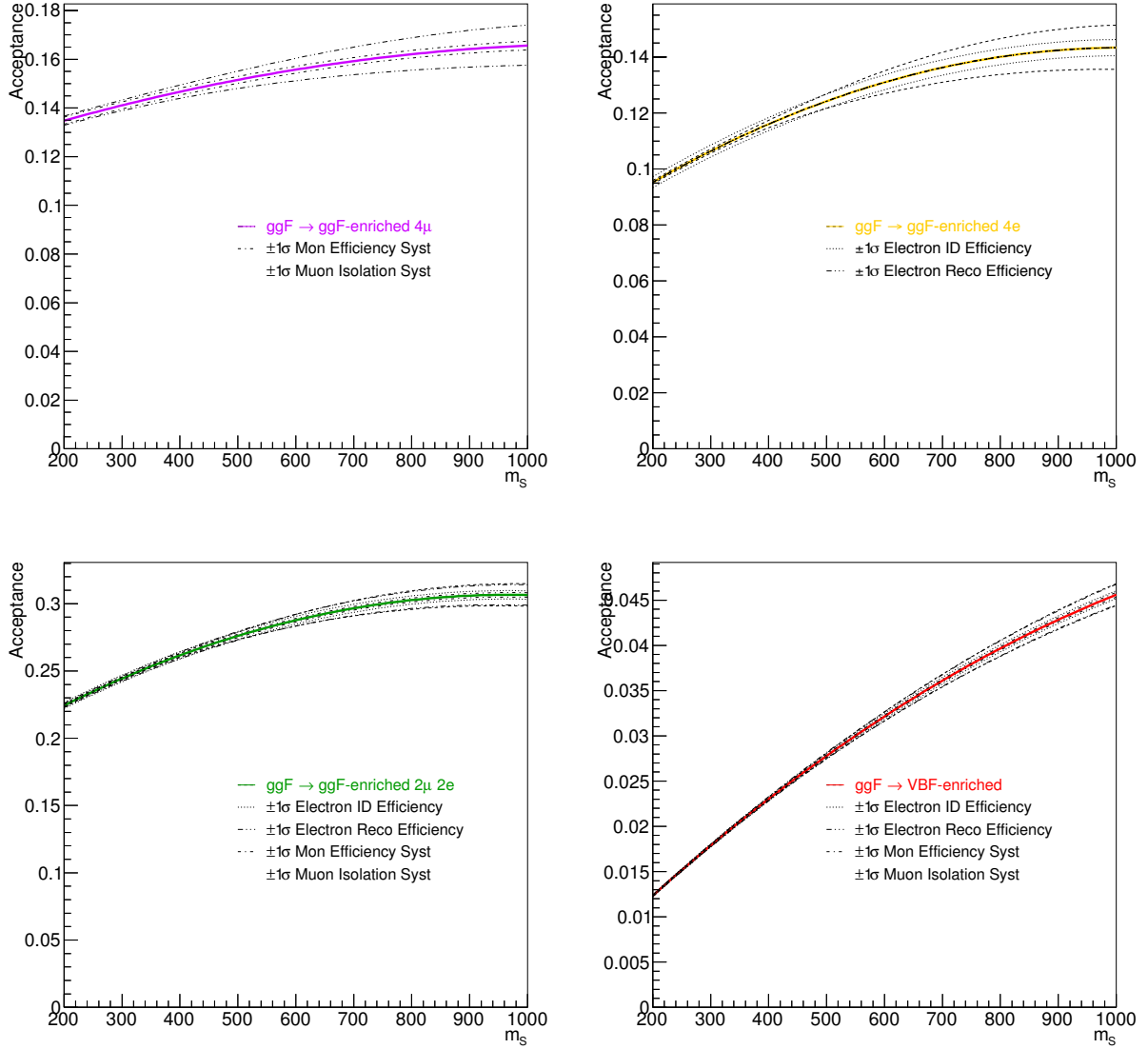


Figure 5.33: The  $\pm 1\sigma$  error bands for different sources of systematic uncertainty on the acceptance functions for ggF production into the categories  $4\mu$  (top-left),  $4e$  (top-right),  $2\mu 2e$  (bottom-left), and VBF (bottom-right).

### 5.6.2 Theoretical systematic uncertainties

Theoretical systematics are caused by the choice of QCD scale, PDF and showering used in the simulation. They are affecting both the signal and the background simulations. Detailed description of the uncertainty estimation is given in Ref. [117], [123]. Theory systematics are evaluated from truth level simulations with different configurations of QCD scale, PDF and showering. An envelope of the yield variation is considered as an uncertainty for a given process and category. The uncertainty is evaluated in different categories for ggF and VBF signal production modes and  $qq \rightarrow ZZ$  background, while the effect on the other background is neglected due to their minor yields to the signal region. All the effects are considered as

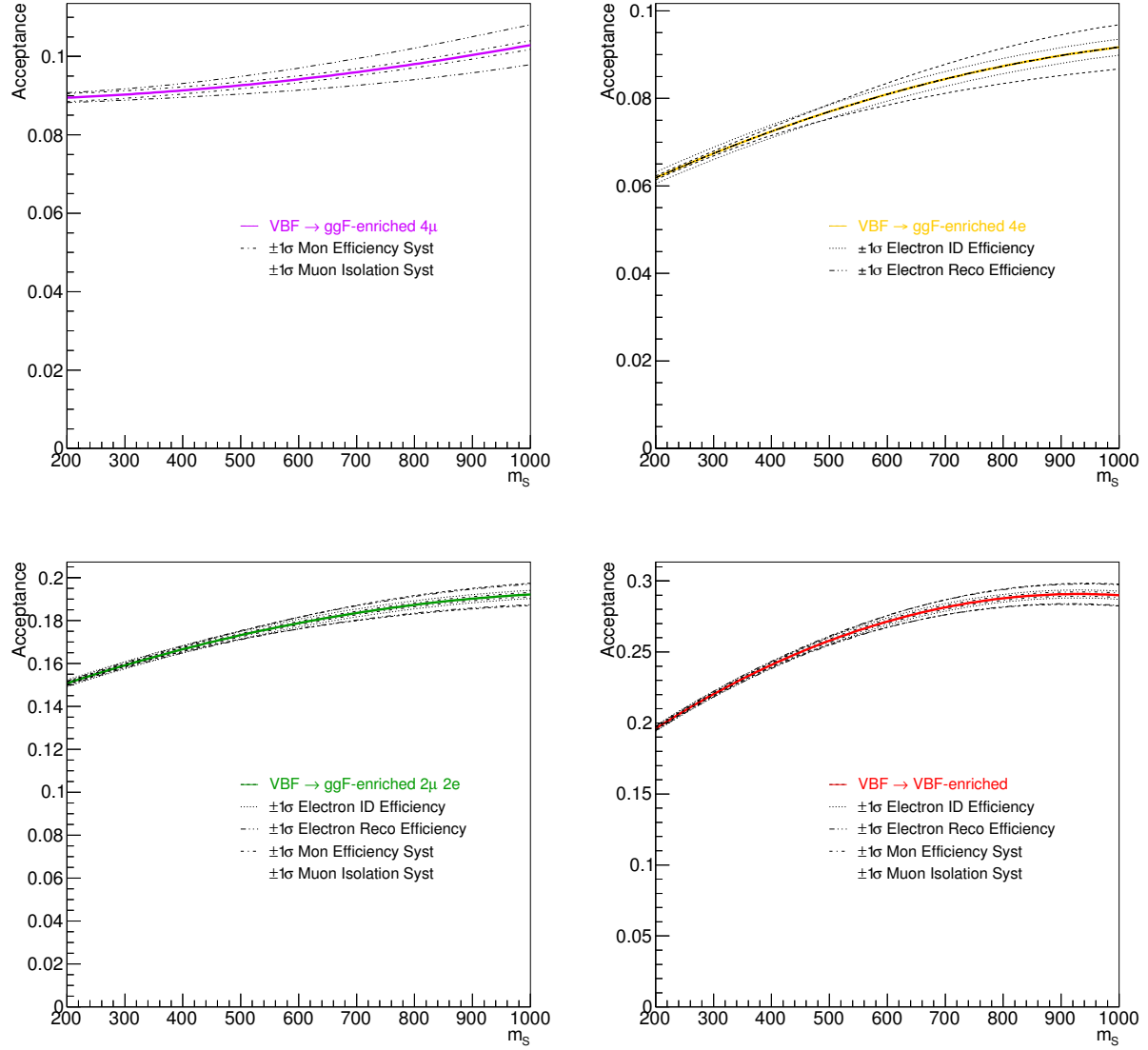


Figure 5.34: The  $\pm 1\sigma$  error bands for different sources of systematic uncertainty on the acceptance functions for VBF production into the categories  $4\mu$  (top-left),  $4e$  (top-right),  $2\mu 2e$  (bottom-left), and VBF (bottom-right).

flat uncertainties.

VBF-like category selection highly rely on the jet environment, in particular number of jets ( $N_{jet}$ ) and invariant mass of two-jet system ( $m_{jj}$ ) in an event. It is known that jets can be poorly simulated due to missing higher order corrections to the theoretical calculation or due to specific generator choice. Therefore, an additional uncertainty is associated to the VBF-like category. This effect is estimated for  $qq \rightarrow ZZ$  by comparing the background acceptance obtained from POWHEG and Sherpa simulations. For the ggF production mode of the signal, the POWHEG simulation was compared to MadGraph FxFx ggF+2jet samples. And for  $gg \rightarrow ZZ$ , since there is no generator that provides reliable simulation of the process with two additional jets, the conservative 90% uncertainty is considered. All the theoretical uncertainties are summarised in Table 5.18.

Table 5.18: Summary of effect of theory systematics on normalisation in analysis categories for different sources in categories. For the ggF and VBF signal a mass  $m_S = 500$  GeV is chosen as an example. Systematics are expressed as percentages in the order up,down (symmetric uncertainties denoted by a single number). Only total systematic uncertainty is shown for VBF-like category.

QCD scale (%)	$qq \rightarrow ZZ$	$gg \rightarrow ZZ$	ggF	VBF
ggF-like $2\mu 2e$	5.0	30	0.4	1.3
ggF-like $4\mu$	5.0	30	0.3	1.2
ggF-like $4e$	5.0	30	0.4	1.3
PDF (%)	$qq \rightarrow ZZ$	$gg \rightarrow ZZ$	ggF	VBF
ggF-like $2\mu 2e$	5.0	8.0	1.6	0.4
ggF-like $4\mu$	5.0	8.0	1.6	0.4
ggF-like $4e$	5.0	8.0	1.8	0.4
Showering (%)	$qq \rightarrow ZZ$	$gg \rightarrow ZZ$	ggF	VBF
ggF-like $2\mu 2e$	0	0	0.2	0.4
ggF-like $4\mu$	0	0	0.1	0.4
ggF-like $4e$	0	0	0.2	0.4
Total in VBF-like (%)	66	90	40	2.2

## 5.7 Observed events with $14.8 \text{ fb}^{-1}$ of 13 TeV data

Figure 5.35 shows the  $m_{4\ell}$  distribution of the selected candidates compared to the background expectation in the signal region without separation into category. The distributions split into the four analysis categories are shown in Figure 5.36. No events are observed beyond the plotted range (840 GeV). The background distributions come from their respective modelling described in Section 5.4.4.

The expected yields from each source within each category, as well as the observed yields, are shown in Table 5.19. An excess of data events is observed in the ggF-like  $4e$  category right above the  $ZZ$  on-shell threshold. The VBF-like category has an excess of data events that is distributed over the whole mass range. It was found that the SM electroweak production of a  $Z$  boson pair have a significant contribution to the VBF-like category, while it is not included into the analysis. Also Sherpa generator provides better description of the event jet environment comparing to POWHEG used here. These two updates are taken into account for the next round of the search with more data described in Chapter 8.

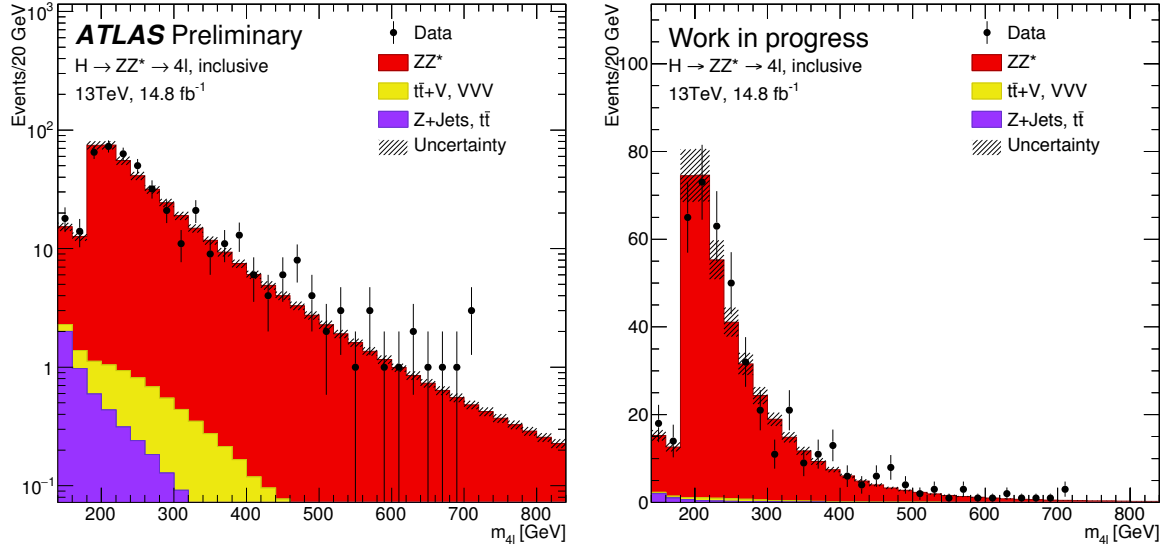


Figure 5.35:  $m_{4\ell}$  distribution of the selected candidates compared to the background expectation inclusive of category in log and linear scale.

Table 5.19: The number of events expected and observed for the four-lepton final states in a range of  $140 < m_{4\ell} < 1300$  GeV. The columns show the number of expected  $ZZ$  and reducible background events together with the number of observed events, for  $14.8 \text{ fb}^{-1}$  at  $\sqrt{s} = 13$  TeV.

Category	$ZZ$	$Z + \text{jets}, t\bar{t}, WZ$	$t\bar{t}V, VVV$	Expected	Observed
ggF - $2\mu 2e$	$205 \pm 17$	$2.5 \pm 0.4$	$2.75 \pm 0.17$	$211 \pm 17$	199
ggF - $4e$	$83 \pm 7$	$1.47 \pm 0.22$	$1.28 \pm 0.08$	$86 \pm 7$	111
ggF - $4\mu$	$125 \pm 10$	$0.95 \pm 0.14$	$1.57 \pm 0.09$	$127 \pm 10$	128
VBF	$4.6 \pm 2.8$	$0.18 \pm 0.05$	$0.268 \pm 0.016$	$5.1 \pm 2.8$	10
Total	$418 \pm 35$	$5.1 \pm 0.7$	$5.87 \pm 0.35$	$429 \pm 35$	448

Since no significant excess was observed, the upper limit on the heavy Higgs boson production cross section was set according to the procedure described in the following section.

## 5.8 Statistical procedure

Limits on additional heavy Higgs bosons are obtained using an unbinned profile likelihood fit. The likelihood function is a product of a Poisson term representing a probability to observe  $n$  events and a weighted sum of both signal and background probability distribution functions (PDFs) evaluated for all observed events.

$$\mathcal{L}(x_1 \dots x_n | \sigma_{ggF}, \sigma_{VBF}) = \text{Pois}(n | S_{ggF} + S_{VBF} + B) \times \left[ \prod_{i=1}^n \frac{S_{ggF} f_{ggF}(x_i) + S_{VBF} f_{VBF}(x_i) + B f_B(x_i)}{S_{ggF} + S_{VBF} + B} \right]$$

where  $f_X$  stands for corresponding PDF,  $S_X$  and  $B$  stand for signal and background normalisation respectively. Both shapes and normalisations are estimated per category. The factors  $B$  and  $f_B(x_i)$  implicitly represent all different background contributions combined, each having different PDFs and yields.

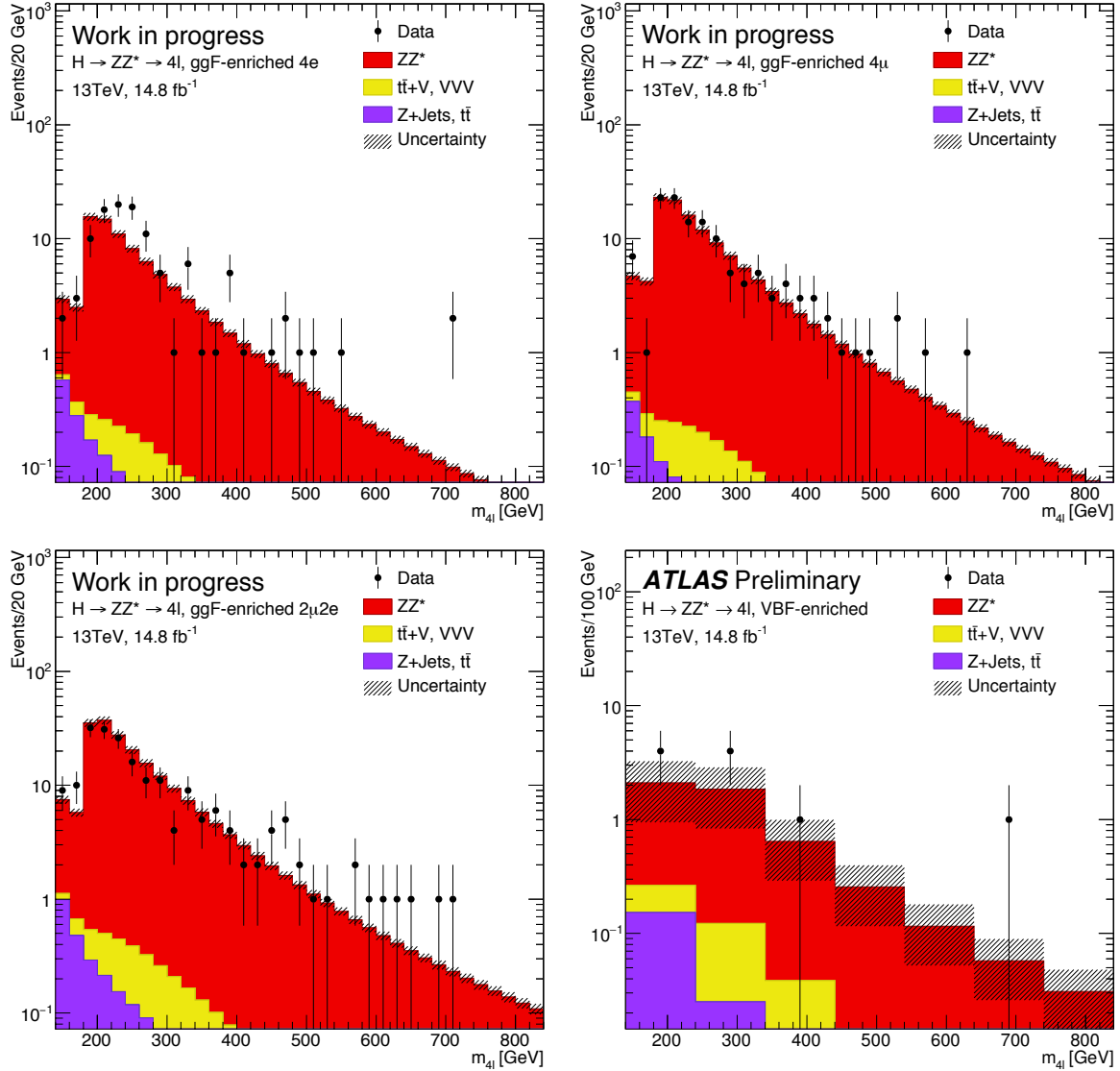


Figure 5.36: Log-scale  $m_{4\ell}$  distribution of the selected candidates compared to the background expectation in ggF-like 4e (top-left), ggF-like 4 $\mu$  (top-right), ggF-like 2 $\mu$ 2e (bottom left) and VBF-like (bottom-right) categories. Note that the VBF-like category is shown with a coarser binning than the other categories only for visual simplicity - all categories use unbinned fits.

The parameters of interest (POI) in the fit are  $\sigma_{ggF}$  and  $\sigma_{VBF}$ . In setting a limit on one of them, the other is treated as unknown free parameter during the minimisation. These POI enter the likelihood inside the expected signal yields  $S_{ggF}$  and  $S_{VBF}$  as follows:

$$S_{ggF(VBF)} = \sigma_{ggF(VBF)} \times BR(S \rightarrow ZZ \rightarrow 4\ell) \times A \times C \times \int \mathcal{L}$$

where  $A \times C$  is the signal acceptance as defined in Section 5.5.1, and  $\int \mathcal{L} = 14.8\text{fb}^{-1}$  is an integrated luminosity of the dataset.

Dependence of the expected number of signal and background events and the shape of the PDFs on the systematic uncertainties is described by a set of nuisance parameters (NP)  $\theta_i$ . Gaussian constraints are used to constrain the NPs to their nominal values within estimated uncertainties. The constraints are implemented via additional "penalty" terms added to the likelihood which will penalise the negative log-likelihood when a nuisance parameter is shifted from its nominal value. The final likelihood function  $\mathcal{L}(\sigma_{ggF}, \sigma_{VBF}, m_H, \theta_i)$ , is therefore a function of  $\sigma_{ggF}$ ,  $\sigma_{VBF}$ ,  $m_H$ , and  $\theta_i$ .

The upper limit for the production cross-section  $\sigma_{ggF(VBF)}$  at a considered Higgs-mass is obtained by setting the  $m_H$  parameter constant at the desired value, and maximising the likelihood function with respect to  $\sigma_{VBF(ggF)}$  and the nuisance parameters. The test statistics  $q_\mu$  is used to set upper limits as described in Ref. [124]. The  $CL_s$  [125] method is used to obtain exclusion limits.

In case of the limit extraction on the inclusive production cross section of the heavy Higgs boson, the same procedure is applied without separating VBF category from the SR. Only one POI  $\sigma_{inclusive}$  is present in such a model.

## 5.9 Upper limits on the heavy Higgs production cross section

The upper limit on the ggF and VBF cross-sections times branching ratio assuming the Narrow Width Approximation is set as a function of signal mass hypothesis. The limit is based on the  $CL_s$  procedure in the asymptotic approximation using the test-statistic as defined in Section 5.8. Figures 5.37(a) and 5.37(b) show the expected and observed limits at 95% confidence level for the ggF and VBF production modes respectively, in a step comparable to the detector resolution. A dashed line shows the expected limit, while green and yellow bands correspond to one and two sigma deviation respectively. The observed limit is shown with a solid line. Both the ggF and the VBF results are dominated by the statistical uncertainty, while the systematic effect is included as well. The largest deviation from the expected limit is observed around  $m_H = 705$  GeV and it correspond to  $2.9\sigma$  of local deviation from the background only hypothesis.

Both ggF and VBF production cross sections of the heavy Higgs boson at the order of few fb were excluded at 95% confidence level. The sensitivity to the VBF production mode is few times better in the low mass region comparing to the ggF one, that could be understood by lower background yield to the VBF-like category. However, the VBF production cross section is usually predicted to be lower comparing to the ggF one. These model independent limits can be further interpreted in terms of EWS and 2HDM benchmark models described in Section 2.3.

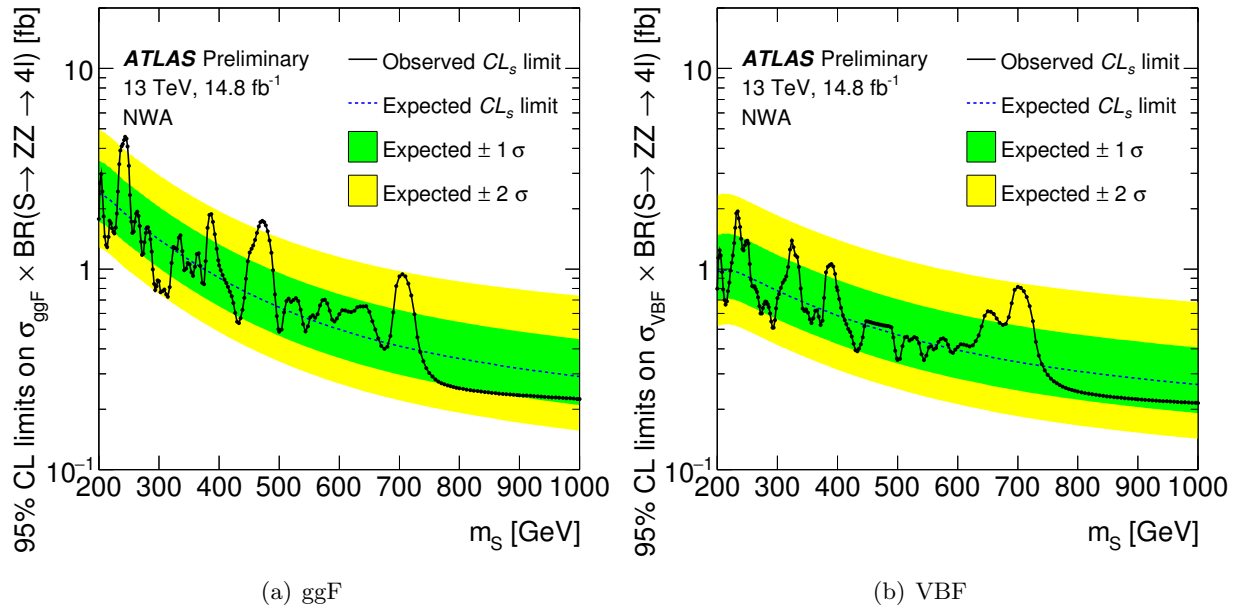


Figure 5.37: 95% confidence limits on  $\sigma \times BR(S \rightarrow ZZ \rightarrow 4\ell)$  for ggF (a) and VBF (b) production modes in the NWA approximation (systematic uncertainty is included).

# Exploration of the large width hypothesis for heavy Higgs boson

---

## 6.1 Overview

This section describes the analysis that is aiming to explore the large width heavy Higgs hypothesis (LWA), with the width up to 15% of the particle mass. Such the wide resonance will have non negligible interference both with the Standard Model Higgs boson and the  $gg \rightarrow ZZ$  background. LWA results will be presented in terms of limits on inclusive production cross section of the hypothetical heavy Higgs boson.

Section 6.5 is showing the results without implementation of the interference that were presented by collaboration on ICHEP conference in 2016, however Section 6.4 discuss the interference modelling, that is included into the next round of the analysis presented in Chapter 8.

The LWA analysis profits from the NWA framework, described in Chapter 5, namely it exploits the same event selection, background estimation and background modelling. Additional MC samples used in the analysis are described in Section 6.2, while the the signal modelling is described in Section 6.3. The large width heavy Higgs search is using the same systematic uncertainties estimate as the narrow width analysis without separation into ggF and VBF categories as described in Section 5.6.

## 6.2 MC samples

In addition to the MC samples described in Section 5.2, some extra MC simulations of the LWA signal and its interference with the SM Higgs and background were used.

The  $H \rightarrow ZZ \rightarrow 4\ell$  signal in LWA is modelled using the MadGraph 5 MC generator [126], which computes the process at next-to-leading order. MadGraph is further interfaced to PYTHIA 8 [105] for showering and hadronisation, which in turn is interfaced to EvtGen [106] for the simulation of B-hadron decays. The NNPDF23 [127] parton distribution is used for the simulation.

The full simulation is available for mass points from 200 to 1000 GeV in a step of 100 GeV, for the resonant width  $\Gamma = 0.15 \times m_H$ . Also there are simulated samples with different width  $\Gamma = 0.05 \times m_H$  and  $\Gamma = 0.10 \times m_H$  at  $m_H = 900$  GeV. The ggF production mode is assumed for this simulation. The LWA samples are mostly used to cross check the LWA signal modelling described in Section 6.3, as well as for the interference studies.

There is a set of MC samples simulated for the interference of the signal with the SM  $gg \rightarrow ZZ$  background. The interference cannot be simulated separately, therefore it is deduced from the total process that includes the signal, the background and the interference



by subtracting the remaining components. These samples for the total process are simulated with MCFM [128] generator at leading order, and they are further interfaced to PYTHIA 8 for showering and hadronisation. The samples are produced with fast detector simulation [129], that use simplified simulation of the ATLAS calorimeter. The fast simulation allows to reduce computing resources without degradation of the simulation quality. The interference is simulated for a set of signal mass hypothesis: 200, 300, 400, 500, 600, 800, 1000, 1200 and 1400 GeV, under the assumption of the width equal to 15% of the signal mass. The  $m_{4\ell}$  window of  $\pm 3 \times \Gamma_H$  is applied to the mass points above 400 GeV. The same simulation is also used to produce extra  $gg \rightarrow ZZ$  background samples for the interference studies. Here the  $m_{4\ell}$  inclusive sample and a sample with  $m_{4\ell} > 700$  GeV are produced, in order to ensure suitable MC statistics along the full mass range.

### 6.3 Signal modelling

#### Signal acceptance

Using the ggF MC samples with the width of  $\Gamma_S = 0.15 \times m_S$ , the acceptance for LWA was compared against the NWA one. These comparisons is shown in Figure 6.1. The acceptance in all the categories is compatible within MC statistics. Therefore, the same NWA ggF acceptance is used for LWA signal.

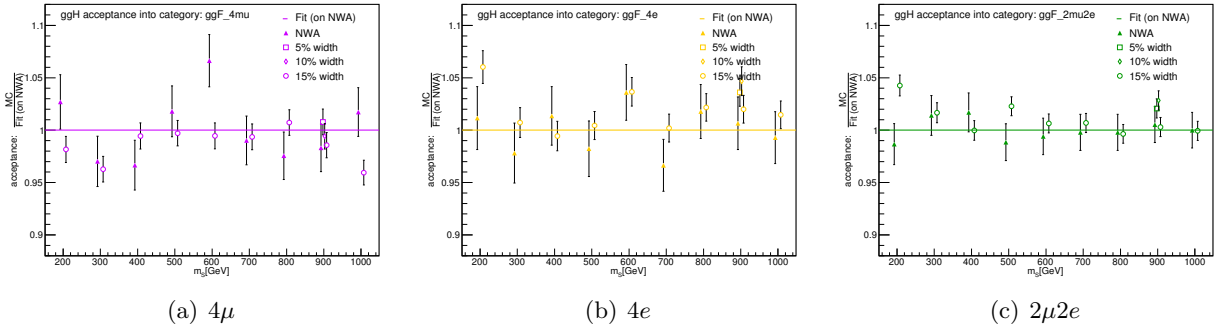


Figure 6.1: Ratio of the acceptance in simulated samples with different mass and width over the NWA parameterisation for signal acceptance.

#### Signal shape

In this analysis the signal width is comparable or larger than the detector resolution, therefore the truth line shape of the signal should be treated carefully. The truth shape of the heavy Higgs resonance was discussed in Section 2.5, and it was shown that the shape can be described by Equation (2.21), that is repeated below:

$$\sigma_{pp \rightarrow H \rightarrow ZZ}(m_{4\ell}) = 2 \cdot m_{4\ell} \cdot \mathcal{L}_{gg}(m_{4\ell}) \cdot \frac{1}{|s - s_H|^2} \cdot \Gamma_{h \rightarrow gg}(m_{4\ell}) \cdot \Gamma_{h \rightarrow ZZ}(m_{4\ell}) \quad (6.1)$$

where  $\frac{1}{s - s_H}$  is a scalar propagator in complex-pole schema,  $\Gamma_{h \rightarrow gg}(m_{4\ell})$  and  $\Gamma_{h \rightarrow ZZ}(m_{4\ell})$  are corresponding partial widths of the signal as a function of invariant mass, and finally  $\mathcal{L}_{gg}$  is a gluon parton luminosity at LHC. The later one is a derivative of a parton distribution function that shows effective interaction rate of two gluons in proton-proton collisions. In this analysis, an expression for the gluon-gluon parton luminosity is taken from Ref. [130] for the NNPDF23 parton distribution function. The gluon-gluon luminosity as a function of the interaction energy is shown in Figure 6.2.

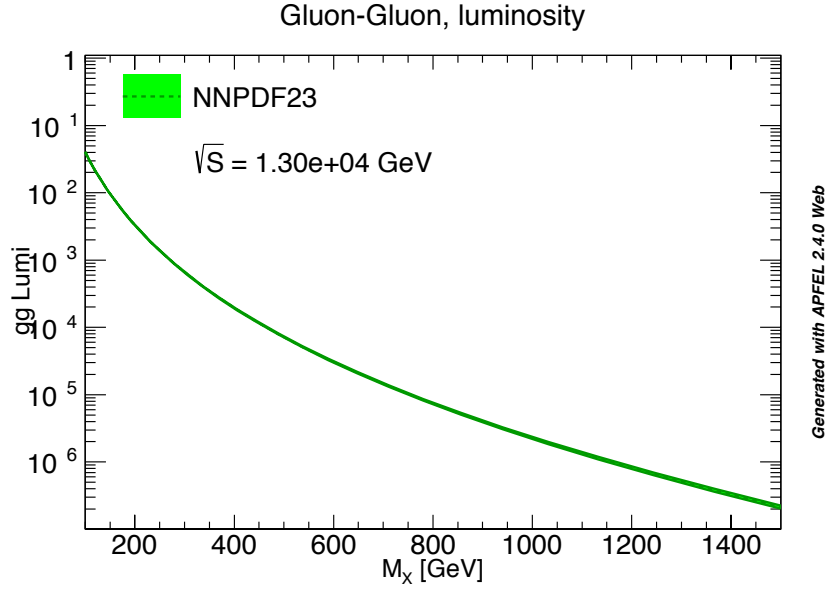


Figure 6.2: Gluon-gluon luminosity in proton-proton collisions of  $\sqrt{s} = 13$  TeV, based on the NNPDF23 parton distribution function. [130]

The analytical description of the signal line shape from Equation (6.1) is compared to the truth  $m_{4\ell}$  distribution in the simulated MC samples in Figure 6.3. The analytical model is matching the truth MC distribution with high precision for the signal mass hypotheses above 300 GeV.

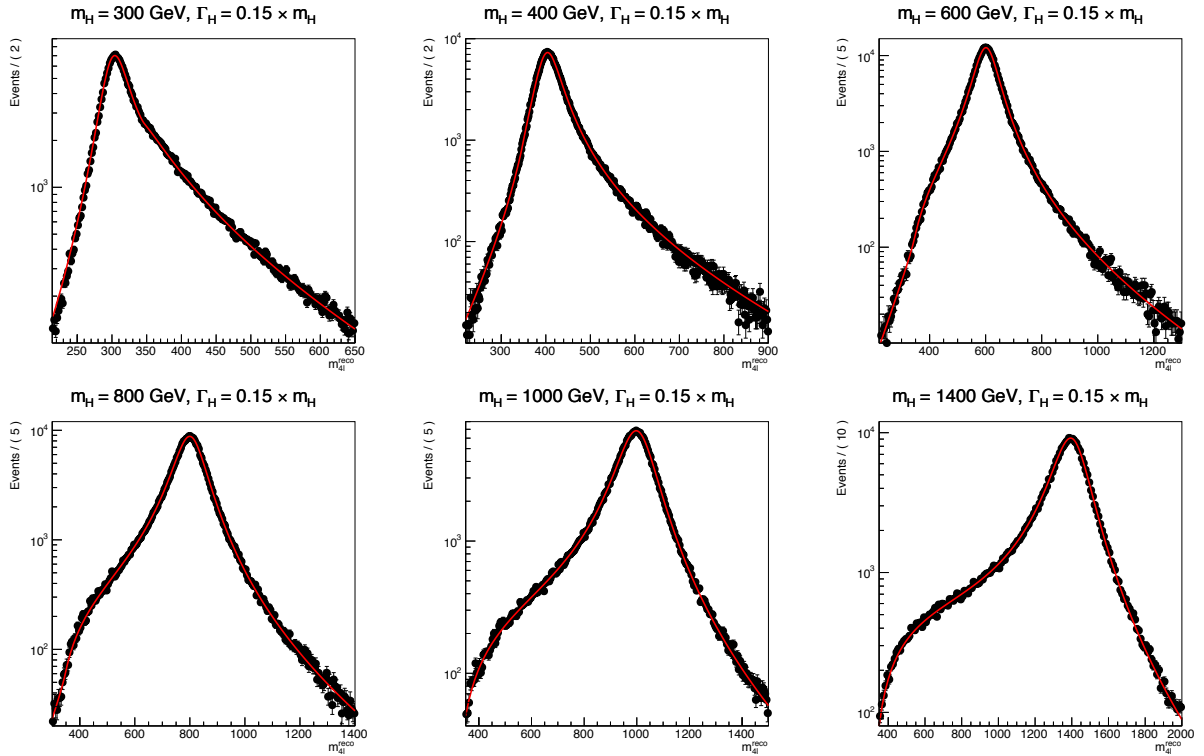


Figure 6.3: Comparison of the analytical shape from Equation (6.1) to a truth  $m_{4\ell}$  distribution in the signal MC samples for the mass range 300-1400 GeV and width equal to 15% of the mass.

Reconstructed distribution can be modelled as the analytical truth shape multiplied by the acceptance function and convoluted with the detector resolution effect for the invariant mass equal to the signal mass hypothesis. The detector resolution is provided by the NWA

signal parametrisation, since the NWA signal width is negligible compared to the detector resolution. This LWA model is well compatible with the reconstructed MC distribution above 400 GeV, that corresponds to the region of interest for the LWA search that ignores the interference effects. Comparison of the modelled shape to the MC distribution is shown in Figures 6.4, 6.5 and 6.6 for  $4\mu$ ,  $4e$  and  $2\mu 2e$  final states respectively.

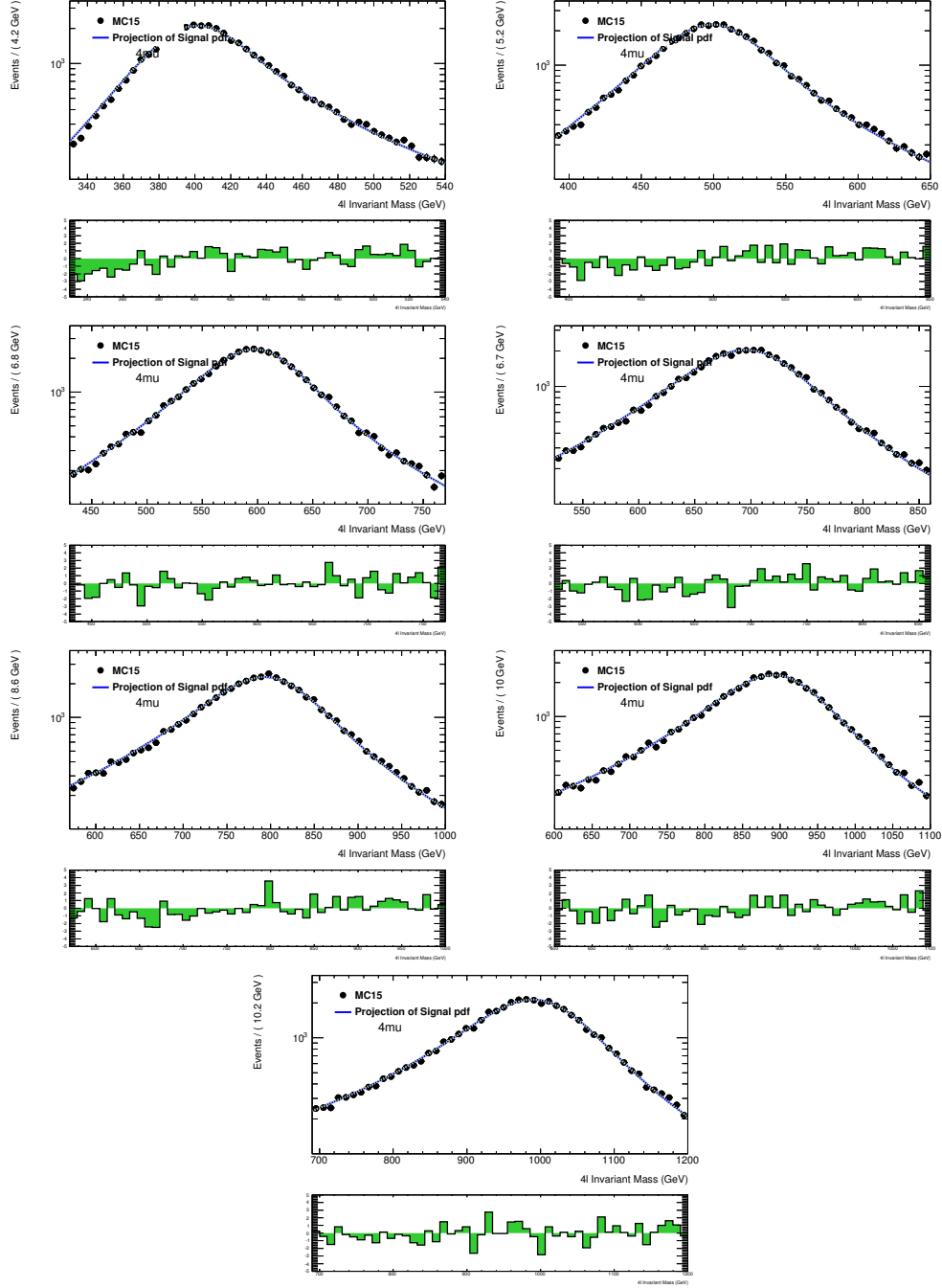


Figure 6.4: Comparison of the analytical shape convoluted with detector effects to reconstructed  $m_{4\mu}$  MC distribution for 400-1000 GeV masses and width equal to 15% of the mass.

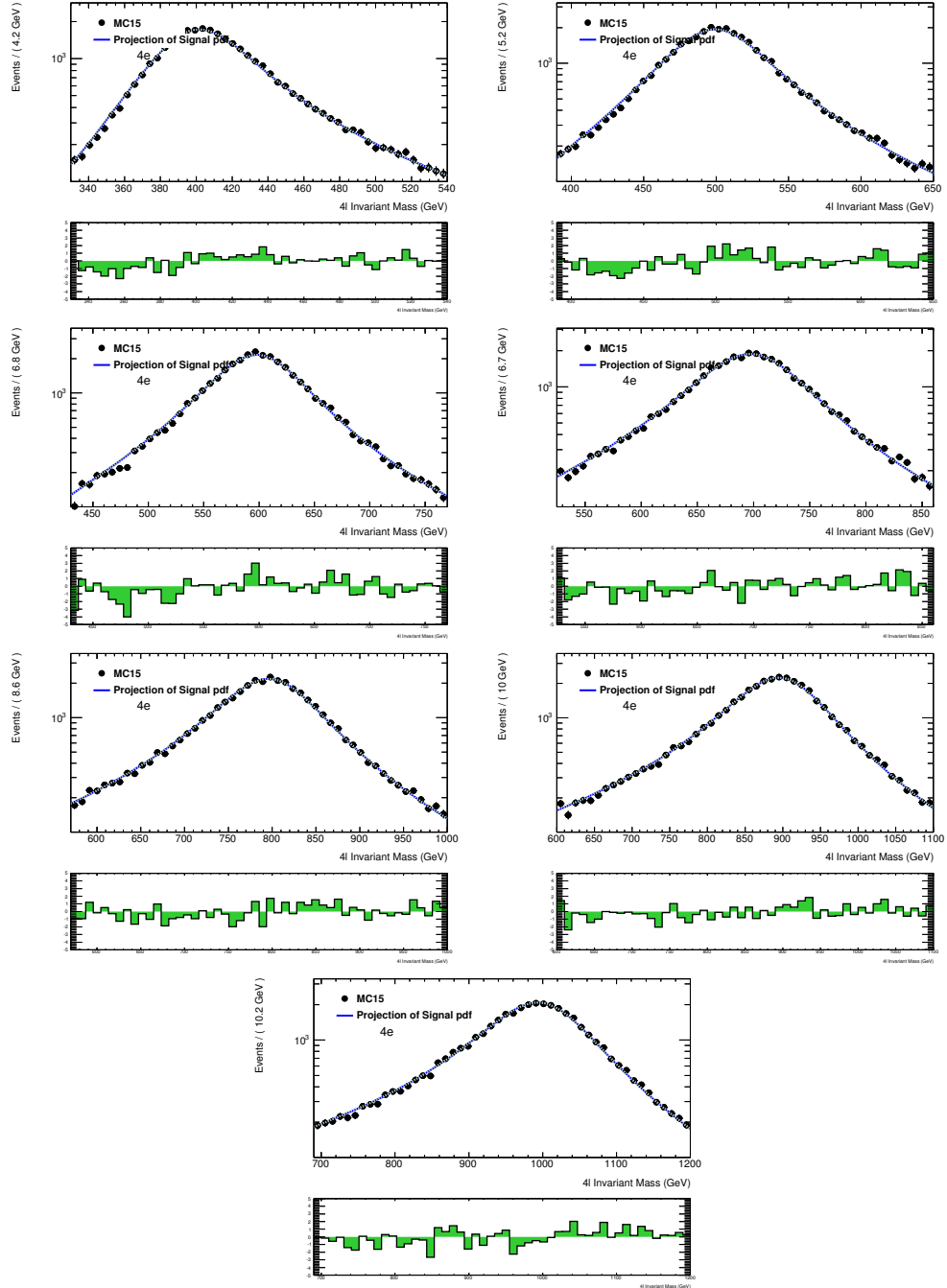


Figure 6.5: Comparison of the analytical shape convoluted with detector effects to reconstructed  $m_{4e}$  MC distribution for 400-1000 GeV masses and width equal to 15% of the mass.

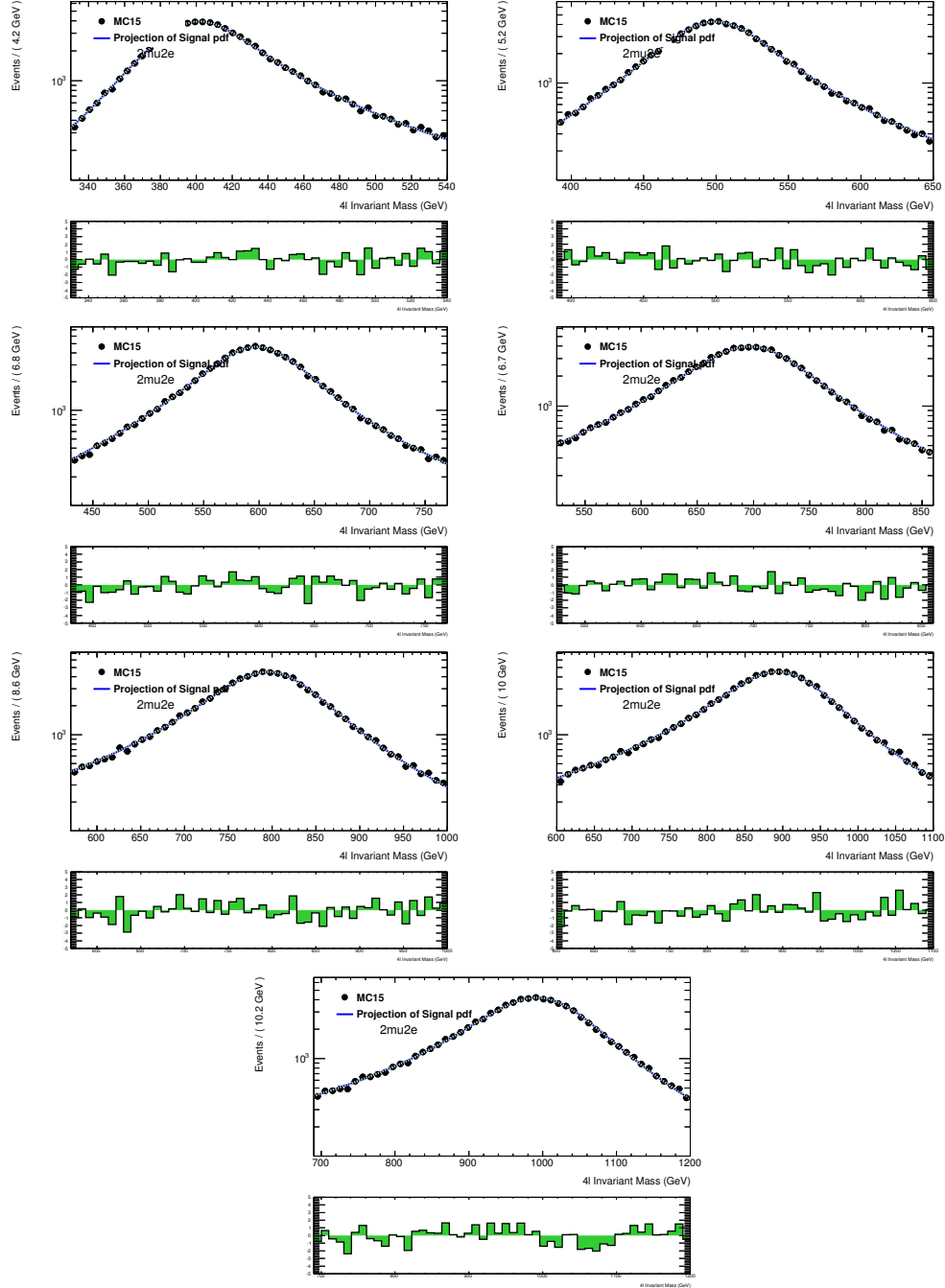


Figure 6.6: Comparison of the analytical shape convoluted with detector effects to reconstructed  $m_{2\mu 2e}$  MC distribution for 400-1000 GeV masses and width equal to 15% of the mass.

## 6.4 Interference modeling

As it is discussed in Section 2.6, the heavy Higgs boson with large width have non negligible interference with the SM Higgs boson and the SM  $gg \rightarrow ZZ$  process. This interference significantly affects the upper limit on the heavy Higgs cross section in LWA, therefore it should be carefully included in the analysis. The modelling of the the heavy Higgs interference with the SM Higgs boson is described in Section 2.6.1, while the modelling of the interference with the SM  $gg \rightarrow ZZ$  background is shown in Section 2.6.2. The validation of the signal model including both interferences is shown in Section 6.4.3.

### 6.4.1 Interference of the heavy Higgs with SM Higgs

Leading order theoretical calculations for the interference of the heavy Higgs boson and the SM Higgs boson (h-H) are shown in Section 2.6.1. Differential cross section for this process is described by Equation (2.26) that is written as:

$$\sigma_{pp}(m_{4\ell}) = 4 \cdot m_{4\ell} \cdot \mathcal{L}_{gg} \cdot \text{Re} \left[ \frac{1}{s - s_H} \cdot \frac{1}{(s - s_h)^*} \right] \cdot \Gamma_{H \rightarrow gg}(m_{4\ell}) \cdot \Gamma_{H \rightarrow ZZ}(m_{4\ell}) \quad (6.2)$$

It is easy to notice that this equation is very similar to the differential cross section of the signal, that was shown in the previous section, with the only difference in the propagator part. Moreover, as discussed at the end of Section 2.6.1, the propagator part that is different for the two processes does not affect kinematics of the final state, therefore these two processes have identical acceptance and detector resolution function. This important observation leads to the conclusion, that the interference process can be reproduced by simple reweighting of the signal MC samples.

Pseudo-MC samples that describe the interference can be built by reweighting the truth  $m_{4\ell}$  distribution of the signal sample by the ratio of the propagator parts of the two processes:

$$w(m_{4\ell}) = \frac{2 \cdot \text{Re} \left[ \frac{1}{s - s_H} \cdot \frac{1}{(s - s_h)^*} \right]}{\frac{1}{|s - s_H|^2}} \quad (6.3)$$

The reweighting procedure can be validated by comparing of a reweighted signal distribution for certain mass and width hypothesis to the nominal MC distribution for the same signal hypothesis. Figure 6.7 shows the comparison of the MC  $m_{4\ell}^{reco}$  distribution for the signal with  $m_H = 900$  GeV and  $\Gamma_H = 0.05 \times m_H$ , to the  $m_{4\ell}^{reco}$  distribution for the same signal hypothesis reweighted from the signal sample with  $m_H = 900$  GeV and  $\Gamma_H = 0.15 \times m_H$ . Good compatibility of the distributions provides a good closure test of the reweighting procedure.

A set of pseudo-MC samples for the interference process is produced with the reweighting procedure. These samples provide precise description of the interference including the reconstruction effects, and they will be further used for the validation of the interference model. Figure 6.8 shows the reconstructed invariant mass distributions for the signal and for the interference under different signal hypotheses. Each of the signal distributions has arbitrary normalisation, while the interference has a proper relative normalisation with respect to the corresponding signal. Moreover, relative normalisation of the interference and the signal

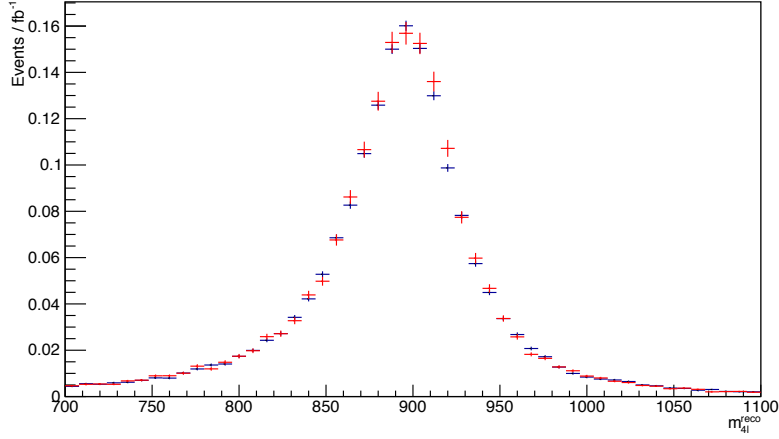


Figure 6.7: Comparison of the MC  $m_{4\ell}^{reco}$  distribution for the signal with  $m_H = 900$  GeV and  $\Gamma_H = 0.05 \times m_H$ , to the pseudo-MC  $m_{4\ell}^{reco}$  distribution for the same process reweighted from the signal sample with  $m_H = 900$  GeV and  $\Gamma_H = 0.15 \times m_H$ . Both MC samples are normalised to  $1 \text{ fb}^{-1}$  assuming SM-like heavy Higgs.

depends on the couplings of the heavy Higgs boson as it will be discussed further in this section. Relative normalisation in Figure 6.8 corresponds to the Standard Model couplings of the heavy Higgs boson.

Modelling of the interference is done in the same way as for the large width signal discussed in Section 6.3. The truth line shape is described by the computation of the leading order Feynman diagram given in Equation (6.2), that is further corrected for the acceptance effect. This model is compared to the pseudo-MC  $m_{4\ell}^{truth}$  distribution in Figure 6.9. The reconstructed shape is modelled by a convolution of the previously described truth model and the detector resolution function taken from the NWA signal parametrisation.

#### 6.4.2 Interference of the heavy Higgs with the SM $gg \rightarrow ZZ$

According to Section 2.6.2, it is not straightforward to perform fully analytical computation for the interference of the heavy Higgs boson and the SM  $gg \rightarrow ZZ$  background (H-B), however its line shape can be described by Equation 2.30 that is written as:

$$\sigma_{pp}(m_{4\ell}) = \mathcal{L}_{gg} \cdot \frac{1}{m_{4\ell}} \cdot \text{Re} \left[ \frac{1}{s - s_H} \cdot ((a_0 + a_1 \cdot m_{4\ell} + \dots) + i \cdot (b_0 + b_1 \cdot m_{4\ell} + \dots)) \right] \quad (6.4)$$

where  $a_i$  and  $b_j$  are unknown parameters. This function does not provide precise determination of the interference shape, however the remaining degrees of freedom can be fixed by fitting the MC  $m_{4\ell}$  distribution. The parameters  $a_i$  and  $b_j$  do not depend neither on signal mass nor on signal width hypotheses, therefore the interference model can be simultaneously fitted to all available interference samples in order to have suitable sensitivity over the full invariant mass range. After performing the fit, this model can be used for every hypothesis in the interesting ranges of signal mass and width. It was chosen to fit the model to the truth  $m_{4\ell}$  distribution after the signal region selection, in this case the shape correction due to acceptance will be absorbed into the unknown polynomials in the interference model. The interference model should be defined for each flavour decay channel separately since it

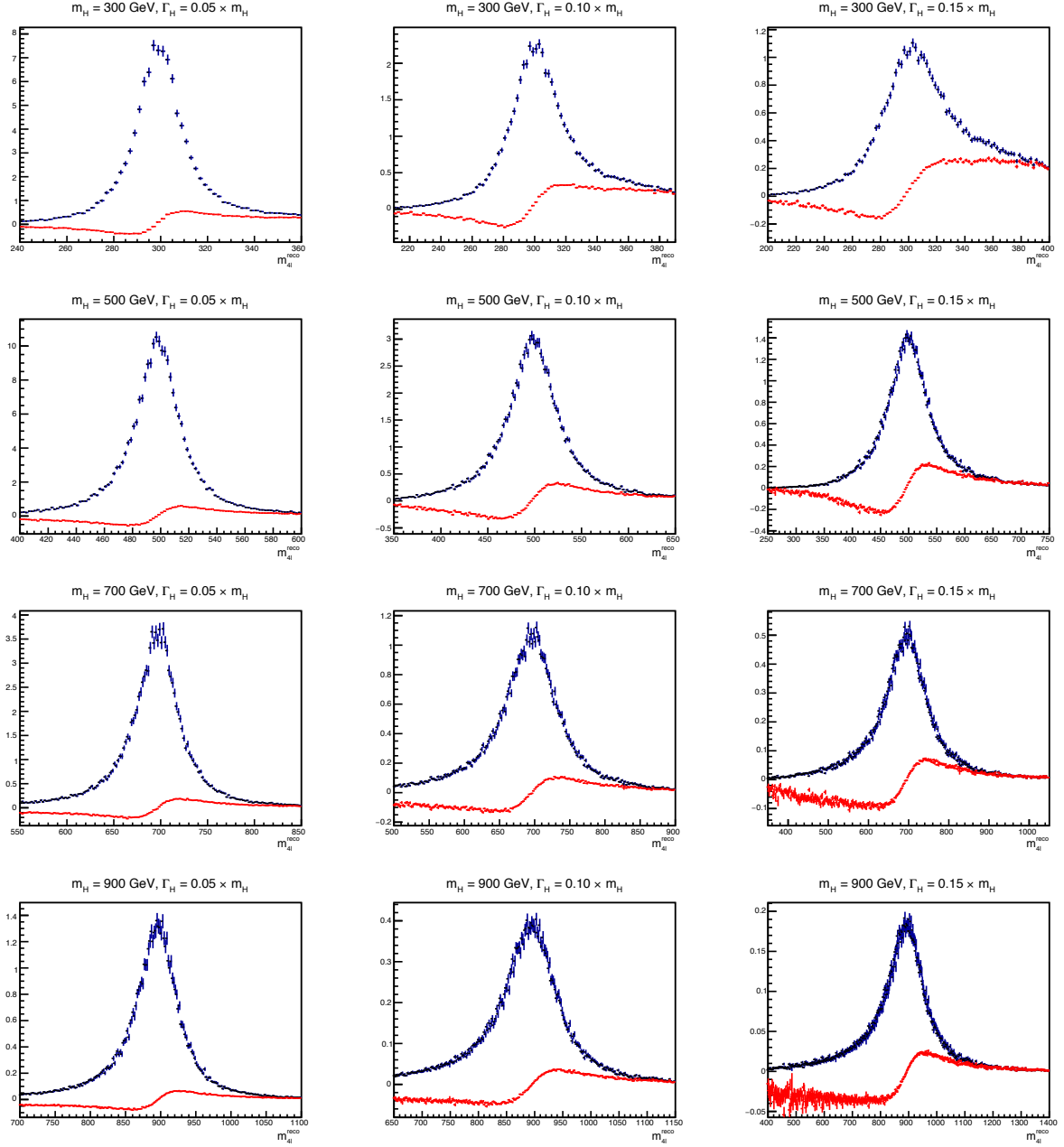


Figure 6.8: An overlay of the pseudo-MC  $m_{4\ell}^{reco}$  distribution for the h-H interference (red) and (pseudo-)MC distributions for the signal (blue) for different signal hypotheses. Each of the signal distribution has arbitrary normalisation, while the interference have a proper relative normalisation with respect to corresponding signal distribution. Signal distribution is taken from MC samples for  $\Gamma_H = 0.15 \times m_H$  hypotheses, while the pseudo-MC distribution is plotted for the others.



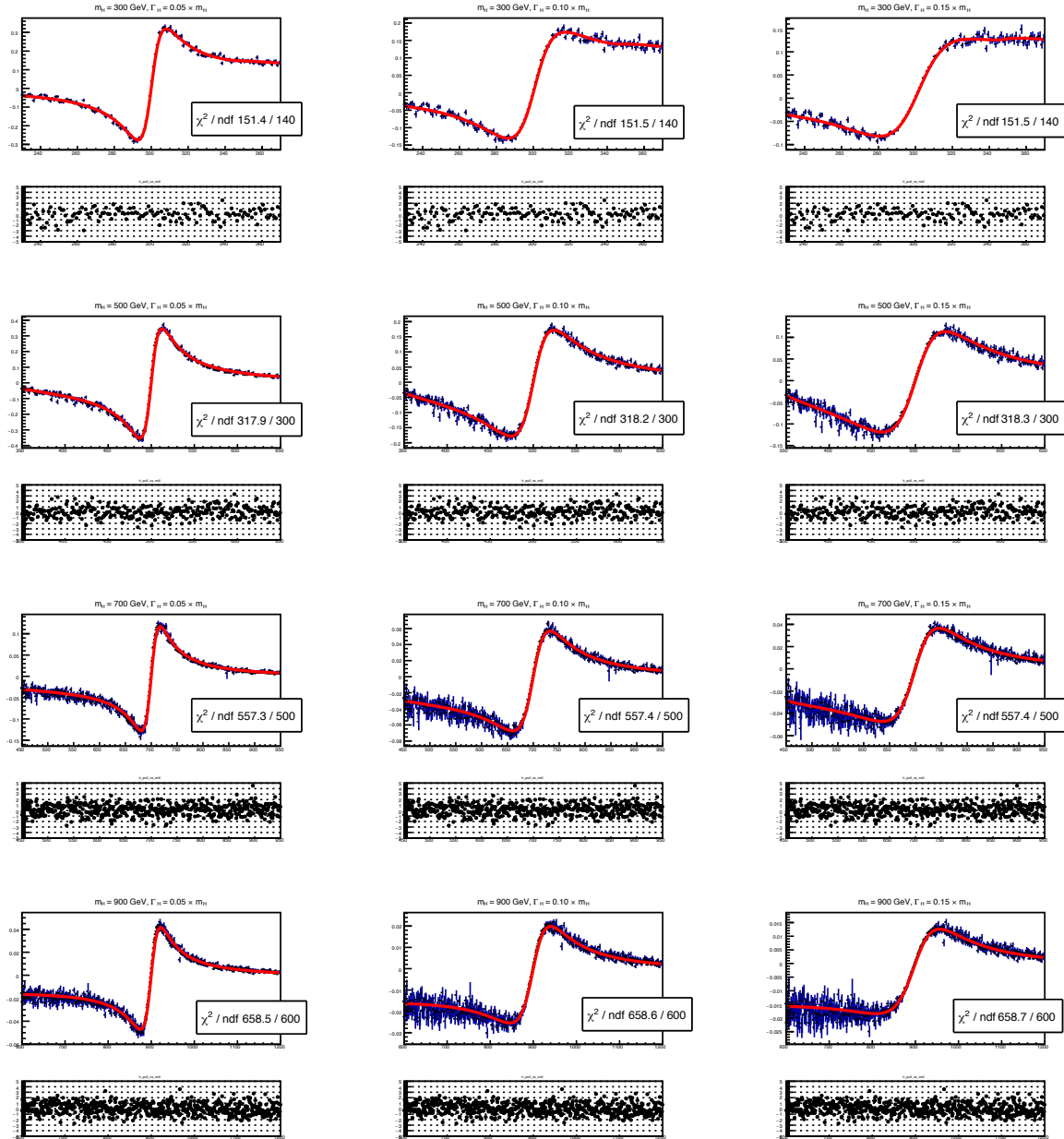


Figure 6.9: Comparison of the truth h-H interference model to the truth pseudo-MC  $m_{4\ell}$  distribution after the signal region selection.

includes the acceptance which is different among the final states. Results of the interference model fit to the MC distribution in different decay channels are shown in Figures 6.10-6.12 for different final states. The fits are of a good quality with the  $\chi^2/NDF$  close to 1.

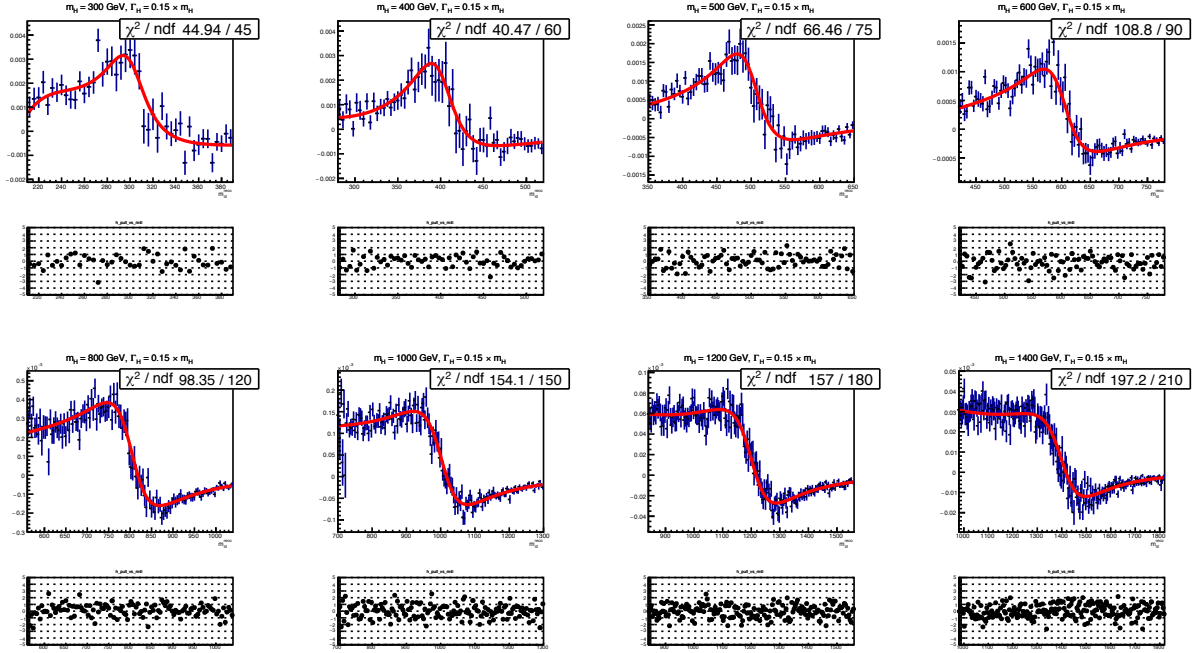


Figure 6.10: The interference (H-B) model fitted to the  $m_{4\ell}^{truth}$  MC distribution after signal region selection for  $4\mu$  decay channel.

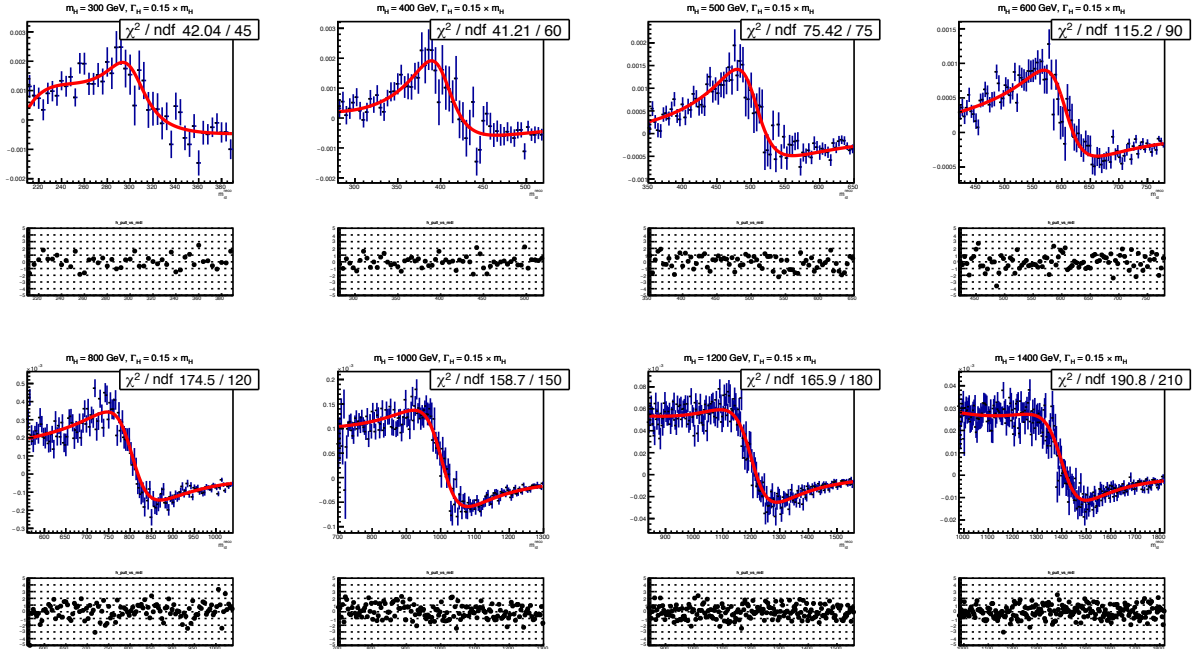


Figure 6.11: The interference (H-B) model fitted to the  $m_{4\ell}^{truth}$  MC distribution after signal region selection for  $4e$  decay channel.

In order to model the reconstructed  $m_{4\ell}$  distribution, the extracted from the fit shape can be convoluted with the detector resolution function. In this analysis, the detector resolution for the interference is assumed to be similar to the signal one, that is described by the NWA

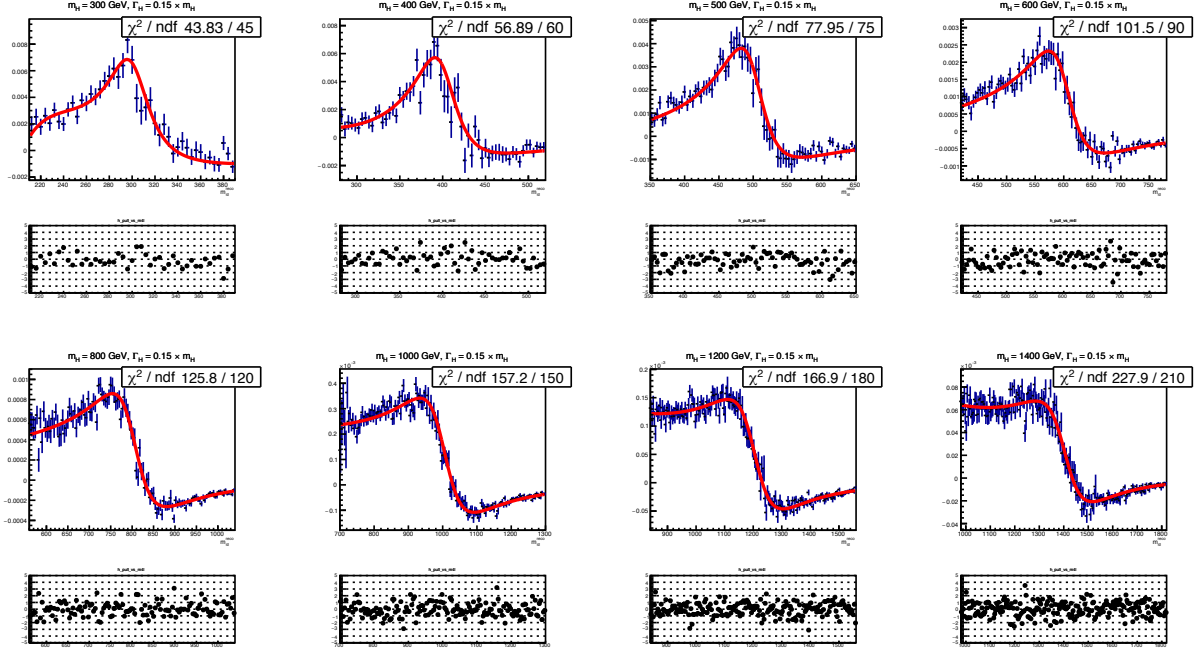


Figure 6.12: The interference (H-B) model fitted to the  $m_{4\ell}^{truth}$  MC distribution after signal region selection for  $2\mu 2e$  decay channel.

signal parametrisation. Validation of the reconstructed shape is shown in the following section.

### 6.4.3 Complete signal model including the interferences

In the previous sections the LWA signal and its interference with the Standard Model processes was discussed, while this section is focussed on the integration of the complete signal plus interference model (further referred as complete signal model) into the analysis. Relative importance of the interference and of the complete signal model for the reconstructed  $m_{4\ell}$  shape will be discussed.

#### Relative importance of the interference

Relative normalisation of the interference with respect to the signal depends on the actual couplings of the heavy Higgs boson. Here while speaking about the coupling we assume that the heavy Higgs boson have the SM-like couplings that are scaled in the same way with a common scale factor  $\kappa$ . In this analysis the upper limit is set on the production cross section times the branching ratio while both the mass and the width of the signal are fixed. The signal cross section is a function of couplings, mass and width only, and the later two are fixed, therefore the cross section limit is directly related to the heavy Higgs couplings that are actually tested:  $\sigma_H \propto \kappa^2$ . While normalisation of the both interferences will have only linear dependance from the heavy Higgs couplings:  $\sigma_{interf} \propto \kappa$ . It means that the relative normalisation of the interference w.r.t. to the signal is actually dependent on the analysis sensitivity, namely importance of the interference will grow with the analysis sensitivity. This feature is carefully taken into account while setting the cross section limit in LWA analysis. The plots in the previous sections are done for the SM-like couplings of the heavy Higgs.

Figure 6.13 shows the overlay of the signal and the both interferences for different mass

and width hypotheses assuming the SM-like couplings for the heavy Higgs boson, while also showing the total line shape. An effect of the interference on the overall signal normalisation is summarised in Table 6.1. Since current analysis sensitivity (the first analysis that includes the interference is based on  $36.1 \text{ fb}^{-1}$  of 13 TeV data) is slightly different from the SM-like assumption, it is more interesting to see the relative importance of the interference with more realistic couplings shown in Figure 6.14, namely the expected limits on the couplings. It is easy to see that the interference is important over the large tested phase space.

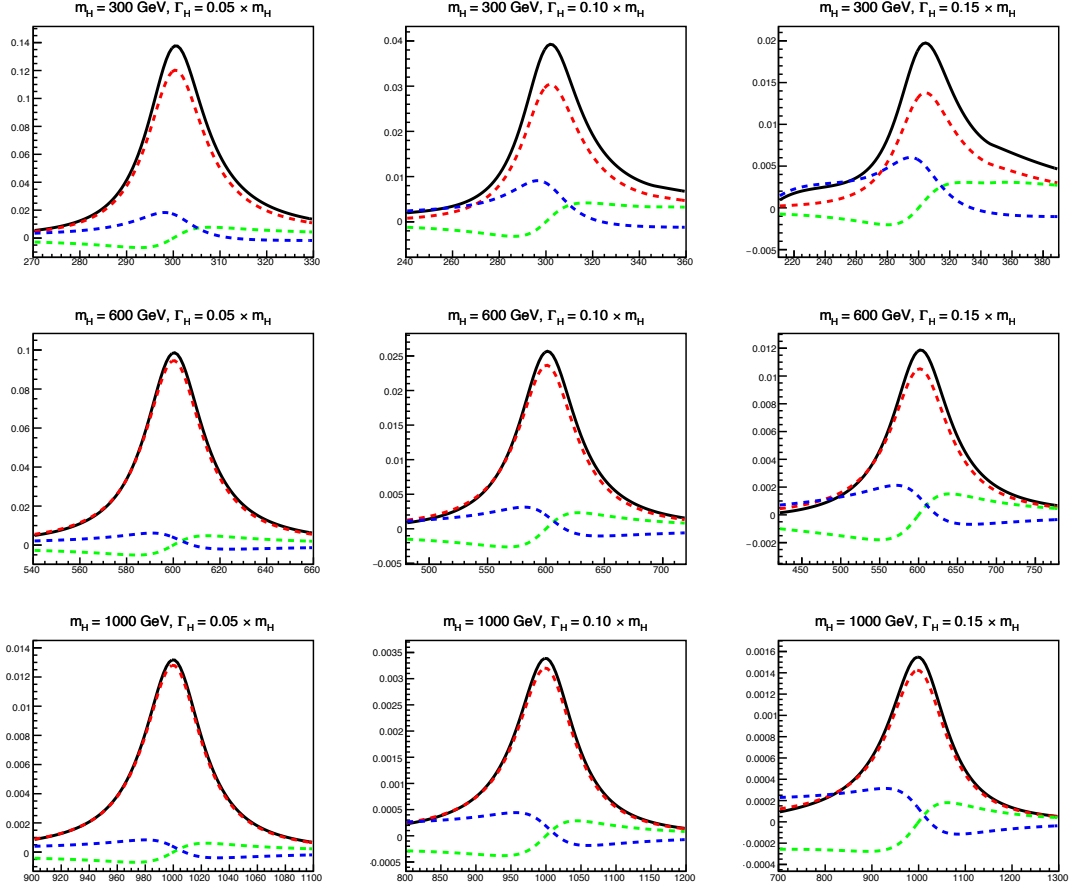


Figure 6.13: Overlay of the truth  $m_{4\ell}$  model for the signal (red), h-H interference (green) and H-B interference (blue) for the SM-like couplings of the signal, while the sum of three processes is shown as well (black).

Table 6.1: An effect of the interference on the overall signal normalisation is shown as a ratio of the total (black) and the signal (red) yields in Figure 6.13. The SM-like couplings of the heavy Higgs boson are assumed.

$\frac{Total}{Signal}$	$\Gamma_H = 0.05 \times m_H$	$\Gamma_H = 0.10 \times m_H$	$\Gamma_H = 0.15 \times m_H$
$m_H = 300 \text{ GeV}$	1.15	1.33	1.54
$m_H = 600 \text{ GeV}$	1.04	1.07	1.09
$m_H = 1000 \text{ GeV}$	1.03	1.05	1.06

### Reconstructed shape

As described in Sections 6.3, 6.4.1 and 6.4.2, all the three processes are modelled by a convolution of the truth shape with the detector resolution function. In practice, since the resolution function is common for all the processes it makes more sense to add up all the three truth shapes with proper relative normalisation and further convolute them with the

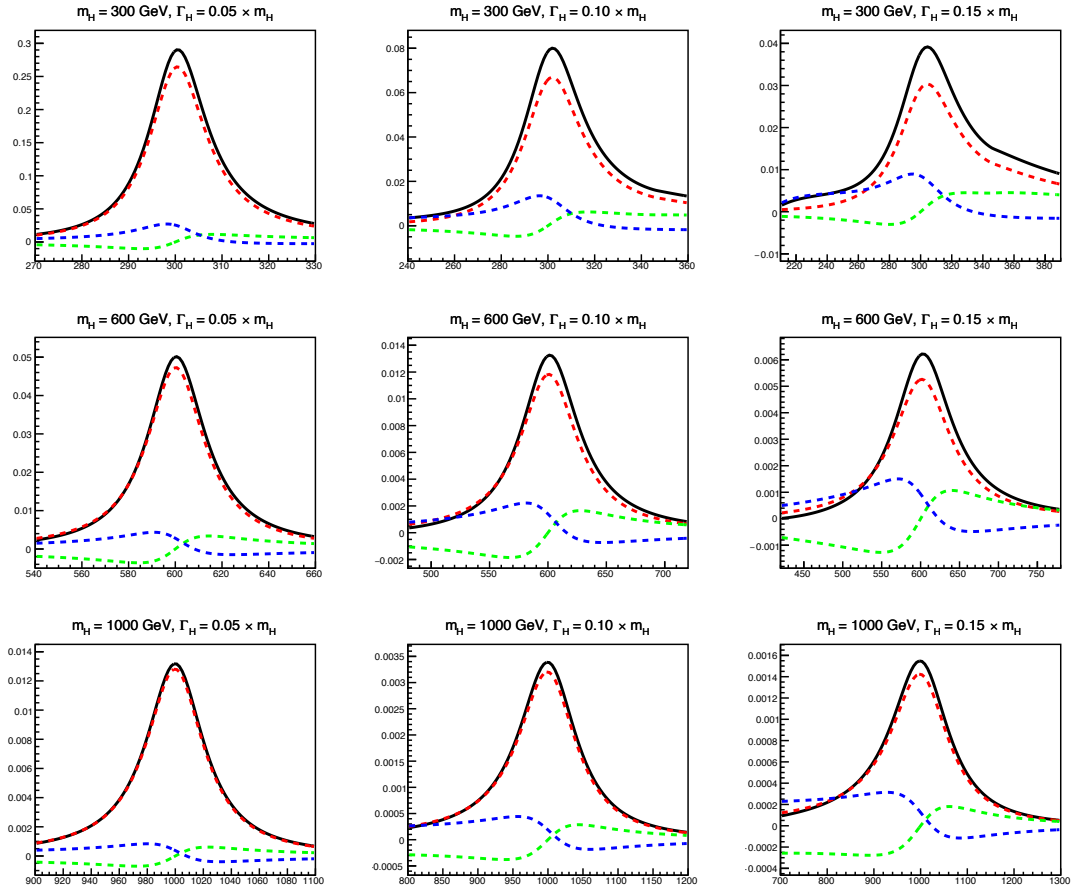


Figure 6.14: Overlay of the truth  $m_{4\ell}$  model for the signal (red), h-H interference (green) and H-B interference (blue) for the for couplings of the signal compatible with the expected analysis sensitivity, while the sum of three processes is shown as well (black).

detector resolution function. This approach allows to optimise the computation procedure, and moreover, it allows to cancel negative parts of individual shapes that could cause some technical problems for implementation of the model.

Unfortunately, there is no fully simulated MC samples that could be used for validation of the signal plus interference model, however it is possible to perform the validation with a sum of MC samples that were used for the modelling of the individual components: LWA signal MC samples, reweighted pseudo-MC samples for h-H interference and MC samples for H-B interference. The sum of samples provides the MC distribution of the signal plus both interferences assuming the SM-like coupling of the heavy Higgs. Comparison of the complete signal model to this MC distribution is shown in Figures 6.15-6.17 for different final states. The model shows good compatibility with the MC distributions. A small mismodelling of the shape in the  $4e$  decay channel can be originated either from the electron resolution mismodelling in the fast simulation used for the H-B interference or from physical difference of the interference and signal resolution due to different kinematics of the final state. However the effect is small and it is not a showstopper for the method.

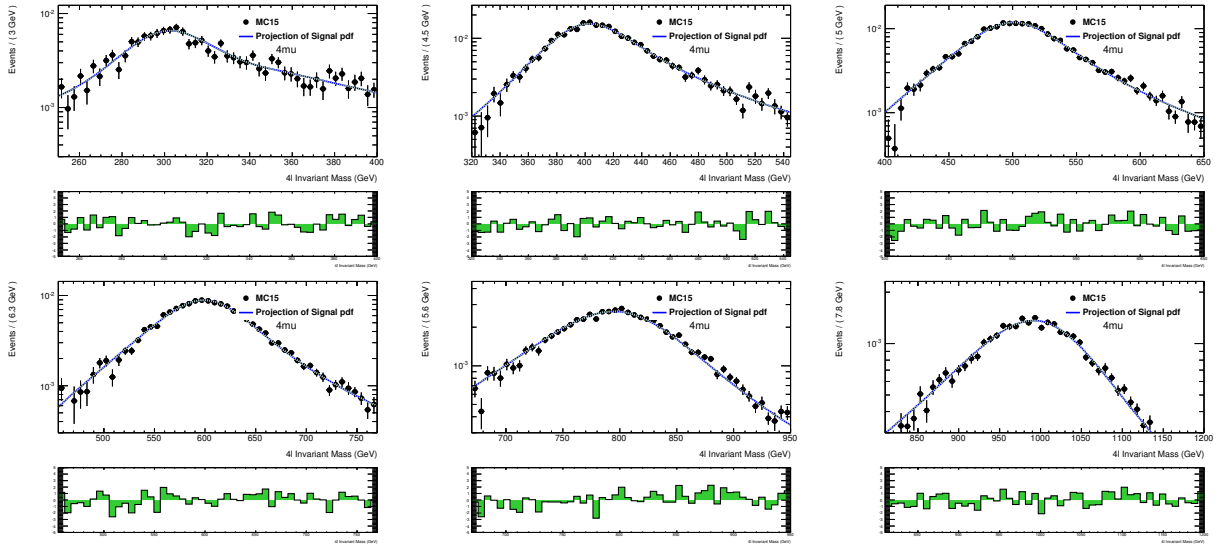


Figure 6.15: Comparison of the complete signal model including the interferences to reconstructed  $m_{4\mu}$  distribution of a sum of the signal and interference MC samples for 300, 400, 500, 600, 800, 1000 GeV masses and width equal to 15% of the mass.

### Interference summary

Complete modelling of the interference was shown in this section. The model allows to include the leading order interference effect into the LWA heavy Higgs search. Minor mismodelling in the  $4e$  decay channel for the signal mass hypotheses above 900 GeV is under investigation, however the effect is minor. The cross section limits shown in this chapter do not include the interference because the modelling was not finalised by that time, however it is included in the updated results presented in Chapter 8.

## 6.5 Results

Data events observed in the signal region as well as the expected background yields are shown in Section 5.7, while the statistical procedure used to set the limits is described in Section 5.8.

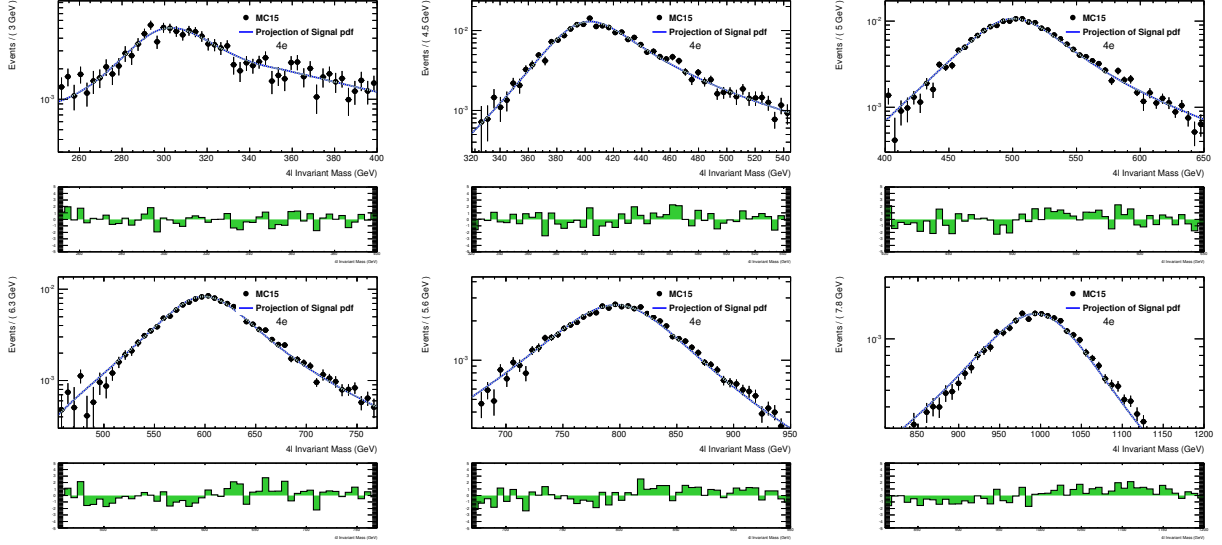


Figure 6.16: Comparison of the complete signal model including the interferences to reconstructed  $m_{4e}$  distribution of a sum of the signal and interference MC samples for 300, 400, 500, 600, 800, 1000 GeV masses and width equal to 15% of the mass.

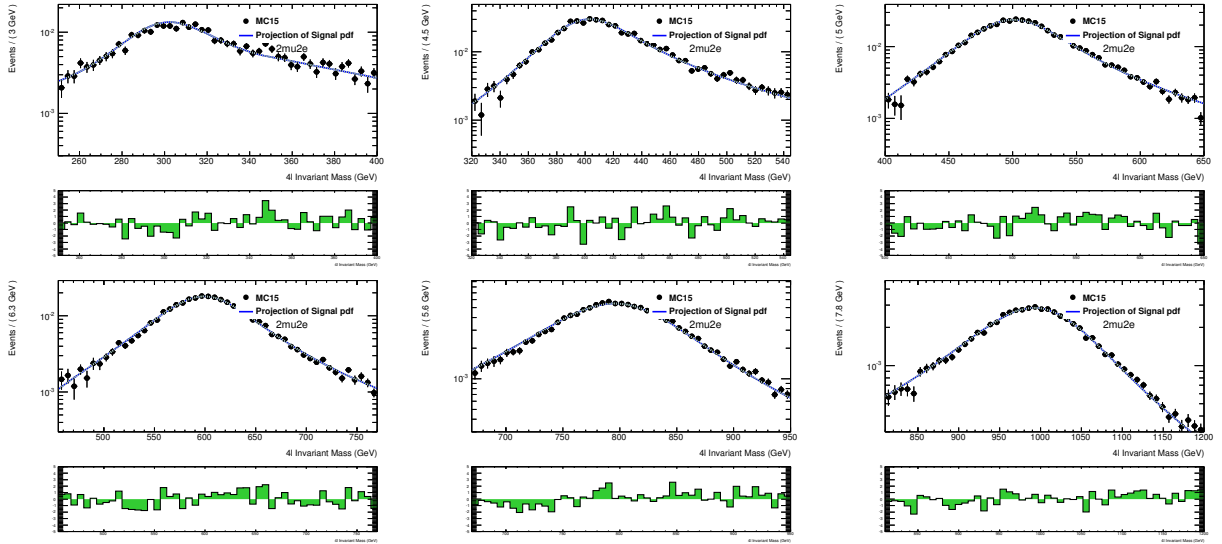


Figure 6.17: Comparison of the complete signal model including the interferences to reconstructed  $m_{2\mu 2e}$  distribution of a sum of the signal and interference MC samples for 300, 400, 500, 600, 800, 1000 GeV masses and width equal to 15% of the mass.

In this section upper limits on the inclusive production cross section times the branching ratio for the heavy Higgs boson with large width are presented. Presented results do not include the interference, thus the search was not performed below 400 GeV where the interference becomes large. Figures 6.18(a), 6.18(b), and 6.18(c) show the limits for the hypotheses of the widths equal to 1%, 5% and 10% of signal mass respectively. No significant excess observed.

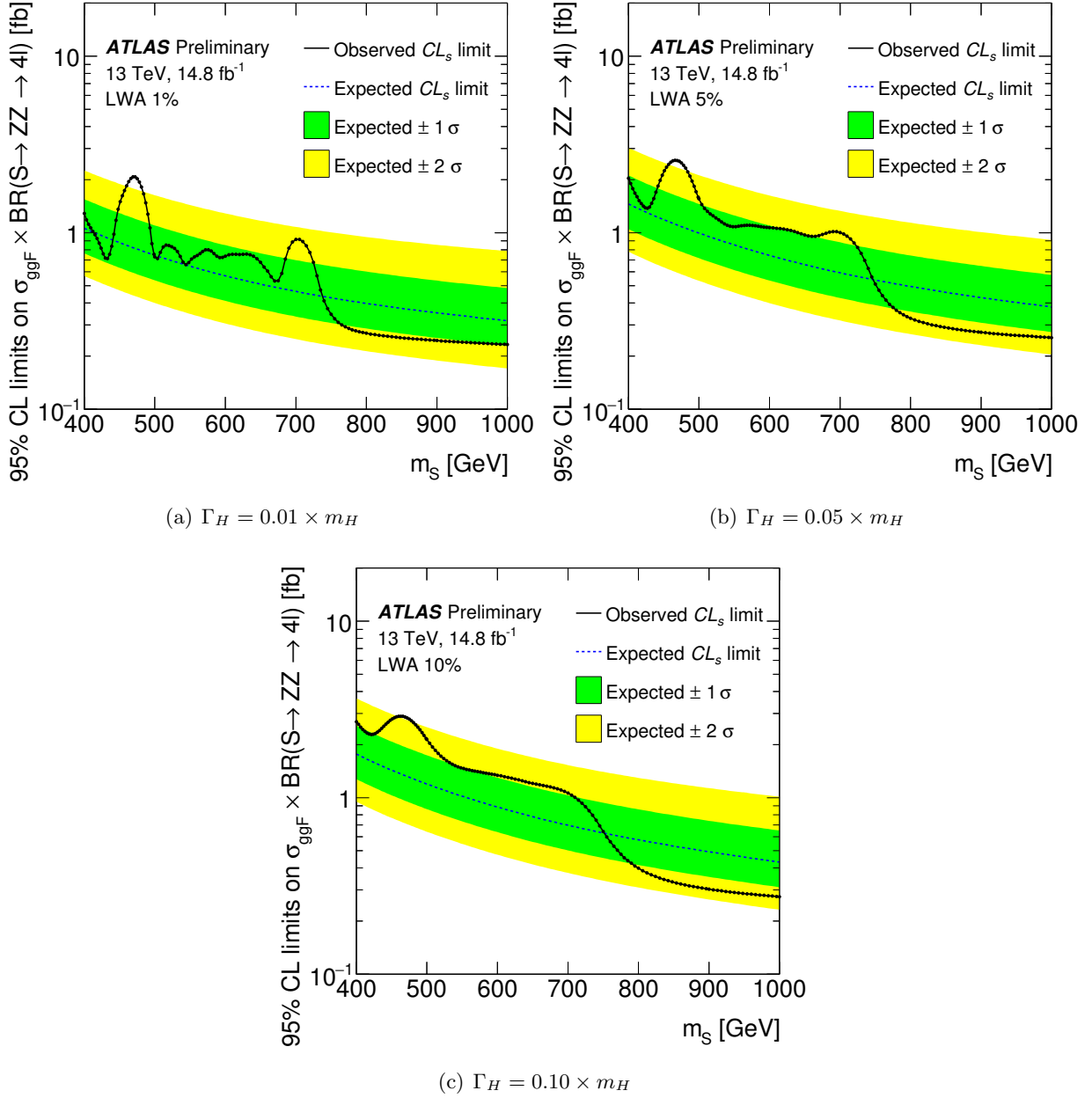


Figure 6.18: 95% confidence limits on  $\sigma \times \text{BR}(S \rightarrow ZZ \rightarrow 4\ell)$  assuming a width 1%, 5% and 10% of  $m_H$ .





# Improvement of the narrow width heavy Higgs search using *MELA* kinematic discriminant

---

## 7.1 Overview

This chapter describes an extension of the heavy Higgs search that is aiming to improve the sensitivity by including extra kinematic discrimination of the signal to background under scalar Higgs hypothesis. The upper limit is set on the inclusive production cross section of a scalar heavy Higgs boson in the Narrow Width Approximation.

Under the assumption of a spin 0 particle, kinematics of the signal final state will be different from the background's one. It can be exploited to increase signal to background ratio and therefore to improve the analysis sensitivity. This idea is implemented by introducing a matrix element based kinematic discriminant (*MELA*) that is aiming to discriminate two processes:  $H \rightarrow ZZ \rightarrow 4\ell$  and  $qq \rightarrow ZZ \rightarrow 4\ell$ .

The kinematic discriminant is used to break down the SR into *MELA* related categories. This categorisation allows to build very clean signal sub-regions, while not cutting any signal acceptance. Another solution could be a 2-D fit of the  $m_{4\ell}$  and *MELA* variables, but this approach was abandoned since it requires much higher MC statistics.

This extension uses the heavy Higgs search analysis framework, such as MC samples, event selection, background estimation and statistical tools. Additional components will be discussed further in this chapter.

There is a number of reasons that introduce some limitations on the method at very low masses:

- it is hard to control the discriminant below 200 GeV (close to  $ZZ$  on-shell threshold), in particular when the signal samples are not available for this mass range due to limited resources;
- Modelling of the *MELA* variable for the reducible background is not straightforward because of very low MC statistics in the SR, while the kinematic distributions in the CRs can be different for the SR ones. Fortunately, contribution of the reducible background is negligible above 200 GeV;
- the irreducible background modelling is much simpler if the off shell part of the  $ZZ^{(*)}$  continuum is not included.

Therefore, the *MELA* improved cross section limit is set for the mass hypothesis from 300 to 1000 GeV, that allows to analyse the  $m_{4\ell}$  spectrum starting from 200 GeV.

Current work is setting limits on the inclusive production cross section only, while assuming

ggF to be the dominant production mode. The analysis cannot consider different production modes separately due to limited MC statistics of signal and background samples. Namely, the available MC statistics is not sufficient for the background estimate and further optimisation of the discriminant in the VBF category, as it is defined in the nominal analysis. Modelling of the ggF events falling into the VBF category would also require additional set on MC samples.

## 7.2 MELA discriminant

Assuming that the signal is a spin 0 particle, kinematics of its final states will be different from the background's one. This feature is capable to add extra separation power between the signal and background, that will lead to an improvement of the analysis sensitivity. Event kinematics can be used in terms of a *MELA* discriminant that is derived from the signal and background matrix elements computed with MadGraph [126]. The matrix element is proportional to the probability of the certain final state to be produced by the given process, therefore it can be considered as a quantity that summarise information about the final state kinematics. The *MELA* variable is defined as follows:

$$MELA = \frac{M_{Higgs}}{M_{Higgs} + c \cdot M_{qqZZ}} \quad (7.1)$$

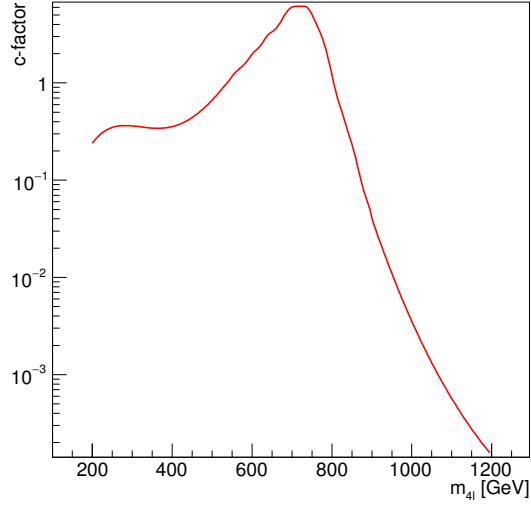
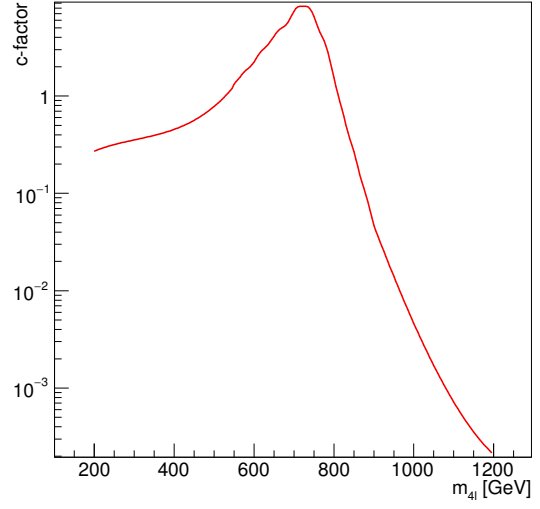
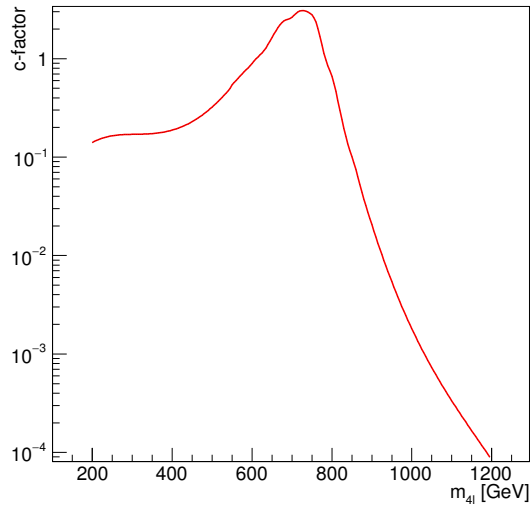
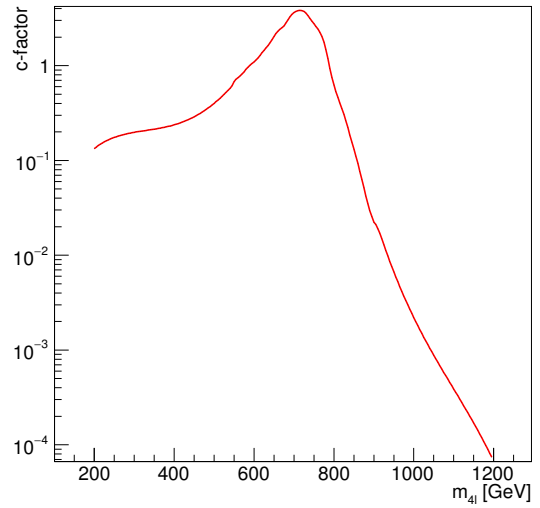
where  $M_{Higgs}$  and  $M_{qqZZ}$  are the matrix elements of the heavy Higgs boson ggF production and the SM  $qq \rightarrow ZZ$  respectively.  $c$ -factor is an arbitrary factor that is aiming to reduce correlation of the *MELA* with the  $m_{4\ell}$ . By construction the *MELA* variable is confined between 0 and 1, that is very convenient for the practical use. Since signal like events will mostly have high values of  $M_{Higgs}$  and low values of  $M_{qqZZ}$ , and vice-versa for background like events, it is easy to see that signal *MELA* distribution will be peaking at higher values than for the background.

The  $c$ -factor is a mass dependent relative normalisation of the background matrix element w.r.t. the signal one. It does not bring any additional separation power, but proper definition of the  $c$ -factor is important to make *MELA* equally distributed between 0 and 1, that is crucial for the binned based approach described further. The  $c$ -factor is built in such a way that an integral of the  $MELA > 0.75$  tail of  $qq \rightarrow ZZ$  distribution remains mostly constant for the whole mass range. In Figure 7.1, the  $c$ -factor is shown as a function of mass for all lepton decay channels.

Comparison of the signal and background *MELA* distributions for different mass points is shown in Figure 7.2.

This discriminant was included into the analysis by performing the 1D fit of  $m_{4\ell}$  in categories that correspond to different *MELA* bins. *MELA* is split into 5 bins of equal width. It can be clearly seen from Figure 7.2 that the first bin  $[0.0, 0.2]$  is highly populated with the background and has very low signal contribution, while the last bin  $[0.8, 1.0]$  has a very clear signal signature. Only 4 last bins are used in the analysis, since the first bin was found not to add any sensitivity. Taking into account lepton flavour based categorisation of the signal region, there are  $3 \times 4 = 12$  separate categories simultaneously fitted to extract the cross section limits.

Signal modelling for each of the categories is shown in Section 7.3, while the background

(a)  $4\mu$ (b)  $4e$ (c)  $2\mu 2e$ (d)  $2e 2\mu$ Figure 7.1:  $c$ -factor as a function of mass for different flavour final states.

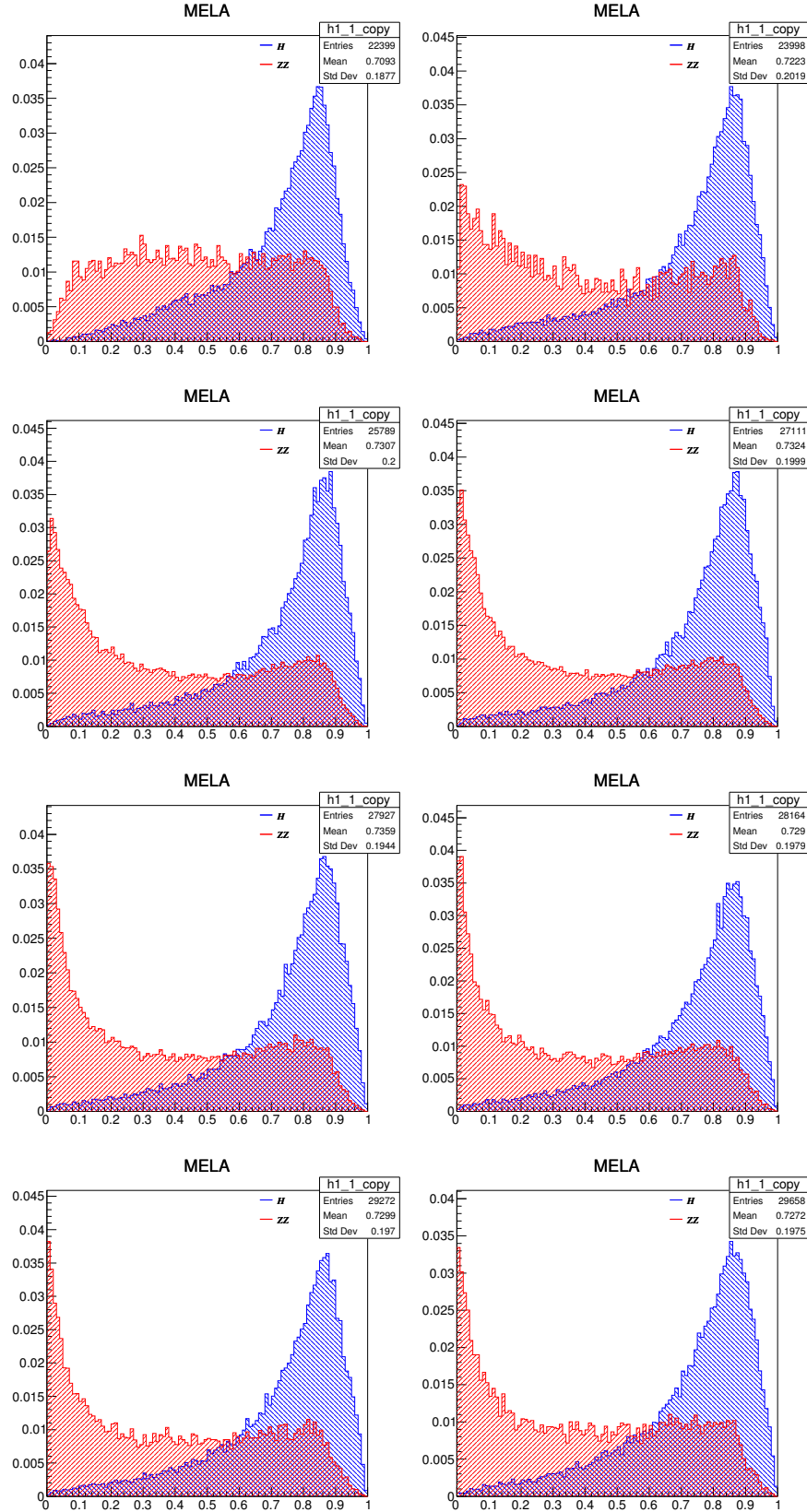


Figure 7.2:  $MELA$  distributions for the signal (blue) and  $qq \rightarrow ZZ$  background (red) around 300, 400, 500, 600, 700, 800, 900 and 1000  $GeV$ .

---

modelling is described in Section 7.4.

### 7.3 Signal modelling

#### Acceptance

The signal acceptance is first computed per lepton flavour decay channel as described in Section 5.5.1. The acceptance for each category is obtained by splitting *MELA*-inclusive one according to signal fractions that fall into each *MELA* bin. This procedure allows to compute the signal acceptance for each available mass point, and for other values it is interpolated using third order polynomial.

Both *MELA*-inclusive and per-bin acceptance is shown in Figure 7.3. The method was checked by comparing the sum of the per bin acceptances to the *MELA*-inclusive one. Small mismatch was observed in  $4\mu$  case, that is still covered by the 1% systematic uncertainty due to acceptance interpolation introduced in Section 5.5.1. Therefore no additional uncertainties associated to the signal acceptance in *MELA* bins.

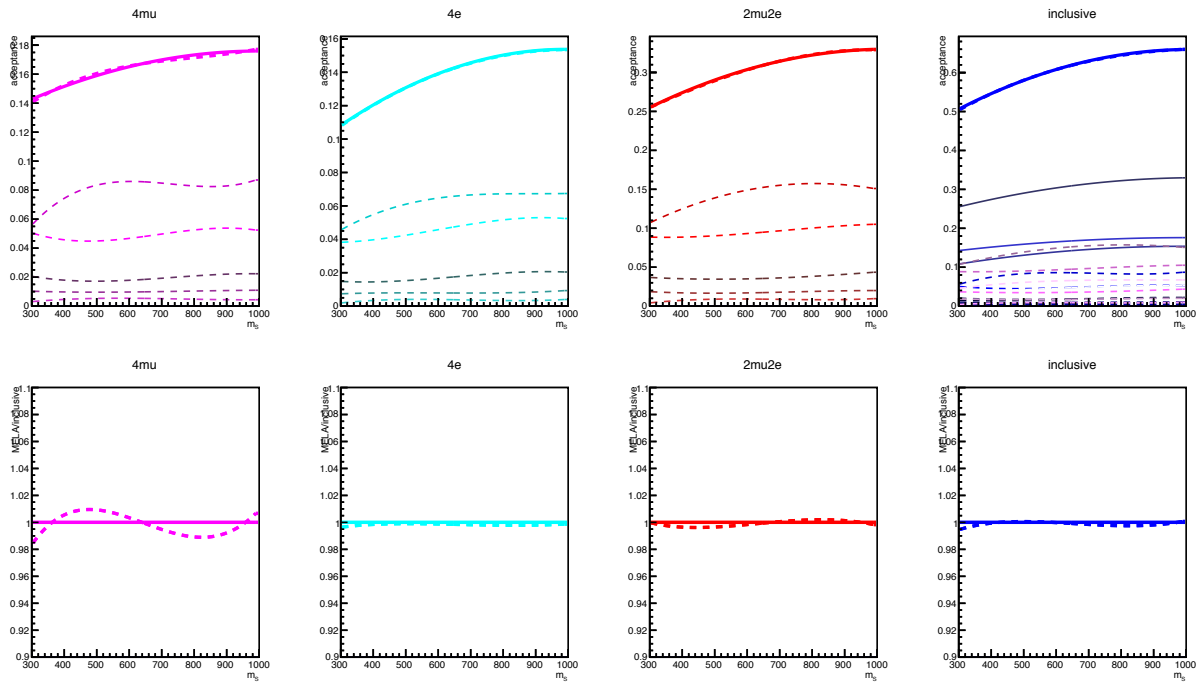


Figure 7.3: The signal acceptance as a function of mass in different flavour decay channel:  $4\mu$ ,  $4e$ ,  $2\mu 2e$  and inclusive. Solid line corresponds to the *MELA*-inclusive acceptance while the dashed lines show the acceptance in *MELA* bins. Bottom plots show the ratio of a sum of the acceptance in all *MELA* bins to *MELA*-inclusive one. This ratio can be understood as an uncertainty due to acceptance interpolation for intermediate mass values.

#### Shape modelling

The same signal  $m_{4\ell}$  shape model as for the nominal analysis is used here as well. Detailed description of the shape model and parameter interpolation is given in Section 5.5.2.

The signal shape is defined individually for each lepton decay channel per *MELA* bin. The  $[0.2, 0.4]$  *MELA* bin has not enough MC statistics to perform the shape extraction, therefore the shape from the nearest bin was used there. The signal shapes in different categories are shown in Figures 7.4 - 7.12, while the normalised Pearson  $\chi^2$  of the fits is given in Table 7.1. The signal model shows a good fit quality with the normalised Pearson  $\chi^2$  below 2.0 for each category.

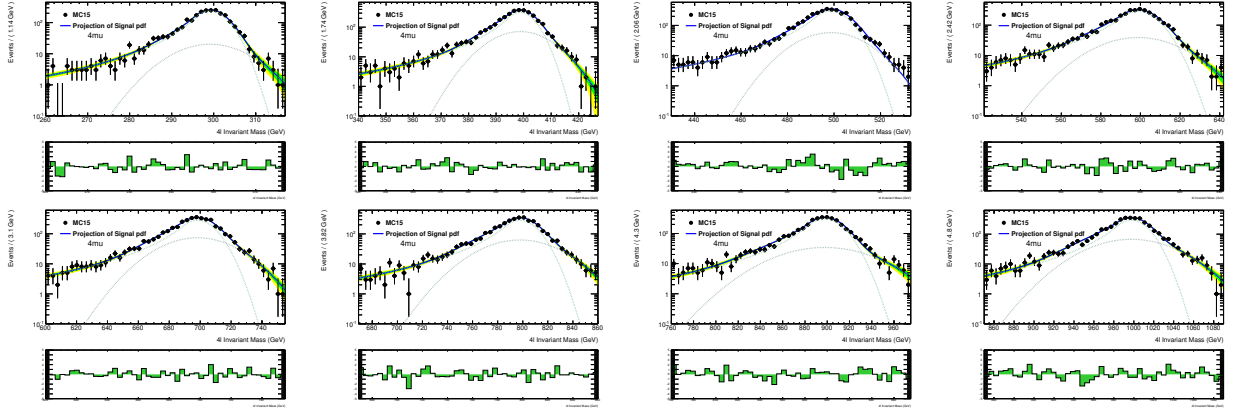


Figure 7.4: Distributions of  $m_{4\mu}$  invariant mass fit projection in the  $[0.8,1.0]$  *MELA* bin of the signal samples from mass of 300 to 1000 GeV in steps of 100 GeV.

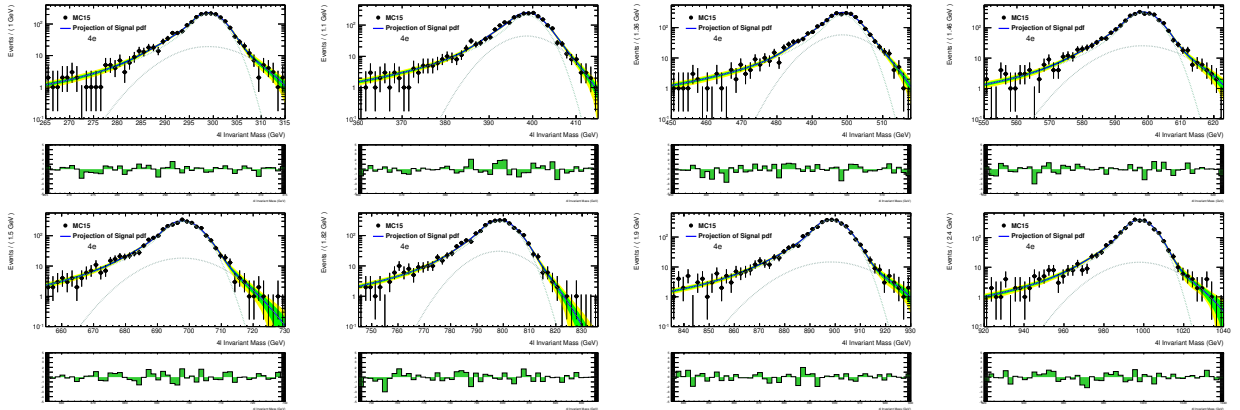


Figure 7.5: Distributions of  $m_{4e}$  invariant mass fit projection in the  $[0.8,1.0]$  *MELA* bin of the signal samples from mass of 300 to 1000 GeV in steps of 100 GeV.

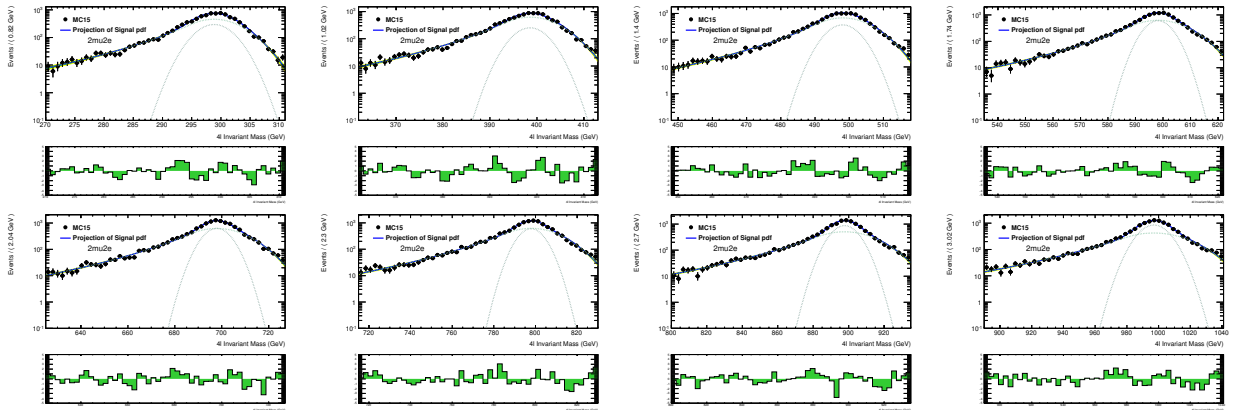


Figure 7.6: Distributions of  $m_{2\mu 2e}$  invariant mass fit projection in the  $[0.8,1.0]$  *MELA* bin of the signal samples from mass of 300 to 1000 GeV in steps of 100 GeV.



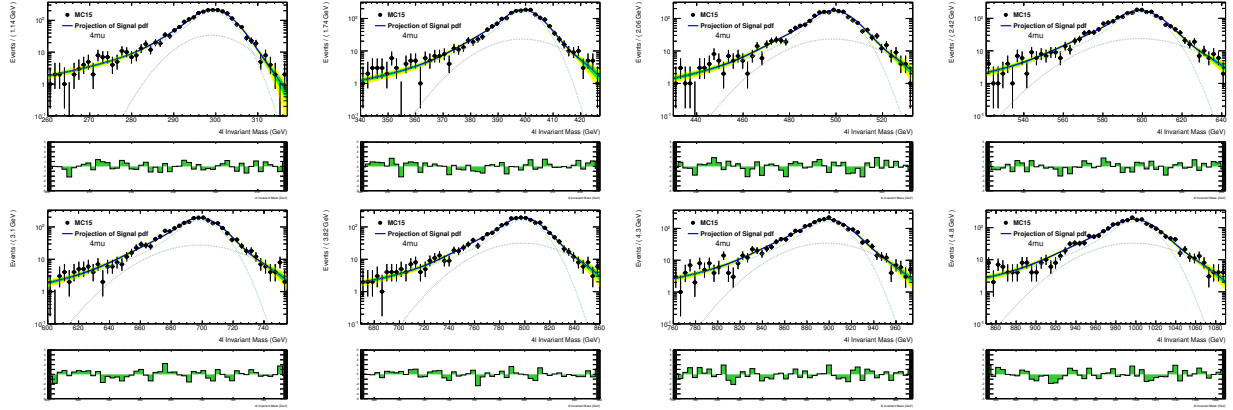


Figure 7.7: Distributions of  $m_{4\mu}$  invariant mass fit projection in the  $[0.6,0.8]$   $MELA$  bin of the signal samples from mass of 300 to 1000 GeV in steps of 100 GeV.

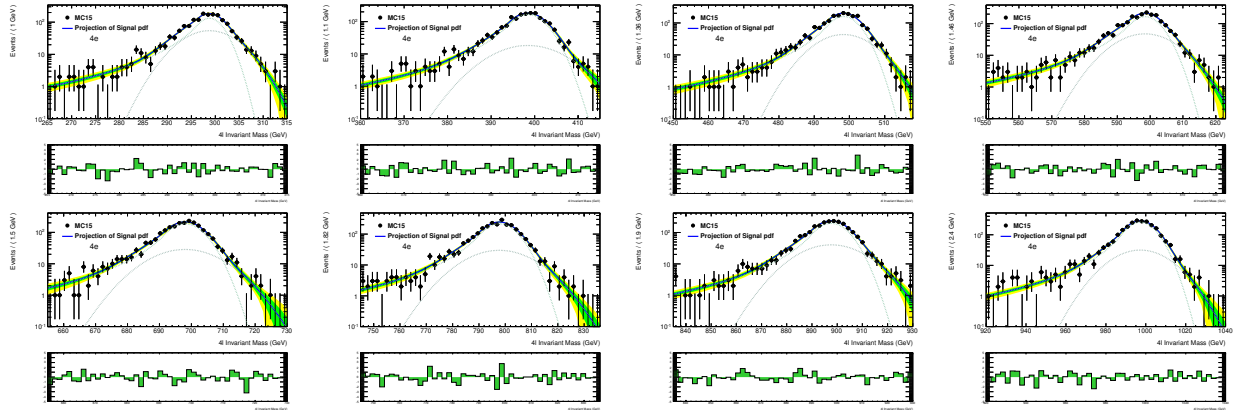


Figure 7.8: Distributions of  $m_{4e}$  invariant mass fit projection in the  $[0.6,0.8]$   $MELA$  bin of the signal samples from mass of 300 to 1000 GeV in steps of 100 GeV.

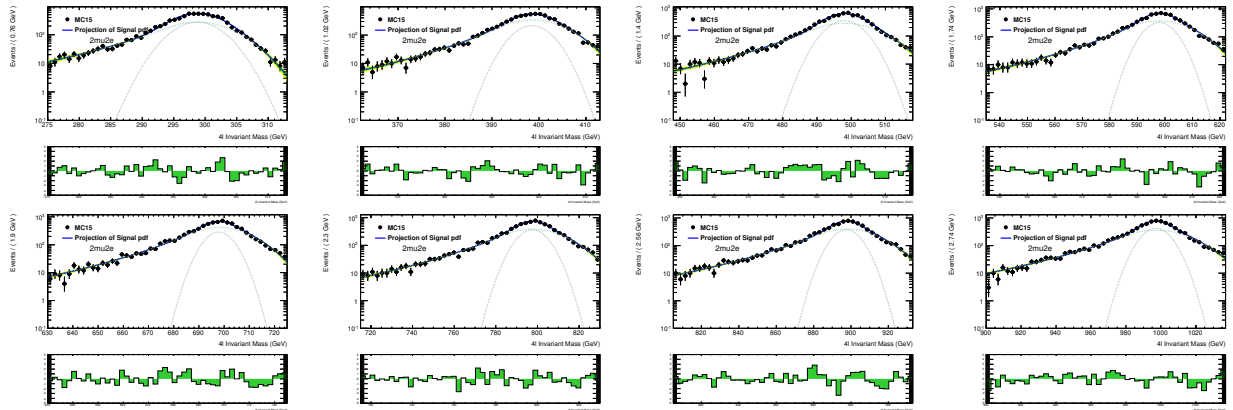


Figure 7.9: Distributions of  $m_{2\mu 2e}$  invariant mass fit projection in the  $[0.6,0.8]$   $MELA$  bin of the signal samples from mass of 300 to 1000 GeV in steps of 100 GeV.

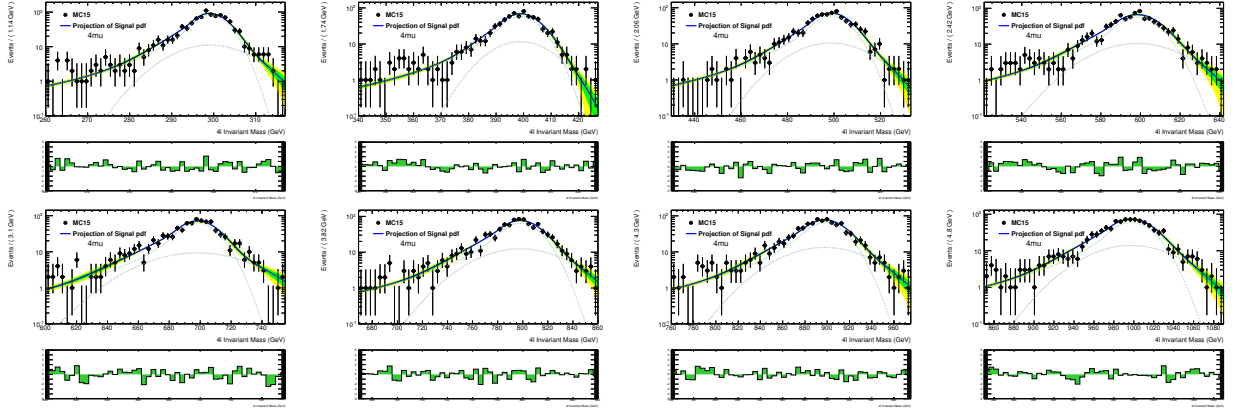


Figure 7.10: Distributions of  $m_{4\mu}$  invariant mass fit projection in the  $[0.4, 0.6]$  *MELA* bin of the signal samples from mass of 300 to 1000 GeV in steps of 100 GeV.

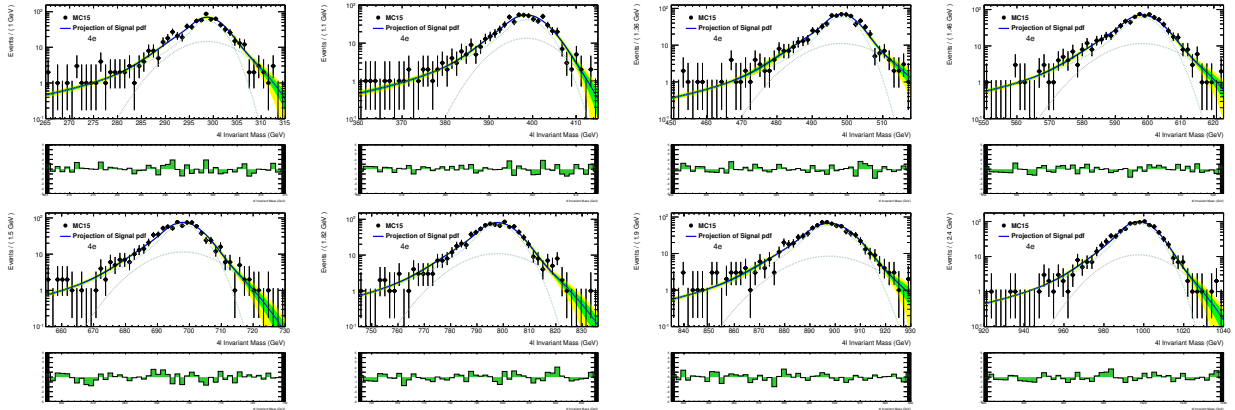


Figure 7.11: Distributions of  $m_{4e}$  invariant mass fit projection in the  $[0.4, 0.6]$  *MELA* bin of the signal samples from mass of 300 to 1000 GeV in steps of 100 GeV.

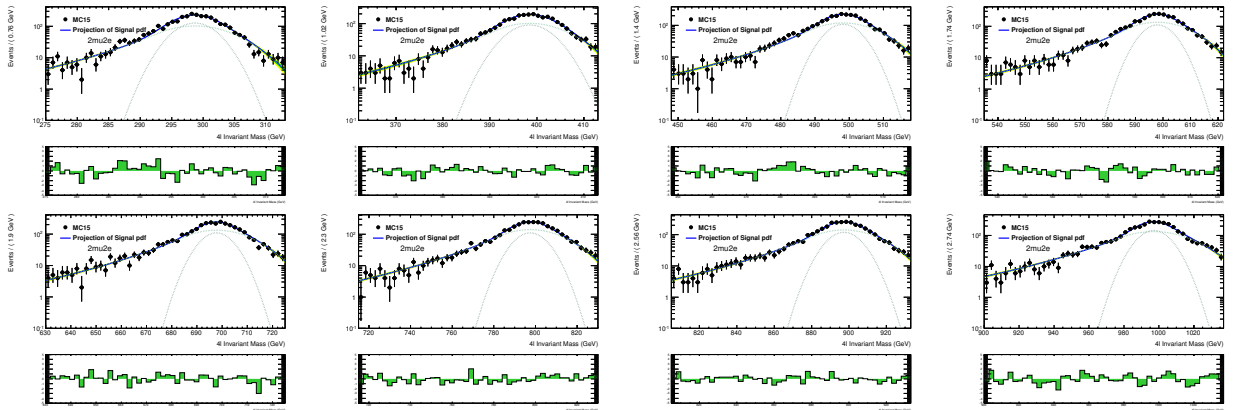


Figure 7.12: Distributions of  $m_{2\mu 2e}$  invariant mass fit projection in the  $[0.4, 0.6]$  *MELA* bin of the signal samples from mass of 300 to 1000 GeV in steps of 100 GeV.

Table 7.1: Summary of the Pearson  $\chi^2$  values obtained from the signal shape fit in all categories.

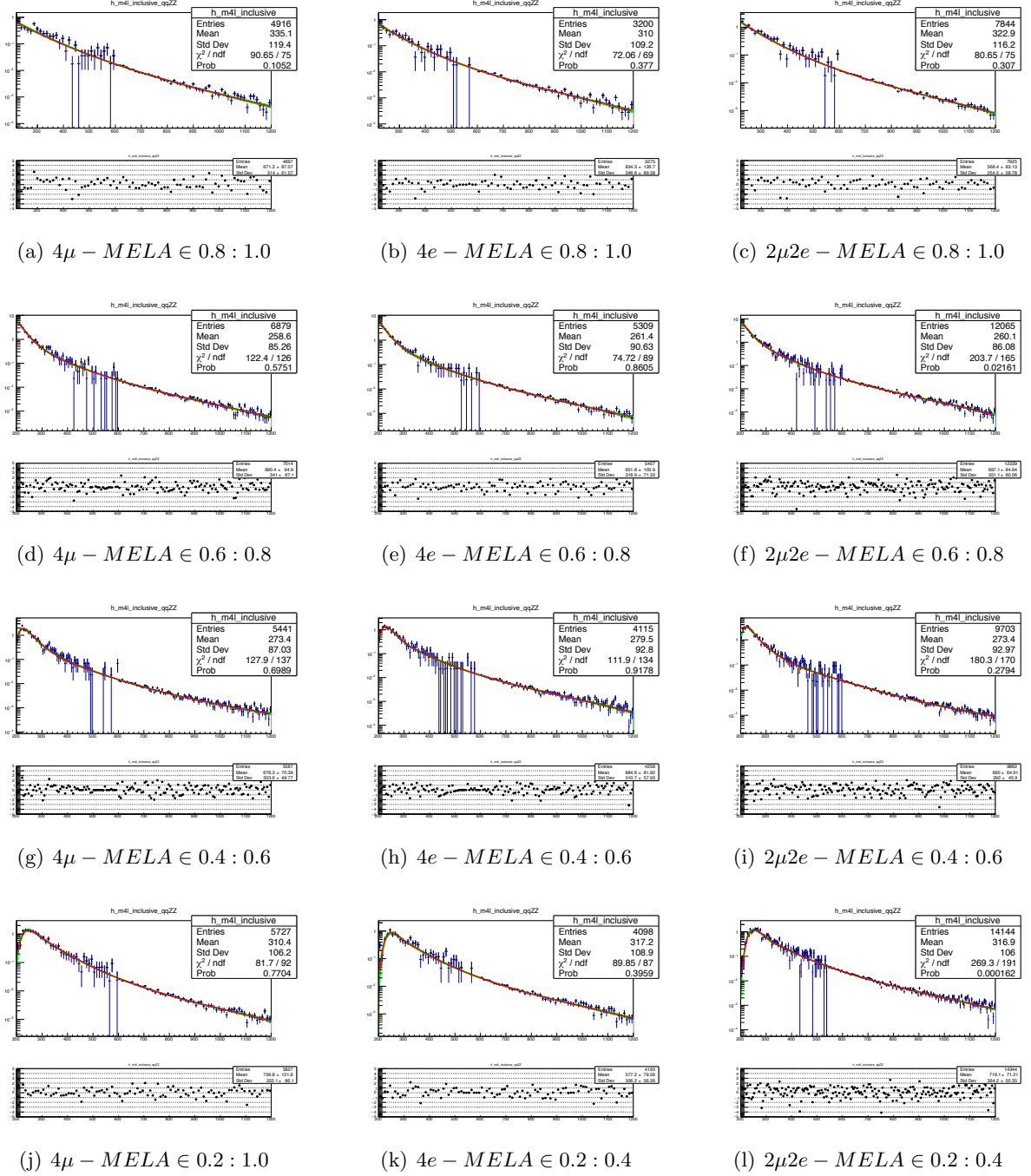
$\chi^2$	MELA [0.8,1.0]			MELA [0.6,0.8]			MELA [0.4,0.6]			MELA [0.2,0.4]		
	$4\mu$	$4e$	$2\mu 2e$	$4\mu$	$4e$	$2\mu 2e$	$4\mu$	$4e$	$2\mu 2e$	$4\mu$	$4e$	$2\mu 2e$
300	1.0	0.8	1.4	0.7	1.6	2.0	1.2	1.1	1.6	1.0	1.1	1.5
400	1.0	1.4	2.0	0.7	1.3	1.2	1.4	1.0	0.6	1.2	0.9	1.4
500	1.6	1.4	1.8	1.3	1.2	1.5	0.9	0.7	0.9	0.8	0.7	0.7
600	1.0	1.7	1.2	0.9	1.2	1.1	1.6	0.5	0.9	1.9	1.1	1.2
700	0.8	1.5	1.4	0.8	0.8	1.5	1.6	1.1	1.1	0.7	1.6	1.0
800	1.0	1.3	1.7	0.8	1.4	1.1	1.0	1.3	0.7	1.2	1.1	1.1
900	1.2	1.1	1.5	1.0	1.2	1.4	0.9	0.8	0.6	1.5	1.4	0.9
1000	1.2	1.5	1.8	1.5	0.8	1.2	1.3	0.7	1.4	1.2	1.5	1.6

## 7.4 Background modelling

Both  $qq \rightarrow ZZ$  and  $gg \rightarrow ZZ$  background shapes are described with the same analytical function, similar to one described in Section 5.4.4. As for the nominal analysis, the background shape consists of the low mass and high mass parts, that are connected at certain mass point. The main changes w.r.t. to the previously described analytical function is that the value of the connection point is now a free parameter of the fit, and the low mass part of the function is replaced by Landau distribution in order to reduce the number of free parameters.

The background shape is estimated for each category separately. The fitted shapes are shown in Figures 7.13 and 7.14 for different *MELA* bins and lepton final states. All the categories shows good fit quality with the average  $\chi^2/NDF \sim 1$ .

For the tri-boson background, the shape is assumed to be the same in all *MELA* bins (the shape is described in Section 5.4.4) and only normalisation is broken down into categories. The reducible background is not included into analysis since its contribution is negligible above 200 GeV.

Figure 7.13: The  $m_{4\ell}$  shape of the  $qq \rightarrow ZZ$  background in different categories.

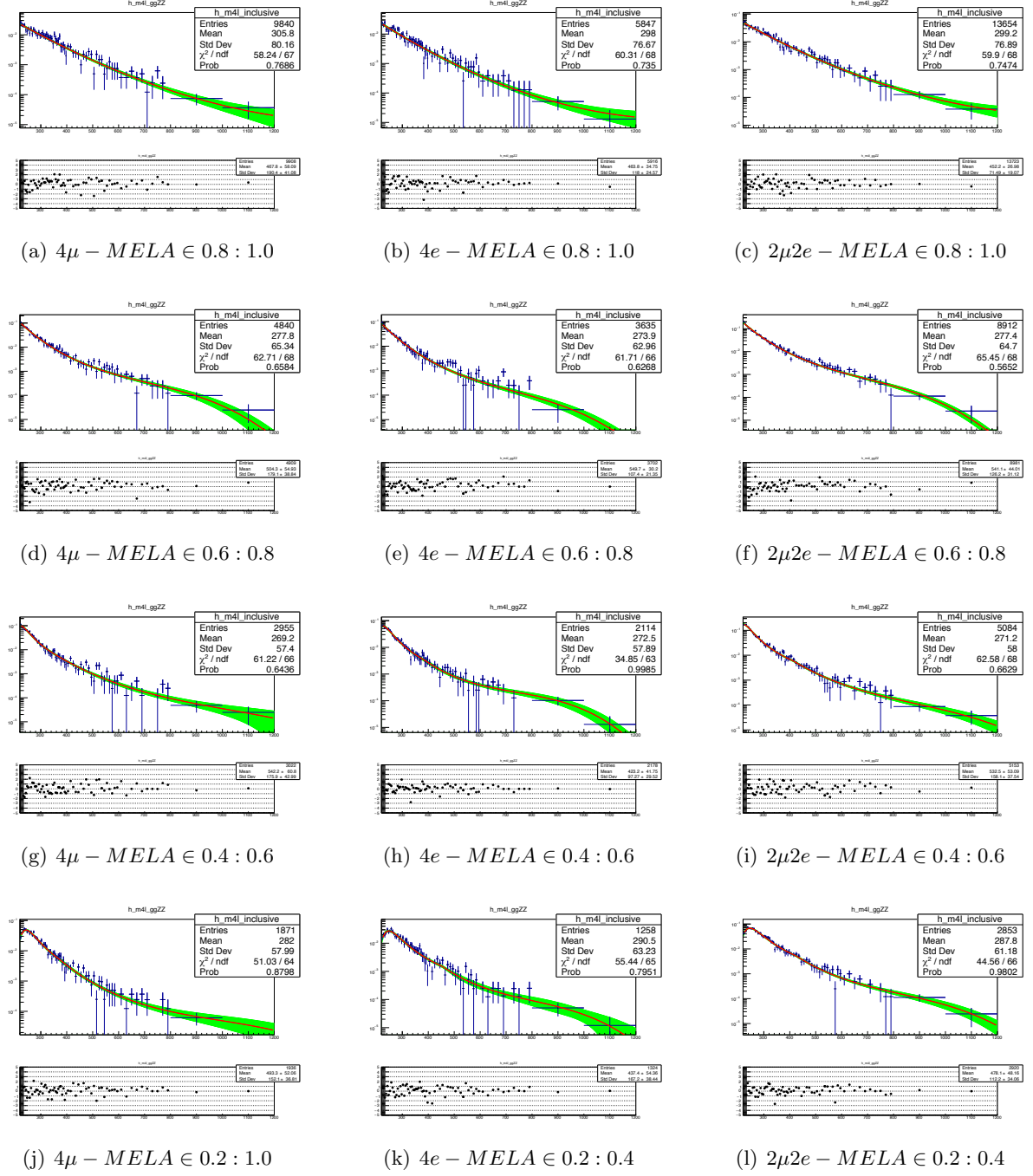


Figure 7.14: The  $m_{4\ell}$  shape of the  $gg \rightarrow ZZ$  background in different categories.

## 7.5 Results

Data events observed in the signal region as well as the expected background yields are shown in Section 5.7, while the statistical procedure used to set the limits is described in Section 5.8.

This section is showing the *MELA* improved upper limits as a function of  $m_H$  on the inclusive production cross section of heavy Higgs boson in the Narrow Width Approximation times its branching ratio of the four lepton decay. This limits does not include systematic uncertainties, but they are foreseen to be included in the next iteration of the heavy Higgs search. This analysis is dominated by the statistical error, therefore the effect of the systematics on the results presented in this section is expected to be minor.

Figure 7.15 shows the *MELA* improved limits on inclusive production cross section times branching ratio, while Figure 7.16 shows the similar limits but without *MELA* variable included into analysis. The second plot can be used as a reference to estimate the sensitivity gain. Including *MELA* variable into analysis improves the sensitivity by 8 – 26% for different masses, as it is summarised in Table 7.2.

Table 7.2: The expected limits on inclusive production cross section times branching ratio are shown both for the nominal analysis (1-st row) described in Chapter 5 and for the *MELA* improved analysis (2-nd row) described in this chapter. Both sets of limits does not include systematic uncertainties. The 3-rd row of the table shows the sensitivity improvement gained by including *MELA* variable into the analysis.

Expected Limits ( $\text{fb}^{-1}$ )	300 GeV	400 GeV	500 GeV	600 GeV	700 GeV	800 GeV	900 GeV	1000 GeV
Nominal	1.39	0.90	0.64	0.50	0.41	0.35	0.32	0.29
<i>MELA</i> -improved	1.02	0.66	0.50	0.41	0.35	0.31	0.28	0.27
Improvement	26%	26%	22%	18%	15%	12%	10%	8%

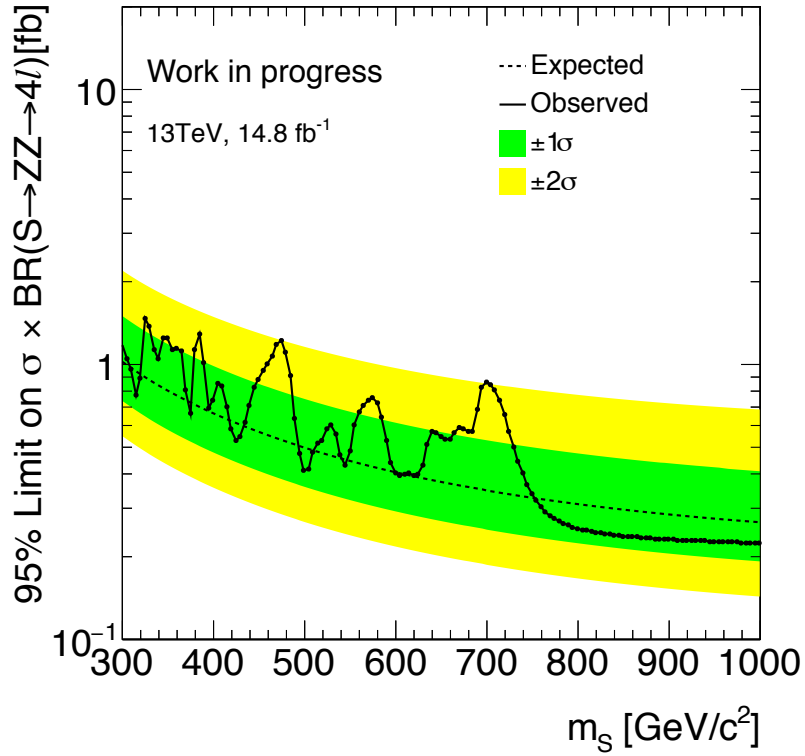


Figure 7.15: 95% confidence limits on  $\sigma \times BR(S \rightarrow ZZ \rightarrow 4\ell)$  in the NWA approximation using the *MELA* discriminant. Systematic uncertainties are not included.

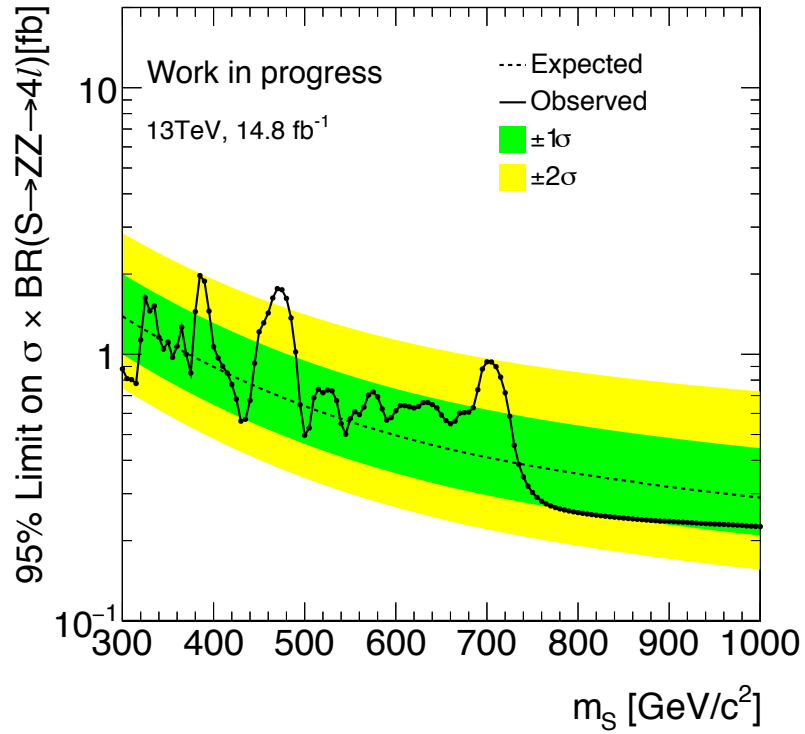


Figure 7.16: 95% confidence limits on  $\sigma \times BR(S \rightarrow ZZ \rightarrow 4\ell)$  in the NWA approximation. Systematic uncertainties are not included. The limits can be compared to the *MELA* improved ones from Figure 7.15 to estimate the sensitivity gain.

# Updated results of the search with 36.1 fb<sup>-1</sup> of 13 TeV data

---

This chapter shows the updated results of the heavy Higgs search with full 2015-2016 dataset: 36.1 fb<sup>-1</sup> of 13 TeV data. This analysis uses the same methodology as the previously described search, however, there are several modifications that are discussed in Section 8.1. This analysis is discussed in more details in Ref. [131].

The updated results include the upper limits on the production cross section times branching ratio for all the signal hypothesis discussed earlier: ggF and VBF production modes in NWA, inclusive production in LWA including the interference.

## 8.1 Modifications of the analysis

### New MC samples

As it was shown in Section 5.7, in the ICHEP analysis an overall excess of data events was observed in the VBF category. It was found that the effect is partially coming from the jet modelling in the  $qq \rightarrow ZZ$  MC simulation. After comparing different options, Sherpa was found to provide the best description of jets in this process, therefore in this round of the analysis Sherpa MC simulation is used to define the  $qq \rightarrow ZZ$  background yields into different signal region categories, while the background shape is still deduced from POWHEG simulation. Also it was found that there is non negligible contribution to the VBF category from the electroweak SM production of  $Z$  boson pair that was not included before. Therefore this process is added to the list of the considered backgrounds for this round of analysis. The relative importance of this background is shown in Table 8.1.

### Extended mass range

This analysis is aiming to explore a mass range as wide as possible for the heavy Higgs mass hypothesis. It is chosen to extend the upper bound for the limit up to 1200 GeV, while this bound is motivated by the facts that there is no data events and poor background MC statistics above this point. The lower bound for the NWA limits is extended down to 140 GeV, since the  $4\ell$  decay channel is the only one sensitive to low mass range among the other  $ZZ$  final states. However, LWA limits still have a lower bound of 300 GeV due to some technical limitations discussed before.

### Interference for LWA search

Contrary to the ICHEP results, the LWA search described in this chapter includes the interference effect discussed in Section 6.4. It allows to cover the full LWA phase space including the parts where the interference is significant:  $m_H$  from 300 to 1200 GeV,  $\Gamma_H$  from 1% to 15% of  $m_H$ . Since the interference have a constructive effect on the signal normalisation,



it actually improves the analysis sensitivity and pushes the heavy Higgs cross section limits down.

## 8.2 Observed events

Figure 8.1 shows the  $m_{4\ell}$  distribution of the selected candidates compared to the background expectation in the signal region without separation into category. The distributions split into the four analysis categories are shown in Figure 8.2. No events are observed beyond the plotted range (1200 GeV).

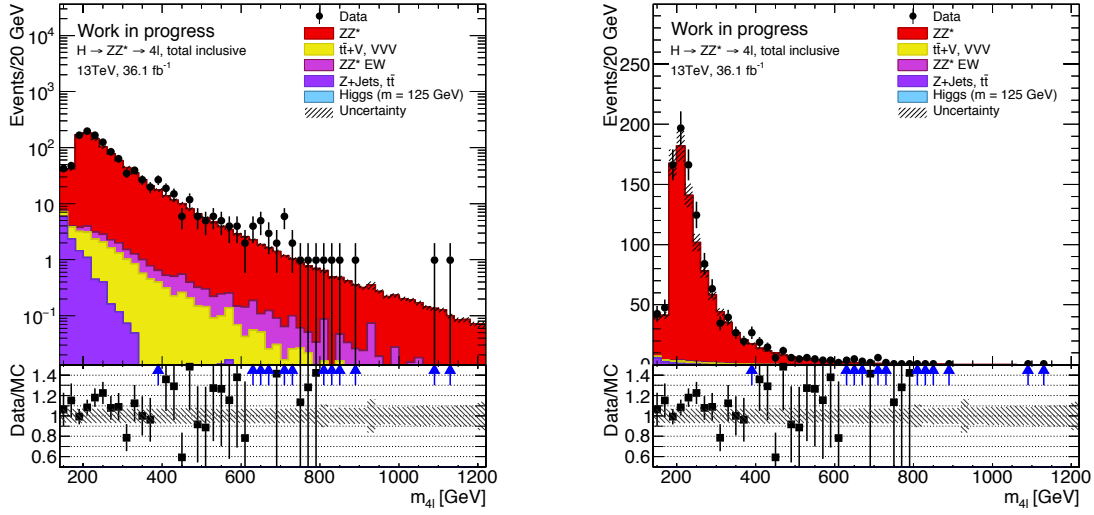


Figure 8.1:  $m_{4\ell}$  distribution of the selected candidates compared to the background expectation inclusive of category in log and linear scale.

The expected yields from each source within each category, as well as the observed yields, are shown in Table 8.1. The excess of data events in the  $4e$  category observed in ICHEP analysis remains with even larger significance, while the excess in the VBF-like category is reduced with new MC samples and more data.

Table 8.1: The expected and observed number of events for the four-lepton final states in a range of  $130 < m_{4\ell} < 1500 \text{ GeV}$  with  $36.1 \text{ fb}^{-1}$  at  $\sqrt{s} = 13 \text{ TeV}$ .

Category	$qq \rightarrow ZZ$	$gg \rightarrow ZZ$	$Z + \text{jets}, t\bar{t}, WZ$	$t\bar{t}V, VVV$	Expected	Observed
ggF - $2\mu 2e$	$451.3 \pm 25.1$	$54.8 \pm 16.8$	$7.8 \pm 1.1$	$8.7 \pm 0.5$	$522.6 \pm 32.3$	545
ggF - $4e$	$181.4 \pm 11.9$	$22.4 \pm 6.9$	$4.4 \pm 0.8$	$4.0 \pm 0.3$	$212.2 \pm 15.0$	256
ggF - $4\mu$	$277.0 \pm 15.8$	$32.8 \pm 10.0$	$3.7 \pm 0.8$	$5.2 \pm 0.3$	$318.6 \pm 20.0$	357
VBF	$15.5 \pm 8.49$	$3.6 \pm 3.67$	$0.37 \pm 0.05$	$0.8 \pm 0.55$	$20.28 \pm 11.94$	31
Total	$925.2 \pm 51.7$	$113.6 \pm 33.9$	$16.2 \pm 2.7$	$18.7 \pm 1.2$	$1073.7 \pm 66.9$	1189

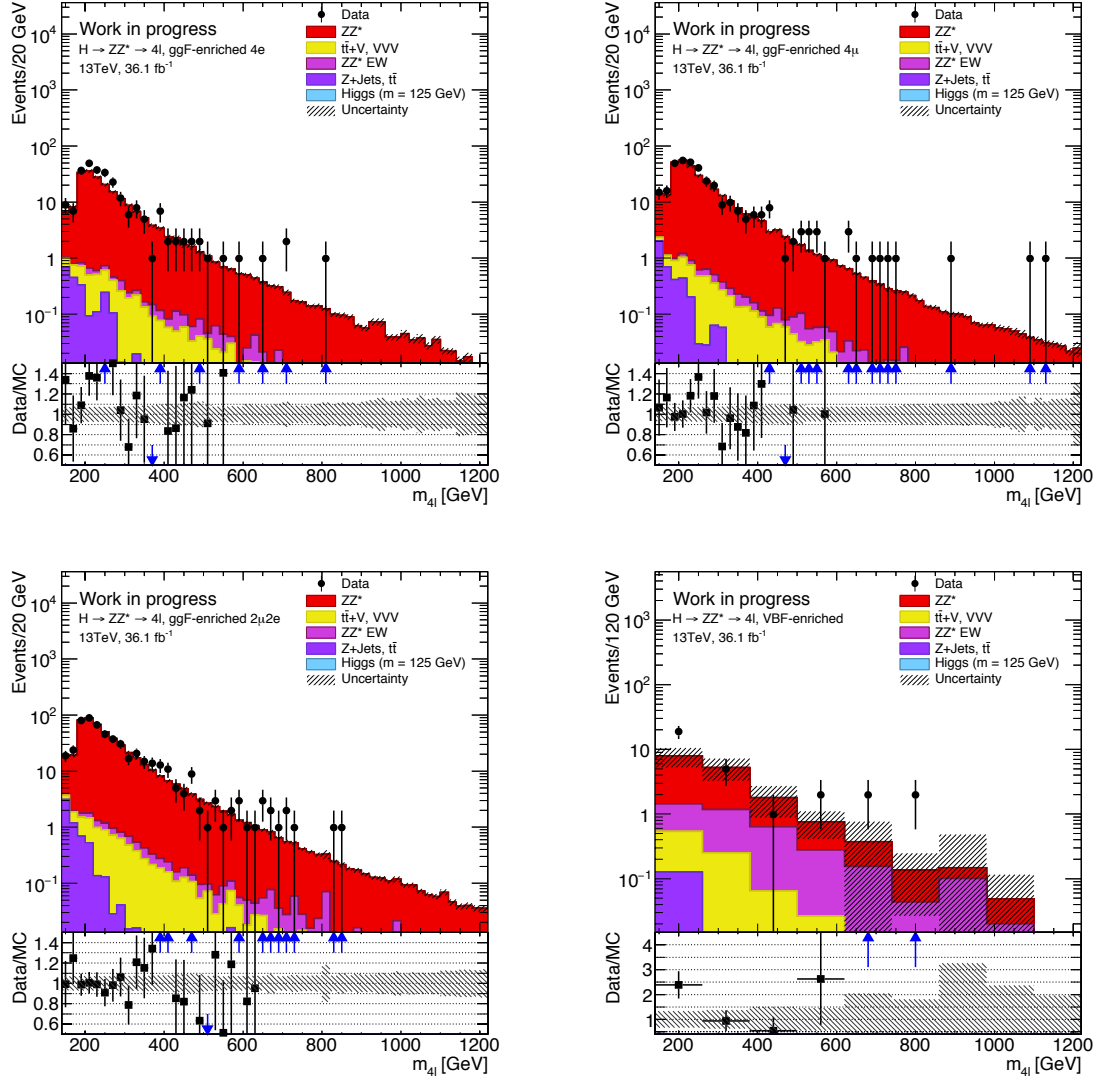


Figure 8.2: Log-scale  $m_{4\ell}$  distribution of the selected candidates compared to the background expectation in ggF-like 4e (top-left), ggF-like 4 $\mu$  (top-right), ggF-like 2 $\mu$ 2e (bottom left) and VBF-like (bottom-right) categories. Note that the VBF-like category is shown with a coarser binning than the other categories only for visual simplicity - all categories use unbinned fits.

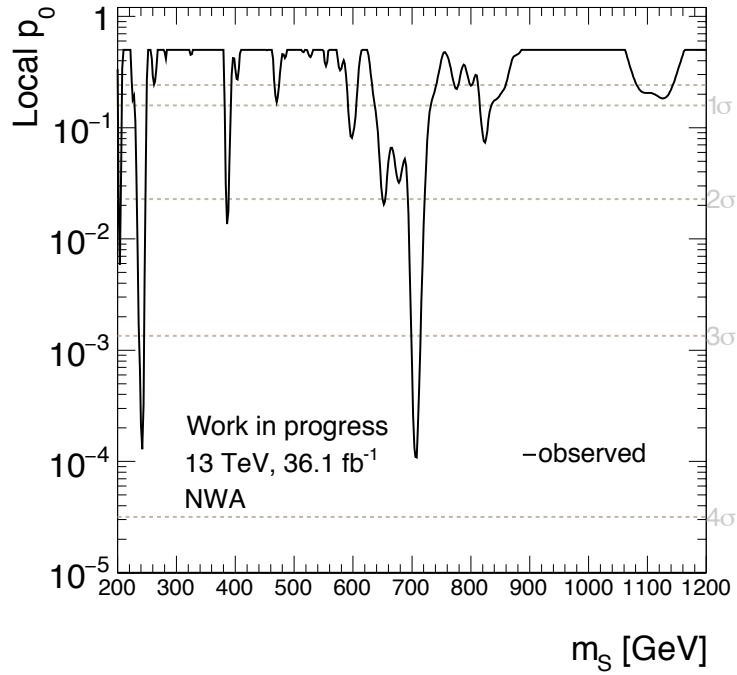


Figure 8.3:  $p_0$  as function of  $m_H$  considering ggF production in NWA.

## 8.3 Cross section limits

### 8.3.1 Narrow width

Compatibility of the observed events and the background-only hypothesis is quantified with profiled likelihood ratio for the background-only and background plus signal hypothesis ( $p_0$ ). Figure 8.3 shows the likelihood ratio as a function of  $m_H$  for the simplest signal model: ggF production only in NWA. Maximal deviation from the background-only hypothesis is observed at Higgs mass  $m_H = 706 \text{ GeV}$  with local significance of  $3.8 \sigma$ , and global significance of  $2.6 \sigma$  when taking into account the possibility of similar deviation can happen elsewhere in the mass range. Moreover, local significance of the excess in the low mass region is about  $3.6 \sigma$ , while it is completely driven by the  $4e$  final state.

Limits on the ggF and VBF cross-sections times branching ratio assuming the Narrow Width Approximation are obtained as a function of  $m_H$  with the  $CL_s$  procedure in the asymptotic limit, using the test-statistic described in Section 5.8. Figures 8.4 presents the expected and observed limits at 95% confidence level on  $\sigma \times BR(S \rightarrow ZZ \rightarrow 4\ell)$  for the ggF and VBF production modes of a heavy Higgs boson. The largest deviation of the observation from the expected limit is around 706 GeV for the ggF production mode.

### 8.3.2 Large width

Upper limits on the inclusive production cross section times the branching ratio for the heavy Higgs boson with large width are presented in Figures 8.5(a), 8.5(b), 8.5(c), and 8.5(d) for the widths equal to 1%, 5%, 10% and 15% of signal mass respectively. Current results include the interference effect that allows to explore broader LWA phase space and increase sensitivity of the analysis due to constructive effect of the interference on the signal normalisation.

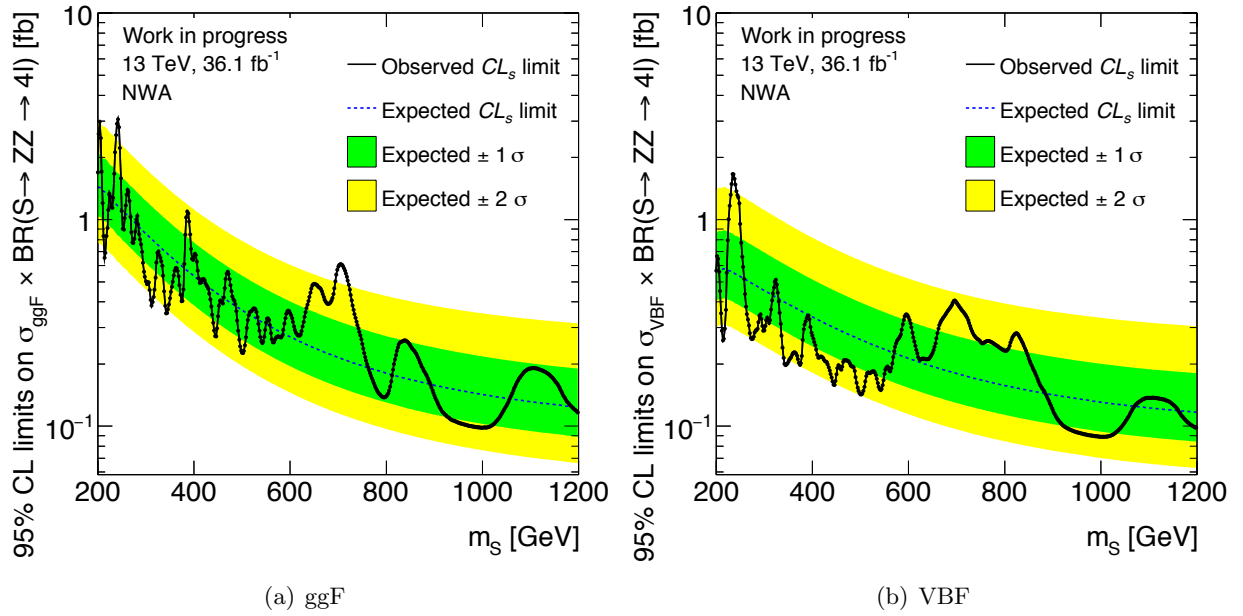


Figure 8.4: The upper limits at 95% confidence level on  $\sigma_{ggF} \times BR(H \rightarrow ZZ \rightarrow 4\ell)$  (left) and  $\sigma_{VBF} \times BR(H \rightarrow ZZ \rightarrow 4\ell)$  (right) for the NWA approximation.

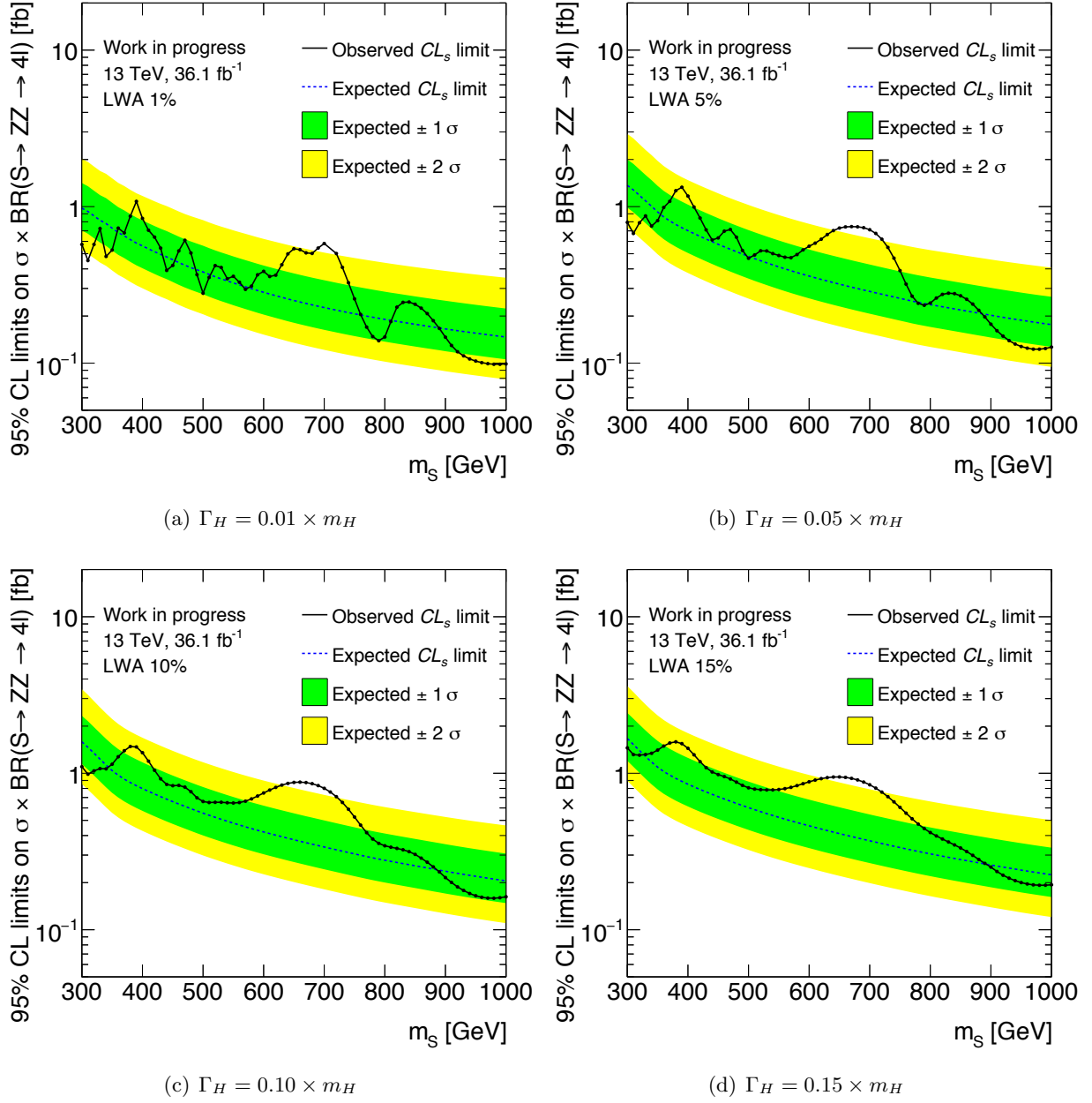


Figure 8.5: 95% confidence limits on  $\sigma \times BR(S \rightarrow ZZ \rightarrow 4\ell)$  assuming a width 1%, 5% , 10% and 15% of  $m_H$ .

# Conclusions

---

This thesis is mostly focused on the model independent heavy Higgs boson search in the four leptons final state with the ATLAS detector. This analysis allows to test a set of BSM models that predict an extension of the Standard Model Higgs sector, namely the Electroweak Singlet and Two Higgs Doublet benchmark models. The latest results of the analysis are based on  $36.1 \text{ fb}^{-1}$  of  $\sqrt{s} = 13 \text{ TeV}$  data, and they cover different signal width assumptions discussed below.

In case of the narrow signal width assumption the upper limits on the production cross section times the branching ratio is set separately for ggF and VBF production modes. A complementary analysis was performed for the scalar signal with the narrow width. In this case, the signal can be discriminated from the background by making use of extra kinematic variables, therefore an improved upper limit for the inclusive Higgs production is set in this case. The upper limit on the heavy Higgs production cross section times the branching ratio of the four leptons decay is set at the level of 1 fb or lower. The largest deviation of the observed data from the expected background yields is observed at  $m_H = 706 \text{ GeV}$ , and it corresponds to  $3.8 \sigma$  local and of  $2.6 \sigma$  global deviation from the background only hypothesis. This excess can be cross checked by performing the heavy Higgs boson search in other  $ZZ$  final states such as  $\ell\ell\nu\nu$ . Moreover, another local  $3.6 \sigma$  deviation from the expected background yields is observed at  $m_H = 245 \text{ GeV}$ . Contrary to the first case,  $4\ell$  is the only sensitive final state at such a low mass range, therefore this excess can be cross checked only by analysing a larger dataset that will be recorded by ATLAS in the nearest future.

Another search scenario considers the large width signal, with the width up to 15% of the signal mass. In this case the upper limit is set taking into account the effect of the signal interference with the SM backgrounds. The interference turns out to be constructive, therefore it improves the analysis sensitivity. The excess of data events around 706 GeV interpreted under the large width signal hypothesis has lower significance than in the narrow width case.



# Résumé

Dans cette thèse nous nous sommes intéressés à la recherche du boson de Higgs se désintégrant en 4 leptons avec les données venant du Run-2 enregistrées avec le détecteur Atlas auprès du Large Hadron Collider (LHC). Cette analyse, présentée à la conférence ICHEP 2016 et avait un lot de données correspondant à  $14.8 \text{ fb}^{-1}$  enregistrés à  $\sqrt{s} = 13 \text{ TeV}$ , sera décrite en détail ainsi qu'une mise à jour avec un échantillon de  $36.1 \text{ fb}^{-1}$ , à une énergie de  $\sqrt{s} = 13 \text{ TeV}$ . La recherche de Higgs lourd a été effectuée indépendamment du modèle et pour différente hypothèse de largeur du signal: approximation de largeur du boson négligeable par rapport à la résolution du détecteur, grande largeur de signal incluant des effets d'interférence possible avec un bruit de fond issu du Modèle Standard.

La production de boson de Higgs est dominé par les processus de fusion de gluons et de fusion de boson vecteur dans les collisions protons-protons comme illustré dans la Fig.9.1, et les importances relatives de production sont indépendant du modèle. C'est la raison pour laquelle cette recherche a été effectuée sans hypothèse sur la production relative de ces différents modes. Cette analyse utilise les désintégrations du boson de Higgs en paire de bosons  $Z$ , qui eux-mêmes se désintègrent en électrons ou muons de charges opposées. Cette topologie d'événements donne un signal clair qui ne peut pas être imité par plusieurs jets de bruit de fond qui sont très probables auprès des collisionneurs de hadrons.

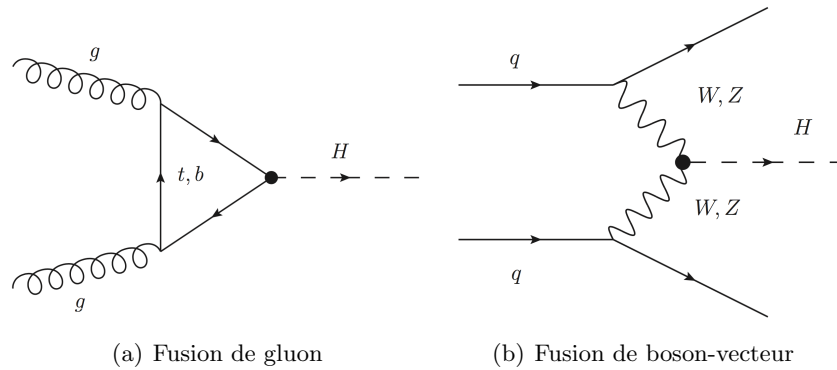


Figure 9.1: Mode dominant de production du boson de Higgs auprès d'un collisionneur à protons.

Le bruit de fond le plus important pour cette analyse provient de la production de deux bosons  $Z$  comme décrit dans le Modèle Standard, provenant des processus suivant:  $qq \rightarrow ZZ$  et  $gg \rightarrow ZZ$  (Fig.9.2). D'autres processus de production prédit par le Modèle Standard sont possible aussi comme la production via des paires de quark top, des  $Z$  avec des jets, mais ils ont une faible contribution au bruit de fond total. Il est à noter qu'il a été développé dans cette thèse une nouvelle estimation des bruit de fond  $ZZ$  par une méthode basée sur les données elles-mêmes, pour les bruits de fond  $t\bar{t}$  et  $Z + jet$ .

La forme du signal dans son approximation de petite largeur peut être empiriquement modélisée par une forme analytique. Une somme de distribution de Gaussienne et de fonction de type Crystal-Ball, a été utilisé toutes deux avec la même valeur moyenne, car elle semblait bien décrire la forme du signal avec le minimum de paramètres libres. Un exemple d'ajustement de cette fonction analytique ajusté sur une distribution obtenue avec la simulation Monte-Carlo est montré sur la Fig.9.3 pour différents type d'états finaux de leptons. La Fig.9.4 montre les gabarits de largeurs de masse utilisées dans l'hypothèse de petite largeur.



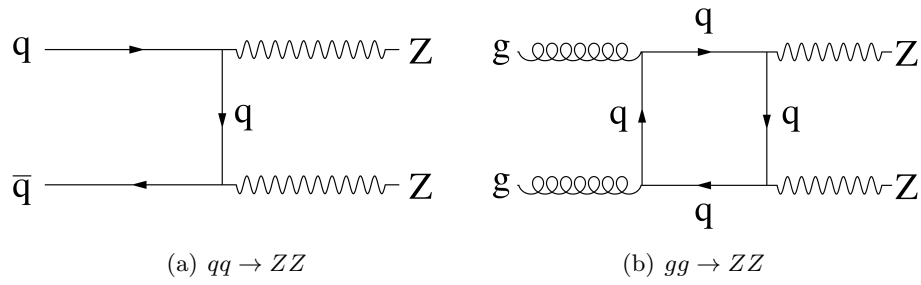


Figure 9.2: Diagramme de Feynman les plus simple du Modèle Standard pour la production de  $qq \rightarrow ZZ$  (a) et  $gg \rightarrow ZZ$  (b), auprès d'un collisionneur  $p-p$ .

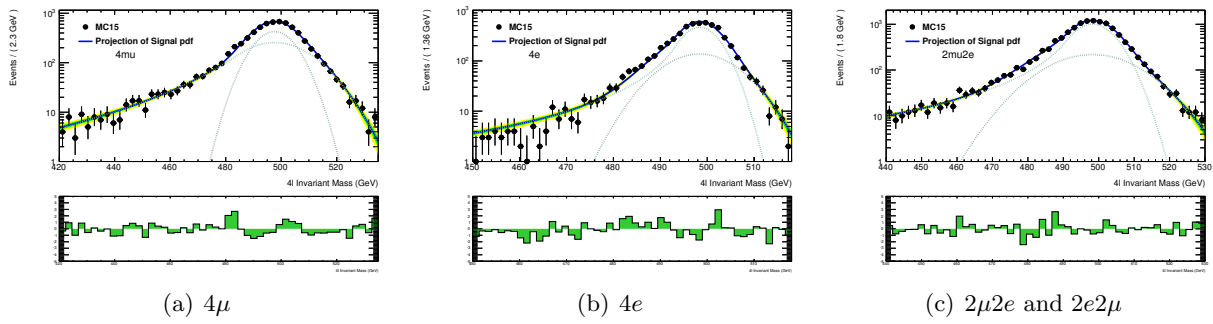


Figure 9.3: Courbe analytique du signal ajusté sur les données Monte-Carlo dans l'hypothèse de petite largeur du signal pour une masse de 500 GeV.

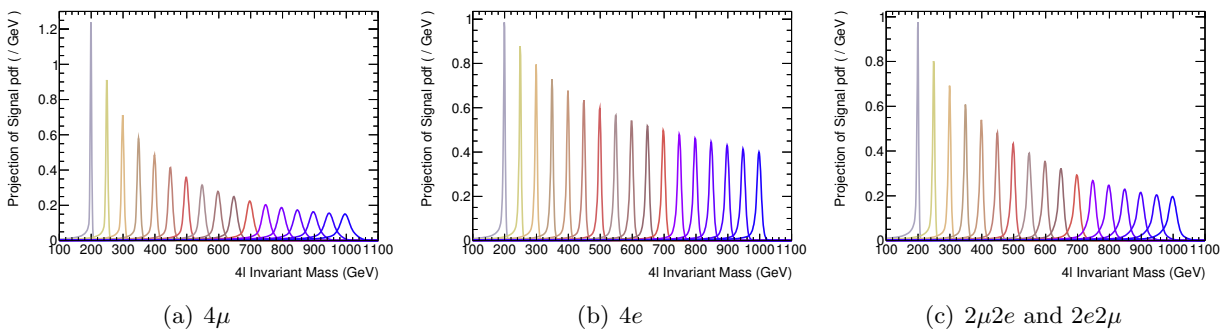


Figure 9.4: Gabarits de largeurs pour différents type d'états finaux.

Dans le cadre de cette thèse, une nouvelle méthode de modélisation du signal a été proposée. La description de la forme du signal de section efficace provenant des calculs théoriques de celle-ci à l'ordre supérieur a été proposée. La Fig.9.5(a) montre la comparaison des distributions provenant des modèles du signal avec le signal Monte-Carlo. Par la suite la forme analytique du signal est corrigée des effets provenant de la résolution du détecteur. La Fig.9.5(b) montre la validité de ce modèle pour l'hypothèse de grande largeur de signal.

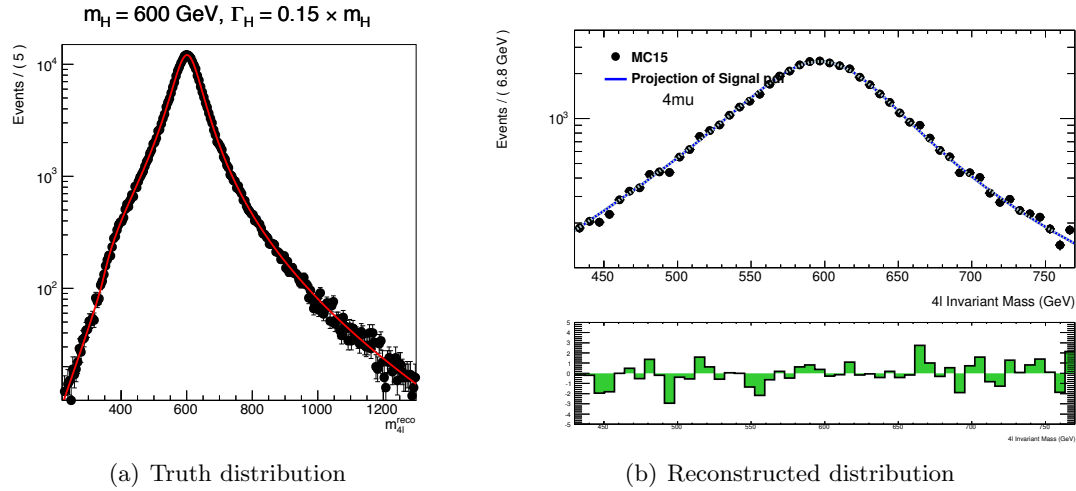


Figure 9.5: Comparaison de la forme analytique avec la truth  $m_{4\ell}$  répartition dans les échantillons MC du signal pour la masse de 600 GeV et la largeur égale à 15% de la masse (a) et la comparaison du modèle de signal large largeur complet à la distribution MC reconstruite correspondante (b).

Le signal dans l'hypothèse de grande largeur de signal devrait avoir une interférence importante avec le bruit de fond issus du Modèle Standard. Un modèle des interférences a été utilisé. La Fig.9.6 montre l'importance relative de l'interférence dans la recherche du signal avec la sensibilité actuelle de l'analyse. L'interférence est plutôt constructive, permettant ainsi de pousser la limite de section efficace du Higgs lourd.

Le résultat des recherches est basé sur des données prises par Atlas en 2015 et 2016 pour  $36.1 \text{ fb}^{-1}$  et  $\sqrt{s} = 13 \text{ TeV}$ . LA Fig.9.7 montre la distribution de la masse invariante des 4 leptons pour les événements de type signal comparé à ceux du bruit de fond, ceci pour différent région du signal. Les taux attendus de chacune des catégories ainsi que les taux mesurés sont dans la Tab.9.1.

Table 9.1: Le nombre attendu et observé d'événements pour les états finaux de 4-lepton dans une gamme de  $130 < m_{4\ell} < 1500 \text{ GeV}$  pour  $36.1 \text{ fb}^{-1}$  à  $\sqrt{s} = 13 \text{ TeV}$ .

Category	$qq \rightarrow ZZ$	$gg \rightarrow ZZ$	$Z + \text{jets}, t\bar{t}, WZ$	$t\bar{t}V, VVV$	Expected	Observed
ggF - $2\mu 2e$	$451.3 \pm 25.1$	$54.8 \pm 16.8$	$7.8 \pm 1.1$	$8.7 \pm 0.5$	$522.6 \pm 32.3$	545
ggF - $4e$	$181.4 \pm 11.9$	$22.4 \pm 6.9$	$4.4 \pm 0.8$	$4.0 \pm 0.3$	$212.2 \pm 15.0$	256
ggF - $4\mu$	$277.0 \pm 15.8$	$32.8 \pm 10.0$	$3.7 \pm 0.8$	$5.2 \pm 0.3$	$318.6 \pm 20.0$	357
VBF	$15.5 \pm 8.49$	$3.6 \pm 3.67$	$0.37 \pm 0.05$	$0.8 \pm 0.55$	$20.28 \pm 11.94$	31
Total	$925.2 \pm 51.7$	$113.6 \pm 33.9$	$16.2 \pm 2.7$	$18.7 \pm 1.2$	$1073.7 \pm 66.9$	1189

La compatibilité entre le nombre d'événements observés pour le signal et bruit de fond est estimé par un ajustement de type maximum de vraisemblance pour les hypothèses de bruit de fond seul et pour le bruit de fond plus signal ( $p_0$ ). Une déviation maximum est observé pour l'hypothèse de bruit de fond seul pour une masse de Higgs de 706 GeV avec une probabilité de  $3.8 \sigma$  localement et  $2.6 \sigma$  globalement lorsque l'on suppose que cette déviation peut se

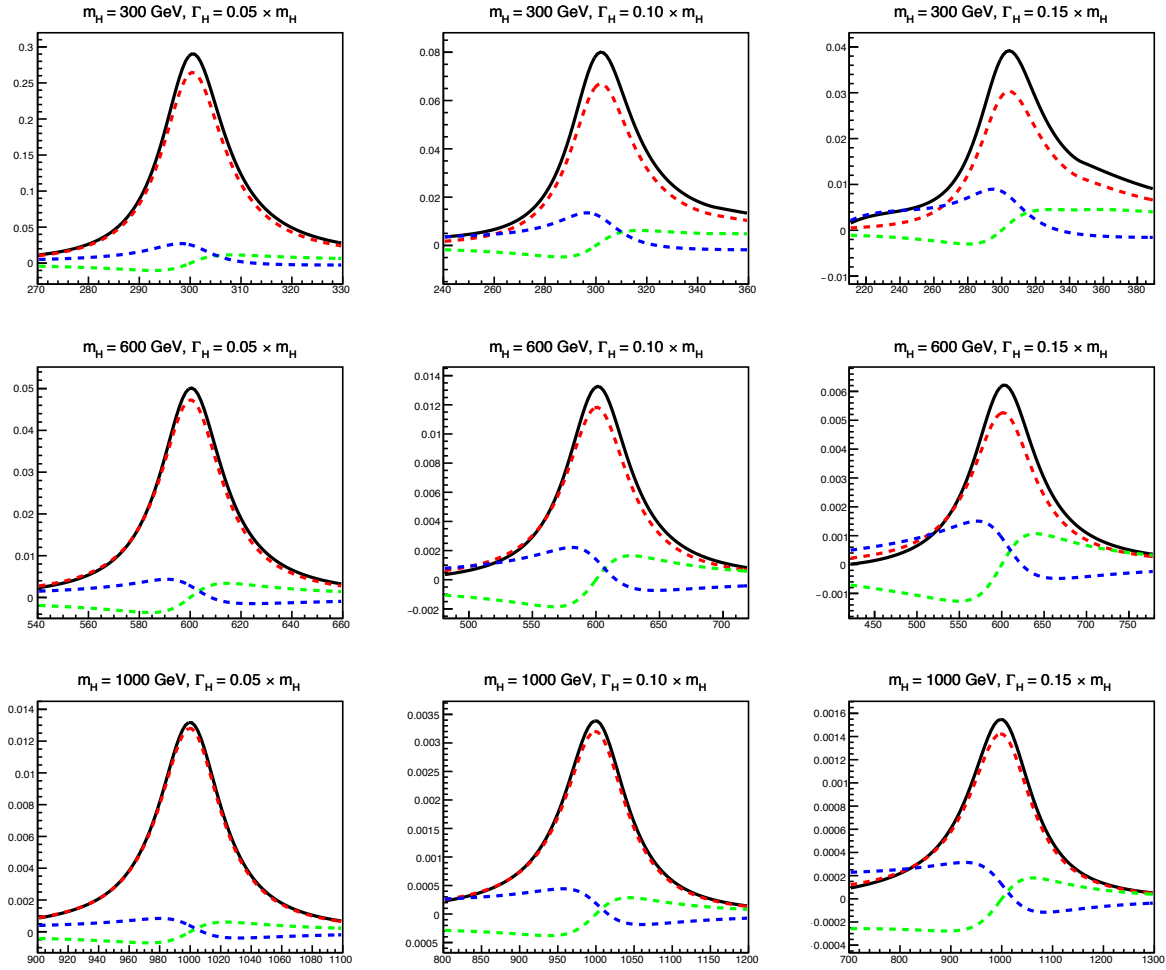


Figure 9.6: Superposition du truth  $m_{4\ell}$  modèle pour le signal (rouge), interférence du SM Higgs et du signal (vert) et interférence du SM  $gg \rightarrow ZZ$  et du signal (bleu) pour les couplages du signal compatibles avec la sensibilité d'analyse attendue, tandis que la somme de trois processus est également présentée (noir).

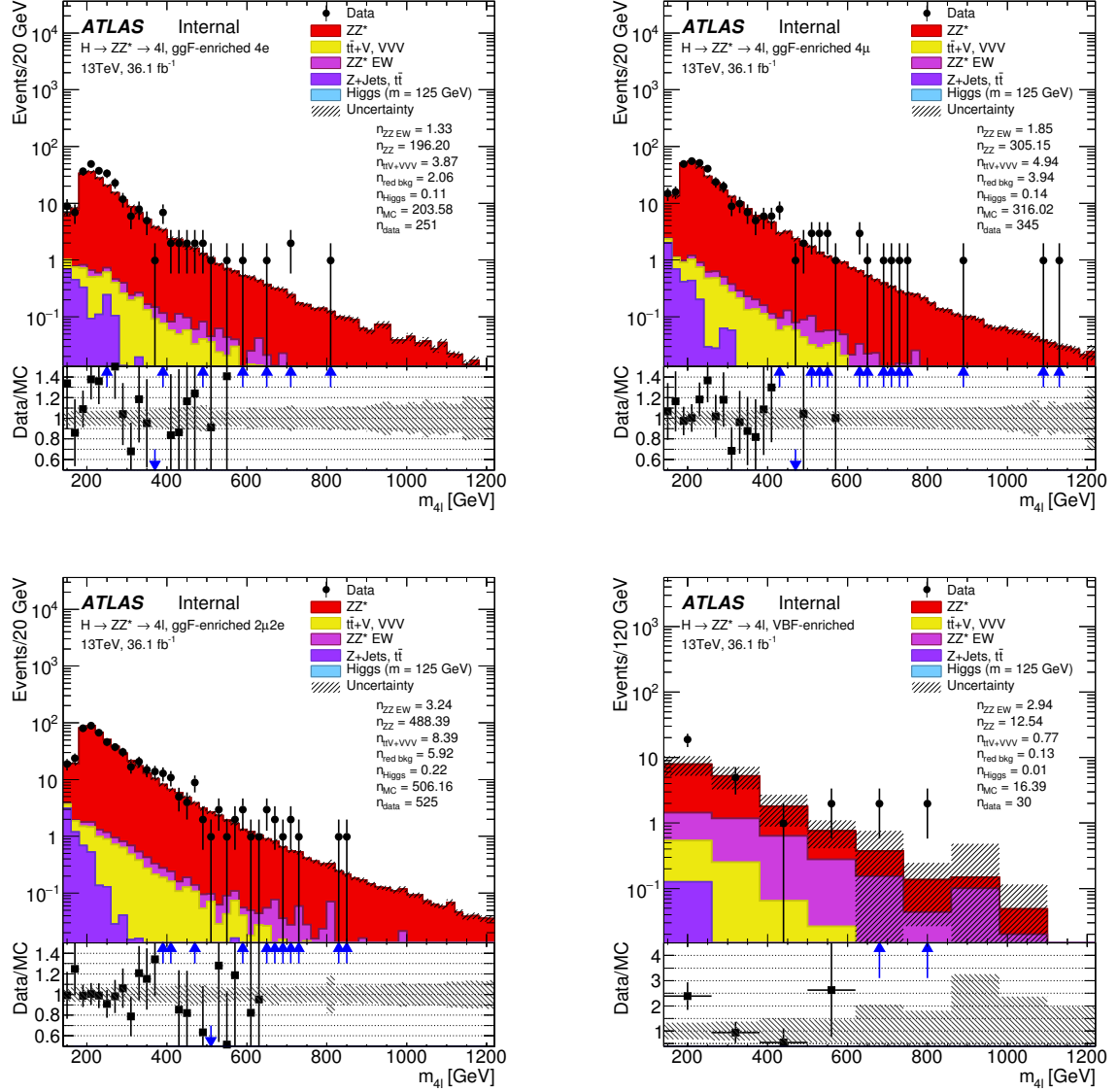


Figure 9.7: Logarithmique  $m_{4\ell}$  répartition des candidats sélectionnés par rapport à l'attente de fond dans les catégories ggF-like 4e (en haut à gauche), ggF-like 4 $\mu$  (en haut à droite), ggF-like 2 $\mu$ 2e (en bas à gauche) et VBF-like (en bas à droite).

produire n'importe où. De plus, la signification locale de  $3.6\sigma$  est provient complètement de l'état final en 4 électrons

Les limites des sections efficaces des taux de branchement ggF et VBF dans l'hypothèse de signal de petite largeur sont obtenus en fonction de  $m_H$  grâce à une procédure dans la limite asymptotique utilisant le test statistique tel qu'il est décrit dans la section 5.8. La Fig.9.8 montre les limites à 95% de confiance sur  $\sigma \times BR(S \rightarrow ZZ \rightarrow 4\ell)$  pour les modes de production d'un Higgs lourd ggF et VBF. Les limites supérieures sur la section efficace de production inclusive du boson Higgs lourd multipliée par le taux de branchement sont présentées sur les Figures 9.9(a), 9.9(b), et 9.9(c) pour, respectivement, des largeurs égales à 5%, 10% et 15% de la masse du signal.

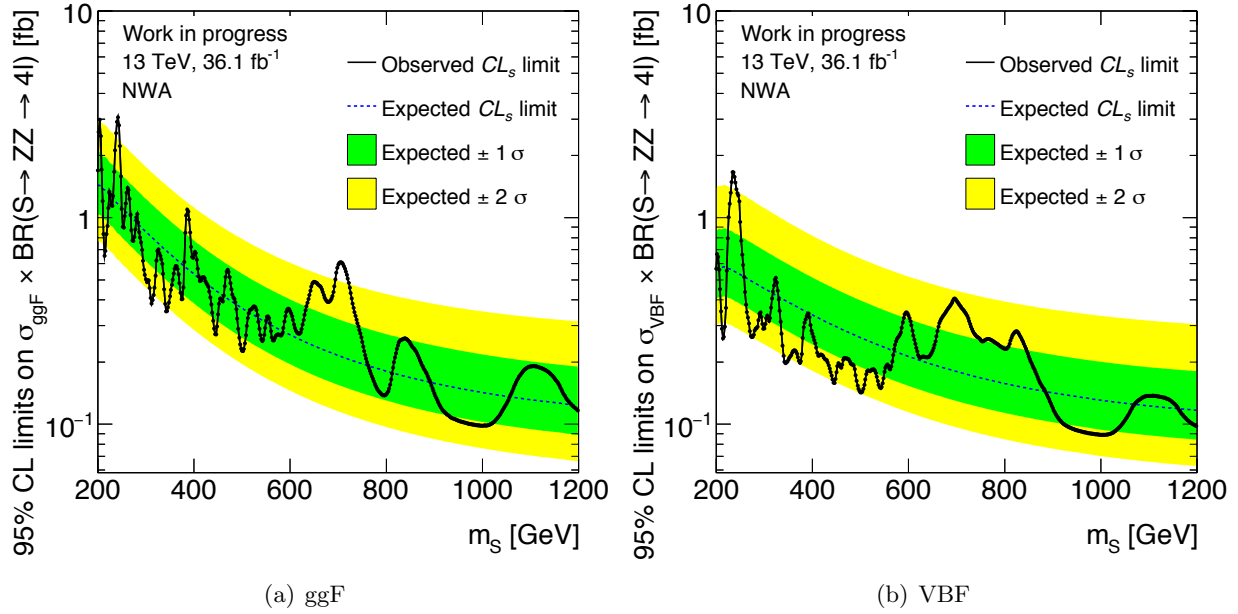


Figure 9.8: 95% limite de confiance sur  $\sigma_{ggF} \times BR(H \rightarrow ZZ \rightarrow 4\ell)$  (gauche) and  $\sigma_{VBF} \times BR(H \rightarrow ZZ \rightarrow 4\ell)$  (droite) pour l'approximation NWA.

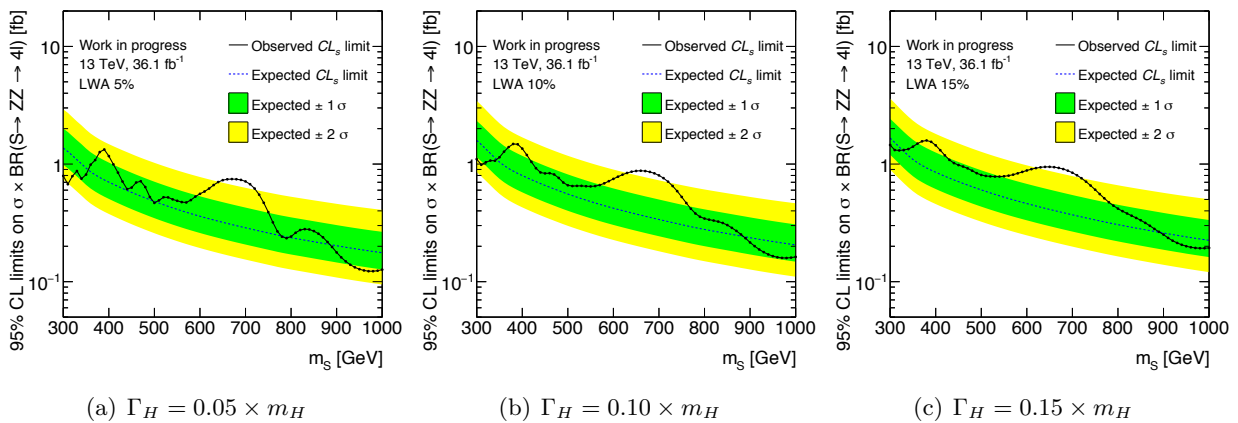


Figure 9.9: 95% limite de confiance sur  $\sigma \times BR(S \rightarrow ZZ \rightarrow 4\ell)$  en supposant une largeur de 5% , 10% and 15% of  $m_H$ .

Nous avons aussi montré que dans le cadre de l'analyse du signal de petite largeur, la sensibilité pouvait être améliorée en utilisant une méthode dite de type Matrice basée sur les discriminant cinématique ? noté *MELA* en anglais. Elle permet de discriminer le signal du bruit de fond. Les distributions de type *MELA* obtenus pour le signal et le principal bruit de fond sont montrés sur la Fig.9.10. Ce discriminant va pouvoir être incorporé dans l'analyse en distinguant le signal dans différentes catégories déterminées par la *MELA*. Il est ainsi montré que l'on peut gagner de 8 à 26% de sensibilité dans l'analyse pour différentes régions de masses. La Tab.9.2 montre l'amélioration de la limite attendue pour différentes hypothèses de masses du signal.

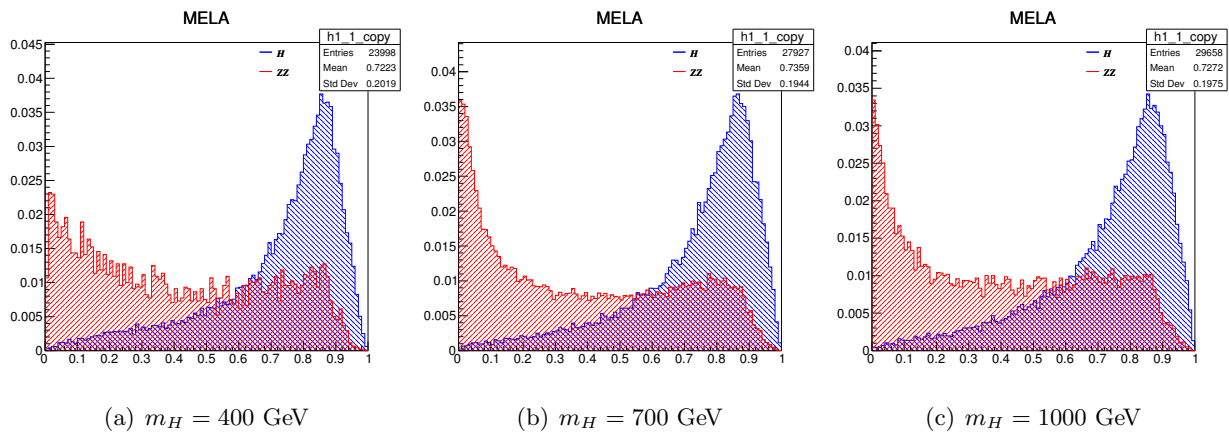


Figure 9.10: Distributions *MELA* pour le signal (bleu) et le bruit de fond (rouge) autour de 400, 700 et 1000 GeV.

Table 9.2: Les limites attendues sur le taux de branchement des temps de section de production inclusifs sont présentées à la fois pour l'analyse nominale (1ère ligne) décrite au Ch.5 et pour l'analyse améliorée *MELA* (2ème ligne) décrite dans ce chapitre. Les deux ensembles de limites n'incluent pas les incertitudes systématiques. La 3ème ligne du tableau montre l'amélioration de la sensibilité obtenue en incluant la variable *MELA* dans l'analyse.

Expected Limits (fb <sup>-1</sup> )	300 GeV	400 GeV	500 GeV	600 GeV	700 GeV	800 GeV	900 GeV	1000 GeV
Nominal	1.39	0.90	0.64	0.50	0.41	0.35	0.32	0.29
<i>MELA</i> -improved	1.02	0.66	0.50	0.41	0.35	0.31	0.28	0.27
Improvement	26%	26%	22%	18%	15%	12%	10%	8%

Dans cette thèse est aussi discuté l'amélioration du spectromètre à muons de l'expérience ATLAS, appelé NSW pour New Small Wheel (en anglais). En particulier sont décrites les simulations du bruit de fond de la caverne que verront les nouveaux détecteurs de type Micromegas. Les premiers tests avec les premiers détecteurs Micromegas fait au CEA-Saclay pour les NSW sont aussi présentés.

The thesis also discusses an upgrade of the ATLAS Muons Spectrometer, namely the New Small Wheel project. In particular, simulation of the cavern background that will affect the upgraded detector and commissioning of the Micromegas modules produced at CEA-Saclay for the New Small Wheel are described.



## Bibliography

- [1] Large Electron-Positron Collider.  
<https://home.cern/about/accelerators/large-electron-positron-collider>.
- [2] Tevatron. <http://www.fnal.gov/pub/tevatron/tevatron-accelerator.html>.
- [3] A. Djouadi, *The Anatomy of electro-weak symmetry breaking. I: The Higgs boson in the standard model*, Phys. Rept. **457** (2008) , [arXiv:hep-ph/0503172](#) [hep-ph].
- [4] T. Hambye and K. Riesselmann Phys. Rev. **D55** (1997) 7255.
- [5] LEP Working Group for Higgs boson searches Collaboration, *Search for the standard model Higgs boson at LEP*, Phys. Lett. **B565** (2003) 61–75, [arXiv:hep-ex/0306033](#) [hep-ex].
- [6] C. The TEVNPH Working Group and D. C. Collaboration, *Updated Combination of CDF and D0 Searches for Standard Model Higgs Boson Production with up to 10.0 fb<sup>-1</sup> of Data*, [arXiv:1207.0449](#) [hep-ex].
- [7] The LEP Electroweak Working Group Collaboration.  
<http://lepewwg.web.cern.ch/LEPEWWG/plots/winter2012/>.
- [8] GFitter group Collaboration. <http://gfitter.desy.de/Files/>.
- [9] C. Anastasiou, C. Duhr, F. Dulat, E. Furlan, T. Gehrmann, F. Herzog, and B. Mistlberger, *Higgs boson gluon fusion production at threshold in N<sup>3</sup>LO QCD*, Phys. Lett. **B737** (2014) 325–328, [arXiv:1403.4616](#) [hep-ph].
- [10] C. Anastasiou, C. Duhr, F. Dulat, E. Furlan, T. Gehrmann, F. Herzog, and B. Mistlberger, *Higgs boson gluon fusion production beyond threshold in N<sup>3</sup>LO QCD*, JHEP **03** (2015) 091, [arXiv:1411.3584](#) [hep-ph].
- [11] C. Anastasiou, C. Duhr, F. Dulat, E. Furlan, T. Gehrmann, F. Herzog, A. Lazopoulos, and B. Mistlberger, *High precision determination of the gluon fusion Higgs boson cross-section at the LHC*, JHEP **05** (2016) 058, [arXiv:1602.00695](#) [hep-ph].
- [12] U. Aglietti, R. Bonciani, G. Degrossi, and A. Vicini, *Two-loop light fermion contribution to Higgs production and decays*, Phys. Lett. **B 595** (2004) 432–441, [arXiv:hep-ph/0404071](#).
- [13] S. Actis, G. Passarino, C. Sturm, and S. Uccirati, *NLO Electroweak Corrections to Higgs Boson Production at Hadron Colliders*, Phys. Lett. **B 670** (2008) 12–17, [arXiv:0809.1301](#) [hep-ph].
- [14] M. Ciccolini, A. Denner, and S. Dittmaier, *Strong and electroweak corrections to the production of Higgs+2jets via weak interactions at the LHC*, Phys. Rev. Lett. **99** (2007) 161803, [arXiv:0707.0381](#) [hep-ph].
- [15] M. Ciccolini, A. Denner, and S. Dittmaier, *Electroweak and QCD corrections to Higgs production via vector-boson fusion at the LHC*, Phys. Rev. **D 77** (2008) 013002, [arXiv:0710.4749](#) [hep-ph].
- [16] K. Arnold et al., *VBFNLO: A parton level Monte Carlo for processes with electroweak bosons*, Comput. Phys. Commun. **180** (2009) 1661–1670, [arXiv:0811.4559](#) [hep-ph].



- [17] P. Bolzoni, F. Maltoni, S.-O. Moch, and M. Zaro, *Higgs production via vector-boson fusion at NNLO in QCD*, Phys. Rev. Lett. **105** (2010) 011801, [arXiv:1003.4451 \[hep-ph\]](#).
- [18] T. Han and S. Willenbrock, *QCD correction to the  $p p \rightarrow W H$  and  $Z H$  total cross-sections*, Phys. Lett. **B 273** (1991) 167–172.
- [19] O. Brein, A. Djouadi, and R. Harlander, *NNLO QCD corrections to the Higgs-strahlung processes at hadron colliders*, Phys. Lett. **B 579** (2004) 149–156, [arXiv:hep-ph/0307206](#).
- [20] M. L. Ciccolini, S. Dittmaier, and M. Kramer, *Electroweak radiative corrections to associated  $WH$  and  $ZH$  production at hadron colliders*, Phys. Rev. **D 68** (2003) 073003, [arXiv:hep-ph/0306234](#).
- [21] LHC Higgs Cross Section Working Group, *Handbook of LHC Higgs Cross Sections: 1. Inclusive observables*, [arXiv:1101.0593 \[hep-ph\]](#).
- [22] ATLAS Collaboration, *Observation of a New Particle in the Search for the Standard Model Higgs Boson with the ATLAS Detector at the LHC*, [arXiv:1207.7214 \[hep-ex\]](#).
- [23] CMS Collaboration, *Observation of a new boson at a mass of 125 GeV with the CMS experiment at the LHC*, [arXiv:1207.7235 \[hep-ex\]](#).
- [24] ATLAS Collaboration, *Combined measurements of the mass and signal strength of the Higgs-like boson with the ATLAS detector using up to  $25 \text{ fb}^{-1}$  of proton-proton collision data*, ATLAS-CONF-2013-014 (March, 2013) .
- [25] ATLAS Collaboration, *Measurements of the properties of the Higgs-like boson in the four lepton decay channel with the ATLAS detector using  $25 \text{ fb}^{-1}$  of proton-proton collision data*, ATLAS-CONF-2013-013 (March, 2013) .
- [26] ATLAS Collaboration, *Study of the spin of the Higgs-like boson in the two photon decay channel using  $20.7 \text{ fb}^{-1}$  of  $pp$  collisions collected at  $\sqrt{s} = 8 \text{ TeV}$  with the ATLAS detector*, ATLAS-CONF-2013-029 (March, 2013) .
- [27] ATLAS Collaboration, *Study of the spin properties of the Higgs-like particle in the  $H \rightarrow WW^{(*)} \rightarrow e\nu\mu\nu$  channel with  $\text{fb}^{-1}$  of  $\sqrt{s} = 8 \text{ TeV}$  data collected with the ATLAS detector*, ATLAS-CONF-2013-031 (March, 2013) .
- [28] John C. Collins and Davison E. Soper, *Angular distribution of dileptons in high-energy hadron collisions*, Phys. Rev. **D16** (1997) .
- [29] ATLAS Collaboration, *Determination of the off-shell Higgs boson signal strength in the high-mass  $ZZ$  final state with the ATLAS detector*, ATLAS-COM-CONF-2014-052 (July, 2014) .
- [30] ATLAS Collaboration, *Combined coupling measurements of the Higgs-like boson with the ATLAS detector using up to  $25 \text{ fb}^{-1}$  of proton-proton collision data*, ATLAS-CONF-2013-034 (March, 2013) .
- [31] ATLAS Collaboration, *Benchmarks for Heavy Higgs boson searches in the electroweak bosons decay channels in the ATLAS detector*, ATL-COM-PHYS-2014-258 (July, 2014) .

- [32] A. Hill and J. van der Bij, *Strongly interacting singlet-doublet Higgs model*, Phys.Rev. **D36** (1987) 3463–3473.
- [33] M. Veltman and F. Yndurain, *Radiative corrections to WW scattering*, Nucl.Phys. **B325** (1989) .
- [34] T. Binoth and J. van der Bij, *Influence of strongly coupled, hidden scalars on Higgs signals*, Z.Phys. **C75** (1997) 17–25, [arXiv:hep-ph/9608245](#) [hep-ph].
- [35] R. Schabinger and J. D. Wells, *A Minimal spontaneously broken hidden sector and its impact on Higgs boson physics at the large hadron collider*, Phys. Rev. **D72** (2005) , [arXiv:hep-ph/9608245](#) [hep-ph].
- [36] B. Patt and F. Wilczek, *Higgs-field portal into hidden sectors*, [arXiv:hep-ph/0605188](#) [hep-ph].
- [37] G. M. Pruna and T. Robens, *The Higgs Singlet extension parameter space in the light of the LHC discovery*, [arXiv:1303.1150](#) [hep-ph].
- [38] LHC Higgs Cross Section Working Group, *Handbook of LHC Higgs Cross Sections: 3. Higgs Properties*, [arXiv:1307.1347](#) [hep-ph].
- [39] A. Djouadi, *The Anatomy of electro-weak symmetry breaking. II: The Higgs bosons in the Minimal Supersymmetric Model*, Phys. Rept. **459** (2008) , [arXiv:hep-ph/0503173](#) [hep-ph].
- [40] J. E. Kim, *Light Pseudoscalars, Particle Physics and Cosmology*, Phys. Rept. **150** (1987) 1–177.
- [41] M. Joyce, T. Prokopec, and N. Turok, *Nonlocal electroweak baryogenesis. Part 2: The Classical regime*, Phys. Rev. **D53** (1996) 2958–2980, [arXiv:hep-ph/9410282](#) [hep-ph].
- [42] ATLAS Collaboration, *Search for an additional, heavy Higgs boson in the  $H \rightarrow ZZ$  decay channel at  $\sqrt{s} = 8$  TeV in pp collision data with the ATLAS detector*, [arXiv:1507.05930](#) [hep-ex].
- [43] John C. Collins and Davison E. Soper, *Search for Scalar Diphoton Resonances in the Mass Range 65–600 GeV with the ATLAS Detector in pp Collision Data at  $\sqrt{s} = 8$  TeV*, PRL **113** (2014) .
- [44] ATLAS Collaboration, *Search for a high-mass Higgs boson decaying to a W boson pair in pp collisions at  $\sqrt{s} = 8$  TeV with the ATLAS detector*, [arXiv:1509.00389](#) [hep-ex].
- [45] S. Gorla, G. Passarino, and D. Rosco, *The Higgs Boson Lineshape*, Nucl.Phys. **B864** (2012) 530–579, [arXiv:1112.5517](#) [hep-ph].
- [46] M. Spira, A. Djouadi, D. Graudenz, and P. M. Zerwas, *Higgs boson production at the LHC*, Nucl. Phys. **B 453** (1995) 17–82, [arXiv:hep-ph/9504378](#).
- [47] D. R. Stefano Gorla, Giampiero Passarino, *The Higgs Boson Lineshape*, [arXiv:1112.5517](#) [hep-ph].
- [48] R. D. Ball et al., *Parton Distribution Benchmarking with LHC Data*, JHEP **04** (2013) 125, [arXiv:1211.5142](#) [hep-ph].
- [49] N. Craig et al., *Searching for Signs of the Second Higgs Doublet*, [arXiv:1305.2424](#) [hep-ph].

- [50] ATLAS Collaboration, *The ATLAS Experiment at the CERN Large Hadron Collider*, Journal of Instrumentation **3** (2008) no. 08, .
- [51] CMS Collaboration, *The CMS Experiment at the CERN LHC*, Journal of Instrumentation **3** (2008) no. 08, .
- [52] ALICE Collaboration, *The ALICE Experiment at the CERN LHC*, Journal of Instrumentation **3** (2008) no. 08, .
- [53] LHCb Collaboration, *The LHCb Detector at the LHC*, Journal of Instrumentation **3** (2008) no. 08, .
- [54] TOTEM Collaboration, *The TOTEM Experiment at the CERN Large Hadron Collider*, Journal of Instrumentation **3** (2008) no. 08, .
- [55] MoEDAL Collaboration, *Technical Design Report of the MoEDAL Experiment*, Tech. Rep. CERN-LHCC-2009-006, CERN, Geneva, 2009.
- [56] LHCf Collaboration, *The LHCf Experiment at the CERN Large Hadron Collider*, Journal of Instrumentation **3** (2008) no. 08, .
- [57] W. Herr and B. Muratori, *Concept of luminosity*, .
- [58] ATLAS Collaboration, *Luminosity determination in pp collisions at  $\sqrt{s} = 8$  TeV using the ATLAS detector at the LHC*, Eur. Phys. J. **C76** (2016) , [arXiv:1608.03953 \[hep-ex\]](https://arxiv.org/abs/1608.03953).
- [59] ATLAS integrated luminosity.  
<https://twiki.cern.ch/twiki/bin/view/AtlasPublic/LuminosityPublicResultsRun2>.
- [60] Rossi L. and Brüning O., *High Luminosity Large Hadron Collider A description for the European Strategy Preparatory Group*, Tech. Rep. CERN-ATS-2012-236, CERN, Geneva, Aug, 2012.
- [61] ATLAS Collaboration Collaboration, *ATLAS inner detector: Technical Design Report, 1*. Technical Design Report ATLAS. CERN, Geneva, 1997.
- [62] ATLAS Collaboration, *The ATLAS TRT Barrel Detector*, Journal of Instrumentation **3** (2008) no. 02, .
- [63] ATLAS Collaboration, *The ATLAS TRT End-Cap detectors*, Journal of Instrumentation **3** (2008) no. 10, .
- [64] ATLAS Collaboration, *Track Reconstruction Performance of the ATLAS Inner Detector at  $\sqrt{s} = 13$  TeV*, Tech. Rep. ATL-PHYS-PUB-2015-018, CERN, Geneva, 2015.
- [65] ATLAS Collaboration, *ATLAS liquid argon calorimeter: Technical Design Report*, .
- [66] ATLAS Collaboration, *Design, Construction and Installation of the ATLAS Hadronic Barrel Scintillator-Tile Calorimeter*, Tech. Rep. ATL-TILECAL-PUB-2008-001, CERN, Geneva, 2007.
- [67] ATLAS Collaboration Collaboration, ATLAS Collaboration, *ATLAS muon spectrometer: Technical Design Report*. Technical Design Report ATLAS. CERN, Geneva, 1997.
- [68] ATLAS magnet system. <http://atlas.cern/discover/detector/magnet-system>.

- [69] S. Hassani, *Studies of the ATLAS Muon Spectrometer with testbeam, cosmics, simulated and real data*, .
- [70] H. van der Graaf et al., *First system performance experience with the ATLAS high-precision muon drift tube chambers*, Nucl. Instrum. Meth. **A419** (1998) 336–341.
- [71] *Electron efficiency measurements with the ATLAS detector using the 2012 LHC proton-proton collision data*, Tech. Rep. ATLAS-CONF-2014-032, CERN, Geneva, Jun, 2014.
- [72] *Electron identification measurements in ATLAS using  $\sqrt{s} = 13$  TeV data with 50 ns bunch spacing*, Tech. Rep. ATL-PHYS-PUB-2015-041, CERN, Geneva, Sep, 2015.
- [73] G. Artoni, G. Barone, K. M. Loew, H. Herde, G. Sciolla, M. Bellomo, M. Goblirsch-Kolb, N. M. Koehler, M. Sioli, R. Nicolaidou, A. Lesage, D. Zhang, S. Hu, S. Zambito, F. Sforza, M. Gignac, I. Nomidis, P. Kluit, and N. van Eldik, *Support Note for 2015 Muon Combined Performance Paper*, Tech. Rep. ATL-COM-PHYS-2015-1149, CERN, Geneva, Sep, 2015.
- [74] M. Cacciari, G. P. Salam, and G. Soyez, *The Anti- $k(t)$  jet clustering algorithm*, JHEP **04** (2008) 063, [arXiv:0802.1189 \[hep-ph\]](#).
- [75] ATLAS Collaboration Collaboration, *Jet energy scale and its systematic uncertainty in proton-proton collisions at  $\sqrt{s}=7$  TeV with ATLAS 2011 data*, Tech. Rep. ATLAS-CONF-2013-004, CERN, Geneva, Jan, 2013.
- [76] C. Sawyer, C. J. Young, C. Issever, and D. Lopez Mateos, *Monte Carlo Calibration and Combination of In-situ Measurements of Jets in ATLAS*, Tech. Rep. ATL-COM-PHYS-2015-071, CERN, Geneva, Jan, 2015.
- [77] *Jet Calibration and Systematic Uncertainties for Jets Reconstructed in the ATLAS Detector at  $\sqrt{s} = 13$  TeV*, Tech. Rep. ATL-PHYS-PUB-2015-015, CERN, Geneva, Jul, 2015.
- [78] A. Collaboration, *Selection of jets produced in 13TeV proton-proton collisions with the ATLAS detector*, Tech. Rep. ATLAS-COM-CONF-2015-024, CERN, Geneva, May, 2015.
- [79] *Tagging and suppression of pileup jets with the ATLAS detector*, Tech. Rep. ATLAS-CONF-2014-018, CERN, Geneva, May, 2014.
- [80] ATLAS Collaboration Collaboration, ATLAS Collaboration, *Technical Design Report for the Phase-I Upgrade of the ATLAS TDAQ System*, Tech. Rep. CERN-LHCC-2013-018. ATLAS-TDR-023, Sep, 2013.
- [81] T. Kawamoto, S. Vlachos, L. Pontecorvo, J. Dubbert, G. Mikenberg, P. Iengo, C. Dallapiccola, C. Amelung, L. Levinson, R. Richter, and D. Lellouch, *New Small Wheel Technical Design Report*, Tech. Rep. CERN-LHCC-2013-006. ATLAS-TDR-020, CERN, Geneva, Jun, 2013.
- [82] ATLAS Collaboration, *ATLAS Liquid Argon Calorimeter Phase-I Upgrade Technical Design Report*, Tech. Rep. CERN-LHCC-2013-017. ATLAS-TDR-022, Sep, 2013.
- [83] S. Majewski, et al., *A Thin Multiwire Chamber Operating In The High Multiplication Mode*, Nucl. Instrum. Meth. **A217** (1983) 265.

- [84] Y. Giomataris, P. Rebougeard, J. Robert, and G. Charpak, *MICROMEGAS: A High granularity position sensitive gaseous detector for high particle flux environments*, Nucl. Instrum. Meth. **A376** (1996) 29–35.
- [85] OPAL experiment. <http://opal.web.cern.ch/Opal/>.
- [86] V. Peskov, M. Cortesi, R. Chechik, and A. Breskin, *Further evaluation of a THGEM UV-photon detector for RICH - comparison with MWPC*, JINST **5** (2010) , [arXiv:1008.0151](https://arxiv.org/abs/1008.0151) [physics.ins-det].
- [87] J. Galan et al., *An ageing study of resistive micromegas for the HL-LHC environment*, [arXiv:1301.7648](https://arxiv.org/abs/1301.7648).
- [88] P. Iengo et al., *Development of large size Micromegas detector for the upgrade of the ATLAS muon system*, Nucl. Instrum. Meth. **A617** (2010) 161–165.
- [89] Nygren D., *Proposal for a PEP Facility based on the TPC*, .
- [90] M<sup>3</sup> experiment.  
<https://indico.cern.ch/event/451078/contributions/1113844>.
- [91] P. Baron, E. Delagnes, C. Flouzat, F. Guilloux, *DREAM, a Front End ASIC for CLAS12 detector. User Manual*, tech. rep., CEA, Saclay, Jan, 2014.
- [92] Lawrence Jones, *APV25-S1 User Guide Version 2.2*, tech. rep., Sep, 2001.
- [93] S. Baranov, M. Bosman, I. Dawson, V. Hedberg, A. Nisati, and M. Shupe, *Estimation of Radiation Background, Impact on Detectors, Activation and Shielding Optimization in ATLAS*, Tech. Rep. ATL-GEN-2005-001, CERN, Geneva, Jan, 2005.
- [94] Geant4 physics lists.  
[http://geant4.cern.ch/support/proc\\_mod\\_catalog/models/](http://geant4.cern.ch/support/proc_mod_catalog/models/).
- [95] Y. Chan, T. Koi, and C. Young, *Expected Muon Spectrometer Background in Run 2*, Tech. Rep. ATL-MUON-INT-2014-004, CERN, Geneva, Jun, 2014.
- [96] J. Bougher, D. Brown, T. Koi, P. Sherwood, D. Wright, and C. Young, *A FLUGG-based Cavern background Simulation Application*, Tech. Rep. ATL-COM-SOFT-2011-032, CERN, Geneva, Oct, 2011.
- [97] Z. Marshal and A. Saproinov, *G4 Cavern Background Simulation plots*, Tech. Rep. ATL-COM-MUON-2014-018, CERN, Geneva, Feb, 2014.
- [98] S. Agostinelli et al., *GEANT4: A simulation toolkit*, Nucl. Instrum. Meth. **A 506** (2003) 250–303.
- [99] J. Apostolakis, G. Folger, V. Grichine, A. Heikkinen, A. Howard, V. Ivanchenko, P. Kaitaniemi, T. Koi, M. Kosov, J. M. Quesada, A. Ribon, V. Uzhinskiy, and D. Wright, *Progress in hadronic physics modelling in Geant4*, Journal of Physics: Conference Series **160** (2009) no. 1, 012073.
- [100] ATHENA software framwork,.  
<http://atlas-computing.web.cern.ch/atlas-computing/packages/athenaCore/athenaCore>
- [101] A. Dell’Acqua, C. Maiani, Z. Marshall, and J. Penwell, *The simulation of cavern background in ATLAS using Geant4*, Tech. Rep. ATL-COM-SOFT-2011-010, CERN, Geneva, May, 2011.

- [102] ATLAS Collaboration, ATLAS Collaboration, *The ATLAS simulation Infrastructure*, Eur. Phys. J. **C 70** (2010) 823–874, [arXiv:1005.4568](#) [physics.ins-det].
- [103] S. Alioli, P. Nason, C. Oleari, and E. Re, *NLO Higgs boson production via gluon fusion matched with shower in POWHEG*, JHEP **04** (2009) 002, [arXiv:0812.0578](#) [hep-ph].
- [104] P. Nason and C. Oleari, *NLO Higgs boson production via vector-boson fusion matched with shower in POWHEG*, JHEP **02** (2010) 037, [arXiv:0911.5299](#) [hep-ph].
- [105] T. Sjostrand, S. Mrenna, and P. Z. Skands, *A Brief Introduction to PYTHIA 8.1*, Comput. Phys. Commun. **178** (2008) 852–867, [arXiv:0710.3820](#) [hep-ph].
- [106] D. J. Lange, *The EvtGen particle decay simulation package*, Nucl. Instrum. Meth. **A462** (2001) 152–155.
- [107] T. Gleisberg, S. Hoeche, F. Krauss, M. Schonherr, S. Schumann, F. Siegert, and J. Winter, *Event generation with SHERPA 1.1*, JHEP **02** (2009) 007, [arXiv:0811.4622](#) [hep-ph].
- [108] T. Sjostrand, S. Mrenna, and P. Z. Skands, *PYTHIA 6.4 Physics and Manual*, JHEP **05** (2006) 026, [arXiv:hep-ph/0603175](#).
- [109] P. Golonka and Z. Was, *PHOTOS Monte Carlo: A Precision tool for QED corrections in Z and W decays*, Eur. Phys. J. **C 45** (2006) 97–107, [arXiv:hep-ph/0506026](#).
- [110] S. Jadach, Z. Was, R. Decker, and J. H. Kuhn, *The tau decay library TAUOLA: Version 2.4*, Comput. Phys. Commun. **76** (1993) 361–380.
- [111] P. Golonka et al., *The tauola-photos-F environment for the TAUOLA and PHOTOS packages, release II*, Comput. Phys. Commun. **174** (2006) 818–835.
- [112] Triggers.  
<https://twiki.cern.ch/twiki/bin/viewauth/AtlasProtected/HiggsZZ1111PreparationRun1>,  
[https://twiki.cern.ch/twiki/bin/view/Atlas/LowestUnprescaled#Triggers\\_in\\_2015](https://twiki.cern.ch/twiki/bin/view/Atlas/LowestUnprescaled#Triggers_in_2015).
- [113] D. Adams and t. . Anastopoulos, et al. tech. rep.
- [114] ATLAS H4l Group, *Common supporting note for the  $H \rightarrow 4\ell$  channel: Event selection, background estimates, performance studies, etc.*, Tech. Rep. ATL-COM-PHYS-2015-1277, CERN, Geneva, Oct, 2015.
- [115] HSG2, *Event selection and background estimation in the  $H \rightarrow 4\ell$  channel at  $\sqrt{s} = 13$  TeV - ICHEP 2016 Analysis*, ATL-COM-PHYS-2016-413.
- [116] ATLAS Collaboration, *Heavy Higgs boson searches in the four-lepton channel with the ATLAS detector using  $\sqrt{s} = 8$  TeV data.*, Tech. Rep. ATL-COM-PHYS-2014-272, CERN, Geneva, Apr, 2014.
- [117] J. Meyer, S. Heim, R. Di Nardo, E. Mountricha, and A. Schaffer, *Theoretical Uncertainties Occuring In  $H \rightarrow ZZ$  analyses.*, .
- [118] K. S. Cranmer, *Kernel estimation in high-energy physics*, Comput. Phys. Commun. **136** (2001) 198–207, [arXiv:hep-ex/0011057](#) [hep-ex].

- [119] ATLAS Collaboration, *Study of the Higgs boson properties and search for high-mass scalar resonances in the  $H \rightarrow ZZ^* \rightarrow 4\ell$  decay channel*, Tech. Rep. ATL-COM-PHYS-2016-896, CERN, Geneva, Jul, 2016.
- [120] Pearson, Karl, *On the criterion that a given system of deviations from the probable in the case of a correlated system of variables is such that it can be reasonably supposed to have arisen from random sampling*, 1900.
- [121] ATLAS Collaboration, *Search for heavy Higgs bosons in the four-lepton decay channel with the ATLAS detector using  $\sqrt{s} = 13$  TeV data.: Supporting note*, Tech. Rep. ATL-COM-PHYS-2015-1276, CERN, Geneva, Oct, 2015.
- [122] L. A. Piegl and W. Tiller, *The NURBS book: Monographs in visual communication*, ch. B-Spline Basis Function. Springer, 2nd ed., 1997.
- [123] ATLAS Collaboration, *Supporting note for the search for additional heavy Higgs bosons in the  $4\ell$  final state*, Tech. Rep. ATL-COM-PHYS-2016-415, CERN, Geneva, May, 2016.
- [124] G. Cowan, K. Cranmer, E. Gross, and O. Vitells, *Asymptotic formulae for likelihood-based tests of new physics*, Eur. Phys. J. **C 71** (2011) 1554, [arXiv:1007.1727](https://arxiv.org/abs/1007.1727) [physics.data-an].
- [125] A. L. Read, *Presentation of search results: The  $CL(s)$  technique*, J. Phys. G **28** (2002) 2693–2704.
- [126] J. Alwall, M. Herquet, F. Maltoni, O. Mattelaer, and T. Stelzer, *MadGraph 5 : Going Beyond*, JHEP **06** (2011) 128, [arXiv:1106.0522](https://arxiv.org/abs/1106.0522) [hep-ph].
- [127] NNPDF. <https://nnpdf.hepforge.org>.
- [128] MCFM. <https://mcfm.fnal.gov>.
- [129] W. Lukas, *Fast Simulation for ATLAS: Atlfast-II and ISF*, Tech. Rep. ATL-SOFT-PROC-2012-065, CERN, Geneva, Jun, 2012.
- [130] Parton luminosity for different PDFs. <http://apfel.mi.infn.it>.
- [131] X. Ju, A. Schaffer, E. Mountricha, D. Denysiuk, R. Nicolaidou, P. Podberezko, H. Yang, J. Li, A. Maslennikov, S. Hassani, S. L. Wu, and M. Cano Bret, *Search for heavy Higgs bosons in the four-lepton decay channel with the ATLAS detector using  $36.5 \text{ fb}^{-1}$  of  $\sqrt{s} = 13$  TeV data*, Tech. Rep. ATL-COM-PHYS-2016-1602, CERN, Geneva, Nov, 2016.
- [132] D. J. Griffiths, *Introduction to elementary particles; 2nd rev. version*. Physics textbook. Wiley, New York, NY, 2008.
- [133] M. E. Peskin and D. V. Schroeder, *An Introduction to Quantum Field Theory; 1995 ed.* Westview, Boulder, CO, 1995.

**Titre:** Recherche de bosons de Higgs de grande masse se désintégrant en 4 leptons a l'expérience ATLAS

**Mots clés:** Higgs boson, LHC, ATLAS

**Résumé:** Le sujet principal de la thèse est sur la recherche de bosons de Higgs de grande masse se désintégrant en 4 leptons grâce aux données du Run-2 obtenues par le détecteur ATLAS auprès du Large Hadron Collider - LHC. L'analyse correspondante, publiée à la conférence ICHEP de 2016 avec un échantillon de données de  $14.8 \text{ fb}^{-1}$  à 13 TeV, est décrite en détail. Et elle a été remise à jour dans cette thèse avec un échantillon de données de  $36.1 \text{ fb}^{-1}$  à 13 TeV. Cette recherche de bosons de Higgs de grande masse se fait indépendamment du modèle pour plusieurs largeurs de masse du boson : approximation de largeur de masse étroite où on suppose la largeur de masse naturelle du signal incluant un effet d'interférence avec le bruit de fond du Modèle Standard. La recherche de signal qui bénéficie le plus de l'ajout de contrainte discriminante est aussi présentée pour l'hypothèse d'un signal de boson scalaire. Cette modification permet d'améliorer la sensibilité de cette analyse de 25%.

Cette thèse présente aussi une amélioration du spectromètre à muons d'Atlas venant du projet de Nouvelle Petite Roue - NSW pour New Small Wheel en anglais. En particulier sont décrits la simulation du bruit de fond de la caverne qui affectera les futurs détecteurs, ainsi que la préparation et la mise en service des modules Micromegas qui seront produits au CEA-Saclay pour l'expérience Atlas.

**Title:** Heavy Higgs boson search in the four lepton decay channel with the ATLAS detector

**Keywords:** Higgs boson, LHC, ATLAS

**Abstract:** The thesis is focused on the heavy Higgs boson search in four lepton decay channel with Run-2 data from the ATLAS detector at the Large Hadron Collider. The analysis published at ICHEP 2016 conference that is based on  $14.8 \text{ fb}^{-1}$  of 13 TeV data is described in details, while the updated results that include  $36.1 \text{ fb}^{-1}$  of 13 TeV data are shown as well. The heavy Higgs search is carried out in a model independent way and it is covering different signal width hypotheses: narrow width approximation that assumes the signal natural width to be negligible comparing to the detector resolution, and the large width assumption including an effect of the interference with the Standard Model backgrounds. The search that benefits from additional kinematic discriminant under the scalar signal assumption is presented as well. This modification allows to increase the analysis sensitivity up to 25%.

The thesis also discusses an upgrade of the ATLAS Muons Spectrometer, namely the New Small Wheel project. In particular, simulation of the cavern background that will affect the upgraded detector and commissioning of the Micromegas modules produced at CEA-Saclay for the New Small Wheel are described.